**CENTRO DE INVESTIGACIÓN Y DE ESTUDIOS AVANZADOS DEL INSTITUTO POLITÉCNICO NACIONAL**

**Unidad Saltillo**

# Síntesis y evaluación de nanocatalizadores basados en Pd soportados en Vulcan funcionalizado con compuestos organometálicos de Cu para las Reacciones de Oxidación de Etanol y de Reducción de Oxígeno

TESIS

Presenta:

M. C. Perla Cecilia Meléndez González

Para obtener el grado de:

Doctor en ciencias

En la especialidad de:

Nanociencias y Nanotecnología

Director de Tesis:

Dr. Francisco Javier Rodríguez Varela

Ciudad de México. Noviembre, 2021

**CENTRO DE INVESTIGACIÓN Y DE ESTUDIOS AVANZADOS DEL INSTITUTO POLITÉCNICO NACIONAL**

**Unidad Saltillo**

# Synthesis and evaluation of Pd-based nanocatalysts supported on Vulcan functionalized with Cu organometallic compounds for the Ethanol Oxidation and Oxygen Reduction Reactions.

THESIS

By:

M. C. Perla Cecilia Meléndez González

A dissertation submitted in partial satisfaction of the requirements for the degree of:

Doctor en ciencias

In:

Nanociencias y Nanotecnología

Thesis Advisor:

Dr. Francisco Javier Rodríguez Varela

Ciudad de México. November, 2021

*I put my heart and soul into my work, and I have lost my mind in the process.*

*Vicent Van Gogh*

## Dedication

With all my love to heaven.

I dedicate this thesis to my admirable and beloved mother.

# Acknowledgments

To God for giving me strength during all this time, and for achieving the culmination of this project. I thank with all my heart to my parents for their unconditional support despite every situation. To my brothers for believing in me and standing by my side. Especially to Rolando Meléndez for all his effort.

I would like to sincerely thank my thesis director Dr. Javier Rodríguez Varela for his time, unconditional support, patience, and dedication. Thank you for letting me be part of this project. I thank Ivonne and the excellent group of collaborators that has been formed. I also thank Dra. Esther Sánchez Castro for her special collaboration. I especially appreciate, to Wilian Pech, for his support always, advice, and excellent talks. In a special way to my lab partners and friends: César Sarabia, Selvia, Juan Carlos, Vianney, Andrea, Gerardo, Maricruz, Anayantzin, Chuyito, Charly, Nora, and Sara. Thank you all for making this job even more fun for the beautiful friendship, and for accompanying me in every moment.

To the Université de Poitiers for the academic stay especially to Dr. Teko W. Napporn for his patience and support. I am infinitely grateful to Paul, Thammyres, Charly, Nolween, Carlos, and Paula. For the much missed "c'est l'heure du café", meals, laughter, encouragement, and for their unconditional support.

I thank CINVESTAV Saltillo and its staff for providing me with the facilities to perform this work. I thank CONACYT for the essential financial support provided for the development of this thesis.

Finally, I would like to thank all the people who shared their knowledge with me to complete this thesis, thanks a lot.

# Content

Acronyms and nomenclature……i

List of tables……..ii

List of figures……..iii

Abstract……..iv

Resumen……. v

Introduction……vi

**Chapter I Background** ..... **1**

1.1 Anion Exchange Membrane Direct Ethanol Fuel Cells (AEM-DEFC) ..... 1

1.1.1 Oxygen Reduction Reaction (ORR) ..... 3

1.1.2 Ethanol Oxidation Reaction (EOR) ..... 4

1.2 Nanocatalysts ..... 5

1.2.1 Pd-based nanocatalyst for the ORR ..... 6

1.2.2 Pd-based nanocatalysts for the EOR ..... 7

1.3 Carbon supports : Vulcan XC-72 (C) ..... 10

1.4 Functionalization of carbon supports ..... 12

1.5 Organometallic compounds as functionalizing agents ..... 13

1.6 References ..... 16

**Chapter II Hypothesis and objectives** ..... **28**

2.1 Hypothesis ..... 29

2.2 General objective ..... 29

2.3 Specific objectives ..... 29

**Chapter III Experimental Section** ..... **31**

3.1 Chemical reagents and gases ..... 32
3.2 Synthesis of copper organometallic compounds……..32
3.2.1 Synthesis of mesityl Cu (Cu-mes) ..... 32
3.2.2 Synthesis of Cu compound coordinated with 3,5 dimethylpyrazole (dmpz) and terephthalic acid (L2) (Cu(dmpz)L2) ..... 33
3.3 Functionalization of C supports: synthesis of $C_{Cu\text{-}mes}$ and $C_{Cu(dmpz)L2}$ ..... 34
3.4 Synthesis of nanocatalysts based on Pd ..... 35
3.5 Physicochemical characterization ..... 36
3.5.1 Nuclear Magnetic Resonance (NRM) ..... 36
3.5.2 Fourier Transform Infrared Spectroscopy (FT-IR) ..... 36
3.5.3 Raman Spectroscopy ..... 36
3.5.4 X-Ray Diffraction (XRD) ..... 37
3.5.5 Scanning Electron Microscopy coupled with Energy Dispersive Spectroscopy (SEM-EDS) ..... 37
3.5.6 High-Resolution Transmission Electron Microscopy (HR-TEM) ..... 38
3.5.7 X-Ray Photoelectron Spectroscopy (XPS) ..... 38
3.6 Electrochemical Characterization ..... 38
3.6.1 Electrochemical half cell ..... 38
3.6.2 Cyclic voltammograms (CVs) ..... 39
3.6.3 Evaluation of catalytic activity for the ORR ..... 40
3.6.4 Evaluation of catalytic activity for the EOR ..... 41
3.6.5 Accelerated degradation test (ADT) ..... 41
3.6.6 CO-stripping ..... 41
3.6.7 Anion Exchange Membrane Direct Ethanol Fuel Cell (AEM-DEFC) ..... 42
3.6.8 Analysis of reaction products by High-Performance Liquid Chromatography (HPLC) ..... 45
3.7 References ..... 46

**Chapter IV Electrochemical evaluation of the bifunctional Pd-$CeO_{2\text{-}NR}$/C nanocatalyst for the EOR and the ORR ..... 49**

4.1 Physicochemical characterization ..... 50

4.1.1 XRD ..... 50

4.1.2 Chemical composition by EDS-SEM ..... 51

4.1.3 Morphology and chemical elemental mapping by FE-SEM ..... 52

4.1.4 Morphology by TEM ..... 54

4.1.5 XPS ..... 55

4.2 Electrochemical Characterization ..... 60

4.2.1 Evaluation of catalytic activity for the ORR ..... 63

4.2.2 Evaluation of catalytic activity for the EOR ..... 71

4.3 Conclusion ..... 74

4.4 References ..... 75

**Chapter V Evaluation of Pd nanocatalysts supported on Vulcan XC-72 functionalized with Cu organometallic compounds for the EOR. ..... 83**

5.1 Physicochemical characterization of Cu organometallic compounds ..... 84

5.1.1 $^{1}$H-NMR ..... 84

5.1.2 FE-SEM and EDS ..... 85

5.1.3 FT-IR ..... 86

5.2 Physicochemical characterization of the functionalized carbon. ..... 87

5.2.1 FT-IR ..... 87

5.2.2 Raman ..... 88

5.2.3 XRD ..... 91

5.2.4 SEM-EDS and FE-SEM ..... 92

5.2.5 XPS ..... 94

5.3 Physicochemical characterization of the nanocatalysts ..... 98

5.3.1 XRD ..... 98
5.3.2 FE-SEM and EDS ..... 100
5.3.3 Raman ..... 102
5.3.4 XPS ..... 104
5.4 Electrochemical characterization of the nanocatalysts ..... 109
5.5 Conclusions ..... 123
5.6 References ..... 124
**Chapter VI Evaluation of Pd-$CeO_{2\text{-}NR}$ nanocatalysts supported on Vulcan XC-72 functionalized with Cu organometallic compounds for the EOR. ..... 133**
6.1 Physicochemical characterization of nanocatalysts ..... 134
6.1.1 XRD ..... 134
6.1.2 FE-SEM and EDS ..... 136
6.1.3 XPS ..... 138
6.2 Electrochemical characterization of nanocatalysts ..... 143
6.3 Conclusions ..... 153
6.4 References ..... 153
**Appendix Academic production ..... 157**

# Acronyms and nomenclature

| | |
|---|---|
| **$^{1}$H-NMR** | Proton Nuclear Magnetic Resonance Spectroscopy |
| **ADT** | Accelerated Degradation Test |
| **AEM-DEFC** | Anion Exchange Membrane Direct Ethanol Fuel Cell |
| **AEMFCs** | Anion Exchange Membrane Fuel Cells |
| **$ECSA_{PdO}$** | Electrochemically active surface area from PdO reduction region |
| **$ECSA_{CO}$** | Electrochemically active surface area from CO-stripping |
| **EOR** | Ethanol Oxidation Reaction |
| **ORR** | Oxygen Reduction Reaction |
| **RHE** | Reversible Hydrogen Electrode |
| **XPS** | X-Ray Photoelectron Spectroscopy |
| **XRD** | X-Ray Diffraction |
| **FT-IR** | Fourier Transformed Infrared Spectroscopy |
| **BE** | Binding energy (eV) |
| **EtOH** | Ethanol |
| **$a_{fcc}$** | Lattice parameter |
| **$CeO_{2\text{-}NR}$** | Cerium oxide nanorods |
| **$CO_{ads}$** | CO adsorbed |
| **Cu(dmpz)L2** | Copper (dmpz= dimethylpyrazole, L2= terephthalic acid) |
| **Cu-mes** | Mesityl copper |
| **d** | Crystallite size |
| **D** | Alloy percentage |
| **$E_{onset}$** | Onset potential |

| | |
|---|---|
| $\mathbf{E_{ox}}$ | $CO_{ads}$ oxidation peak potential |
| $\mathbf{E_a}$ | Anode open circuit potential |
| $\mathbf{E_c}$ | Cathode open circuit potential |
| $\mathbf{H_{ads}}$ | Hydrogen adsorption region |
| $\mathbf{H_{des}}$ | Hydrogen desorption region |
| $\mathbf{HO_2^-}$ | Hydroperoxyl ion |
| **n** | Electron transfer number |
| **i** | Current |
| $\mathbf{i_k}$ | Kinetic current |
| $\mathbf{i_R}$ | Ring current |
| $\mathbf{i_m}$ | Mass activity |
| $\mathbf{i_s}$ | Specific activity |
| **j** | Current density |
| $\mathbf{j_b}$ | Peak current of the EOR in the backward scan |
| $\mathbf{j_f}$ | Peak current of the EOR in the forward scan |
| $\mathbf{j_m}$ | Mass current density |
| $\mathbf{P_{cell}}$ | Cell power density |

# List of tables

**Table 4.1** Physicochemical characteristics of Pd-$CeO_{2\text{-}NR}$/C and Pd/C. ..... 51
**Table 4.2** XPS parameters of Pd/C and Pd-$CeO_{2\text{-}NR}$/C. ..... 58
**Table 4.3** ECSA values and electrochemical parameters of the nanocatalysts during the ORR before and after ADT ..... 62
**Table 4.4** Electrochemical parameters of the ORR at Pd-baes nanocatalysts. ..... 67
**Table 4.5** Mass and specific activity of Pd/C and Pd-$CeO_{2\text{-}NR}$/C for the ORR. ..... 70
**Table 4.6** Electrochemical parameters for EOR at Pd/C and Pd-$CeO_{2\text{-}NR}$/C. ..... 73
**Table 5.1.** $^{1}$H-NMR chemical shift of Cu-mes. ..... 85
**Table 5.2.** Chemical composition of Cu-mes. ..... 85
**Table 5.3** Raman data of C, $C_{Cu\text{-}mes}$, and $C_{CudmpzL2}$. ..... 91
**Table 5.4.**Chemical composition of C, $C_{Cu\text{-}mes}$ and $C_{Cu(dmpz)L2}$. ..... 93
**Table 5.5** XPS parameters of $C_{Cu\text{-}mes}$ and $C_{Cu(dmpz)L2}$. ..... 97
**Table 5.6** Crystallite size and structural parameters of nanocatalysts. ..... 100
**Table 5.7**. Chemical composition of Pd/$C_{Cu\text{-}mes}$ ..... 101
**Table 5.8** Raman data of Pd/C, Pd/$C_{Cu\text{-}mes}$ and Pd/$C_{Cu(dmpz)L2}$. ..... 104
**Table 5.9** XPS parameters of Pd/$C_{Cu\text{-}mes}$ and Pd/$C_{Cu(dmpz)L2}$. ..... 107
**Table 5.10** Electrochemical parameters of the CO-stripping at the nanocatalysts. 112
**Table 5.11** Electrochemical parameters of the EOR and $ECSA_{PdO}$ values at the nanocatalysts. ..... 114
**Table 5.12** Electrochemical parameters of the EOR at Pd-based nanocatalysts. ..... 118
**Table 5.13** Percentage of acetate formed during electrolysis of ethanol at 0.8 V/RHE on the nanocatalysts. ..... 120
**Table 5.14** OCV and $P_{cell}$ values of Pd/C, Pd/$C_{Cu\text{-}mes}$ and Pd/$C_{Cu(dmpz)L2}$. ..... 123
**Table 5.15** OCV and $P_{cell}$ at Pd-based nanocatalysts. ..... 123
**Table 6.1** Crystallite size of nanocatalysts. ..... 135
**Table 6.2** Structural parameters of nanocatalysts obtained from the (111) plane. 136
**Table 6.3**. Chemical composition of Pd-$CeO_{2\text{-}NR}$/$C_{Cu\text{-}mes}$. ..... 137
**Table 6.4** XPS parameters of Pd-$CeO_{2\text{-}NR}$/$C_{Cu\text{-}mes}$ and Pd Pd-$CeO_{2\text{-}NR}$ /$C_{Cu(dmpz)L2}$. ..... 142
**Table 6.5** Electrochemical parameters of the EOR at the nanocatalysts. ..... 146
**Table 6.6** Electrochemical parameters of the EOR at Pd-based nanocatalysts. ..... 149
**Table 6.7** Percentage of acetate ion produced during electrolysis for 4 h at 0.8 V/RHE on the nanocatalysts. ..... 150

# List of figures

**Figure 1.1** Scheme of an AEM-DEFC. 2
**Figure 1.2** Pathways of the ORR in alkaline media. 4
**Figure 1.3** Schematic representation of Vulcan XC-72 structure 11
**Figure 1.4** TEM micrograph of a Pd/C nanocatalysts showing the morphology of Vulcan. 11
**Figure 1.5** Structure of mesytil copper. 15
**Figure 1.6** Structure of Cu(dmpz)L2. 16
**Figure 3.1** Reactions during the synthesis of Cu-mes. 33
**Figure 3.2** Reactions during the synthesis of Cu(dmpz)L2. 34
**Figure 3.3** Scheme of the experimental procedure for the synthesis of $C_{Cu\text{-}mes}$. 35
**Figure 3.4** Scheme of the reactions of the experimental procedure to synthesize Pd-$CeO_{2\text{-}NR}$/C by the polyol method. 36
**Figure 3.5** CV of Pd/C. Electrolyte: $N_2$-satured 0.5 mol $L^{-1}$ KOH. Scan rate: 20 mV $s^{-1}$. 39
**Figure 3.6** CO-stripping at Pd/C. The $CO_{des}$ peak is highlighted in grey. Electrolyte: Ar-satured 0.5 mol $L^{-1}$ KOH. Scan rate: 20 mV $s^{-1}$. 42
**Figure 3.7** a) AEM-DEFC set up and b) imagen of the one of the electrodes used in the fuel cell. 44
**Figure 3.8** Scheme of the fuel cell configuration 45
**Figure 3.9** Configuration of the AEM-DEFC during electrolysis of ethanol. 46
**Figure 4.1** XRD patterns of Pd/C and Pd-$CeO_{2\text{-}NR}$/C. 50
**Figure 4.2** High magnification FE-SEM micrographs of a) Pd/C and b) Pd-$CeO_{2\text{-}NR}$/C. 52
**Figure 4.3** a) FE-SEM image and b) C, c) Pd, and d) O elemental mapping of Pd/C. 53
**Figure 4.4** a) FE-SEM image and b) C, c) Pd, d) O and e) Ce elemental mapping of Pd-$CeO_{2\text{-}NR}$/C 53
**Figure 4.5** TEM micrographs and histograms of average metal particle size distribution of Pd/C (a-b) and Pd-$CeO_{2\text{-}NR}$/C (c-d). 54
**Figure 4.6** XPS spectra of Pd/C in the a) Pd 3d, b) C 1s and c) O 1s regions, and Pd-$CeO_{2\text{-}NR}$/C in the d) Pd 3d, e) C 1s, f) O 1s and g) Ce 3d regions. 56
**Figure 4.7** CVs before and after of ADT of a) Pd/C, and b) Pd-$CeO_{2\text{-}NR}$/C. Electrolyte: $N_2$-satured 0.5 mol $L^{-1}$ KOH. Scan rate: 20 mV $s^{-1}$. 61

**Figure 4.8** ECSA retention after ADT of Pd/C and Pd-$CeO_{2-NR}$/C. ..... 62
**Figure 4.9** Polarization curves of the ORR (a-b) and $i_R$ collected (c-d) before and after ADT at Pd/C. Scan rate 5 mV $s^{-1}$. Electrolyte: $O_2$-satured 0.5 mol $L^{-1}$ KOH. Ring polarized at 1.2 V/RHE. ..... 63
**Figure 4.10** Polarization curves of the ORR (a-b) and $i_R$ collected (c-d) before and after ADT at Pd-$CeO_{2-NR}$/C. Scan rate 5 mV $s^{-1}$. Electrolyte: $O_2$-satured 0.5 mol $L^{-1}$ KOH. Ring polarized at 1.2 V/RHE. ..... 65
**Figure 4.11** Curves of % $HO_2^-$ (a-b) and n (c-d) during the ORR in Pd/C and Pd-$CeO_{2-NR}$/C before and after of ADT. Electrolyte: 0.5 mol $L^{-1}$ KOH saturated with $O_2$. $\omega$= 1600 rpm. ..... 66
**Figure 4.12** Mass and specific activity plots before (a-b) and after (c-d) ADT of the ORR on Pd/C and Pd-$CeO_{2-NR}$/C nanocatalysts. Electrolyte: 0.5 mol $L^{-1}$ KOH saturated with $O_2$. $\omega$= 1600 rpm. ..... 68
**Figure 4.13** Polarization curves for EOR before and after ADT at a) Pd/C and b) Pd-$CeO_{2-NR}$/C. Electrolyte: $N_2$-satured 0.5 mol $L^{-1}$ KOH. Scan rate: 20 mV $s^{-1}$. ..... 72
**Figure 5.1.** $^1$H-NMR ($(CD_3)CO$, 500mHz) spectrum of Cu-mes. ..... 845
**Figure 5.2** a) and b) high magnification FE-SEM micrographs of Cu-mes. ..... **¡Error! Marcador no definido.**7
**Figure 5.3** FT-IR spectra of the Cu-mes and Cu(dmpz)L2organometallic compounds. ..... 878
**Figure 5.4** FT-IR spectra of C, $C_{Cu\text{-}mes}$ and $C_{Cu(dmpz)L2}$. ..... 889
**Figure 5.5** Raman spectra of a) C, b) $C_{Cu\text{-}mes}$ and c) $C_{Cu(dmpz)L2}$. ..... 90
**Figure 5.6** Schematic representation of the interaction between organometallic compounds and C. ..... 891
**Figure 5.7** XRD patterns of C, $C_{Cu\text{-}mes}$ and $C_{Cu(dmpz)L2}$. ..... 923
**Figure 5.8** a) and b) high magnification FE-SEM micrographs of $C_{Cu\text{-}mes}$. ..... 934
**Figure 5.9** a) Distribution of C, O, and Cu elements and b) C, c) O and d) Cu the elemental mapping of $C_{Cu\text{-}mes}$. ..... 945
**Figure 5.10** XPS spectra of $C_{Cu\text{-}mes}$ in the a) C 1s, b) O 1s and c) Cu 2p regions, and $C_{Cu(dmpz)L2}$ in the d) C 1s, e) O 1s and f) Cu 2p regions. ..... 967
**Figure 5.11** XRD patterns of nanocatalysts. ..... 100
**Figure 5.12** a) and b) high magnification FE-SEM micrographs of Pd/$C_{Cu\text{-}mes}$. ..... 10102
**Figure 5.13** a) FE-SEM imagen and b) C, c) Pd, d) O and e) Cu elemental mapping of Pd/$C_{Cu\text{-}mes}$. ..... **¡Error! Marcador no definido.**3

**Figure 5.14** Raman spectra of a) Pd/C, b) Pd/$C_{Cu\text{-}mes}$, and c) Pd/$C_{Cu(dmpz)L2}$. ..... 1034
**Figure 5.15** XPS spectra of Pd/$C_{Cu\text{-}mes}$ in the a) C 1s, b) O 1s, c) Pd 3d and d) Cu 2p regions. ..... 1056
**Figure 5.16** XPS spectra of Pd/$C_{Cu(dmpz)L2}$ in the a) C 1s, b) O 1s, c) Pd 3d and d) Cu 2p regions. ..... 1078
**Figure 5.17** CVs of Pd/C, Pd/$C_{Cu\text{-}mes}$ and Pd/$C_{Cu(dmpz)L2}$. Electrolyte: 0.5 mol $L^{-1}$ KOH. Scan rate: 20 mV $s^{-1}$. ..... 110
**Figure 5.18** CO-stripping curves at the nanocatalysts. Electrolyte: 0.5 mol $L^{-1}$ KOH. Scan rate: 20 mV $s^{-1}$. ..... 1112
**Figure 5.19** Polarization curves of the EOR at Pd/C, Pd/$C_{Cu\text{-}mes}$ and Pd/$C_{Cu(dmpz)L2}$. Electrolyte: 0.5 KOH mol $L^{-1}$+ 0.5 mol $L^{-1}$ solution EtOH. Scan rate: 20 mV $s^{-1}$..... 1134
**Figure 5.20** a) CVs and b) polarization curves of EOR before and after of ADT of Pd/$C_{Cu\text{-}mes}$. Electrolyte: $N_2$-saturade 0.5 mol $L^{-1}$ KOH and 0.5 mol $L^{-1}$ KOH + 0.5 mol $L^{-1}$ EtOH solution. Scan rate: 20 mV $s^{-1}$. ..... 1167
**Figure 5.21** a) CVs and b) polarization curves before and after of ADT of Pd/$C_{Cu(dmpz)L2}$. Electrolyte: $N_2$-saturade 0.5 mol $L^{-1}$ KOH. Scan rate: 20 mV $s^{-1}$. ..... 1189
**Figure 5.22** Ethanol consumed during 4 h at the nanocatalysts. Polarization potential: 0.8 V/RHE. ..... 12021
**Figure 5.23** Individual polarization curves of the nanocatalysts showing the behavior of a) the anode potential, $E_a$, and b) the cathode potential, $E_c$. ..... 12122
**Figure 5.24** a) Polarization curves and b) power density curves of the AEM-DEFC equipped with the nanocatalysts as anodes and cathodes. Fuel: 0.5 mol $L^{-1}$ EtOH + 0.5 mol $L^{-1}$ KOH. AEM: Fumatech® FAA. Feed at the cathode: $O_2$ + 0.5 mol $L^{-1}$ KOH. ..... 12223
**Figure 6.1** XRD patterns of the Pd-$CeO_{2\text{-}NR}$/C, Pd-$CeO_{2\text{-}NR}$/$C_{Cu\text{-}mes}$ and Pd-$CeO_{2\text{-}NR}$/$C_{Cu(dmpz)L2}$ nanocatalysts. ..... 135
**Figure 6.2** a) and b) high magnification FE-SEM micrographs of Pd-$CeO_{2\text{-}NR}$/$C_{Cu\text{-}mes}$.. ..... 137
**Figure 6.3** a) FE-SEM imagen and b) C, c) Pd, d) Cu, e) Ce and f) O elemental mapping of Pd-$CeO_{2\text{-}NR}$/$C_{Cu\text{-}mes}$.. ..... 138
**Figure 6.4** XPS spectra of Pd-$CeO_{2\text{-}NR}$/$C_{Cu\text{-}mes}$ in the a) C 1s, b) O 1s, c) Pd 3d, and d) Cu 2p regions. ..... 139
**Figure 6. 5** XPS spectra of Pd-$CeO_{2\text{-}NR}$/$C_{Cu(dmpz)L2}$ in the a) C 1s, b) O 1s, c) Pd 3d, and d) Cu 2p regions. ..... 141

**Figure 6.6** CVs of Pd-$CeO_{2\text{-}NR}$/C, Pd-$CeO_{2\text{-}NR}$/$C_{Cu\text{-}mes}$ and Pd-$CeO_{2\text{-}NR}$/$C_{Cu(dmpz)L2}$. Electrolyte: 0.5 mol $L^{-1}$ KOH. Scan rate: 20 mV $s^{-1}$. ..... 144
**Figure 6.7** Polarization curves of the EOR at Pd-$CeO_{2\text{-}NR}$/C, Pd-$CeO_{2\text{-}NR}$/$C_{Cu\text{-}mes}$ and Pd-$CeO_{2\text{-}NR}$/$C_{Cu(dmpz)L2}$. Electrolyte: 0.5 mol $L^{-1}$KOH + 0.5 mol $L^{-1}$ EtOH. Scan rate: 20 mV $s^{-1}$. ..... 146
**Figure 6.8** a) CVs and b) polarization curves of EOR before and after of ADT of Pd-$CeO_{2\text{-}NR}$/$C_{Cu\text{-}mes}$. Electrolyte: $N_2$-saturaded 0.5 mol $L^{-1}$ KOH, and 0.5 mol $L^{-1}$ KOH + mol $L^{-1}$ EtOH, respectively. Scan rate: 20 mV $s^{-1}$. ..... 147
**Figure 6.9** a) CVs and b) polarization curves of EOR before and after of ADT of Pd-$CeO_{2\text{-}NR}$/$C_{Cu(dmpz)L2}$. Electrolyte: $N_2$-saturaded 0.5 mol $L^{-1}$ KOH, and 0.5 mol $L^{-1}$ KOH + mol $L^{-1}$ EtOH, respectively. Scan rate: 20 mV $s^{-1}$. ..... 148
**Figure 6.10** Ethanol consumed during 4 h at the nanocatalysts. Polarization potential: 0.8 V/RHE. ..... 150
**Figure 6.11** In dividual polarization curves of the nanocatalysts showing the behavior of a) the anode potential, $E_a$, and b) the cathode potential, $E_c$. ..... 151
**Figure 6.12** OCV, $E_{cell}$ and $P_{cell}$ values of Pd-$CeO_{2\text{-}NR}$/C, Pd-$CeO_{2\text{-}NR}$ /$C_{Cu\text{-}mes}$ and Pd-$CeO_{2\text{-}NR}$/$C_{Cu(dmpz)L2}$. ..... 152
**Figure 6.13** a) Polarization curves and b) power density curves of the AEM-DEFC equipped with the nanocatalysts as anodes and cathodes. Fuel: 0.5 mol $L^{-1}$ EtOH + 0.5 mol $L^{-1}$ KOH. AEM: Fumatech® FAA. Feed at the cathode: $O_2$ + 0.5 mol $L^{-1}$ KOH. ..... 152

# Abstract

In the present thesis, Pd-$CeO_{2\text{-}NR}$/C bifunctional nanocatalyst synthesized by the polyol method was evaluated for the Oxygen Reduction Reaction (ORR) and the Ethanol Oxidation Reaction (EOR). For comparative purposes, monometallic Pd/C was also synthesized.

It was observed that after accelerated degradation test (ADT), Pd-$CeO_{2\text{-}NR}$/C retains ~98 % of electrochemically active surface area (ECSA), a value higher than the ~ 51 % of Pd/C.

Evaluation of the catalytic activity for the ORR by the rotating ring disk electrode (RRDE) technique showed that Pd-$CeO_{2\text{-}NR}$/C promotes the reaction with a hydroperoxyl ion production percentage (% $HO_2^-$) between 2 and 4 %, and an electron transfer number (n) close to 4. Tafel plots revealed higher mass and specific activity of Pd-$CeO_{2\text{-}NR}$/C compared to Pd/C. After ADT, the performance of Pd-$CeO_{2\text{-}NR}$/C remained comparable to that of the monometallic.

Meanwhile, the polarization curves of the EOR showed higher mass catalytic activity (i.e., mass current density ($j_m$), and more negative onset potential ($E_{onset}$) of Pd-$CeO_{2\text{-}NR}$/C compared to Pd/C. Interestingly, its performance for the reaction increased significantly higher after ADT, maintaining an enhanced performance related to Pd/C. Therefore, the addition of $CeO_{2\text{-}NR}$ promotes the electrocatalytic activity and electrochemical stability of Pd for the ORR and the EOR.

In the second part of the thesis, the synthesis of the $(C_6H_2Me_3)_2Cu$ (Cu-mes) and Cu(dmpz)L2 (dmpz= 3,5- dimethylpyrazole, $L_2$= terephthalic acid) organometallic compounds was carried out. The compounds were used as functionalizing agents of the commercial Vulcan XC-72, the resulting supports labeled as $C_{Cu\text{-}mes}$ and $C_{Cu(dmpz)L2}$. The functionalized supports were subsequently implemented in the synthesis of the Pd/$C_{Cu\text{-}mes}$, Pd/$C_{Cu(dmpz)L2}$, Pd-$CeO_{2\text{-}NR}$/$C_{Cu\text{-}mes}$ and Pd-$CeO_{2\text{-}NR}$/$C_{Cu(dmpz)L2}$ nanocatalysts.

Evaluation of the catalytic activity for the EOR showed more negative $E_{onset}$ and j (i.e., geometric current density) values for Pd/$C_{Cu\text{-}mes}$ and Pd/$C_{Cu(dmpz)L2}$ compared to Pd/C. During CO-stripping tests, $E_{onset}$ and $CO_{ads}$ oxidation peak potential ($E_{ox}$) shifted to more negative values at Pd/$C_{Cu\text{-}mes}$ and Pd/$C_{Cu(dmpz)L2}$, which indicated an

easier adsorption and oxidation of the molecule on the nanocatalysts supported on functionalized Vulcan. After ADT, the ECSA of both materials showed a decrease. While the performance for the EOR decreased slightly at $Pd/C_{Cu\text{-}mes,}$ it increased on $Pd/C_{Cu(dmpz)L2}$.

In Anion Exchange Membrane Direct Ethanol Fuel Cell (AEM-DEFC) tests, $Pd/C_{Cu\text{-}mes}$ showed the highest catalytic performance in terms of anode ($E_a$), and cathode open circuit potential ($E_c$), the polarization curves of both electrodes, cell polarization curve and cell power density ($P_{cell}$). In addition, an ethanol electrolysis test was performed to determine the formed subproducts.

The $Pd\text{-}CeO_{2\text{-}NR}/C_{Cu\text{-}mes}$, and $Pd\text{-}CeO_{2\text{-}NR}/C_{Cu(dmpz)L2}$ nanocatalysts were also evaluated and compared with $Pd\text{-}CeO_{2\text{-}NR}/C$. $Pd\text{-}CeO_{2\text{-}NR}/C_{Cu(dmpz)L2}$ presented higher catalytic performance for the EOR in terms of $E_{onset}$, and j compared to $Pd\text{-}CeO_{2\text{-}NR}/C_{Cu\text{-}mes}$ and $Pd\text{-}CeO_{2\text{-}NR}/C$. After ADT, $Pd\text{-}CeO_{2\text{-}NR}/C_{Cu\text{-}mes}$ showed a 15 % increase in j of the reaction, while that of $Pd\text{-}CeO_{2\text{-}NR}/C_{Cu(dmpz)L2}$ decreased by 11 %. Nevertheless, the performance of the latter remained higher. In AEM-DEFC tests, $Pd\text{-}CeO_{2\text{-}NR}/C_{Cu(dmpz)L2}$ demonstrated the highest catalytic performance considering $E_a$, anode polarization curve, cell polarization curve and $P_{cell}$. It also showed a fairly good $E_c$, but its performance as cathode at high j values decreased sharply.

# Resumen


En la presente tesis, se evaluó el nanocatalizador bifuncional Pd-$CeO_{2\text{-}NR}$/C sintetizado por el método del poliol para la Reacción de Reducción de Oxígeno (ORR, por sus siglas en inglés) y la Reacción de Oxidación del Etanol (EOR, por sus siglas en inglés). Con fines comparativos, también se sintetizó Pd/C monometálico.

Se observó que después de la prueba de degradación acelerada (ADT, por sus siglas en inglés), Pd-$CeO_{2\text{-}NR}$/C conserva el ~98 % del área superficial electroquímicamente activa (ECSA, por sus siglas en inglés), un valor superior al ~ 51 % del Pd/C.

La evaluación de la actividad catalítica para la ORR se llevó a cabo mediante la técnica de electrodo disco-anillo rotatorio (RRDE, por sus siglas en inglés). Pd-$CeO_{2\text{-}NR}$/C mostró que promueve la reacción con un porcentaje de generación de iones hidroperóxilo (% $HO_2^-$) entre el 2 y el 4 %, y un número de transferencia de electrones (n) cercano a 4. Las pendientes de Tafel revelaron una mayor actividad másica y específica para Pd-$CeO_{2\text{-}NR}$/C en comparación con Pd/C. Después de ADT, el rendimiento del Pd-$CeO_{2\text{-}NR}$/C siguió siendo comparable al del monometálico.

Mientras tanto, las curvas de polarización de la EOR mostraron una mayor actividad catalítica másica, es decir, densidad de corriente másica ($j_m$) y un potencial de inicio ($E_{onset}$) más negativo para Pd-$CeO_{2\text{-}NR}$/C en comparación con Pd/C. El desempeño de Pd-$CeO_{2\text{-}NR}$/C para la reacción aumentó significativamente después de la ADT en relación con Pd/C. Por lo tanto, la adición de $CeO_{2\text{-}NR}$ promueve la actividad electrocatalítica y la estabilidad electroquímica del Pd para la ORR y la EOR.

En la segunda parte de la tesis, se llevó a cabo la síntesis de los compuestos organometálicos $(C_6H_2Me_3)_2Cu$ (Cu-mes) and Cu(dmpz)L2 (dmpz= 3,5-dimetilpirazol, $L_2$= ácido teraftálico). Los compuestos se utilizaron como agentes funcionalizantes del Vulcan XC-72 comercial, siendo los soportes resultantes etiquetados como $C_{Cu\text{-}mes}$ y $C_{Cu(dmpz)L2}$. Los soportes funcionalizados se implementaron posteriormente en la síntesis de los nanocatalizadores Pd/$C_{Cu\text{-}mes}$, Pd/$C_{Cu(dmpz)L2}$, Pd-$CeO_{2\text{-}NR}$/$C_{Cu\text{-}mes}$ y Pd-$CeO_{2\text{-}NR}$/$C_{Cu(dmpz)L2}$.

La evaluación de la actividad catalítica para la EOR mostró valores de $E_{onset}$ y j (densidad de corriente geométrica) más negativos para Pd/$C_{Cu\text{-}mes}$ y Pd/$C_{Cu(dmpz)L2}$ en comparación con Pd/C. Durante las pruebas de CO-stripping, el $E_{onset}$ y el potencial de pico de oxidación de $CO_{ads}$ ($E_{ox}$) se desplazaron a valores más negativos en Pd/$C_{Cu\text{-}mes}$ y Pd/$C_{Cu(dmpz)L2}$, lo que indico una mayor facilidad de adsorción y oxidación de la molécula en los nanocatalizadores soportados sobre Vulcan funcionalizado. Después de ADT, el ECSA de ambos materiales mostró una disminución. Mientras que el desempeño para la EOR disminuyó ligeramente en Pd/$C_{Cu\text{-}mes}$, y aumentó en Pd/$C_{Cu(dmpz)L2}$.

Las pruebas en Celda de Combustible de Etanol Directa con Membrana de Intercambio Aniónico (AEM-DEFC, por sus siglas en inglés), Pd/$C_{Cu\text{-}mes}$ mostró el mayor desempeño catalítico en términos de potencial de circuito abierto del ánodo ($E_a$), y del cátodo ($E_c$), en las curvas de polarización de ambos electrodos, en la curva de polarización de celda y en la densidad de potencia de celda ($P_{cell}$). También se realizó una prueba de electrolisis de etanol con el fin de determinar los subproductos formados.

De igual forma se evaluaron los nanocatalizadores Pd-$CeO_{2\text{-}NR}$/$C_{Cu\text{-}mes}$, y Pd-$CeO_{2\text{-}NR}$/$C_{Cu(dmpz)L2}$ y se compararon con Pd-$CeO_{2\text{-}NR}$/C. Pd-$CeO_{2\text{-}NR}$/$C_{Cu(dmpz)L2}$ presentó un mayor desempeño catalítico para la EOR en términos de $E_{onset}$ y j en comparación con Pd-$CeO_{2\text{-}NR}$/$C_{Cu\text{-}mes}$ y Pd-$CeO_{2\text{-}NR}$/C. Después de ADT, Pd-$CeO_{2\text{-}NR}$/$C_{Cu\text{-}mes}$ mostró un aumento del 15 % en j de la reacción, mientras que Pd-$CeO_{2\text{-}NR}$/$C_{Cu(dmpz)L2}$ disminuyó 11 %. No obstante, el desempeño de este último siguió siendo superior. En las pruebas en AEM-DEFC, Pd-$CeO_{2\text{-}NR}$/$C_{Cu(dmpz)L2}$ demostró el mayor desempeño catalítico teniendo en cuenta $E_a$, la curva de polarización del ánodo, la curva de polarización de celda y $P_{cell}$. También mostró un valor comparable de $E_c$, pero su rendimiento como cátodo a altos valores de j disminuyó bruscamente.

# Introduction

During the last decades, nanomaterials and nanoparticles have received great attention as they are functional materials with extensive applications in catalysis, electronics, sensors, electrochemistry and in the energy sector [1]. Within this field, it is necessary to develop novel sustainable nanotechnology-based devices for energy generation and storage. In this sense, Anion Exchange Membrane Direct Ethanol Fuel Cells (AEM-DEFCs) emerge as promising devices for clean energy generation [2].

AEM-DEFCs have drawn the attention of international research groups because of their kinetically fast electrochemical reactions, low corrosion rate, and the attractive use of ethanol as fuel. This molecule has a high theoretical energy density and offers the advantage of being obtained from biomass as an alternative to conventional processes [3]. One way in which nanotechnology optimizes the efficiency of AEM-DEFCs is by developing nanocatalysts with improved catalytic activity for the reactions. Typically, nanoparticles show higher surface area available for the reactions than other geometries, thus enhancing the catalytic properties and promoting a more efficient reaction. Such characteristics lead to improved fuel cell performance. Moreover, as pointed out by the US Department of Energy (DOE), the electrochemical stability of fuel cell nanocatalysts is of paramount relevance to advance in the commercialization of these electrochemical devices [4].

Pd-based nanocatalysts are a feasible alternative to Pt to promote both the Ethanol Oxidation Reaction (EOR) and the Oxygen Reduction Reaction (ORR) in alkaline media. Even more, it has been reported that Pd-metal oxide nanocatalysts show improved catalytic activity, with an increase in electrochemical stability and a reduction in costs, since metal oxides are relatively cheap materials [5]. Moreover, cerium oxide ($CeO_2$) is a promising rare earth co-catalyst for electrocatalytic applications, because it can form surface $OH^-$ species at relatively negative potentials, which promote the generation of a high current density from the oxidation of alcohols [6].

Vulcan XC-72 is one of the most used carbonaceous supports, since it has suitable surface chemistry for anchoring nanoparticles, along with a high electrical conductivity [7]. Having a relatively high hydrophobic surface, it has been

submitted to diverse oxidative functionalizing treatments that modify its textural properties, nevertheless decreasing its electrical conductivity [8, 9].

In this context, it is important to point out that a broad family of organometallic compounds are less aggressive functionalizing agents than their oxidative treatments counterparts, but strong enough to chemically modify the carbonaceous surface creating functional groups that promote the anchorage and homogeneous dispersion of nanoparticles. Furthermore, the surface modification creates active metal sites that promote the formation of alloy phases with the base metal (in this case Pd) that is deposited on the carbon surface [10, 11].

In the first part of the present work, the catalytic activity and electrochemical stability of the bifunctional Pd-$CeO_{2\text{-}NR}$/C nanocatalyst for the ORR and the EOR are evaluated in alkaline media. The aim is to evaluate the positive effect of adding cerium on the electrochemical behavior of Pd for the above-mentioned reactions.

In the second part, the synthesis of the Cu-mes and Cu(dmpz)L2 copper organometallic compounds is reported. The compounds are used as functionalizing agents of Vulcan. Pd-based nanocatalysts supported on functionalized supports have been synthesized and labeled as Pd/$C_{Cu\text{-}mes}$, Pd/$C_{Cu(dmpz)L2}$, Pd-$CeO_{2\text{-}NR}$/$C_{Cu\text{-}mes}$, and Pd-$CeO_{2\text{-}NR}$/$C_{Cu(dmpz)L2}$, which are evaluated as anodes for the EOR in alkaline media. Moreover, the nanocatalysts have also been evaluated in a full AEM-DEFC device. From the previous experience of the group with organometallic compounds, an improvement in the catalytic activity is expected from the nanocatalysts supported on functionalized Vulcan.

**References**

[1] K. Share, A. Westover, M. Li, C.L. Pint. Surface engineering of nanomaterials for improved energy storage – A review. Chem. Eng. Sci. 154 (2016) 3-19.
[2] E.A. Monyoncho, T.K. Woo, E.A. Baranova, Ethanol electrooxidation reaction in alkaline media for direct ethanol fuel cells, in: Electrochemistry: Volume 15, The Royal Society of Chemistry, 2019, pp. 1-57.
[3] T.S. Almeida, Y. Yu, A.R. de Andrade, H.D. Abruña. Employing iron and nickel to enhance ethanol oxidation of Pd-based anodes in alkaline medium. Electrochim. Acta. 295 (2019) 751-758.

[4] S. Gottesfeld, D.R. Dekel, M. Page, C. Bae, Y. Yan, P. Zelenay, Y.S. Kim. Anion exchange membrane fuel cells: Current status and remaining challenges. J. Power Sources. 375 (2018) 170.
[5] E.L.S. A.M. Sheikh, L. Moares, L. M. Antonini, Mohammed Y. Abellah, C.F. Malfatti. Pd-based catalyst for ethanol oxidation in alkaline electrolyte. J. Min. Metall. 2 (2014) 64-69.
[6] S. Agarwal, L. Lefferts, B.L. Mojet. Ceria Nanocatalysts: shape dependent reactivity and formation of OH. ChemCatChem. 5 (2013) 479-489.
[7] L.C. M.J. Lázaro, V. Celorrio, J.I. Pardo, S. Perathoner, R. Moliner, Study and Application of carbon black Vulcan CX-72 in polymeric electrolyte fuel cells, in: T.L.P. I.J. Sanders (Ed.) Carbon Black: Production, Properties and Uses, Nova Science Publishers, New York, 2011, pp. 41-68.
[8] S. Yin, L. Luo, C. Xu, Y. Zhao, Y. Qiang, S. Mu. Functionalizing carbon nanotubes for effective electrocatalysts supports by an intermittent microwave heating method. J. Power Sources. 198 (2012) 1-6.
[9] S. Yang, X. Zhang, H. Mi, X. Ye. Pd nanoparticles supported on functionalized multi-walled carbon nanotubes (MWCNTs) and electrooxidation for formic acid. J. Power Sources. 175 (2008) 26-32.
[10] J.C. Martínez-Loyola, A.A. Siller-Ceniceros, M.E. Sánchez-Castro, M. Sánchez, J.R. Torres-Lubián, B. Escobar-Morales, C. Ornelas, I.L. Alonso-Lemus, F.J. Rodríguez-Varela. High performance Pt nanocatalysts for the oxidation of methanol and ethanol in acid media by effect of functionalizing carbon supports with Ru organometallic compounds. J. Electrochem. Soc. 167 (2020) 164502.
[11] A.A. Siller-Ceniceros, M.E. Sánchez-Castro, D. Morales-Acosta, J.R. Torres-Lubian, E. Martínez G, F.J. Rodríguez-Varela. Innovative functionalization of Vulcan XC-72 with Ru organometallic complex: Significant enhancement in catalytic activity of Pt/C electrocatalyst for the methanol oxidation reaction (MOR). App. Cat. B-Environ. 209 (2017) 455-467

# Chapter I
# Background

# Chapter I
# Background

## 1.1 Anion Exchange Membrane Direct Ethanol Fuel Cells (AEM-DEFCs)

The Anion Exchange Membrane Fuel Cells (AEMFCs) are high-efficiency energy conversion devices, considered sustainable energy sources with very low emissions of pollutants. These devices have high-power density, show enhanced reaction kinetics, and have high tolerance to subproducts which can decrease the cell performance by poisoning the nanocatalysts at the electrodes [1]. This is relevant since recently the DOE has established an operating stability of up to 2000 h as a new criterion for their commercialization [2-4].

The main challenge on which studies have focused is the development of anion exchange membranes (AEM), an issue where important improvements have been reached. Great efforts have been made to reduce the chemical degradation of anion conducting ionomers and to limit carbonation issues within AEMFCs [5, 6]. Therefore, studies are focused on increasing hydroxide conductivity, and to promoted chemical and mechanical stabilities at high pH values, leading to higher cell performances [7-9].

Hydrogen is the most used fuel to feed AEMFCs. Its electrochemical oxidation is kinetically fast, forming water molecules as the only subproduct. Nevertheless, the production of pure hydrogen is expensive, and the gas is difficult to transport and store. An alternative to hydrogen is based on the application of several liquid alcohols, which have a high energy density and are easier to transport, handle and store. Among them, ethanol is the best option, because is less toxic than other alcohols, has a higher energy density (8.0 kW h/kg), and can be produced from biomass sources [10-12].

Due to the alkaline environment in AEM-DEFCs, the EOR and the ORR show faster electro-kinetics, as well as lower corrosion rate compared to fuel cells operating in acid media. These electrochemical devices consist of three fundamental components [13]:

i) The anode, where ethanol is oxidized to generate electrons, water, and $CO_2$ according to reaction 1.1:

$$CH_3CH_2OH + 12OH^- \rightarrow 2CO_2 + 9H_2O + 12e^- \qquad \text{Reaction 1.1}$$

Here it is important to mention that the $CO_2$ produced during the reaction can be considered as a carbon-neutral cycle as it can be reabsorbed by crops and plants, which in due course can be transformed into biomass [14]. If direct oxidation is not carried out, subproducts such as acetic acid may be formed when reacting with hydroxyl ions to form acetate ions. Acetaldehyde is also an important subproduct. Moreover, CO-species which strongly adsorb on metal active sites poisoning the nanocatalysts, are also produced from the reaction.

ii) The cathode, where the oxygen reacts with water and electrons from the anode to produce hydroxide ions, according to Reaction 1.2:

$$3O_2 + 6H_2O + 12e^- \rightarrow 12OH^- \qquad \text{Reaction 1.2}$$

The ideal overall reaction in AEM-DEFCs is:

$$CH_3CH_2OH + 3O_2 \rightarrow 2CO_2 + 3H_2O \qquad \text{Reaction 1.3}$$

iii) The AEM, through which anions diffuse from cathode to anode, and which separates the electrodes avoiding short-circuits, as shown in Figure 1.1.

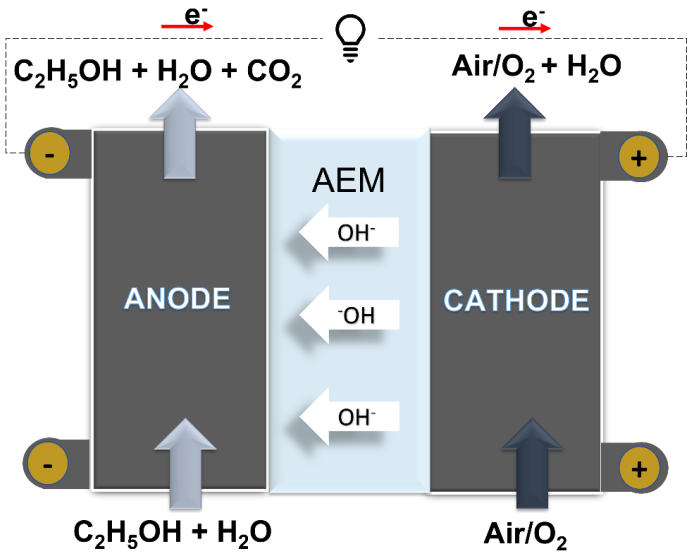


**Figure 1.1** Scheme of an AEM-DEFC.

Overall, the performance of the cell is limited by the kinetics of the reactions. Thus, AEM-DEFCs requires the development of nanocatalysts with high catalytic

activity to promote the complete oxidation of ethanol, along with important electrochemical stability. Nanocatalysts based on Pd are an attractive alternative for the reactions mentioned here-above. Pd nanocatalysts have demonstrated high electrochemical performance for the EOR and the ORR in alkaline media. Their high tolerance to CO-species, has also been demonstrated [15-19].

### 1.1.1 Oxygen Reduction Reaction (ORR)

The complex ORR remains a challenge for researchers engaged in fuel cell catalysis. It is a relatively slow reaction, which typically starts at high overpotentials, resulting in significant voltage losses at the fuel cell [20]. To achieve a high efficiency, it is desirable that the cathodes trigger the ORR as close to thermodynamic equilibrium conditions as possible (i.e., with a low overpotential). Due to the highly irreversible nature of the cathode reaction, the use of nanocatalysts is of paramount importance to minimize the overpotential [21]. Pd-based nanocatalysts have been considered as a promising catalyst for the electrochemical ORR in alkaline environments.

The mechanism of the ORR in alkaline solutions starts with the adsorption of $O_2$ to form $O_{2ads}$, followed by the $O_2^-$ species on the nanocatalyst surface. Then the next steps can follow one of two paths, as shown in Figure 1.2:

i) Direct mechanism: $O_2$ is reduced directly to $OH^-$ in a 4 $e^-$ transfer (Reaction 1.4).

ii) Two-steps mechanism: the first step involves the transfer of 2 $e^-$ to reduce $O_2$ to the $HO_2^-$ species as an intermediate, which in turn is reduced to $OH^-$ (Reaction 1.6) [17, 22, 23].

Direct: $O_2 + 2\,H_2O + 4\,e^- \rightarrow 4OH^-$ (0.401 V vs SHE) Reaction 1.4

Series: $O_2 + H_2O + 2\,e^- \rightarrow HO_2^- + OH^-$ (-0.076V vs SHE) Reaction 1.5

$HO_2^- + H_2O + 2e^- \rightarrow 3OH^-$ (0.878 V vs SHE) Reaction 1.6

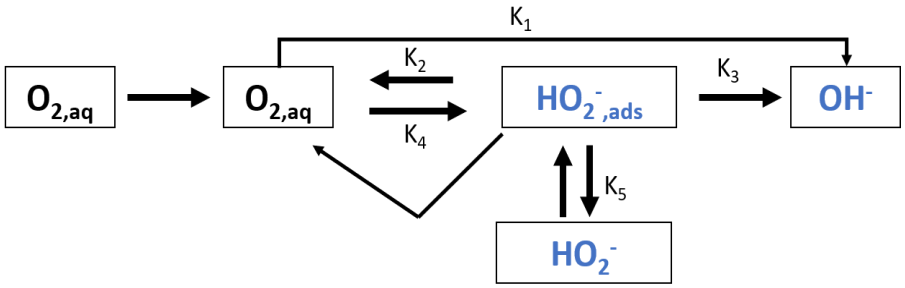


**Figure 1.2** Pathways of the ORR in alkaline media.

### 1.1.2 Ethanol Oxidation Reaction (EOR)

The relatively slow kinetics for the EOR remains a challenge for the development and broad commercialization of AEM-DEFCs. Pd/C nanocatalysts are the most suitable anode materials for the reaction in alkaline solutions, an electrocatalytic behavior that can be attributed to their oxophilic character and improved C-C bond cleavage on the Pd active sites. Furthermore, Pd is known to have higher stability and to be less susceptible to poisoning by reaction intermediates than other noble metals [24].

The complete ethanol oxidation involves a 12 $e^-$ transfer mechanism that leads to the formation of $CO_2$ and water, as mentioned above (Reaction 1.1). However, very often low performance nanocatalysts promote an incomplete, 4 $e^-$ oxidation reaction, resulting in the formation of acetic acid ($CH_2COOH$, or the acetate ion, $CH_2COO^-$) as intermediate. Therefore, it is important to explore novel Pd-based nanocatalysts with a high C-C bond cleavage capacity to catalyze the complete oxidation of ethanol and thus increase the efficiency of the fuel cell [25].

The generally accepted mechanism of the EOR on Pd nanocatalysts in alkaline media is described in the following reactions [26]:

$$Pd^0 + OH^- \leftrightarrows Pd^0\text{-}OH_{ads} + e^- \quad \text{Reaction 1.7}$$

$$Pd^0 + CH_3CH_2OH \leftrightarrows Pd\text{-}(CH_3CH_2OH)_{ads} \quad \text{Reaction 1.8}$$

$$Pd\text{-}(CH_2CHOH)_{ads} + 3OH^- \leftrightarrows Pd\text{-}(CH_3CO)_{ads} + 3H_2O + 3e^- \quad \text{Reaction 1.9}$$

$$Pd\text{-}(CH_3CO)_{ads} + Pd\text{-}OH_{ads} \leftrightarrows Pd\text{-}(CH_3COOH)_{ads} + Pd^0 \quad \text{Reaction 1.10}$$

$$Pd\text{-}(CH_3COOH)_{ads} + OH^- \leftrightarrows Pd^0 + CH_3COO^- + H_2O \quad \text{Reaction 1.11}$$

The first electron transfer occurs with the adsorption of hydroxyl ions on the Pd metal active sites (Reaction 1.7). Then, ethanol molecules adsorb and dissociate on Pd sites producing adsorbed acetyl ions, i.e. $(CH_3CO)_{ads}$, and 3 water molecules, while transferring 3 $e^-$ (Reactions 1.8 and 1.9). Reaction 1.10 is considered to be the rate determining step. Finally, the desorption of the acetate ion and $H_2O$ occurs, making $Pd^0$ sites available to continue with the reaction (Reaction 1.11) [27, 28].

## 1.2 Nanocatalysts

The overall function of a nanocatalyst is to increase the kinetics of the reactions occurring in fuel cells. In the most common configuration, powders of nanocatalysts are deposited on the surface of electrodes and actively promote the electron transfer at the membrane-electrode interface. The kinetics of the reaction depends on the geometrical and electronic properties of the materials catalyzing it. Due to the complex reactions that occur at the electrodes of AEM-DEFCs, it is necessary to use nanocatalysts with high tolerance to the reaction intermediates formed during the EOR and the ORR. In recent years, work has been carried out on the development of nanomaterials with the aim of increasing the catalytic activity of anodes and cathodes [29].

In order to improve the performance of monometallic nanocatalysts, multiple investigations attribute enhanced kinetics (higher catalytic activity) of the ORR and the EOR to Pd-alloys or Pd-metal oxide nanocatalysts [30, 31].

### 1.2.1 Pd-based nanocatalyst for the ORR

Studies have focused on the design and development of cathode nanocatalysts that promote the ORR via the direct 4 $e^-$ mechanism, limiting the overpotential and the rate of hydroperoxyl ion production (%$HO_2^-$) [32, 33].

Pd-based nanocatalysts possess a high catalytic activity for the ORR in alkaline media. In order to enhance the catalytic properties and the electrochemical stability of Pd, workers have proposed the alloying with a second metal. The Pd-alloys improve the kinetics of the reaction and avoids high overpotentials due to a synergistic effect between both metals, in which the second metal modifies the electronic structure of Pd [34, 35].

As a result of the formation of the alloy, an electron transfer between Pd and the second metal takes place, which modifies the *d*-valence band of the former. Such modification has a positive effect of easing the adsorption energy of $O_2$ and reaction intermediates, therefore increasing their catalytic activity for the ORR. [36, 37].

Pd-alloys such as PdCo [38-40], PdCu [41], PdFe [42], PdNi [43], and PdSn [44] have been developed, demonstrating an improvement in electrochemical activity for the ORR in terms of onset potential and limiting current, compared with monometallic Pd/C.

Alternatively, metal oxides have also been reported as co-catalysts of Pd, particularly cerium oxide ($CeO_2$), which is of interest in this thesis project. Ceria-based catalysts have been extensively studied due to their unique chemical and thermal stabilities, as well as good optical and magnetic properties [45]. Moreover, $CeO_2$ is a promising rare earth co-catalyst for electrocatalytic applications, due to its oxygen storage and release capability that is achieved by alternating oxidation states between $Ce^{3+}$ and $Ce^{4+}$ [46, 47]. Furthermore, it has been indicated that $CeO_2$ has

enhanced oxyphilic properties that promote electrons transfer during the electrochemical reactions.

Song et al. [48], have reported the synthesis of PdO-$CeO_2$/C which exhibits an high electrocatalytic activity for the ORR in alkaline media in terms of mass activity and electrochemical stability compared with Pt/C. The enhanced performance of PdO-$CeO_2$/C is attributed to the interaction between PdO and $CeO_2$ as well as to the favorable interface for oxygen adsorption and desorption. Rodríguez-Varela et al. [49], have demonstrated the good electrochemical stability of the Pd-$CeO_{2\text{-}NR}$/C nanocatalyst along with its high promotion of electrocatalytic activity for the ORR in alkaline media. Pd-$CeO_{2\text{-}NR}$/C shows higher mass and specific activities compared with Pd/C, ascribed to the formation of surface oxide species, i.e., $CeO_{2\text{-}NR}$ formed $OH^-$ which facilitated the electrochemical reactions.

The addition of $CeO_2$ enhances the electrocatalytic behavior and electrochemical stability of Pd towards the ORR, due to a synergistic effect between $CeO_{2\text{-}NR}$ and Pd. This modification leads to beneficial electronic effect and the activation of the bifunctional mechanism that promote the suitable adsorption and desorption of oxygen species during the reaction, resulting in improved kinetics of the reaction.

### 1.2.2 Pd based nanocatalysts for the EOR

The design of highly active nanocatalysts as anode materials for AEM-DEFC remains a challenge because the ethanol oxidation is a multi-step, complex reaction with relatively slow kinetics. The most active catalyst for the EOR in alkaline solutions is Pd. Nevertheless, Pd-based nanocatalysts still form reaction intermediates that block their active sites, limiting the long-term stability of AEM-DEFCs [50].

In order to improve the electrochemical activity of Pd nanocatalysts, research has addressed their modification. The most common strategy is the addition of complementary metals or metal oxides (co-catalysts) to form alloys or metal-metal oxide nanostructures. The modification can also develop nanocomposites (core-

shell, or bimetallic nanostructures, or heterogeneous structures). The incorporation of alloying elements or metal oxides can facilitate the adsorption of molecules, their dissociation, as well as the desorption of poisoning intermediates. The modification can also enhance the electrochemical stability of the nanocastalysts [51-53].

The formation of alloys increases the catalytic activity of Pd through the bifunctional mechanism and the electronic effect. The first one acts when the co-catalyst provides oxygen species (such as $OH^-$) at negative potentials to Pd active sites, facilitating the oxidation of adsorbed ethanol and reaction intermediates such as $CO_{ads}$. The electronic effect occurs because of the electron transfer between the alloying element and Pd. Such interaction modifies the *d*-band of Pd, which modifies the adsorption energy of reacting species and intermediates promoting the overall reaction [54].

Recent works have reported research on Pd-based alloys such as PdRu [55], PdAg [56, 57], PdBi [58], PdNi [59], PdCo [60], PdTi [61], PdIr [62], PdAu [63], PdPb [64], PdSn [65, 66], and PdCu [67]. The reports have made evident that both the bifunctional mechanism and the electronic effect contribute significantly to increasing the catalytic activity and electrochemical stability of the Pd-alloys nanocatalysts for the EOR.

Modifying Pd with cheaper transition metals such as Cu increases its electrochemical performance for EOR as well, due to a synergistic effect. The alloying between Pd and Cu is of particular interest in this work, because when functionalizing Vulcan with Cu organometallic compounds and afterwards using it as a support of Pd nanoparticles, the creation of alloyed Pd-Cu phases is expected.

Guo et al. [68], have studied the performance of PdCu/C and Cu@PdCu/C (core-shell nanostructure) for the EOR in alkaline media, obtaining a higher current density than Pd/C. The study also shows an enhanced electrochemical stability and the ability to prevent $CO_{ads}$ poisoning of the novel nanocatalysts, which is mainly ascribed to the synergistic effect between Pd and Cu (such as geometric and electronic effects, and the bifunctional mechanism). Yang et al. [69] report the synthesis of PdCu nanoalloys anchored on porous carbon whit high specific catalytic activity and stability for the EOR, tolerance to poisoning species compared to

commercial Pd/C. The high performance of the nanoalloys has been attributed to the uniform dispersion of PdCu nanoparticles on the support, and to strong metal-support interactions.

Zhai et al. [70] have reported a 3D PdCu network nanostructure with higher electrochemical activity for the EOR than Pd/C. The study suggests that the porous 3D structure allows the internal surface of the catalyst to be accessible to the reactants, which increased the electrochemically active surface area (ECSA), exposing more active sites for the oxidation of the alcohol. The high catalytic activity of the 3D PdCu nanocatalysts has been correlated to a promotion of the bifunctional mechanism by the incorporation of Cu atoms into the Pd lattice.

In their work, Chen et al. [71] demonstrate a superior electrocatalytic performance of $Pd_xCu_{100-x}$ networks compared to Pd/C for the EOR in alkaline media in terms of mass activity, long-term stability, and better tolerance to reaction intermediates. Such behavior has been ascribed to important strain and ligand effects due to the presence of Cu atoms modifying the electronic structure of Pd.

These studies show that the alloying of Pd and Cu improves the electrochemical activity for the EOR regarding current density, one-set oxidation potential, electrochemical stability, ECSA, and tolerance towards reaction intermediates. The results ascribe the enhanced performance to a synergistic effect between the two metals which activate the bifunctional mechanism, and the electronic and strain effects.

On this matter, the addition of metal oxides such as $CeO_2$ to Pd also induces a positive effect on its electrochemical activity towards the EOR. $CeO_2$ can absorb and desorb $OH^-$ species at relatively negative potentials, which it shares with Pd. By doing so, it promotes the oxidation of ethanol at more negative potentials.

Shen et al. [72], have shown that the effect of adding $CeO_2$ to Pd/C nanocatalysts is an enhanced catalytic activity for the EOR in alkaline media, compared with Pd/C. The Pd-$CeO_2$/C nanocatalyst forms $OH^-$ species at relatively negative potentials to release Pd atoms from CO-like poisonous species, allowing the active sites to perform the electro-oxidation of ethanol. Vizza et al. [73] have reported that the power density obtained from an AEM-DEFCs equipped with the Pd-$CeO_2$/C

nanocatalysts as anode and FeCo/C as cathode, is twice as high as that delivered by Pd/C. The presence of ceria contributes to start the EOR at more negative onset potential. It is proposed by the authors that ceria promoted the formation at low potentials of Pd-$OH_{ads}$ bonds that are responsible for the oxidation of the alcohol with a high current density.

**1.3 Carbon supports : Vulcan XC-72 (C)**

It is acknowledged that the textural and surface chemical properties of the support play an important role in the catalytic activity of Pd/C nanocatalysts. The choice of support has an effect on particle size and dispersion, average particle size distribution, and electrochemical stability. In addition, since the metallic nanoparticles are attached to the support, the bond interactions can potentially influence their catalytic activity by modifying their electronic structure. Thus, supports with adequate properties may improve the metal-carbon interactions, increasing the performance and durability of the nanocatalysts [33, 74, 75].

In this context, nanocatalysts for fuel cells applications require carbon supports with the following characteristics: 1) surface chemical properties to achieve high nanoparticles dispersion; 2) suitable pore structure for the adequate diffusion of reactants and subproducts; 3) high electrical conductivity for electrons to be fast and easily transferred; and 4) high corrosion resistance to avoid its deterioration which might affect the performance and stability of the nanocatalysts [76-78]. In addition, a longer lifetime of the support ensures a more durable stable operation of the fuel cell. This is relevant since long-term stability of fuel cells is one of the most important challenges to be solved for their large-scale commercialization.

The most used support in low temperature fuel cell applications is Vulcan XC-72, a low-cost (1 USD/g) carbon black commercialized by Cabot Corp. It is obtained from the pyrolysis of hydrocarbons such as natural gas or some petroleum fractions. Vulcan consists of quasi-amorphous carbon spheres with diameters between 30-60 nm as shown in Figures 1.3 and 1.4, having an electrical conductivity reported as 2.77 S $cm^{-1}$ and a surface area of ~250 $m^2$ $g^{-1}$ [79]. Moreover, Vulcan

typically shows hydrophilic properties and the presence of surface oxygen functional groups that favor a good dispersion and anchorage of metal particles [80].

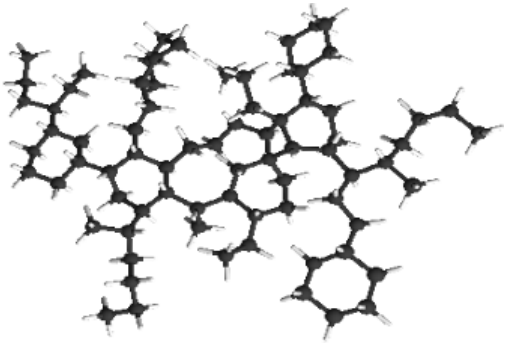

**Figure 1.3** Scheme of the structure of Vulcan XC-72.

Meanwhile, the mean pore diameter of Vulcan (10.4 nm) may affect the diffusion of reagents and products during the electrochemical reactions, decreasing the performance of the fuel cell [81]. In addition, its limited chemical stability under extreme operating conditions (high positive potentials, low pH values) promotes its surface oxidation, generating the agglomeration of nanoparticles, among other negative issues [82, 83].

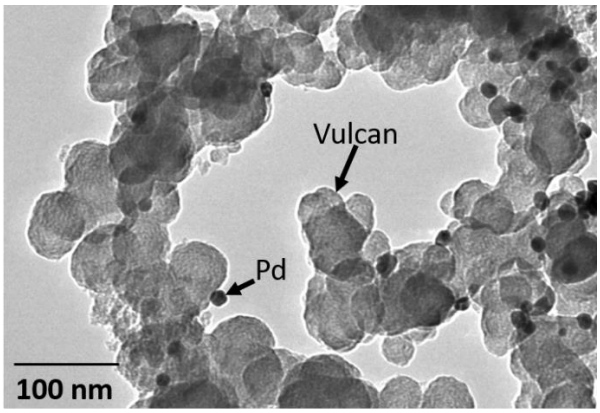


**Figure 1.4** TEM micrograph of a Pd/C nanocatalysts showing the morphology of Vulcan.

Nevertheless, Vulcan shows the best properties among the carbon blacks (Ketjenblack, acetylene black, black pearls) to be used as support [84].

## 1.4 Functionalization of carbon supports

Functionalization is the modification of the surface of a material through chemical interactions. The advantages provided by the functionalization of carbons that are used as a support are: i) improved chemical and electrochemical stability; ii) formation of surface functional groups that act as anchoring sites for nanoparticles; and iii) modification of electronic properties improving their electrical conductivity [85].

Covalent and non-covalent modification methods have been used to functionalize carbon supports. Covalent functionalization, probably the most widely used, involves the permanent modification of the carbon surface. It uses chemical agents such as $HNO_3$, $H_2SO_4$, $C_6H_8O_7$, $CH_3COOH$, $KMnO_4$, $K_2Cr_2O_7$, KOH and $H_2O_2$ to introduce surface hydroxyl, carboxyl, and carbonyl functional groups. These oxygenated species serve as nucleation and anchoring sites of nanoparticles, creating bonds between carbon and metal nanoparticles. [86].

Non-covalent functionalization is based only on electrostatic interactions, Van der Waals forces, hydrogen bonding, and other type of attractive forces. For example, the association of carbon with polymers such as poly(vinyl pyrrolidone) and poly(styrene sulfonate) disrupt their intrinsic hydrophobic interface allowing their solubilization in water. Additionally, the reactive groups of the polymers can interact with specific molecules [87, 88].

Functionalization of carbon nanostructures has become a useful strategy to improve their properties by modifying their surface. The activity, selectivity, and stability of the nanocatalysts are strongly influenced by the surface characteristics, as well as by the physicochemical properties of the support. The use of carbon without any treatment can result in a poor performance of the nanocatalysts, since it may contain traces of ash and hydrophobic surface groups that limit the nucleation and dispersion of nanoparticles [89].

The procedures more used to create surface functional groups on carbon involve acid solutions and aggressive agents, requiring high temperatures and several hours of treatment [90-92].

### 1.4.1 Use of Cu in the functionalization of carbon supports.

Functionalization of diverse allotropic forms of carbon with different Cu compounds has been reported, envisioning different applications in the medical field [93], in the treatment of nuclear waste [94], and in sensors research [95].

There are very few reports where Cu compounds have been used for the functionalization of carbon materials for application in fuel cells. For example, Du et al. report the synthesis of cuprous phosphide as a functionalizing agent of reduced graphene oxide (RGO). The catalytic activity for EOR and MOR as well as durability of the Pd-$Cu_3P$/RGO nanocatalyst obtained increases compared to Pd/C or Pd/RGO, due to a promoting effect of the $Cu_3P$/RGO) hybrid material resulting from the functionalization. The high performance of Pd-$Cu_3P$/RGO has been attributed to the beneficial electronic structure change of Pd as well as the bifunctional effect between copper phosphide and Pd [96, 97].

## 1.5 Organometallic compounds as functionalizing agents

There are several reports in the literature showing the successful functionalization of carbon materials with organometallic compounds. Some of the most studied compounds are based on Cr and Ru.

Haddon et al. have patented a method for the functionalization of carbon nanostructures such as graphite, graphene, and carbon nanotubes using Cr organometallic compounds. The group has studied the surface modification of the carbon structures with chromium organometallic compounds such as $(Cr(CO)_6$ and $[(\eta^6\text{-}C_6H_6)Cr(CO)_3]$. They proposed a method for introducing chemical functionalities onto a graphitic system with minimal or no disruptions at all of the structural integrity of the $sp^2$-hybridized carbon atoms.

The functionalization process developed by the group is a covalent chemisorption interaction, in which the formation of an organometallic hexahapto ($\eta^6$)-metal fragment preserves the graphitic structure of the carbon (i.e., a constructive rehybridization) The authors show that the electric conductivity of nanotubes increases by incorporating transition metals (Cr, Mo and W) [98-101].

Rodríguez-Varela et al. report the functionalization of Vulcan and rGO by the Haddon's method with the $[(\eta^6\text{-}C_6H_5OCH_2CH_2OH)RuCl_2]_2$ (Ru-dim) and $[(\eta^6\text{-}C_6H_4(CHMe_2)Me)RuCl_2]_2$ (Ru–cym) organometallic compounds. The modified carbon has been used as supports to synthesize Pt-based nanocatalysts. HRTEM analysis have shown a good dispersion of nanoparticles on the supports. The catalytic activity of the nanocatalyst for the MOR has been evaluated in acid media. The $Pt/C_{Ru\text{-}dim}$ and $Pt/rGO_{Ru\text{-}dim}$ nanocatalysts show an enhanced performance compared to Pt/C (on non-functionalized Vulcan), in terms of a higher current density generated and a more negative onset potential. The increase in catalytic activity of $Pt/C_{Ru\text{-}dim}$ and $Pt/rGO_{Ru\text{-}dim}$ is attributed to the formation of alloyed phases between Pt and Ru, a feature that activates the bifunctional mechanism [102-104].

### 1.5.1 Cu organometallic compounds

The organometallic chemistry of transition metals is one of the areas of interest worldwide due to the different applications of these complexes. Particularly, copper derivatives have found widespread application in homogeneous catalysts. Copper is a relatively cheap, earth-abundant, and non-toxic metal. Cu compounds have been classified as high valence complexes because of their capability to form Cu-C bonds, due to their different oxidation states (1+, 2+, and 3+). Some of the advantages of these materials include: i) the relatively easy synthesis of Cu compounds; ii) feasible carbon-carbon and carbon-heteroatoms bonding; and iii) high-valent Cu intermediates to improve catalytic reactions [105].

On the other hand, one of the main disadvantages of Cu organometallic compounds is their poor chemical stability, which has been associated with the redox properties of the metal. It is widely established that the thermal stability of organocuprates increases in the following order of substituents: alkyl < aryl ~ alkenyl

< alkynyl [106]. Alkyl being the substituent that provides the highest thermal stability, which improves the physical properties of the compound.

One of the most used Cu organometallic compounds is the mesityl copper (identified as Cu-mes in this work), formed by an aryl substituent and three methyl groups (Figure 1.5). This compound is easy to synthesize because mesityl halides as starting compounds have good solubility in benzene, ether, and THF. Also, their cost is relatively low. Mesityl copper can be synthesized by a metathesis reaction between copper(I) chloride and mesityl magnesium bromide in THF, under anhydrous and oxygen-free conditions, because of its high sensitivity to this gas and humidity [107-109].

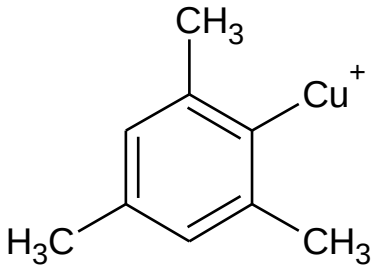


**Figure 1.5** Structure of mesytil copper.

Barriér et al. report the synthesis of Cu nanoparticles by a vapor deposition technique used as precursor mesityl copper. The use of this type of organometallic compounds is proposed because few Cu precursors give satisfactory results [110].

One alternative is to synthesize a coordination compound assembled with copper acetate, 3,5-dimethylpyrazole, and terephthalic acid (Figure 1.6), which in this work is labeled as Cu(dmpz)L2. These coordinated compounds can be obtained by simple synthesis methods and exhibit excellent chemical stability. For fuel cell applications, due to the inter-bond interactions, an easy anchoring of the compound on the Vulcan is expected [111].

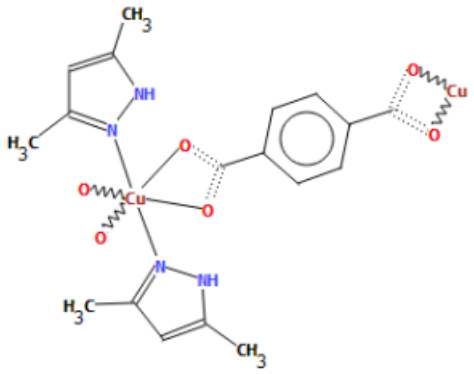


**Figure 1.6** Structure of Cu(dmpz)L2.

Given that the study of these nanomaterials is at an early stage of development, Cu organometallic compounds are potential candidates to increase the catalytic activity of Pd based nanocatalysts for the EOR. As far as is has been possible to revise the literature, this is the first time that the effect of functionalizing Vulcan with Cu organometallic compounds on the catalytic activity of Pd nanocatalysts supported on the modified carbons has been studied.

## 1.6 References

[1] Z. Sun, J. Pan, J. Guo, F. Yan. The alkaline stability of anion exchange membrane for fuel cell applications: the effects of alkaline media. Adv. Sci. 5 (2018) 1800065.

[2] W.E. Mustain, M. Chatenet, M. Page, Y.S. Kim. Durability challenges of anion exchange membrane fuel cells. Energy Environ. Sci. 13 (2020) 2805-2838.

[3] A. Hernández-Ramírez, F.J. Rodríguez-Varela, P.C. Meléndez-González, M.E. Sánchez-Castro. Catalytic activity of Pt–$CoTiO_3$ nanocatalysts supported on reduced graphene oxide functionalized with Cr organometallic compounds for the oxygen reduction reaction. J. Mater. Res. (2021).

[4] N. Ul Hassan, M. Mandal, G. Huang, H.A. Firouzjaie, P.A. Kohl, W.E. Mustain. Achieving high-performance and 2000 h stability in anion exchange membrane fuel cells by manipulating ionomer properties and electrode optimization. Adv. Energy Mater. 10 (2020) 2001986.

[5] D.R. Dekel, I.G. Rasin, S. Brandon. Predicting performance stability of anion exchange membrane fuel cells. J. Power Sources. 420 (2019) 118-123.
[6] R.K. Singh, E.S. Davydova, J. Douglin, A.O. Godoy, H. Tan, M. Bellini, B.J. Allen, J. Jankovic, H.A. Miller, A.C. Alba-Rubio, D.R. Dekel. Synthesis of $CeO_x$-decorated Pd/C catalysts by controlled surface reactions for hydrogen oxidation in anion exchange membrane fuel cells. Adv. Funct. Mater. 30 (2020) 2002087.
[7] Z. Sun, B. Lin, F. Yan. Anion-exchange membranes for alkaline fuel-cell applications: the effects of cations. ChemSusChem. 11 (2018) 58-70.
[8] D.R. Dekel. Review of cell performance in anion exchange membrane fuel cells. J. Power Sources. 375 (2018) 158-169.
[9] J. Lilloja, E. Kibena-Põldsepp, A. Sarapuu, M. Kodali, Y. Chen, T. Asset, M. Käärik, M. Merisalu, P. Paiste, J. Aruväli, A. Treshchalov, M. Rähn, J. Leis, V. Sammelselg, S. Holdcroft, P. Atanassov, K. Tammeveski. Cathode catalysts based on cobalt- and nitrogen-doped nanocarbon composites for anion exchange membrane fuel cells. ACS Appl. Energy Mater. 3 (2020) 5375-5384.
[10] T.S. Zhao, Y.S. Li, S.Y. Shen. Anion-exchange membrane direct ethanol fuel cells: Status and perspective. Front. Energy. 4 (2010) 443-458.
[11] N. Fujiwara, Z. Siroma, S.-i. Yamazaki, T. Ioroi, H. Senoh, K. Yasuda. Direct ethanol fuel cells using an anion exchange membrane. J. Power Sources. 185 (2008) 621-626.
[12] Y.S. Li, T.S. Zhao. A passive anion-exchange membrane direct ethanol fuel cell stack and its applications. Int. J. Hydrogen Energy. 41 (2016) 20336-20342.
[13] C. Bianchini, P.K. Shen. Palladium-based electrocatalysts for alcohol oxidation in half cells and in direct alcohol fuel cells. Chem. Rev. 109 (2009) 4183-4206.
[14] F.M. Souza, P. Böhnstedt, V.S. Pinheiro, L.A. Oliveira, B.L. Batista, L.S. Parreira, R.A. Antunes, M.C. Santos. Niobium increasing the electrocatalytic activity of palladium for alkaline direct ethanol fuel cell. J. Electroanal. Chem. 858 (2020) 113824.
[15] Y. Yang, G. Chen, R. Zeng, A.M. Villarino, F.J. DiSalvo, R.B. van Dover, H.D. Abruña. Combinatorial studies of palladium-based oxygen reduction electrocatalysts for alkaline fuel cells. J. Am. Chem. Soc. 142 (2020) 3980-3988.

[16] H. Yang, K. Wang, Z. Tang, Z. Liu, S. Chen. Bimetallic PdZn nanoparticles for oxygen reduction reaction in alkaline medium: The effects of surface structure. J. Catal. 382 (2020) 181-191.
[17] T. Wang, A. Chutia, D.J.L. Brett, P.R. Shearing, G. He, G. Chai, I.P. Parkin. Palladium alloys used as electrocatalysts for the oxygen reduction reaction. Energy Environ. Sci. 14 (2021) 2639-2669.
[18] J. Guo, R. Chen, F.-C. Zhu, S.-G. Sun, H.M. Villullas. New understandings of ethanol oxidation reaction mechanism on Pd/C and $Pd_2Ru$/C catalysts in alkaline direct ethanol fuel cells. Appl. Catal B-Environ. 224 (2018) 602-611.
[19] P. Raghavendra, G. Vishwakshan Reddy, R. Sivasubramanian, P. Sri Chandana, L. Subramanyam Sarma. Reduced graphene oxide-supported Pd@Au bimetallic nano electrocatalyst for enhanced oxygen reduction reaction in alkaline media. Int. J. Hydrogen Energy. 43 (2018) 4125-4135.
[20] Y. Nie, L. Li, Z. Wei. Recent advancements in Pt and Pt-free catalysts for oxygen reduction reaction. Chem. Soc. Rev. 44 (2015) 2168-2201.
[21] X. Ge, A. Sumboja, D. Wuu, T. An, B. Li, F.W.T. Goh, T.S.A. Hor, Y. Zong, Z. Liu. Oxygen reduction in alkaline media: from mechanisms to recent advances of catalysts. ACS Catalysis. 5 (2015) 4643-4667.
[22] J. He, S. Luo, Y. Li, H. Mi, L. Sun, X. Ren. First-principles study of binary and ternary alloys based on PdCu as oxygen reduction catalysts. Chem. Phys. Lett. 758 (2020) 137932.
[23] R. Ma, G. Lin, Y. Zhou, Q. Liu, T. Zhang, G. Shan, M. Yang, J. Wang. A review of oxygen reduction mechanisms for metal-free carbon-based electrocatalysts. Npj Comput. Mater. 5 (2019) 78.
[24] J.L. Tan, A.M. De Jesus, S.L. Chua, J. Sanetuntikul, S. Shanmugam, B.J.V. Tongol, H. Kim. Preparation and characterization of palladium-nickel on graphene oxide support as anode catalyst for alkaline direct ethanol fuel cell. App Catal A-Gen. 531 (2017) 29-35.
[25] L.L. Wang, Q.X. Li, T.Y. Zhan, Q.J. Xu. A Review of Pd-based electrocatalyst for the ethanol oxidation reaction in alkaline medium. Open J. Adv. Mater. Res. 860-863 (2014) 826-830.
[26] B. Cermenek, B. Genorio, T. Winter, S. Wolf, J.G. Connell, M. Roschger, I. Letofsky-Papst, N. Kienzl, B. Bitschnau, V. Hacker. Alkaline ethanol oxidation

reaction on carbon supported ternary PdNiBi nanocatalyst using modified instant reduction synthesis method. Electrocatalysis. 11 (2020) 203-214.
[27] Z.X. Liang, T.S. Zhao, J.B. Xu, L.D. Zhu. Mechanism study of the ethanol oxidation reaction on palladium in alkaline media. Electrochim. Acta. 54 (2009) 2203-2208.
[28] L.M. Palma, T.S. Almeida, A.R. de Andrade. Comparative study of catalyst effect on ethanol electrooxidation in alkaline medium: Pt- and Pd-based catalysts containing Sn and Ru. J. Electroanal. Chem. 878 (2020) 114592.
[29] J. Ribeiro, D.M. Anjos, K.B. Kokoh, C. Coutanceau, J.M. Léger, P. Olivi, A.R. de Andrade, G. Tremiliosi-Filho. Carbon-supported ternary PtSnIr catalysts for direct ethanol fuel cell. Electrochim. Acta. 52 (2007) 6997-7006.
[30] Y. Fornazier Filho, A.C.C. da Cruz, R. Pedicini, J.R.C. Salgado, P.P. Luz, J. Ribeiro. Development of palladium catalysts modified by ruthenium and molybdenum as anode in direct ethanol fuel cell. Mater. Renew. Sustain. Energy. 10 (2021) 5.
[31] E. Antolini. Palladium in fuel cell catalysis. Energy Environ. Sci. 2 (2009) 915-931.
[32] X. Lu, M. Ahmadi, F.J. DiSalvo, H.D. Abruña. Enhancing the electrocatalytic activity of Pd/M (M = Ni, Mn) nanoparticles for the oxygen reduction reaction in alkaline media through electrochemical dealloying. ACS Catalysis. 10 (2020) 5891-5898.
[33] C. Lo Vecchio, C. Alegre, D. Sebastián, A. Stassi, A.S. Aricò, V. Baglio. Investigation of supported Pd-based electrocatalysts for the oxygen reduction reaction: performance, durability and methanol tolerance. Materials. 8 (2015) 7997-8008.
[34] C. Zhang, S. Yu, Y. Xie, W. Zhang, K. Zheng, N.E. Drewett, S.J. Yoo, Z. Wang, L. Shao, H. Tian, J.-G. Kim, W. Zheng. Suppressing the Pd-C interaction through B-doping for highly efficient oxygen reduction. Carbon. 149 (2019) 370-379.
[35] M. Lüsi, H. Erikson, M. Merisalu, M. Rähn, V. Sammelselg, K. Tammeveski. Electrochemical reduction of oxygen in alkaline solution on Pd/C catalysts prepared by electrodeposition on various carbon nanomaterials. J. Electroanal. Chem. 834 (2019) 223-232.

[36] G. Bampos, L. Sygellou, S. Bebelis. Oxygen reduction reaction activity of Pd-based bimetallic electrocatalysts in alkaline medium. Catal. Today. 355 (2020) 685-697.
[37] R.K. Singh, R. Rahul, M. Neergat. Stability issues in Pd-based catalysts: the role of surface Pt in improving the stability and oxygen reduction reaction (ORR) activity. PCCP. 15 (2013) 13044-13051.
[38] W. Wang, D. Zheng, C.-X. Du, Z. Zou, X. Zhang, B. Xia, H. Yang, D. Akins. Carbon-supported Pd-Co bimetallic nanoparticles as electrocatalysts for the oxygen reduction reaction. J. Power Sources. 167 (2007) 243-249.
[39] M.R. Tarasevich, A.E. Chalykh, V.A. Bogdanovskaya, L.N. Kuznetsova, N.A. Kapustina, B.N. Efremov, M.R. Ehrenburg, L.A. Reznikova. Kinetics and mechanism of oxygen reduction reaction at CoPd system synthesized on XC72. Electrochim. Acta. 51 (2006) 4455-4462.
[40] H. Liu, A. Manthiram. Tuning the electrocatalytic activity and durability of low cost $Pd_{70}Co_{30}$ nanoalloy for oxygen reduction reaction in fuel cells. Electrochem. Commun. 10 (2008) 740-744.
[41] X. Wang, N. Kariuki, J.T. Vaughey, J. Goodpaster, R. Kumar, D.J. Myers. Bimetallic Pd–Cu oxygen reduction electrocatalysts. J. Electrochem. Soc. 155 (2008) B602.
[42] M.R. Tarasevich, G.V. Zhutaeva, V.A. Bogdanovskaya, M.V. Radina, M.R. Ehrenburg, A.E. Chalykh. Oxygen kinetics and mechanism at electrocatalysts on the base of palladium–iron system. Electrochim. Acta. 52 (2007) 5108-5118.
[43] B. Li, J. Prakash. Oxygen reduction reaction on carbon supported Palladium–Nickel alloys in alkaline media. Electrochem. Commun. 11 (2009) 1162-1165.
[44] J. Kim, J.-E. Park, T. Momma, T. Osaka. Synthesis of Pd–Sn nanoparticles by ultrasonic irradiation and their electrocatalytic activity for oxygen reduction. Electrochim. Acta. 54 (2009) 3412-3418.
[45] L. Li, H. Wang, L. Zou, X. Wang. Controllable synthesis, photocatalytic and electrocatalytic properties of $CeO_2$ nanocrystals. RSC Advances. 5 (2015) 41506-41512.
[46] W. Yang, X. Wang, S. Song, H. Zhang. Syntheses and Applications of Noble-Metal-free $CeO_2$-Based Mixed-Oxide Nanocatalysts. Chem. 5 (2019) 1743-1774.

[47] H. Yu, S. Zhong, B. Zhu, W. Huang, S. Zhang. Synthesis and CO oxidation activity of 1D mixed binary oxide $CeO_2$-$LaO_x$ supported gold catalysts. Nanoscale Res. Lett. 12 (2017) 579.
[48] C. Qiu, S. Wang, R. Gao, J. Qin, W. Li, X. Wang, Z. Zhai, D. Tian, Y. Song. Low-temperature synthesis of PdO-CeO2/C toward efficient oxygen reduction reaction. Mater. Today Energy. 18 (2020) 100557.
[49] P.C. Meléndez-González, E. Sánchez-Castro, I.L. Alonso-Lemus, R. Pérez-Hernández, B. Escobar-Morales, A.M. Garay-Tapia, W.J. Pech-Rodríguez, J. Rodríguez-Varela. Bifunctional Pd-$CeO_2$ nanorods/C nanocatalyst with high electrochemical stability and catalytic activity for the ORR and EOR in alkaline media. ChemistrySelect. 5 (2020) 14032-14040.
[50] M.Z. Yazdan-Abad, M. Noroozifar, N. Alfi, A.R. Modarresi-Alam, H. Saravani. Pd nanonetwork decorated on rGO as a high-performance electrocatalyst for ethanol oxidation. Appl. Surf. Sci. 462 (2018) 112-117.
[51] R. Carrera-Cerritos, R. Fuentes-Ramírez, F.M. Cuevas-Muñiz, J. Ledesma-García, L.G. Arriaga. Performance and stability of Pd nanostructures in an alkaline direct ethanol fuel cell. J. Power Sources. 269 (2014) 370-378.
[52] F. Zhu, M. Wang, Y. He, G. Ma, Z. Zhang, X. Wang. A comparative study of elemental additives (Ni, Co and Ag) on electrocatalytic activity improvement of PdSn-based catalysts for ethanol and formic acid electro-oxidation. Electrochim. Acta. 148 (2014) 291-301.
[53] R.M. Abdel Hameed. Facile preparation of Pd-metal oxide/C electrocatalysts and their application in the electrocatalytic oxidation of ethanol. Appl. Surf. Sci. 411 (2017) 91-104.
[54] A.N. Geraldes, D. Furtunato da Silva, J.C. Martins da Silva, O. Antonio de Sá, E.V. Spinacé, A.O. Neto, M. Coelho dos Santos. Palladium and palladium–tin supported on multi wall carbon nanotubes or carbon for alkaline direct ethanol fuel cell. J. Power Sources. 275 (2015) 189-199.
[55] L. Ma, H. He, A. Hsu, R. Chen. PdRu/C catalysts for ethanol oxidation in anion-exchange membrane direct ethanol fuel cells. J. Power Sources. 241 (2013) 696-702.
[56] Y. Zhang, Q. Yi, H. Chu, H. Nie. Catalytic activity of Pd-Ag nanoparticles supported on carbon nanotubes for the electro-oxidation of ethanol and propanol. J. Fuel Chem.Technol. 45 (2017) 475-483.

[57] X. Lao, M. Yang, J. Chen, L.Y. Zhang, P. Guo. The ethanol oxidation reaction on bimetallic $Pd_xAg_{1-x}$ nanosheets in alkaline media and their mechanism study. Electrochim. Acta. 374 (2021) 137912.
[58] S. Ren, D. Du, L. Ma, C. Li. Mesoporous PdBi film as efficient electrocatalyst for ethanol oxidation reaction. J. Phys. Materials. 4 (2021) 034001.
[59] Z. Qi, H. Geng, X. Wang, C. Zhao, H. Ji, C. Zhang, J. Xu, Z. Zhang. Novel nanocrystalline PdNi alloy catalyst for methanol and ethanol electro-oxidation in alkaline media. J. Power Sources. 196 (2011) 5823-5828.
[60] S. Sankar, G.M. Anilkumar, T. Tamaki, T. Yamaguchi. Cobalt-modified palladium bimetallic catalyst: a multifunctional electrocatalyst with enhanced efficiency and stability toward the oxidation of ethanol and formate in alkaline medium. ACS Applied Energy Materials. 1 (2018) 4140-4149.
[61] X. Wang, G. Ma, F. Zhu, N. Lin, B. Tang, Z. Zhang. Preparation and characterization of micro-arc-induced Pd/TM(TM=Ni, Co and Ti) catalysts and comparison of their electrocatalytic activities toward ethanol oxidation. Electrochim. Acta. 114 (2013) 500-508.
[62] A.O. Neto, S.G. da Silva, G.S. Buzzo, R.F.B. de Souza, M.H.M.T. Assumpção, E.V. Spinacé, J.C.M. Silva. Ethanol electrooxidation on PdIr/C electrocatalysts in alkaline media: electrochemical and fuel cell studies. Ionics. 21 (2015) 487-495.
[63] H. Yang, Z. Yu, S. Li, Q. Zhang, J. Jin, J. Ma. Ultrafine palladium-gold-phosphorus ternary alloyed nanoparticles anchored on ionic liquids-noncovalently functionalized carbon nanotubes with excellent electrocatalytic property for ethanol oxidation reaction in alkaline media. J. Catal. 353 (2017) 256-264.
[64] Y. Zhang, X.-L. Yuan, F.-L. Lyu, X.-C. Wang, X.-J. Jiang, M.-H. Cao, Q. Zhang. Facile one-step synthesis of PdPb nanochains for high-performance electrocatalytic ethanol oxidation. Rare Metals. 39 (2020) 792-799.
[65] H. Mao, L. Wang, P. Zhu, Q. Xu, Q. Li. Carbon-supported PdSn–$SnO_2$ catalyst for ethanol electro-oxidation in alkaline media. Int. J. Hydrogen Energy. 39 (2014) 17583-17588.
[66] A. Zalineeva, A. Serov, M. Padilla, U. Martinez, K. Artyushkova, S. Baranton, C. Coutanceau, P. Atanassov. Nano-structured Pd-Sn catalysts for alcohol electro-oxidation in alkaline medium. Electrochem. Commun. 57 (2015) 48-51.

[67] A. Shafaei Douk, H. Saravani, M. Noroozifar. Novel fabrication of PdCu nanostructures decorated on graphene as excellent electrocatalyst toward ethanol oxidation. Int. J. Hydrogen Energy. 42 (2017) 15149-15159.
[68] J. Cai, Y. Zeng, Y. Guo. Copper@palladium–copper core–shell nanospheres as a highly effective electrocatalyst for ethanol electro-oxidation in alkaline media. J. Power Sources. 270 (2014) 257-261.
[69] W. Yang, H. Wang, F. Fu. PdCu nanoalloys deposited on porous carbon as a highly efficient catalyst for ethanol oxidation. Mater. Chem. Phys. 228 (2019) 175-179.
[70] Z. Xiong, B. Yan, K. Zhang, C. Wang, S. Li, H. Xu, Y. Du, C. Zhai. A facile synthesis of 3D network PdCu nanostructure with enhanced electrocatalytic activity towards ethanol oxidation. J. Taiwan Ins Chem Eng. 75 (2017) 12-17.
[71] X. Zhao, J. Zhang, L. Wang, Z. Liu, W. Chen. PdxCu100−x networks: an active and durable electrocatalyst for ethanol oxidation in alkaline medium. J. Mater. Chem. A. 2 (2014) 20933-20938.
[72] C. Xu, P.k. Shen, Y. Liu. Ethanol electrooxidation on Pt/C and Pd/C catalysts promoted with oxide. J. Power Sources. 164 (2007) 527-531.
[73] V. Bambagioni, C. Bianchini, Y. Chen, J. Filippi, P. Fornasiero, M. Innocenti, A. Lavacchi, A. Marchionni, W. Oberhauser, F. Vizza. Energy Efficiency Enhancement of ethanol electrooxidation on Pd–$CeO_2$/C in passive and active polymer electrolyte-membrane fuel cells. ChemSusChem. 5 (2012) 1266-1273.
[74] E. Antolini. Carbon supports for low-temperature fuel cell catalysts. App. Catal. B: Environ. 88 (2009) 1-24.
[75] L.M. Rivera Gavidia, D. Sebastián, E. Pastor, A.S. Aricò, V. Baglio. Carbon-supported Pd and PdFe alloy catalysts for direct methanol fuel cell cathodes. Materials. 10 (2017).
[76] H. Huang, X. Wang. Recent progress on carbon-based support materials for electrocatalysts of direct methanol fuel cells. J. Mater. Chem. A. 2 (2014) 6266-6291.
[77] J. Wang, G. Yin, Y. Shao, S. Zhang, Z. Wang, Y. Gao. Effect of carbon black support corrosion on the durability of Pt/C catalyst. J. Power Sources. 171 (2007) 331-339.

[78] J. Zhang, S. Lu, Y. Xiang, S.P. Jiang. Intrinsic effect of carbon supports on the activity and stability of precious metal based catalysts for electrocatalytic alcohol oxidation in fuel cells: A review. ChemSusChem. 13 (2020) 2484-2502.
[79] S. Pérez-Rodríguez, E. Pastor, M.J. Lázaro. Electrochemical behavior of the carbon black Vulcan XC-72R: Influence of the surface chemistry. Int. J. Hydrogen Energy. 43 (2018) 7911-7922.
[80] P. Ferreira-Aparicio, Carbon Blacks in Electrochemical Energy Conversion Devices: Uses and Application in Fuel Cells, in: T.L.P. Ian J. Sanders (Ed.) Carbon Black: Production, Properties and uses, Nova Science Publishers, New York, 2011, pp. 1-40.
[81] A.D. Moore, S.M. Holmes, E.P.L. Roberts. Evaluation of porous carbon substrates as catalyst supports for the cathode of direct methanol fuel cells. RSC Advances. 2 (2012) 1669-1674.
[82] M. Noked, A. Soffer, D. Aurbach. The electrochemistry of activated carbonaceous materials: past, present, and future. J. Solid State Electrochem. 15 (2011) 1563.
[83] F. Fathirad, D. Afzali, A. Mostafavi. Bimetallic Pd–Zn nanoalloys supported on Vulcan XC-72R carbon as anode catalysts for oxidation process in formic acid fuel cell. Int. J. Hydrogen Energy. 41 (2016) 13220-13226.
[84] L.C. M.J. Lázaro, V. Celorrio, J.I. Pardo, S. Perathoner, R. Moliner, Study and Application of carbon black Vulcan CX-72 in Polymeric Electrolyte Fuel Cells, in: T.L.P. I.J. Sanders (Ed.) Carbon Black: Production, Properties and Uses, Nova Science Publishers, New York, 2011, pp. 41-68.
[85] M. Laskowska, M. Oyama, I. Kityk, M. Marszalek, M. Dulski, L. Laskowski. Surface functionalization by silver-containing molecules with controlled distribution of functionalities. Appl. Surf. Sci. 481 (2019) 433-436.
[86] H. Schmies, E. Hornberger, B. Anke, T. Jurzinsky, H.N. Nong, F. Dionigi, S. Kühl, J. Drnec, M. Lerch, C. Cremers, P. Strasser. Impact of carbon support functionalization on the electrochemical stability of Pt fuel cell catalysts. Chem. Mater. 30 (2018) 7287-7295.
[87] A. Vaseashta, D. Dimova-Malinovska. Nanostructured and nanoscale devices, sensors and detectors. Sci Technol Adv Mater. 6 (2005) 312-318.

[88] S. Banerjee, T. Hemraj-Benny, S.S. Wong. Covalent surface chemistry of single-walled carbon nanotubes. Adv. Mater. 17 (2005) 17-29.
[89] S. Yin, P.K. Shen, S. Song, S.P. Jiang. Functionalization of carbon nanotubes by an effective intermittent microwave heating-assisted HF/$H_2O_2$ treatment for electrocatalyst support of fuel cells. Electrochim. Acta. 54 (2009) 6954-6958.
[90] N. Lakshmi, N. Rajalakshmi, K.S. Dhathathreyan. Functionalization of various carbons for proton exchange membrane fuel cell electrodes: analysis and characterization. J. Phys. D: Appl. Phys. 39 (2006) 2785-2790.
[91] S.M.S. Kumar, N. Hidyatai, J.S. Herrero, S. Irusta, K. Scott. Efficient tuning of the Pt nano-particle mono-dispersion on Vulcan XC-72R by selective pre-treatment and electrochemical evaluation of hydrogen oxidation and oxygen reduction reactions. Int. J. Hydrogen Energy. 36 (2011) 5453-5465.
[92] C.K. Poh, S.H. Lim, H. Pan, J. Lin, J.Y. Lee. Citric acid functionalized carbon materials for fuel cell applications. J. Power Sources. 176 (2008) 70-75.
[93] J. Zheng, J. Wang, D. Song, J. Xu, M. Zhang. Electrochemical Aptasensor of Carcinoembryonic Antigen Based on Concanavalin A-Functionalized Magnetic Copper Silicate Carbon Microtubes and Gold-Nanocluster-Assisted Signal Amplification. ACS Appl. Nano Mater. 3 (2020) 3449-3458.
[94] H.-K. Lee, J.W. Choi, W. Oh, S.-J. Choi. Sorption of cesium ions from aqueous solutions by multi-walled carbon nanotubes functionalized with copper ferrocyanide. J. Radioanal. Nucl. Chem. 309 (2016) 477-484.
[95] C. Yuan, B. Liu, F. Liu, M.-Y. Han, Z. Zhang. Fluorescence "turn on" detection of mercuric ion based on Bis(dithiocarbamato)copper(II) complex functionalized carbon nanodots. Anal. Chem. 86 (2014) 1123-1130.
[96] S. Gentil, J.K. Molloy, M. Carrière, G. Gellon, C. Philouze, D. Serre, F. Thomas, A. Le Goff. Substituent effects in carbon-nanotube-supported copper phenolato complexes for oxygen reduction reaction. Inorg. Chem. 60 (2021) 6922-6929.
[97] K. Zhang, Z. Xiong, S. Li, B. Yan, J. Wang, Y. Du. Cu3P/RGO promoted Pd catalysts for alcohol electro-oxidation. J. Alloys Compd. 706 (2017) 89-96.
[98] S. Sarkar, M.L. Moser, X. Tian, X. Zhang, Y.F. Al-Hadeethi, R.C. Haddon. Metals on graphene and carbon nanotube surfaces: from mobile atoms to atomtronics to bulk metals to clusters and catalysts. Chem. Mater. 26 (2014) 184-195.

[99] F. Wang, M.E. Itkis, E.B. Bekyarova, X. Tian, S. Sarkar, A. Pekker, I. Kalinina, M.L. Moser, R.C. Haddon. Effect of first row transition metals on the conductivity of semiconducting single-walled carbon nanotube networks. Appl. Phys. Lett. 100 (2012) 223111.
[100] E. Bekyarova, S. Sarkar, F. Wang, M.E. Itkis, I. Kalinina, X. Tian, R.C. Haddon. Effect of covalent chemistry on the electronic structure and properties of carbon nanotubes and graphene. Acc. Chem. Res. 46 (2013) 65-76.
[101] I. Kalinina, E. Bekyarova, S. Sarkar, F. Wang, M.E. Itkis, X. Tian, S. Niyogi, N. Jha, R.C. Haddon. Hexahapto-metal complexes of single-walled carbon nanotubes. Macromol. Chem. Phys. 213 (2012) 1001-1019.
[102] J.C. Martínez-Loyola, A.A. Siller-Ceniceros, M.E. Sánchez-Castro, M. Sánchez, J.R. Torres-Lubián, B. Escobar-Morales, C. Ornelas, I.L. Alonso-Lemus, F.J. Rodríguez-Varela. High performance Pt nanocatalysts for the oxidation of methanol and ethanol in acid media by effect of functionalizing carbon supports with Ru organometallic compounds. J. Electrochem. Soc. 167 (2020) 164502.
[103] A.A. Siller-Ceniceros, E. Sánchez-Castro, D. Morales-Acosta, J.R. Torres-Lubián, E. Martínez-Guerra, J. Rodríguez-Varela. Functionalizing reduced graphene oxide with Ru-organometallic compounds as an effective strategy to produce high-performance Pt nanocatalysts for the methanol oxidation reaction. ChemElectroChem. 6 (2019) 4902-4916.
[104] A.A. Siller-Ceniceros, M.E. Sánchez-Castro, D. Morales-Acosta, J.R. Torres-Lubian, E. Martínez G, F.J. Rodríguez-Varela. Innovative functionalization of Vulcan XC-72 with Ru organometallic complex: Significant enhancement in catalytic activity of Pt/C electrocatalyst for the methanol oxidation reaction (MOR). App. Catal. B: Environ. 209 (2017) 455-467.
[105] A.J. Hickman, M.S. Sanford. High-valent organometallic copper and palladium in catalysis. Nature. 484 (2012) 177-185.
[106] R.M. Gschwind. Organocuprates and diamagnetic copper complexes: structures and NMR spectroscopic structure elucidation in solution. Chem. Rev. 108 (2008) 3029-3053.
[107] H. Eriksson, M. Håkansson. Mesitylcopper: tetrameric and pentameric. organometallics. 16 (1997) 4243-4244.

[108] M. Stollenz, F. Meyer. Mesitylcopper – a powerful tool in synthetic chemistry. Organometallics. 31 (2012) 7708-7727.
[109] T. Tsuda, T. Yazawa, K. Watanabe, T. Fujii, T. Saegusa. Preparation of thermally stable and soluble mesitylcopper(I) and its application in organic synthesis. J. Org. Chem. 46 (1981) 192-194.
[110] C. Barrière, G. Alcaraz, O. Margeat, P. Fau, J.B. Quoirin, C. Anceau, B. Chaudret. Copper nanoparticles and organometallic chemical liquid deposition (OMCLD) for substrate metallization. J. Mater. Chem. 18 (2008) 3084-3086.
[111] S.-W. Jin, X.-H. Ye, L. Jin, L. Zheng, J.-W. Li, B.-P. Jin, D.-Q. Wang. Syntheses and structural characterization of nine coordination compounds assembled from copper acetate, 3,5-dimethylpyrazole and carboxylates. Polyhedron. 81 (2014) 382-395.

# Chapter II
# Hypothesis and objectives

# Chapter II
# Hypothesis and objectives

## 2.1 Hypothesis

The addition of $CeO_{2\text{-}NR}$ will enhance the electrochemical stability of Pd-based nanocatalysts, promoting their catalytic activity for the EOR and the ORR. The functionalization of C with Cu organometallic compounds will form metal active sites and surface functional groups, promoting a high dispersion of nanoparticles, the creation of alloyed Pd-Cu phases, and the modification of the electronic structure of Pd, resulting in nanocatalysts with high catalytic activity for the EOR.

## 2.2 General objective

To study the effect of implementing $CeO_{2\text{-}NR}$ as co-catalyst as well as that of functionalizing C with Cu organometallic compounds forming modified supports on the catalytic activity of Pd-based nanocatalysts for the ORR and the EOR in alkaline media, by evaluating the electronic and structural modification of Pd, for their possible use in cathodes and anodes of AEM-DEFC.

## 2.3 Specific objectives

- To analyze the effect of implementing $CeO_{2\text{-}NR}$ as co-catalyst on the catalytic activity, bifunctionality and electrochemical stability of Pd-$CeO_{2\text{-}NR}$/C nanocatalyst for the ORR and the EOR.
- To propose a methodology to functionalize commercial Vulcan (C) with the Cu-mes and Cu(dmpz)L2 organometallic compounds.
- To study the $C_{Cu\text{-}mes}$ and $C_{Cu(dmpz)L2}$ functionalized supports aiming to evaluate the capacity of the Cu compounds to modify the structure and surface of Vulcan.
- To study the electronic and structural modifications of Pd resulting from interactions with Cu-sites from the organometallic functionalization.
- To correlate such modifications with the catalytic activity of Pd-based nanocatalysts for the EOR.

- To evaluate the catalytic activity of the Pd-based nanocatalysts supported on $C_{Cu\text{-}mes}$ and $C_{Cu(dmpz)L2}$ in an AEM-DEFC.

# Chapter III
# Experimental Section

## 3.1 Chemical reagents and gases

The chemical reagents were of analytical grade: Ammonium hexachloropalladate (IV) ($PdCl_6(NH_4)_2$) (99 %), ethylene glycol ($C_2H_6O_2$) (99.8 %), sulfuric acid ($H_2SO_4$) (95-99 %), sodium hydroxide (NaOH) (97 %), copper (I) chloride (CuCl (I)) (99.9 %), 1,4-dioxano ($C_4H_8O_2$) (99.8 %), ethylic ether ($(C_2H_5)_2O$) (99 %), 3,5 dimethyl pyrazole ($C_5H_8N_2$) (99 %), copper (II) acetate monohydrate ($Cu(CO_2CH_3)2{\cdot}H_2O$) (99 %), terephthalic acid ($C_8H_6O_4$) (97.5 %), tetrahydrofuran (THF, $C_4H_8O$) (99.9 %), potassium hydroxide (KOH) (90 %), deuterated acetone ($(CD_3)_2CO$) (99.98 %), benzene ($C_6D_6$) (99.99%), Nafion® solution (5 wt. %), 2-propanol ($C_3H_8O$) (95 %), and ethanol ($C_2H_5OH$) (99.8 %) were purchased from Sigma-Aldrich and used as received. $CeO_{2\text{-}NR}$ were synthesized as described previously [1]. Metallic sodium ($Na^0$) and deionized water were acquired from Jalmeck. Vulcan XC-72 was obtained from Cabot. UHP Ar and $O_2$ were purchased from Infra (purity > 99%).

## 3.2 Synthesis of copper organometallic compounds

### 3.2.1 Synthesis of mesityl Cu (Cu-mes)

The preparation of the Cu-mes was carried out following the methodology reported in [2], with slight modifications under Ar atmosphere using a Schlenk line. The glassware was previously washed and heated at 95 °C overnight to eliminate moisture. The solvents (dioxane, THF, and ether) were distilled before use with $Na^0$ in refluxing conditions by 2 h, to avoid the formation of metallic oxides.

A suspension of CuCl (I) (10.9 g, 110 mmol) in THF (100 mL) was ultrasonically mixed for 1 h. Then 100 mL of mesityl BrMg were added under vigorous magnetic stirring for 12 h at room temperature in Ar atmosphere. A change of color from green to brown was observed. Dioxane (50 mL) was added to the mixture, maintaining stirring for 2 h, allowing precipitation for 1 h. The BrMgCl salt obtained had a white color.

The recovered yellow liquid remaining was mixed with 50 mL of ether and the solution allowed to precipitate for 30 min. The resulting crystals were filtered and

dried in vacuum to obtain Cu-mes as yellow/brown powder with 43.79 % (6g, 32 mmol) reaction yield.

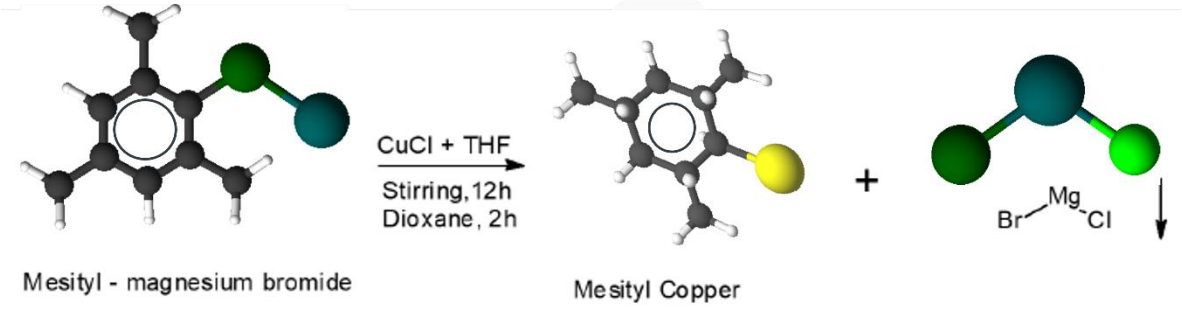


**Figure 3.1** Reactions during the synthesis of Cu-mes.

### 3.2.2 Synthesis of Cu compound coordinated with 3,5 dimethylpyrazole (dmpz) and terephthalic acid (L2) (Cu(dmpz)L2)

Cu(dmpz)L2 was synthesized as follows [3]: a solution of copper (II) acetate (0.199 g) in methanol (15 mL) was mixed with 12 mL of methanol containing dmpz (0.192 g) and terephthalic acid (L2) (0.28 g) under continuous stirring. The resulting solution was dispersed for 45 min by ultrasound at room temperature. Afterwards, 1 mL of $NH_4OH$ was added, allowing precipitation for 1 h. The color changed from blue/green a to purple. The resulting product was filtered, washed with methanol, and dried to obtain Cu(dmpz)L2 as a blue powder with 77.7 % (0.7 g) reaction yield.

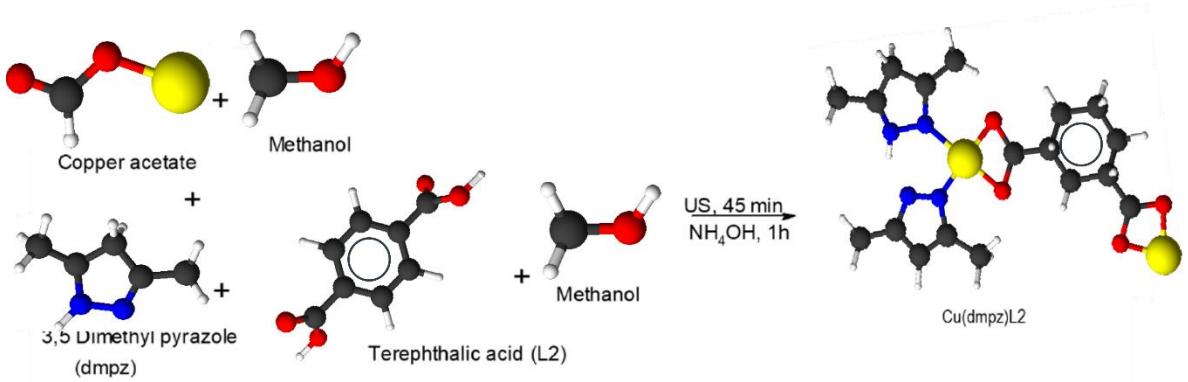


**Figure 3.2** Reactions during the synthesis of Cu(dmpz)L2.

### 3.3 Functionalization of C supports: synthesis of $C_{Cu\text{-}mes}$ and $C_{Cu(dmpz)L2}$

$C_{Cu\text{-}mes}$ was obtained from the functionalization of Vulcan XC-72 with 0.4 g of Cu-mes and 0.6 g of C ($C_{Cu\text{-}mes}$: C molar ratio of 1:10 [4]) were stirred in 80 mL of THF under Ar atmosphere and refluxing conditions for 48 h at 130 °C. The black solution generated was transferred into a Schlenk tube, filtered through a cannula, washed with dried THF, ethanol, and water. The product was finally dried in vacuum for 3 h, resulting in a black powder.

$C_{Cu(dmpz)L2}$ was obtained following the same procedure using 0.7 g of Cu(dmpz)L2 and 0.2 g of C, resulting also in a black powder.

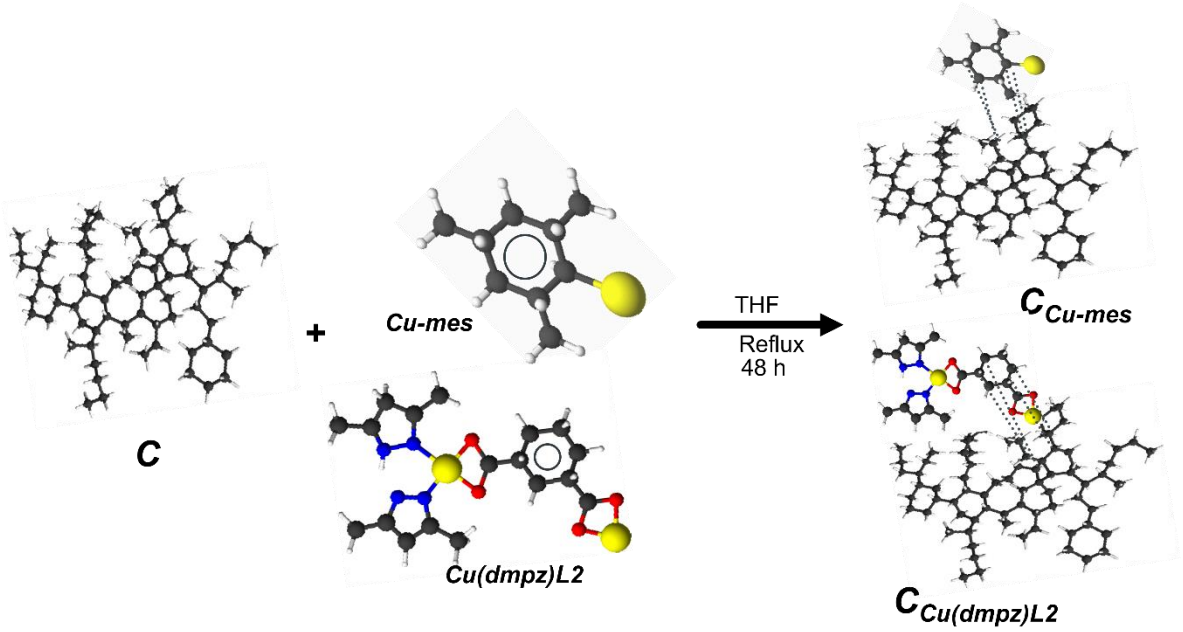


**Figure 3.3** Scheme of the experimental procedure of Vulcan functionalization.

### 3.4 Synthesis of nanocatalysts based on Pd

The 20 wt. % Pd-$CeO_{2\text{-}NR}$/C nanocatalyst with a 1:1 nominal Pd:$CeO_{2\text{-}NR}$ atomic ratio was synthesized by the polyol method [5]. C (0.08 g) was dispersed in 46 mL of ethylene glycol (EG), while the Pd precursor ($PdCl_6(NH_4)_2$ (0.025 g) and the $CeO_{2\text{-}NR}$ (0.012 g) were separately mixed in 2 mL of ethanol. The dispersions were sonicated for 1 h. Afterward, the solutions containing $CeO_{2\text{-}NR}$ and Pd were added dropwise to that of C, then stirred for 30 min in ambient conditions.

Subsequently, the pH was adjusted to 12 by adding NaOH (1 mol $L^{-1}$), the temperature increased to 160°C and maintained for 3 h under refluxing and stirring conditions. At the end of this time, the mixture was allowed to cool down to room temperature, and 1 mol $L^{-1}$ $H_2SO_4$ was added to adjust the pH to 2. Finally, the product was filtered, washed, and dried.

The same procedure was followed used for the Pd-$CeO_{2\text{-}NR}$/$C_{Cumes}$, Pd-$CeO_{2\text{-}NR}$/$C_{Cu(dmpz)L2}$, Pd/$C_{Cu\text{-}mes}$, Pd/$C_{Cu(dmpz)L2}$ and Pd/C nanocatalysts. In the last three cases, the addition of $CeO_{2\text{-}NR}$ was omitted.

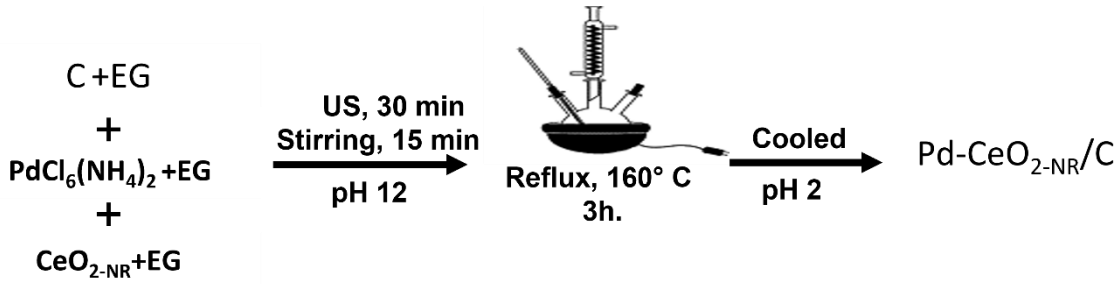


**Figure 3.4** Scheme of the reactions of the experimental procedure to synthesize Pd-$CeO_{2\text{-}NR}$/C by the polyol method.

## 3.5 Physicochemical characterization

### 3.5.1 Nuclear Magnetic Resonance (NMR)

Cu-mes was characterized by $^{1}$H-NMR spectroscopy. Chemical analyses were obtained in a 500 MHZ Bruker Advance III apparatus (using 5 mm direct broad band with Z-grad (PABBO-1H/D Z-GRAD). The $^{1}$H chemical shifts were referenced to residual no deuterated solvent. Cu-mes was dissolved in $(CD_3)_2CO$.

### 3.5.2 Fourier Transform Infrared Spectroscopy (FT-IR)

Cu-mes, Cu(dmpz)L2, $C_{Cu\text{-}mes}$, and $C_{Cu(dmpz)L2}$ were characterized by FT-IR in a WQF-S10A FT-IR Rayleigh instrument. FT-IR spectra were acquired in transmission mode at 4 $cm^{-1}$ resolutions in the scan range of 4000 to 500 $cm^{-1}$ using KBr pellets.

### 3.5.3 Raman Spectroscopy

Raman microanalyses were carried out using a DXRZ Thermo Scientific equipment ($\lambda$=633 nm, in a range= between 400 and 3500 $cm^{-1}$). The ratio between the D and G band intensities ($I_D/I_G$ ratio) was used to study the rehybridization of the carbon supports. Three microanalyses were performed, the average of which is reported.

### 3.5.4 X-Ray Diffraction (XRD)

The nanocatalysts were characterized by X-ray diffraction (XRD) using a Philips X'Pert diffractometer, with CuK$\alpha$ radiation ($\lambda$=1.5418 Å). The crystallite size (d) was estimated using values of the (220) of Pd plane with the aid of the Scherrer equation [6].

$$d = \frac{0.9\lambda}{\beta cos\theta} \qquad \text{Equation 3.1}$$

where d is the crystallite size, 0.9 is a correction factor or the Scherrer constant, that applies to powder samples; $\lambda$ is the wavelength of the radiation emitted by the Cu K$\alpha$ lamp (1.5418 Å); β is the full width at half maximum in radians, and θ is the angle at the peak maximum.

The lattice parameter $a_{fcc}$ of the nanocatalysts was calculated with Bragg's law using data from the Pd (111) peak [7, 8]:

$$a_{fcc} = \frac{\sqrt{2}\,\lambda}{sin\,\theta} \qquad \text{Equation 3.2}$$

where $\lambda$ and θ have the same meaning as in Equation 3.1.

Following the procedure described in the literature [9], the fraction of Cu alloyed (D) in the nanocatalysts was calculated with equation:

$$D = \left[\left(\frac{a_{fcc} - a_0}{a_s - a_0}\right)\right] x_s \qquad \text{Equation 3.3}$$

where $a_{fcc}$ is the experimental lattice parameter (Table 5.6), $a_0$ is the experimental lattice parameter of the synthesized Pd/C (Table 5.6), $a_s$ is the lattice parameter of ca. 100 % alloyed Pd-Cu/C, $x_s$ is the Cu atomic fraction in the nanocatalysts.

### 3.5.5 Scanning Electron Microscopy coupled with Energy Dispersive Spectroscopy (SEM-EDS)

The chemical composition was determined in a Philips XL30 Scanning Electron Microscope, equipped with an EDS detector, under an accelerating voltage of 20 kV. Five quantitative microanalyses were performed in different areas of the samples, the average of which was obtained and reported here.

### 3.5.6 High-Resolution Transmission Electron Microscopy (HR-TEM)

The nanocatalysts were characterized by HR-TEM, in a Hitachi 7700 transmission electron microscope obtaining the particle size by the averaging the diameter of 100 particles, using the Gatan digital micrograph software.

### 3.5.7 X-Ray Photoelectron Spectroscopy (XPS)

The surface oxidation state was characterized by X-ray photoelectron spectroscopy (XPS) using a Thermo Scientific ESCALAB 25OXi (Al-Ká, 20 eV) spectrometer. Deconvolutions of the spectra with baseline correction were performed using the Shirley-Sherwood method. The binding energies (BE) were calibrated to 284.8 eV due to adventitious carbon (C 1s peak). The relative composition (% at.) of the nanocatalysts was reported.

## 3.6 Electrochemical Characterization

### 3.6.1 Electrochemical half cell

Electrochemical measurements were carried out in a three-electrode electrochemical cell. All the measurements were performed at room temperature. The counter-electrode was a Pt wire in a separate compartment with a membrane at the tip, while the reference electrode was of the Ag/AgCl type in saturated 3M NaCl solution placed in Luggin capillary, also with a membrane at the tip. The potentials have been referred to the Reversible Hydrogen Electrode (RHE). The catalytic ink was prepared by separately mixing 10 mg of each nanocatalysts, 5μL of Nafion®, and 1 mL of 2-propanol, by sonification for 40 min. The working electrode was fabricated by transferring an aliquot of 10 μL of the catalytic ink into a glassy carbon disk (geometric area= 0.196 $cm^2$).

The electrochemical behavior of the nanomaterials was evaluated in 0.5 mol $L^{-1}$ KOH under Ar atmosphere in a VSP-300 Bio-Logic bipotenciostat connected to a rotating ring-disk electrode set-up (RRDE, Pine Inst).

### 3.6.2 Cyclic voltammograms (CVs)

The nanocatalysts were activated by cyclic voltammetry in a potential window between 0.05 and 1.2 V/RHE at 50 mV $s^{-1}$ for 40 cycles. With this procedure, impurities on the electrode surface were removed and the cleanliness of the nanocatalyst was ensured. Subsequently, CVs were obtained in the same potential range at a sweep rate of 20 mV $s^{-1}$.

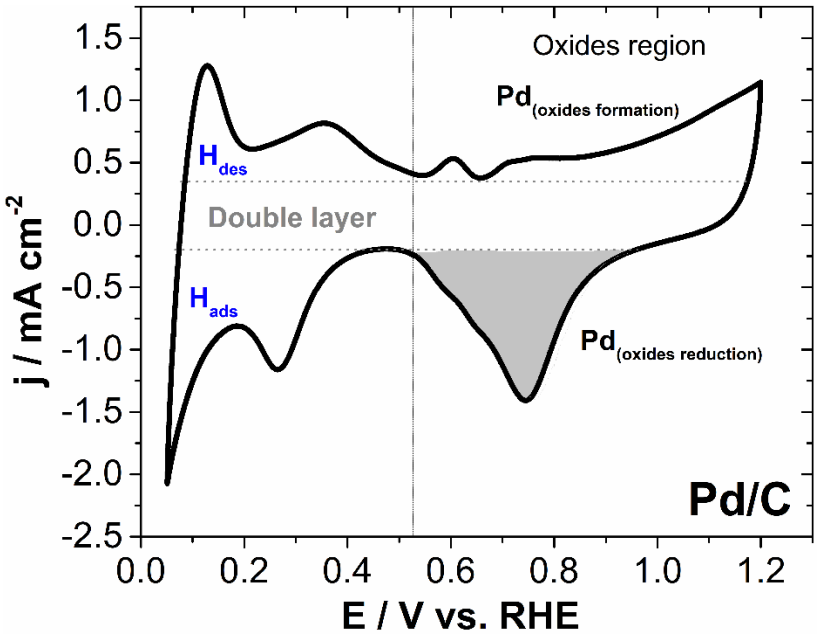


**Figure 3.5** CV of Pd/C. Electrolyte: $N_2$-satured 0.5 mol $L^{-1}$ KOH. Scan rate: 20 mV $s^{-1}$.

The electrochemically active specific surface area (ECSA, $m^2$ $g^{-1}$) of the nanocatalyst was estimated by integrating the coulombic charge of $Pd_{(oxides\ reduction)}$ peak highlighted in Figure 3.5 ($Q_0$, µC $cm^{-2}$.) and assuming a theoretical charge ($Q_{theo,\ PdO}$) of 420 µC $cm^{-2}$ for the reduction of a monolayer of oxides [10], using the following equation:

$$ECSA_{PdO} = \frac{Q_0}{Q_{theo,PdO} \times L_{Pd}} \qquad \text{Equation 3.4}$$

where $L_{Pd}$ (μg) is the amount of palladium on the electrode determined from chemical composition analysis.

### 3.6.3 Evaluation of catalytic activity for the ORR

The electrolyte was saturated with $O_2$ for 20 min before obtaining the CVs at four different rotation rates (ω = 400, 800, 1200, and 1600 rpm). The potential interval was the same as indicated in the previous section, with a scan rate of 5 mV $s^{-1}$. The current density of the ORR was determined by subtracting the background current obtained in Ar atmosphere at the same scan rate. The ring was polarized at 1.2 V/RHE and the current measured was used to estimate % $HO_2^-$ (percent of hydroperoxyl ion) and n (electron transfer number).

The % $HO_2^-$ and n values have been determined using equations 3.5 and 3.6, as reported previously: [11]

$$\% HO_2^- = 200 \frac{\frac{i_R}{N}}{i_D + \frac{i_R}{N}} \quad \text{Equation 3. 5}$$

$$n = \frac{4\, i_D}{\left(i_D + \frac{i_R}{N}\right)} \quad \text{Equation 3.6}$$

where $i_D$ is the disk current, $i_R$ is the ring current, and N is the collection efficiency (N= 0.37).

Mass and specific activities were calculated by normalizing the kinetic current ($i_k$) with respect to the Pd load ($mg_{Pd}$, experimental Pd mass based in the EDS results) deposited in the electrode and with the Pd real surface area ($A_{Pd}$ in $cm^2$), respectively, obtained from the following relationship:

$$A_{Pd} = \frac{Q_o}{Q_{theo,PdO}} \quad \text{Equation 3.7}$$

$Q_o$ and $Q_{theo,\,PdO}$ are the same as described in equation 3.4.

### 3.6.4 Evaluation of catalytic activity for the EOR

Characterization of the catalytic activity of the nanocatalysts for the EOR was carried out in a Pine Wave Driver 20 bipotentiostat. Polarization curves were obtained adding a solution 0.5 mol $L^{-1}$ $C_2H_5OH$ to the 0.5 mol $L^{-1}$ KOH electrolyte in the same potential interval and sweep rate as indicated in section 3.6.2. The current of the reaction was normalized with respect to the experimental Pd mass content, to obtain the mass current density ($j_m$).

### 3.6.5 Accelerated degradation test (ADT)

In the case of the ORR, ADT were performed by submitting the nanocatalysts to 3000 cycles at 50 mV $s^{-1}$ in the 0.6 – 1.0 V/RHE potential range, following the protocol proposed by the US Department of Energy (DOE) [12]. ECSA values, CVs and polarization curves of the ORR were compared before and after of the tests (Chapter IV).

Regarding the EOR, the nanocatalysts were submitted to 2000 cycles at 200 mV $s^{-1}$ in the 0.05 – 1.2 V/RHE potential interval. The measurements allowed to compare CVs and polarization curves of the EOR at the nanocatalysts before and after the cycling (Chapters V and VI).

### 3.6.6 CO-stripping

CO–stripping measurements were carried out bubbling CO into the cell for 10 min while polarizing the electrode at 50 mV/RHE, followed by purging with Ar for 30 min. Then, two CVs were recorded at 20 mV $s^{-1}$ in the range of 0.05 to 1.2 V/RHE, detecting the CO desorption ($CO_{des}$) peak in the first cycle (Figure 3.6).

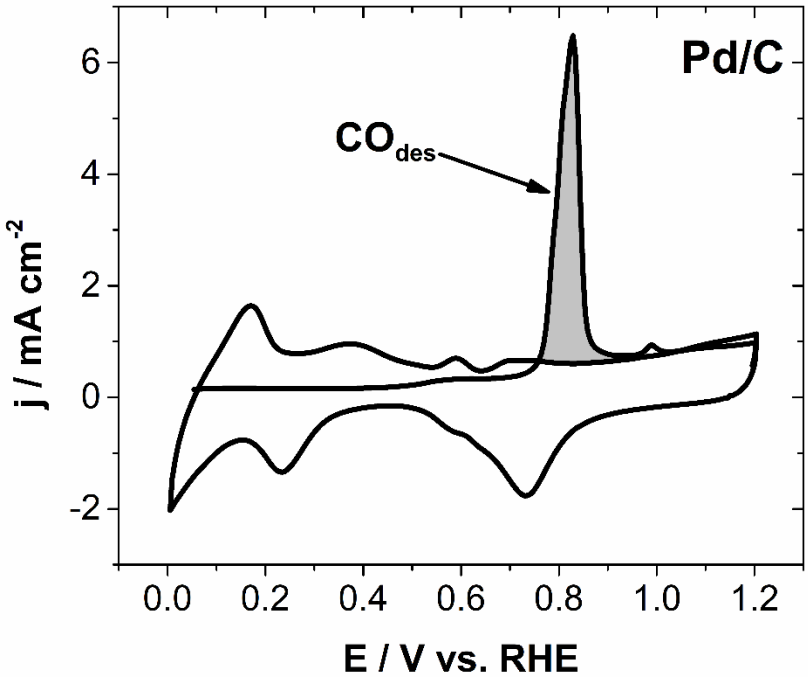


**Figure 3.6** CO-stripping at Pd/C. The $CO_{des}$ peak is highlighted in grey. Electrolyte: Ar-satured 0.5 mol $L^{-1}$ KOH. Scan rate: 20 mV $s^{-1}$.

$ECSA_{CO}$ values (i.e., from CO-stripping) were calculated from the integration of the experimental charge associated to $CO_{des}$ peak according to the following Equation 3.8.

$$ECSA_{CO} = \frac{Q_{CO}}{Q_{theo,CO} \times L_{Pd}} \qquad \text{Equation 3 8}$$

where $Q_{CO}$ (μC) is the charge due to the oxidation of $CO_{des}$ shown in Figure 3.6, $Q_{theo,CO}$ is the theoretical charge for the oxidation of a monolayer of CO on a Pd electrode (420 μC $cm^{-2}$) and $L_{Pd}$ (μg) the amount of palladium on the electrode [10].

### 3.6.7 Anion Exchange Membrane Direct Ethanol Fuel Cell (AEM-DEFC)

The nanocatalysts were studied in a home-made ethanol/$O_2$ Teflon cell to compare their catalytic performance. Measurements were acquired using an Autolab Potentiostat/Galvanostat (PGSTAT302N) at room temperature. The interest

was to evaluate the performance of the nanocatalysts particularly for the oxidation of ethanol, i.e., in the anode of the cell. The cell design included two Teflon compartments each filled with 25 mL of carrier electrolyte solution, separated by a Fumatech Fumasep FAA anion exchange membrane (AEM). The AEM was treated by impregnating it during 24 h with 1 mol $L^{-1}$ of KOH solution at room temperature [13]. The electrolytes used were 0.5 mol $L^{-1}$ KOH in the cathode and 0.5 mol $L^{-1}$ ethanol + 0.5 mol $L^{-1}$ KOH in the anode.

Each compartment cover had four inlets, used to introduce electrodes and gases. During each experiment, $N_2$ and $O_2$ were bubbled into the anode and cathode compartments, respectively. Pt wires embedded in sealed glass tubes to avoid contamination of the electrolytes acted as electric contacts with the electrodes constituting the anode and the cathode. Glass tubes immersed in a water container served as bubbling indicator. The fourth inlet was used to insert a small reference electrode (Basi®). A voltmeter was installed on each side of the cell between anode, cathode, and reference electrode, to separately measure the potential of each electrode during the experiments, as shown in Figure 3.7 a).

To fabricate the anodes and cathodes used in the AEM-DEFC, conductive Toray carbon paper (2050-L FuelCell Store) was used as support electrode. Pieces having of 5 x 5 mm area were cut, at which the nanocatalysts were deposited, as shown in Figure 3.7 b). The catalytic ink was prepared by mixing 2 mg of nanocatalyst with 95 μL of isopropanol and 5 μL of Nafion®. The mixture was homogenized ultrasonically before its deposition 5 μL on each side of carbon paper and dried under $N_2$ flow. The metal load on each anode and cathode was 0.20 $mg_{metal}$ $cm^{-2}$.

In the fuel cell configuration proposed, anodes and cathodes contained the same nanocatalyst during each study. The method used to characterize the performance of the cell was chronopotentiometry.

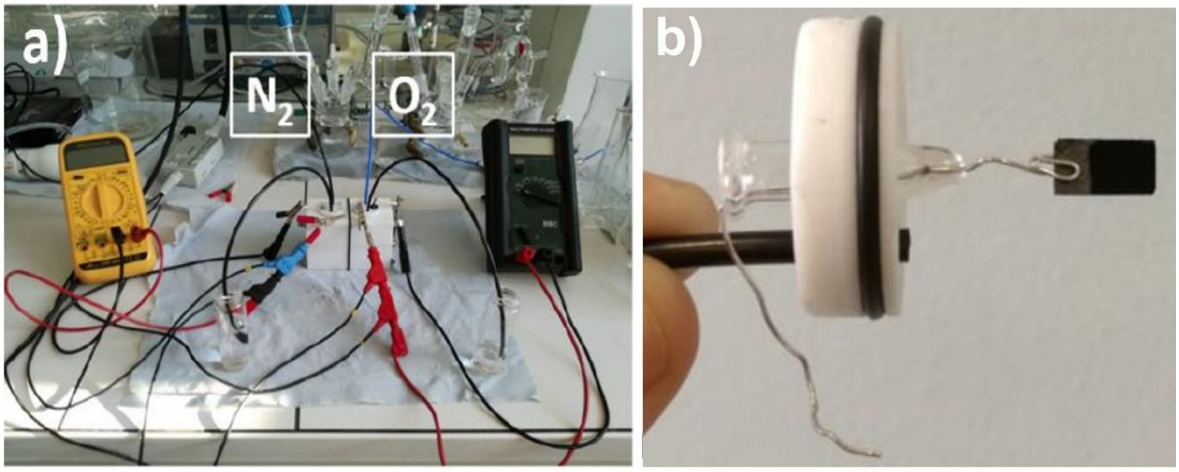


**Figure 3.7** a) AEM-DEFC set up and b) imagen of the one of the electrodes used in the fuel cell.

Chronopotenciometry

It consisted of applying controlled current (*i*) between anode and cathode in galvanostatic mode. The plugs of counter and reference electrodes (REF) of the potentiostat were connected to the anode, while the working electrode (WE) was connected to the cathode (Figure 3.8), so the *i* imposed was negative (-50 μA at -1 mA). The measured voltage difference between the anode and the cathode, was the fuel cell voltage (U).

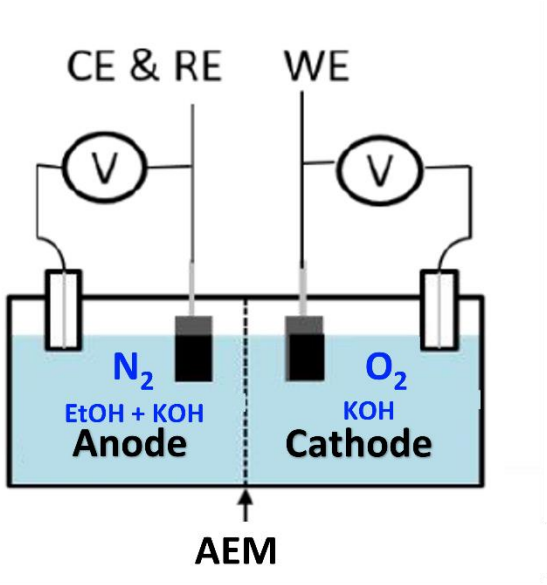


**Figure 3.8** Scheme of the fuel cell configuration.

The performance of the nanocatalysts was compared by obtaining polarization curves of the anode ($E_a$) and cathode ($E_c$) potentials as a function of current density (j). The fuel cell power density ($P_{cell}$) was determined using the Ohm relationship (Equation 3.9):

$$P_{cell} = j \times U \qquad \text{Equation 3.9}$$

Therefore, $P_{cell}$ vs. j curves were also plotted.

### 3.6.8 Analysis of reaction products by High-Performance Liquid Chromatography (HPLC)

The species produced from the ethanol oxidation were quantified by HPLC after electrolysis for 4 h at an applied potential of 0.8 V/RHE. The configuration of the AEM-DEFC changed slightly compared with that in Figure 3.8. As seen in Figure 3.9, WE were the nanocatalysts evaluated as anodes, the cathode was of the Fe/N-rGO type [14] which worked as CE, and RE was the same described in the previous section.

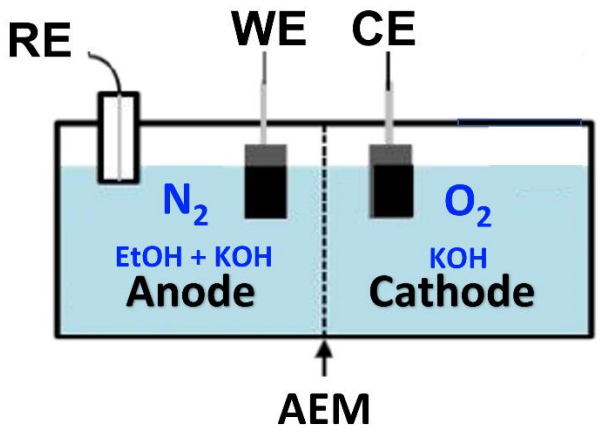


**Figure 3.9** Configuration of the AEM-DEFC during electrolysis of ethanol.

Using this method, it was possible to obtain the percentage of ethanol consumed as well as the percentage of the subproducts due to its oxidation. The subproducts were separated in a Biorad HPLC organic Acid Analysis Column (Animex ® HPX-87) operating under isocratic conditions. The mobile phase consisted of 3.33 mmol $L^{-1}$ sulfuric acid at a flow rate of 0.6 mL $min^{-1}$ using He (99 %, alphagaz). Aliquots were collected each hour and injected into a Thermo Scientific Dionex Ultimated 3000 UHPLC. The reaction products were quantitatively determined by comparing their retention times with those of pure commercial standards injected under the same analysis conditions.

### 3.7 References

[1] R. Pérez-Hernández, G. Mondragón-Galicia, A. Allende Maravilla, J. Palacios. Nano-dimensional $CeO_2$ nanorods for high Ni loading catalysts: H2 production by autothermal steam reforming of methanol reaction. PCCP. 15 (2013) 12702-12708.
[2] M. Stollenz, F. Meyer. Mesitylcopper – A Powerful Tool in Synthetic Chemistry. Organometallics. 31 (2012) 7708-7727.

[3] S.-W. Jin, X.-H. Ye, L. Jin, L. Zheng, J.-W. Li, B.-P. Jin, D.-Q. Wang. Syntheses and structural characterization of nine coordination compounds assembled from copper acetate, 3,5-dimethylpyrazole and carboxylates. Polyhedron. 81 (2014) 382-395.
[4] A.A. Siller-Ceniceros, M.E. Sánchez-Castro, D. Morales-Acosta, J.R. Torres-Lubian, E. Martínez G, F.J. Rodríguez-Varela. Innovative functionalization of Vulcan XC-72 with Ru organometallic complex: Significant enhancement in catalytic activity of Pt/C electrocatalyst for the methanol oxidation reaction (MOR). Appl. Catal. B: Environ. 209 (2017) 455-467.
[5] D. Gonzalez-Quijano, W.J. Pech-Rodriguez, J.I. Escalante-Garcia, G. Vargas-Gutierrez, F.J. Rodriguez-Varela. Highly Active Pt-Sn/C Catalysts for ethanol electro-oxidation prepared by a polyol-alcohol reduction process. ECS Transactions. 61 (2014) 1-9.
[6] W.J. Pech-Rodríguez, C. Calles-Arriaga, D. González-Quijano, G. Vargas-Gutiérrez, C. Morais, T.W. Napporn, F.J. Rodríguez-Varela. Electrocatalysis of the ethylene glycol oxidation reaction and in situ Fourier-transform infared study on PtMo/C electrocatalysts in alkaline and acid media. J. Power Sources. 375 (2018) 335-344.
[7] F. Zhang, Y. Tong, K. Jin, H. Bei, W.J. Weber, Y. Zhang. Lattice distortion and phase stability of Pd-doped NiCoFeCr solid-solution alloys. Entropy. 20 (2018).
[8] T. Kawaguchi, W. Cha, V. Latyshev, S. Vorobiov, V. Komanicky, H. You. Study of the internal compositions of binary alloy Pd-Rh nanoparticles by using bragg coherent diffraction imaging. J. Korean Phy. Soc. 75 (2019) 528-533.
[9] V. Raghuveer, P.J. Ferreira, A. Manthiram. Comparison of Pd–Co–Au electrocatalysts prepared by conventional borohydride and microemulsion methods for oxygen reduction in fuel cells. Electrochem. Commun. 8 (2006) 807-814.
[10] A.B.A.A. Nassr, A. Quetschke, E. Koslowski, M. Bron. Electrocatalytic oxidation of formic acid on Pd/MWCNTs nanocatalysts prepared by the polyol method. Electrochim. Acta. 102 (2013) 202-211.
[11] I.L. Alonso-Lemus, B. Escobar-Morales, D. Lardizabal-Gutierrez, L. de la Torre-Saenz, P. Quintana-Owen, F.J. Rodriguez-Varela. Onion skin waste-derived biocarbon as alternative non-noble metal electrocatalyst towards ORR in alkaline media. Int. J. Hydrogen Energy. 44 (2019) 12409-12414.

[12] S. Gottesfeld, D.R. Dekel, M. Page, C. Bae, Y. Yan, P. Zelenay, Y.S. Kim. Anion exchange membrane fuel cells: Current status and remaining challenges. J. Power Sources. 375 (2018) 170.

[13] M. Hren, M. Božič, D. Fakin, K.S. Kleinschek, S. Gorgieva. Alkaline membrane fuel cells: anion exchange membranes and fuels. Sustain. Energy Fuels. 5 (2021) 604-637.

[14] C. Lemoine. (2019). *Synthèse de Nanocatalyseurs Métalliques Supportés pour l'Électrooxydation du Glucose : Application en Pile Implantable*. Doctoral Thesis. Université de Poitiers.

# Chapter IV

# Electrochemical evaluation of the bifunctional Pd-$CeO_{2\text{-}NR}$/C nanocatalyst for the EOR and the ORR

## 4.1 Physicochemical characterization

### 4.1.1 XRD

The XRD patterns of Pd/C and Pd-$CeO_{2\text{-}NR}$/C in Figure 4.1 show a peak attributed to the (002) plane of the carbon support (2θ = 26.59°) (JCPDS 74-2329). The remaining reflections correspond to the fcc crystal structure of Pd, and are ascribed to its (111), (200), (220) and (311) planes at 39.78, 46.22, and 67.62°, in the 2θ scale, respectively (JCPDS 87-0638). In addition to the C and Pd planes, reflections are observed in the diffractogram of Pd-$CeO_{2\text{-}NR}$/C at 28.6, 32.5 and 56.1° (2θ), corresponding to the (111), (200) and (311) planes of the fluorite structure of $CeO_2$ (JCPDS 43-1002) [1].

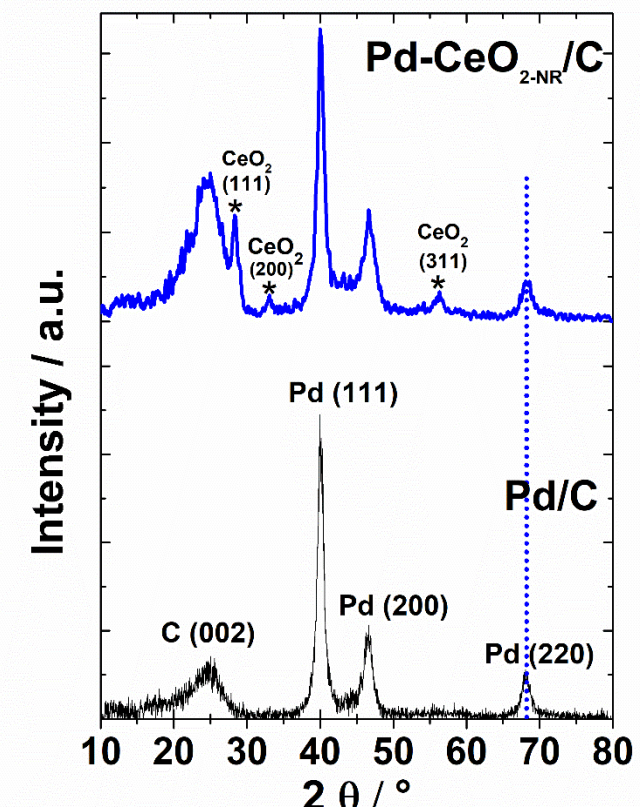


**Figure 4.3** XRD patterns of Pd/C and Pd-$CeO_{2\text{-}NR}$/C.

No shift of the peaks of Pd neither $CeO_{2\text{-}NR}$ is observed on the Pd-$CeO_{2\text{-}NR}$/C, indicating that the addition of $CeO_{2\text{-}NR}$ during the synthesis of the nanocatalysts does not modify the lattice parameter of Pd. The crystallite size (d) of the nanocatalysts is estimated from data of the (220) Pd plane, using the Scherrer equation, [2] with values of 6.6 and 7.9 nm for Pd-$CeO_{2\text{-}NR}$/C and Pd/C, respectively (Table 4.1). The smaller d value at former can be attributed to a stabilization effect of $CeO_{2\text{-}NR}$ on Pd nanoparticles, avoiding their agglomeration and segregation [3]. Moreover, some Pd nanoparticles may tend to deposit on $CeO_{2\text{-}NR}$, promoting and enhanced dispersion of nanoparticles [4].

### 4.1.2 Chemical composition by EDS-SEM

The chemical composition of the Pd/C and Pd-$CeO_{2\text{-}NR}$/C is shown in Table 4.1. In both cases, the C content is fairly close to the theoretically expected value of 80 wt. %. The Pd content is 16.08 and 8.44 (wt. %) at Pd/C and Pd-$CeO_{2\text{-}NR}$/C, respectively. Additionally, Pd-$CeO_{2\text{-}NR}$/C has 9.3 (wt. %) of $CeO_{2\text{-}NR}$, with a Pd:$CeO_2$ atomic ratio of 1.46:1, slightly higher than the 1:1 nominally expected. The results in Table 4.1 show that the chemical composition of the nanocatalysts is well controlled by the polyol method.

**Table 4.1** Physicochemical characteristics of Pd-$CeO_{2\text{-}NR}$/C and Pd/C.

| **Nanocatalyst** | **d, XRD (nm)** | **d, TEM (nm)** | **Chemical composition (wt. %)** | | | **Atomic ratio (at. %)** |
|---|---|---|---|---|---|---|
| | | | **C** | **Pd** | **$CeO_2$** | **Pd:$CeO_2$** |
| Pd-$CeO_{2\text{-}NR}$/C | 6.6 | 5.5±1.2 | 82.1± 0.7 | 8.4±1.6 | 9.3 ± 0.5 | 1.46:1 |
| Pd/C | 7.9 | 10±3.2 | 83.9± 0.4 | 16±0.4 | - | - |

-Undetermined

### 4.1.3 Morphology and chemical elemental mapping by FE-SEM

The FE-SEM micrographs in Figure 4.2 show the morphology of a) Pd/C and b) Pd-$CeO_{2\text{-}NR}$/C, with semi-spherical particles corresponding to Vulcan and brighter sites attributed to Pd nanoparticles [5]. $CeO_2$ nanorods can also be seen at Pd-$CeO_{2\text{-}NR}$/C, one of them indicated by an arrow. Figures 4.3 and 4.4 show FE-SEM images and elemental mapping of Pd/C and Pd-$CeO_{2\text{-}NR}$/C, respectively, confirming the homogeneous dispersion of C, Pd, O, and Ce.

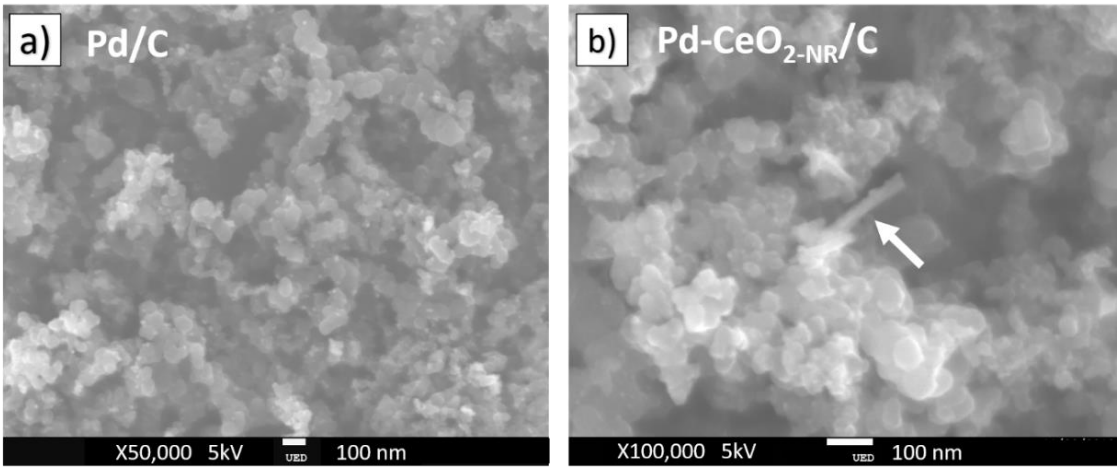


**Figure 4.2** High magnification FE-SEM micrographs of a) Pd/C and b) Pd-$CeO_{2\text{-}NR}$/C.

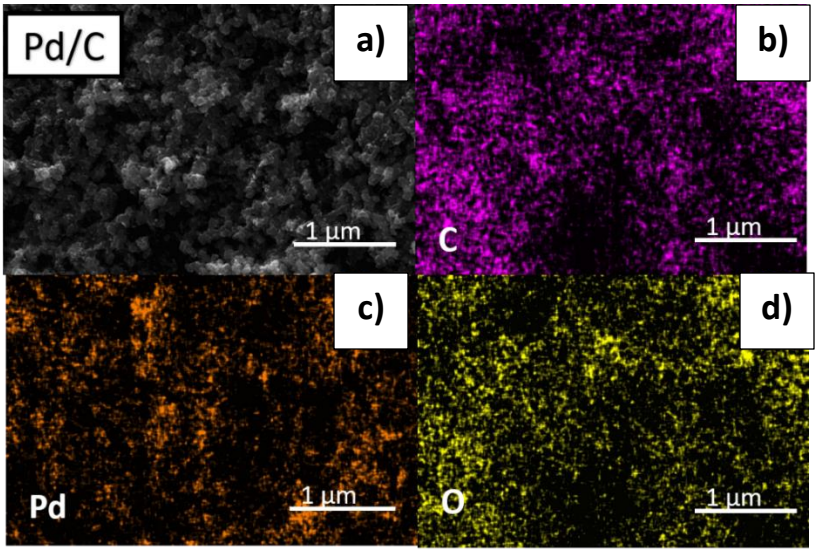


**Figure 4.3** a) FE-SEM image and b) C, c) Pd, and d) O elemental mapping of Pd/C.

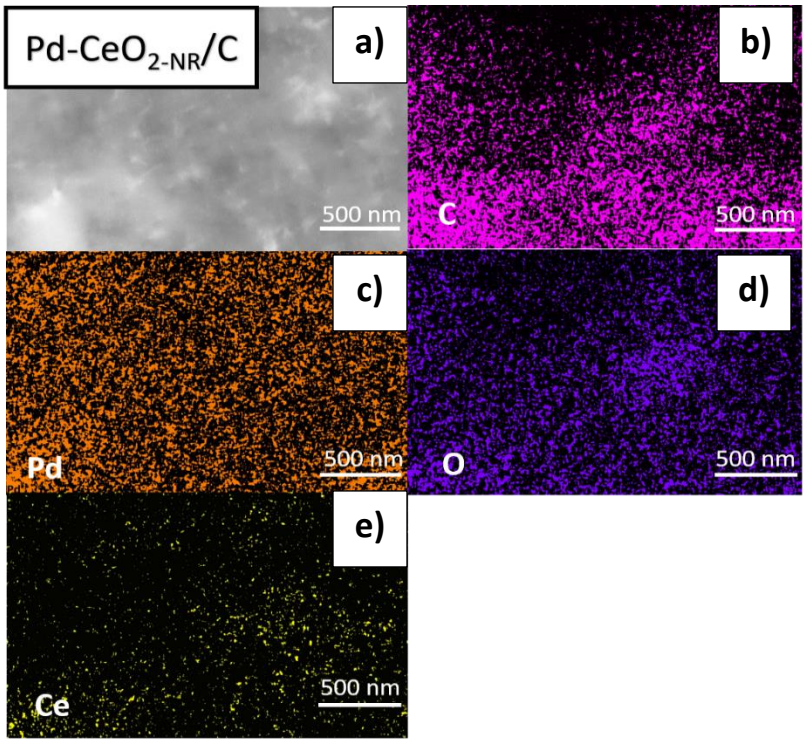


**Figure 4.4** a) FE-SEM image and b) C, c) Pd, d) O and e) Ce elemental mapping of Pd-$CeO_{2\text{-}NR}$ /C.

### 4.1.4 Morphology by TEM

Figure 4.5 a) shows TEM micrographs of the Pd/C nanocatalyst. Dispersed nanoparticles (darkest spots) are observed on the support, and they were attributed to Pd. The histogram in Figure 4.5 b) shows its particle size distribution with an average d= 10.0 ± 3.2 nm (Table 4.1), slightly higher than that obtained by XRD.

Figure 4.5 c) corresponds to the TEM image of Pd-$CeO_{2\text{-}NR}$/C, with a morphology where Pd and Vulcan nanoparticles, as well as cerium oxide nanorods, can be seen. Pd nanoparticles are dispersed over Vulcan, but some of them were supported on the nanorods as well. The $CeO_{2\text{-}NR}$ has the characteristics previously reported, i.e., 8-10 nm width and 60-70 nm length [6]. The histogram of average metal particle size distribution on Pd-$CeO_{2\text{-}NR}$/C in Figure 4.5 d) indicates d= 5.5 ± 1.2 nm, which correlates well with the value obtained by XRD (Table 4.1) and confirms the positive effect of the nanorods to limit the growth of Pd nanoparticles.

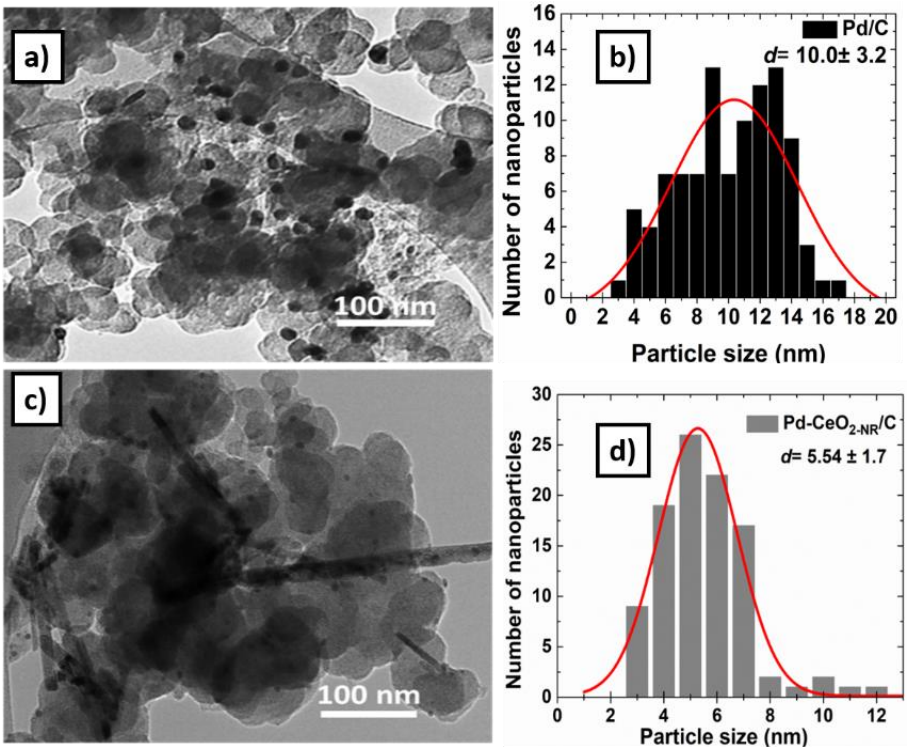


**Figure 4.4 5** TEM micrographs and histograms of average metal particle size distribution of Pd/C (a-b) and Pd-$CeO_{2\text{-}NR}$/C (c-d).

### 4.1.5 XPS

Figure 4.6 displays the deconvoluted spectra of Pd/C in the a) Pd 3d, b) C 1s, and c) O 1s regions. Three doublets in the Pd $3d_{5/2}$ and Pd $3d_{3/2}$ states confirm the formation of metallic Pd ($Pd^0$, BE= 335.14 and 341.93 eV), PdO ($Pd^{2+}$, BE= 336.62 and 341.93 eV) and $PdO_2$ ($Pd^{4+}$, BE= 338.21 and 343.50 eV) on Pd/C, as can be seen in Figure 4.6 a) [7-9]. The higher relative concentration is that of $Pd^0$ (56.3 at. %), $Pd^{4+}$ being relatively intense (28.1 at. %). Meanwhile, $Pd^{2+}$ has a lower relative concentration as was reported in Table 4.2.

The C 1s region is deconvoluted into five peaks (Figure 4.6 b), with the most intense signal being that of the $sp^2$ hybridization (C=C bond, BE= 284.70 eV), followed by the less intense $sp^3$ (C-C bond), along with the C-O-C, C=O, and O-C=C species [10]. Meanwhile, Figure 4.6 c) shows the O 1s region, having signals at 530.80 and 532.50 eV assigned to PdO and $PdO_2$ bonds, respectively, confirming palladium and oxygen interactions due to the overlap between the Pd $3p_{3/2}$ and O 1s regions [11-13]. The high intensity of the $PdO_2$ peak correlates well with the relatively high concentration of this species in Figure 4.6 a). The other peaks in Figure 4.6 c) correspond to C=O, C-O, and O-C=O groups from the carbon support [14, 15].

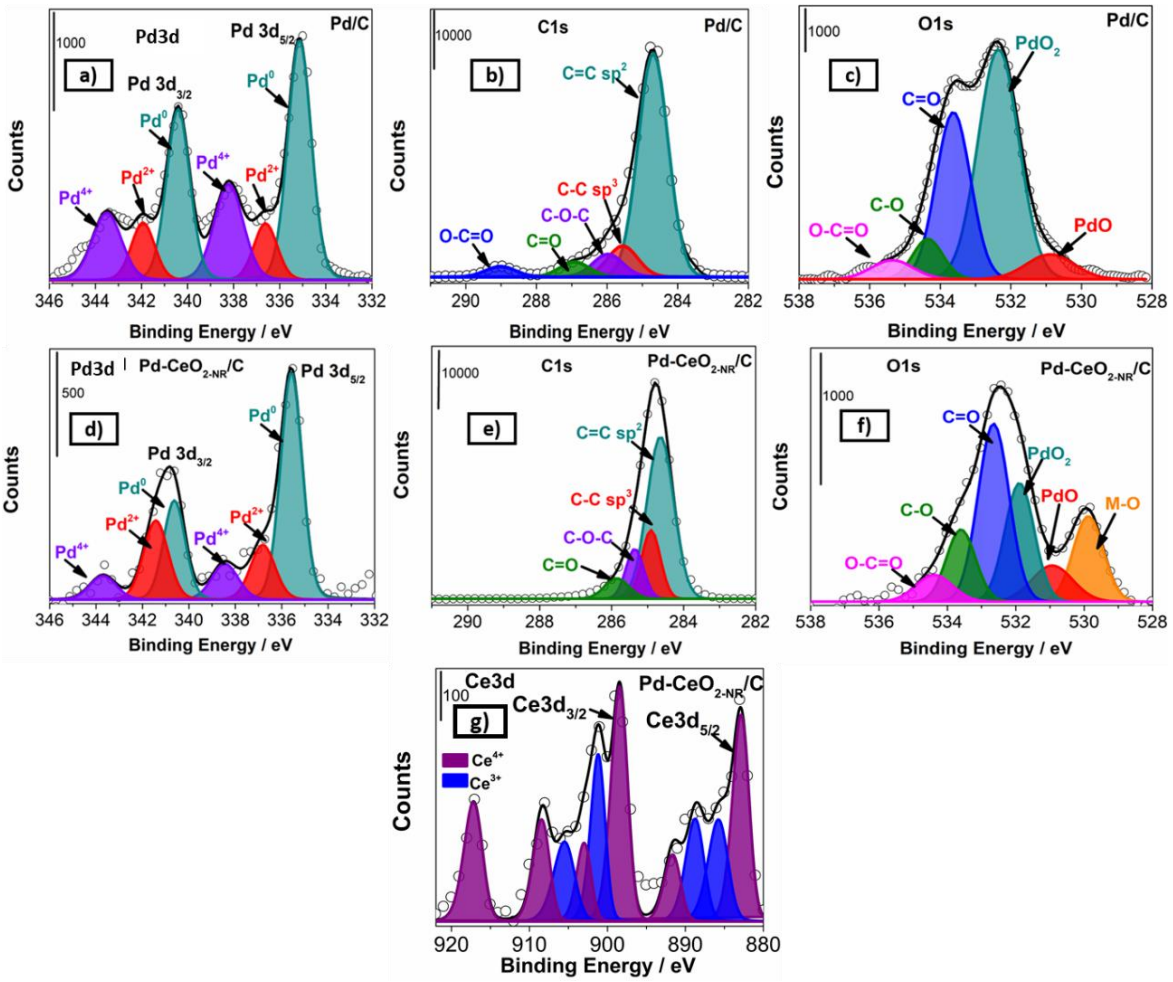


**Figure 4.6** XPS spectra of Pd/C in the a) Pd 3d, b) C 1s and c) O 1s regions, and Pd-$CeO_{2\text{-}NR}$/C in the d) Pd 3d, e) C 1s, f) O 1s and g) Ce 3d regions.

The signals in the Pd 3d region of Pd-$CeO_{2\text{-}NR}$/C (deconvoluted spectra in Figure 4.6 d) confirm doublets ascribed to the $Pd^0$, $Pd^{2+}$, and $Pd^{4+}$ species. $Pd^0$ has also the highest relative concentration, however in this case followed by $Pd^{2+}$ (59.1 and 27.6 at %, respectively, Table 4.2), i.e., more PdO species are formed at Pd-$CeO_{2\text{-}NR}$/C than at Pd/C. A high concentration of Pd in such an oxidized state in the presence of $CeO_2$ has been attributed to a spillover effect of ceria, due to strong chemical interactions with Pd [16]. Moreover, it has been reported that supported Pd-$CeO_2$ nanocatalysts having 2-5 nm particle size, such as the Pd-$CeO_{2\text{-}NR}$/C

material in this study, develop a higher Pd (II)/Pd (0) ratio compared to samples with larger diameters [17].

In this work, the Pd-$CeO_{2\text{-}NR}$/C nanocatalyst shows a particle size of around 5.5 nm (Table 4.1), with a Pd (II)/ Pd (0) ratio of 227.6/59.1 (Table 4.2, considering the Pd $3d_{5/2}$ and Pd $3d_{3/2}$ states), higher than 15.7/56.3 of Pd/C. The aforementioned chemical interactions between ceria and palladium also provoke a shift to higher BE of the Pd doublets in Pd-$CeO_{2\text{-}NR}$/C compared to Pd/C, in good agreement with reports elsewhere [18, 19].

The most intense signal in the C 1s region (Figure 4.6 e) is the $sp^2$ hybridization peak positioned at BE= 284.65 eV (C=C bond). The less intense signals correspond to the C-C, C-O-C, and C=O species. Meanwhile, the O 1s region (Figure 4.6 f) shows an intense metal-oxygen interaction (M-O) signal at 529.88 eV, due to bonds between surface O and Pd and/or Ce species [20]. It should be noted that this species is not detected on the Pd/C. Moreover, the relative concentration of the PdO species at BE= 530.93 eV is higher at Pd-$CeO_{2\text{-}NR}$/C compared to Pd/C (Table 4.2), in agreement with the relevant presence of this species in the Pd 3d region of the former.

On this matter, the relative concentration of the $PdO_2$ species in Figure 4.6 f) is significantly lower in the presence of $CeO_{2\text{-}NR}$ compared to the monometallic nanocatalyst, correlating also well with its behavior in the Pd 3d region. The C=O, C-O, and O-C=O species are also detected in Figure 4.6 f) [21].

The Ce 3d spectrum of Pd-$CeO_{2\text{-}NR}$/C in Figure 4.6 g) is deconvoluted into several peaks, indicative of the spin-orbit splitting into the Ce $3d_{5/2}$ and Ce $3d_{3/2}$ states. The characteristic oxidation states of $CeO_2$, i.e., those attributed to $Ce^{4+}$ and $Ce^{3+}$ are shown [22]. Overall, the peaks in this spectrum correlate well with those reported in our previous work using $CeO_{2\text{-}NR}$, with shifts in the BE of the species attributed to the use of Vulcan as support here, instead of graphene earlier [23].

**Table 4.2** XPS parameters of Pd/C and Pd-$CeO_{2\text{-}NR}$/C.

| Nanocatalyst | State | Species | BE (eV) | Composition (at %) |
|---|---|---|---|---|
| **Pd/C** | Pd $3d_{5/2}$ | $Pd^0$ | 335.14 | 32.9 |
| | Pd $3d_{5/2}$ | $Pd^{2+}$ | 336.62 | 7.8 |
| | Pd $3d_{5/2}$ | $Pd^{4+}$ | 338.21 | 16.5 |
| | Pd $3d_{3/2}$ | $Pd^0$ | 340.41 | 23.4 |
| | Pd $3d_{3/2}$ | $Pd^{2+}$ | 341.93 | 7.9 |
| | Pd $3d_{3/2}$ | $Pd^{4+}$ | 343.50 | 11.6 |
| | C 1s | C=C $sp^2$ | 284.70 | 72.9 |
| | C 1s | C-C $sp^3$ | 285.55 | 10.1 |
| | C 1s | C-O | 285.98 | 7.4 |
| | C 1s | C=O | 286.93 | 4.9 |
| | C 1s | O-C=O | 289.01 | 3.4 |
| | O 1s | PdO | 530.88 | 6.5 |
| | O 1s | $PdO_2$ | 532.35 | 51.1 |
| | O 1s | C=O | 533.63 | 31.4 |
| | O 1s | C-O | 534.35 | 6.6 |
| | O 1s | O-C=O | 535.36 | 4.4 |
| **Pd-$CeO_{2\text{-}NR}$/C** | | | | |
| | Pd $3d_{5/2}$ | $Pd^0$ | 335.58 | 41.1 |
| | Pd $3d_{5/2}$ | $Pd^{2+}$ | 336.82 | 11.3 |

| | | | |
|---|---|---|---|
| Pd $3d_{5/2}$ | $Pd^{4+}$ | 338.44 | 8.0 |
| Pd $3d_{3/2}$ | $Pd^{0}$ | 340.63 | 18.0 |
| Pd $3d_{3/2}$ | $Pd^{2+}$ | 341.42 | 16.3 |
| Pd $3d_{3/2}$ | $Pd^{4+}$ | 343.70 | 5.3 |
| C 1s | C=C $sp^2$ | 284.65 | 61.9 |
| C 1s | C-C $sp^3$ | 284.91 | 18.2 |
| C 1s | C-O-C | 285.36 | 12.7 |
| C 1s | C=O | 285.86 | 7.1 |
| O 1s | M-O | 529.88 | 16.0 |
| O 1s | PdO | 530.93 | 9.1 |
| O 1s | $PdO_2$ | 531.89 | 21.5 |
| O 1s | C=O | 532.65 | 34.3 |
| O 1s | C-O | 533.60 | 13.0 |
| O 1s | O-C=O | 534.39 | 6.1 |
| Ce $3d_{5/2}$ | $Ce^{4+}$ | 882.87 | 15.9 |
| Ce $3d_{5/2}$ | $Ce^{3+}$ | 885.77 | 9.5 |
| Ce $3d_{5/2}$ | $Ce^{3+}$ | 888.75 | 8.9 |
| Ce $3d_{5/2}$ | $Ce^{4+}$ | 891.64 | 5.2 |
| Ce $3d_{5/2}$ | $Ce^{4+}$ | 898.44 | 18.1 |
| Ce $3d_{3/2}$ | $Ce^{3+}$ | 901.19 | 11.3 |
| Ce $3d_{3/2}$ | $Ce^{4+}$ | 902.99 | 5.3 |
| Ce $3d_{3/2}$ | $Ce^{3+}$ | 905.51 | 7.8 |

| | | | | |
|---|---|---|---|---|
| | Ce $3d_{3/2}$ | $Ce^{4+}$ | 908.44 | 7.9 |
| | Ce $3d_{3/2}$ | $Ce^{4+}$ | 917.17 | 10.3 |

**4.2 Electrochemical Characterization**

The CVs before and after ADT of a) Pd/C and b) Pd-$CeO_{2\text{-}NR}$/C are shown in Figure 4.7. The current density (j) peaks and the shape of the plots before ADT are those typical of supported Pd-based nanocatalysts. It can be remarked that the j values at Pd-$CeO_{2\text{-}NR}$/C are significantly lower. Particularly, the region attributed to formation/reduction of Pd-oxides is inhibited in the presence of $CeO_{2\text{-}NR}$, a behavior that has been ascribed to the modulation of the electronic structure of Pd [24].

Before ADT, Pd/C has an ECSA of 29.43 $m^2\ g^{-1}$, while that of Pd-$CeO_{2\text{-}NR}$/C is 24.13 $m^2\ g^{-1}$ (Table 4.3). The smaller ECSA in Pd-$CeO_{2\text{-}NR}$/C can be attributed to its lower Pd content and to the effect of ceria already discussed above and observed in Figure 4.7 b). After submitting Pd/C to ADT, the intensity of the peak due to the reduction of Pd-oxides decreases and shifts towards more negative potentials (Figure 4.7 a), suggesting that its relative concentration of $Pd^0$ lessens [25].

In contrast, no significant changes in the CV of Pd-$CeO_{2\text{-}NR}$/C are observed after ADT. The positive effect of $CeO_{2\text{-}NR}$ on the electrochemical stability of Pd nanoparticles can be asserted from the variation in ECSA values before and after ADT, since the percentage of ECSA retention is ca. 98% at Pd-$CeO_{2\text{-}NR}$/C, while that of Pd/C is only 51% (Figure 4.8).

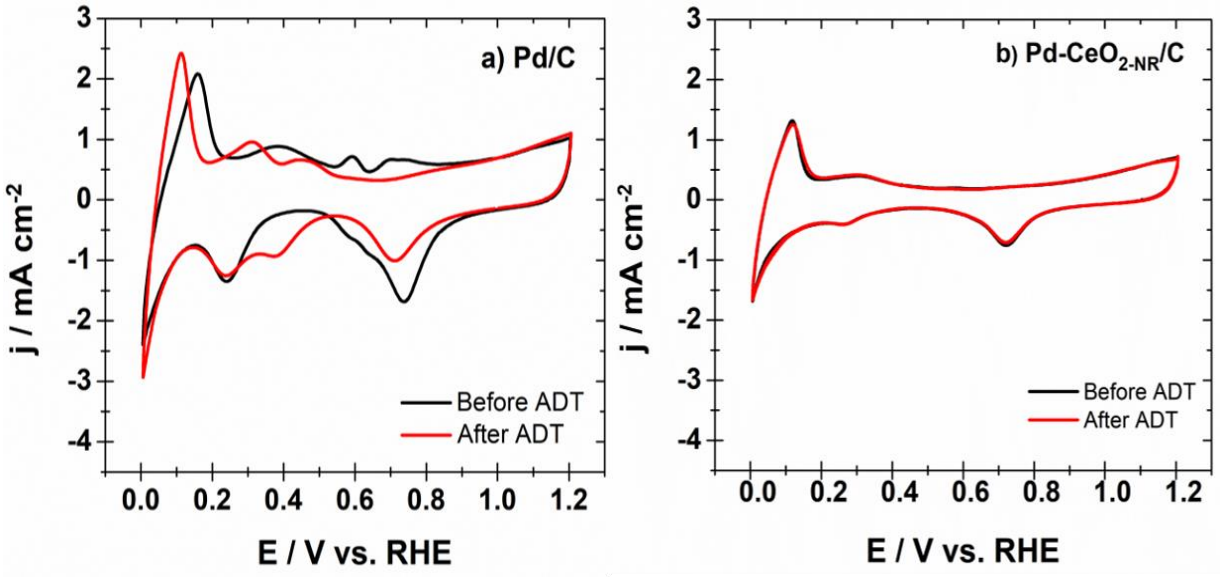


**Figure 4.7** CVs before and after of ADT of a) Pd/C, and b) Pd-$CeO_{2\text{-}NR}$/C. Electrolyte: $N_2$-satured 0.5 mol $L^{-1}$ KOH. Scan rate: 20 mV $s^{-1}$.

In recent studies, it has been reported that $CeO_x$ overlayers have a protective effect and intimate contact with Pd nanoparticles, preventing its dissolution, in addition to the observation that ceria is insoluble in alkaline pH [26, 27]. Therefore, the excellent electrochemical stability of Pd-$CeO_{2\text{-}NR}$/C can be associated to a strong electronic interaction between the cerium oxide nanorods and palladium nanoparticles, resulting in a low dissolution rate of the latter [28]. Even more, since some Pd nanoparticles are dispersed on the nanorods (Figure 4.5 c), their detachment may have decreased.

The ECSA values of Pd/C and Pd-$CeO_{2\text{-}NR}$/C in this work are smaller than those reported previously (29.43 and 24.55 $m^2g^{-1}$ compared with 46.9 and 26.2 for Pd/C and Pd-$CeO_2$/C, respectively) [27] in part attributed to the smaller particle size obtained in that reference. Even though, it can be mentioned that the ECSA value of Pd-$CeO_{2\text{-}NR}$/C here, having a $CeO_2$/Pd at ratio of 0.68 (see discussion of data shown in table 4.1), is 24.55 $m^2g^{-1}$ (Table 4.3) similar to that of the nanocatalysts with a 0.59 Ce/Pd at ratio with 26.2 $m^2g^{-1}$ reported by elsewhere [27].

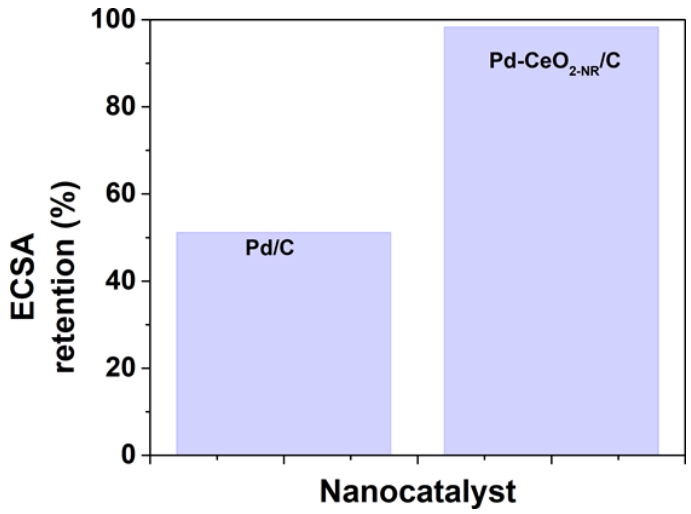


**Figure 4.*8*** ECSA retention after ADT of Pd/C and Pd-$CeO_{2\text{-}NR}$/C.

**Table 4.3** ECSA values and electrochemical parameters of the nanocatalysts during the ORR before and after ADT

| **Nanocatalyst** | **ECSA ($m^2\ g^{-1}$)** | **$E_{onset}$ (V/RHE)** | **$E_{1/2}$** | **j at 0.9 V ($mA\ cm^{-2}$)** | **$i_R$ (μA)** |
|---|---|---|---|---|---|
| **Before ADT** | | | | | |
| Pd/C | 29.43 | 0.97 | 0.87 | -1.32 | 4.52 |
| Pd-$CeO_{2\text{-}NR}$/C | 24.55 | 0.97 | 0.87 | -0.46 | 5.31 |
| **After ADT** | | | | | |
| Pd/C | 15.05 | 0.95 | 0.84 | -0.24 | 2.41 |
| Pd-$CeO_{2\text{-}NR}$/C | 24.13 | 0.92 | 0.82 | -0.007 | 5.43 |

### 4.2.1 Evaluation of catalytic activity for the ORR

The polarization curves of the ORR at Pd/C at ω= 400, 800, 1200, and 1600 rpm, are shown in Figures 4.9 a) and b) before and after of ADT, respectively. At Pd/C, the onset potential ($E_{onset}$) shifts from 1.00 to 0.95 V/RHE after ADT, i.e., a 50 mV displacement (Table 4.3). The half-wave potential ($E_{1/2}$) decreases from 0.87 to 0.84 V/RHE after ADT, due to agglomeration and/or dissolution of Pd nanoparticles during cycling. Such displacement can also be associated to corrosion of Vulcan given the potential interval of the test [29, 30]. Meanwhile, j at 0.9 V/RHE decreases from -1.32 to -0.24 mA $cm^{-2}$ (roughly 80% decrease).

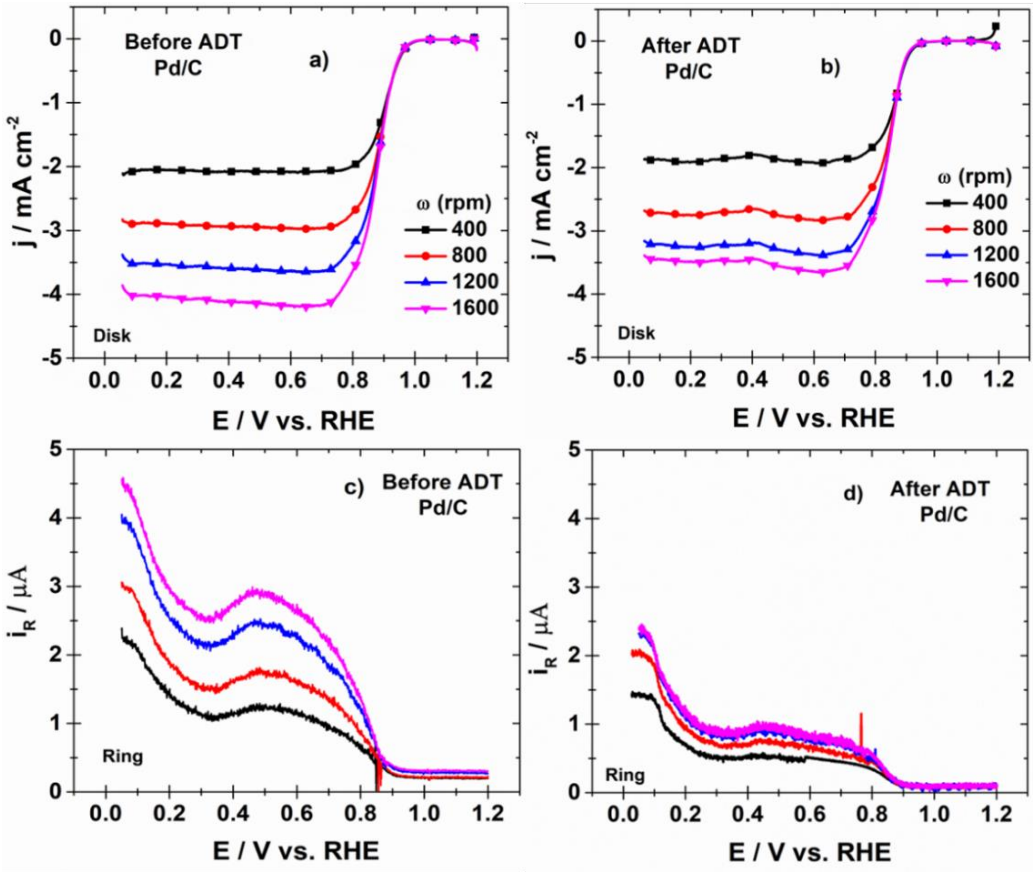


**Figure 4.9** Polarization curves of the ORR (a-b) and $i_R$ collected (c-d) before and after ADT at Pd/C. Scan rate 5 mV $s^{-1}$. Electrolyte: $O_2$-satured 0.5 mol $L^{-1}$ KOH. Ring polarized at 1.2 V/RHE.

Figures 4.9 c and d) show the current collected by the ring during the ORR ($i_R$) at Pd/C before and after ADT, respectively. Surprisingly, it decreases after the polarization test. For example, the maximum value ($i_R$) at $\omega$= 1600 rpm is 4.52 and 2.41 μA before and after ADT, respectively (Table 4.3). Such enhanced behavior entails a lesser amount of $HO_2^-$ species produced during the ORR after ADT, indicating the activation of Pd sites that promote the ORR via a mechanism that involves a 4 $e^-$ transfer [31].

Figures 4.10 a and b) show the polarization curves of the ORR at Pd-$CeO_{2\text{-}NR}$/C before and after ADT, respectively. The value of $E_{onset}$ before is 0.97 V/RHE, close to that of Pd/C, which decreases to 0.92 V/RHE after the test (a 50 mV displacement, similar to Pd/C), as shown in Table 4.3. Meanwhile, $E_{1/2}$= 0.87 V/RHE before ADT, the same as Pd/C, and shifts to 0.82 V/RHE after the cycling. Moreover, j at 0.9 V/RHE decreases from -0.46 to -0.07 mA $cm^{-2}$ after ADT (Table 4.3), a loss of about 85%. Figures 4.10 c and d) show that $i_R$ increases only slightly after ADT at Pd-$CeO_{2\text{-}NR}$/C (Table 4.3).

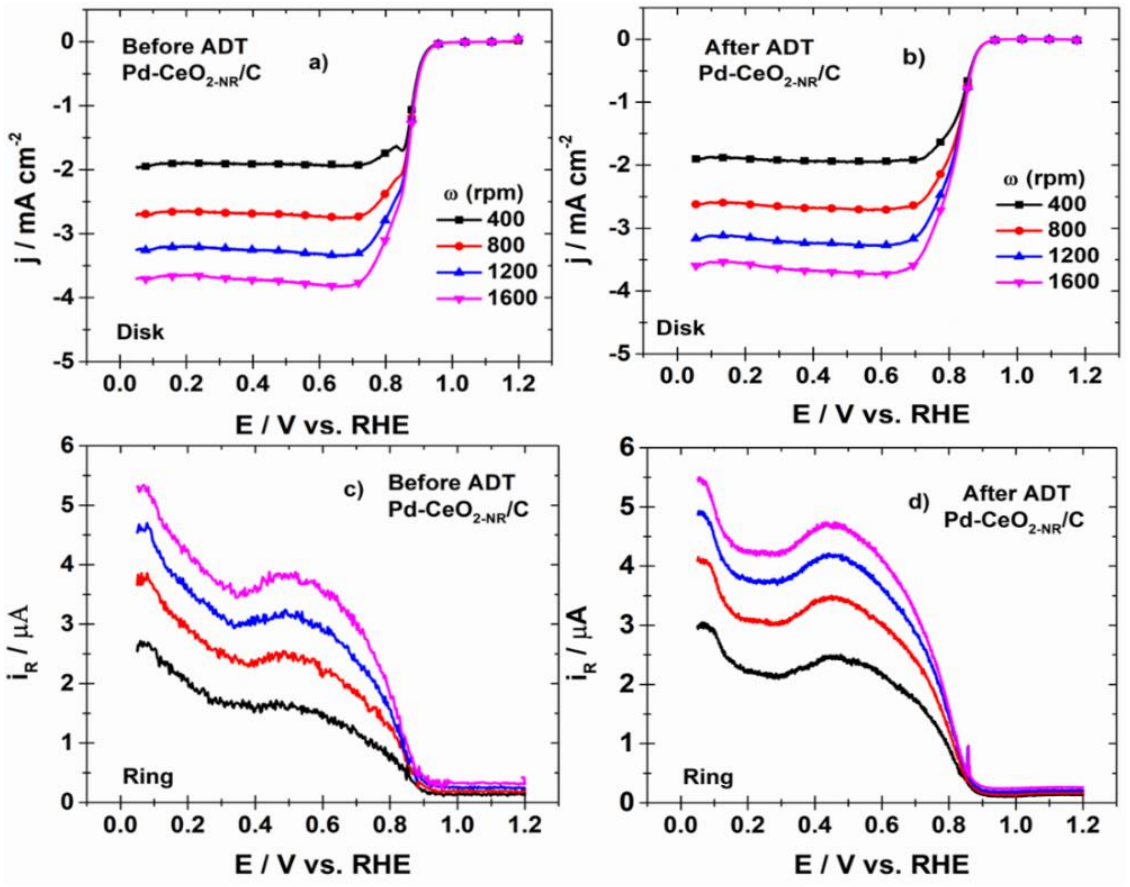


**Figure 4.5** Polarization curves of the ORR (a-b) and $i_R$ collected (c-d) before and after ADT at Pd-$CeO_{2\text{-}NR}$/C. Scan rate 5 mV $s^{-1}$. Electrolyte: $O_2$-satured 0.5 mol $L^{-1}$ KOH. Ring polarized at 1.2 V/RHE.

Figure 4.11 shows the curves of % $HO_2^-$ at a) Pd/C and b) Pd-$CeO_{2\text{-}NR}$/C before and after ADT. At Pd/C, it decreases after cycling, leading to a less than 2% $HO_2^-$ production. It is also lower after ADT at Pd-$CeO_{2\text{-}NR}$/C, with values below ~ 4%. These values of % $HO_2^-$ at both nanocatalysts are lower compared to the results reported elsewhere for Pd-based cathodes [32, 33]. Figure 4.11 also shows the curves of n at c) Pd/C and d) Pd-$CeO_{2\text{-}NR}$/C. In both cases, it increases after ADT, with values close to the theoretical 4 $e^-$ transfer of the ORR in alkaline media, highlighting their high catalytic activity for the ORR.

The parameters are shown in Figure 4.11 demonstrate that the performance of Pd-$CeO_{2\text{-}NR}$/C and Pd/C for the ORR enhances after ADT. In the case of Pd-$CeO_{2\text{-}NR}$/C, such high performance after potential cycling for the ORR is related to the stabilizing effect of $CeO_{2\text{-}NR}$ on Pd. A similar effect has been reported for Pd-based catalysts modified with metal oxides [34].

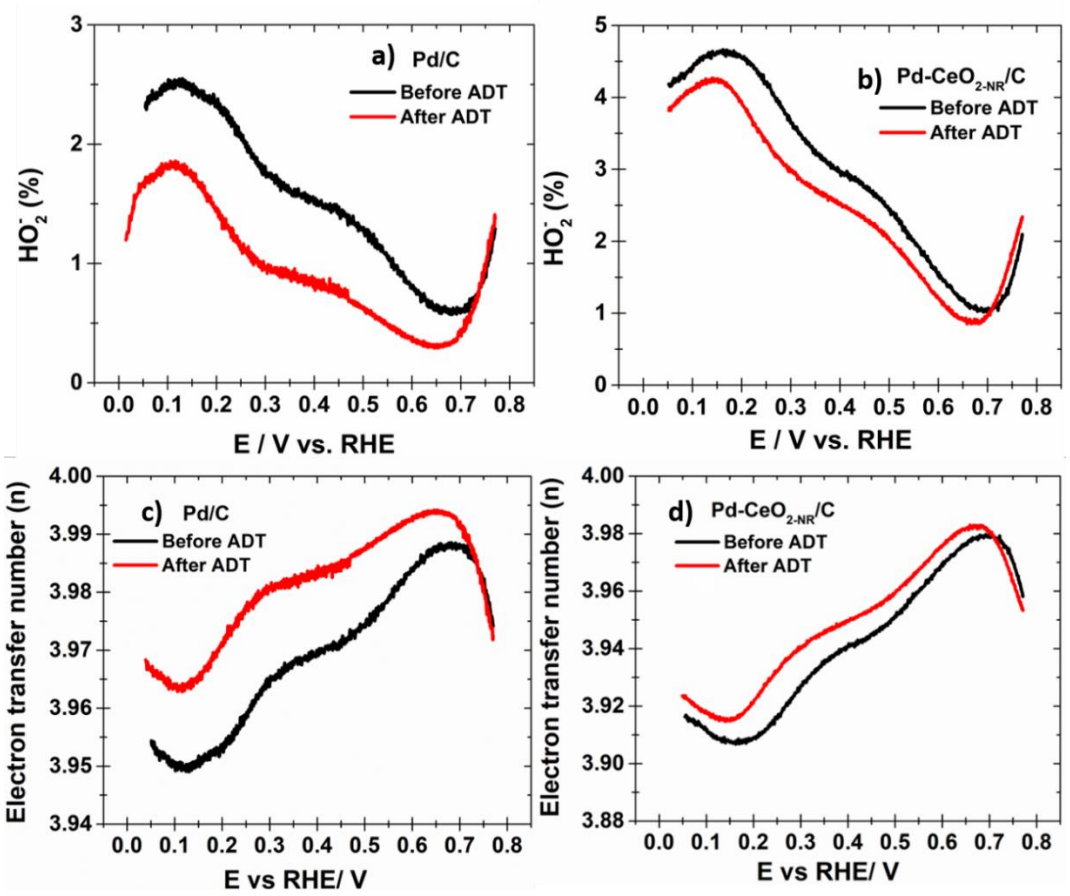


**Figure 4.11** Curves of % $HO_2^-$ (a-b) and n (c-d) during the ORR in Pd/C and Pd-$CeO_{2\text{-}NR}$/C before and after of ADT. Electrolyte: 0.5 mol $L^{-1}$ KOH saturated with $O_2$. $\omega$= 1600 rpm.

Table 4.4 depicts a comparison of some parameters of the ORR obtained from Pd-$CeO_{2\text{-}NR}$/C before ADT, with those of Pd-based nanocatalysts reported in the literature. As can be seen, Pd-$CeO_{2\text{-}NR}$/C with a lower Pd content shows excellent values in most of the parameters and compare favorably against those nanocatalysts studied elsewhere. In particular, the low % $HO_2^-$ and high n values can be highlighted at this nanocatalyst.

**Table 4.4** Electrochemical parameters of the ORR at Pd-based nanocatalysts.

| **Catalyst** | **$E_{onset}$ (V/RHE)** | **$E_{1/2}$** | **j at 0.9 V (mA $cm^{-2}$)** | **% $HO_2^-$** | **n** | **Electrolyte** | **Ref** |
|---|---|---|---|---|---|---|---|
| **Pd@Zn_core-shell** | 0.98 | 0.82 | -0.48 | 3 | 3.9 | KOH | [35] |
| **PdNi/CNFO** | 0.98 | - | -0.70 | 33 | 3.5 | KOH | [36] |
| **Dealloyed PdNi/C** | 0.97 | 0.87 | -1.20 | - | - | NaOH | [37] |
| **PdCu/C** | 0.97 | 0.80 | -1.2 | - | 4 | KOH | [38] |
| **$Mo_2C$-Pd-9%** | 0.96 | 0.80 | -0.90 | 8.4 | 3.9 | KOH | [39] |
| **$Pd_3$/Co-nanofilms/C** | 0.96 | 0.91 | -0.80 | - | - | NaOH | [40] |
| **PdAg/NCC** | 0.95 | 0.89 | -0.90 | 10 | 4 | KOH | [41] |
| **Pd-$CeO_{2\text{-}NR}$/C** | **0.97** | **0.87** | **-0.46** | **< 4.5** | **4** | **KOH** | **This work** |

Mass activity plots have been built from the ORR polarization curves at 1600 rpm by applying a mass-transport correction and normalizing the current by the Pd

content (Table 4.1), [39] obtaining the mass current density $i_m$ (A $mg^{-1}_{Pd}$). Also, specific activity plots have been obtained by normalizing the current by the Pd real surface area, which has been determined from the charge due to the reduction of the Pd-oxides peaks after double-layer correction, resulting in is (μA $cm^{-2}_{Pd}$).

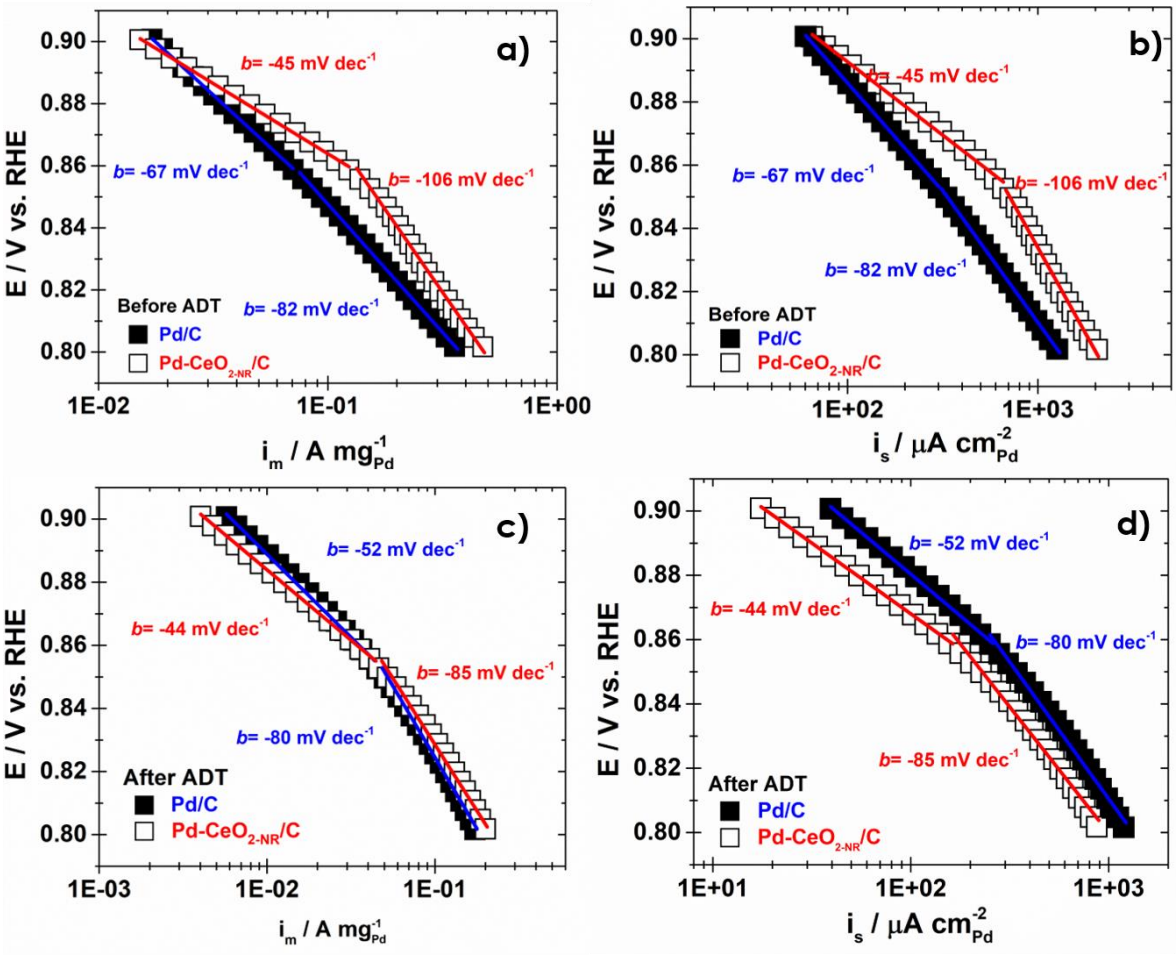


**Figure 4.12** Mass and specific activity plots before (a-b) and after (c-d) ADT of the ORR on Pd/C and Pd-$CeO_{2\text{-}NR}$/C nanocatalysts. Electrolyte: 0.5 mol $L^{-1}$ KOH saturated with $O_2$. ω= 1600 rpm.

Figure 4.12 a) shows the mass activity plots before ADT of the nanocatalysts. In the region at low overpotentials (lop) related to a mechanism controlled by a Temkin adsorption at which the surface coverage by oxides either from intermediates from the ORR or from the electrolyte is relatively high, [42] Tafel slopes b= 67 and 45 mV $dec^{-1}$ are calculated for Pd/C and Pd-$CeO_{2\text{-}NR}$/C, respectively (Table 4.5).

The value of Pd/C is only slightly higher that 60 mV $dec^{-1}$ theoretically expected for the ORR in alkaline electrolyte at such overpotentials under Temkin isotherm [43]. The lower slope of Pd-$CeO_{2\text{-}NR}$/C may be attributed to the presence of cerium oxide, not only in terms of the likely formation of an oxide layer over the Pd nanoparticles but also because of a higher porosity due to the nanorods [44].

Meanwhile, at high overpotentials (hop) under a Langmuir adsorption mechanism where the rate determining step is the first electron transfer [45, 46] (0.86 V/RHE and below), b= 107 mV $dec^{-1}$ at the cerium-containing nanocatalysts (Table 4.5), closer than the monometallic to the theoretical 120 mV $dec^{-1}$ slope. The low slope shown by Pd/C can be ascribed to its surface oxidation state [47, 48]. The clear differences in b values indicate that the mechanism of the ORR follows a different path at these nanocatalysts, even though a 4 $e^-$ transfer has been determined for the reaction (Figure 4.11).

Table 4.5 shows the mass and specific activities at 0.9 V/RHE of both nanocatalysts, at which their performance is similar. Nevertheless, it can be observed that over a large potential interval in Figure 4.12 a), the mass activity of Pd-$CeO_{2\text{-}NR}$/C is higher than that of Pd/C. Even more, Figure 4.12 b) shows that despite the presence of the oxide, which may have induced a screening effect on Pd nanoparticles [49], the specific activity of Pd-$CeO_{2\text{-}NR}$/C is also higher over the potential range studied.

**Table 4.5** Mass and specific activity of Pd/C and Pd-$CeO_{2\text{-}NR}$/C for the ORR.

| **Nanocatalyst** | **b** | | **Mass activity** | **Specific activity** |
|---|---|---|---|---|
| | **at lop** | **at hop** | **$i_m$ at 0.9 V** | **$i_s$ at 0.9 V** |
| | **(mV $dec^{-1}$)** | **(mV $dec^{-1}$)** | **(A $mg^{-1}_{Pd}$)** | **(μA $cm^{-2}_{Pd}$)** |
| **Before ADT** | | | | |
| Pd/C | 67 | 82 | 0.017 | 60.42 |
| Pd-$CeO_{2\text{-}NR}$/C | 45 | 106 | 0.015 | 66.33 |
| **After ADT** | | | | |
| Pd/C | 52 | 80 | 0.005 | 39.40 |
| Pd-$CeO_{2\text{-}NR}$/C | 44 | 85 | 0.004 | 17.52 |

From the results evaluated so far, by comparing the behavior of Pd-$CeO_{2\text{-}NR}$/C and Pd/C before ADT, the former has the same value of $E_{1/2}$ as that of the monometallic. Furthermore, it shows a much lower Tafel slope at lop, indicative of faster reaction kinetics for the ORR [44, 50]. Thus, the catalytic activity of Pd-$CeO_{2\text{-}NR}$/C for the ORR is higher than that of Pd/C.

After ADT (Figures 4.12 c and d), changes in the slopes are observed. At lop, the b value of Pd-$CeO_{2\text{-}NR}$/C remains the same while that of Pd/C decreases, perhaps related to oxidation of Pd nanoparticles and Vulcan. Showing the same b value between 0.9 and 0.86 V/RHE is also an indication of the stability of Pd-$CeO_{2\text{-}NR}$/C despite being submitted to potential cycling. At hop, the slope that clearly decreases is that of Pd-$CeO_{2\text{-}NR}$/C. Interestingly, such changes make the plots look alike, likely approaching the mechanistic pathways of the ORR at the nanocatalysts. Over the potential interval, their mass activity remains similar, while the specific activity is slightly higher at Pd/C.

The values at 0.9 V/RHE are shown in Table 4.5. Pd-$CeO_{2\text{-}NR}$/C sustains a high performance after ADT, which reflects the participation of Pd active sites in the reaction, indicating a high catalytic activity for the ORR promoted by $CeO_2$ in alkaline media in agreement with previous reports [51, 52].

### 4.2.2 Evaluation of catalytic activity for the EOR

Figure 4.13 shows the polarization curves of the EOR before and after ADT at a) Pd/C and b) Pd-$CeO_{2\text{-}NR}$/C. It is noteworthy that in the forward scan, the polarization curve at Pd/C before ADT shows a broad shoulder which continues in a small mass current density ($j_m$) peak at about 1.1 V/RHE, contrary to the behavior where a sharp drop in current takes place due to the formation of an oxide layer that hinders the Pd active sites. These features suggest that the oxidation of ethanol and reaction intermediates occurs on PdO-rich surface or one where oxides layers have been at high potentials.

Furthermore, two small peaks followed by a larger one in the backward scan can be observed, due to the reaction of absorbed intermediate species. The former two seem to emerge at potentials more positive than the reduction of PdO. The peaks can be attributed to the presence of species such as acetyl, acetate, and $CO_{ads}$ as reported elsewhere [53]. These features are no longer observed after ADT, which indicates a modification of the surface of Pd/C because of the potential cycling.

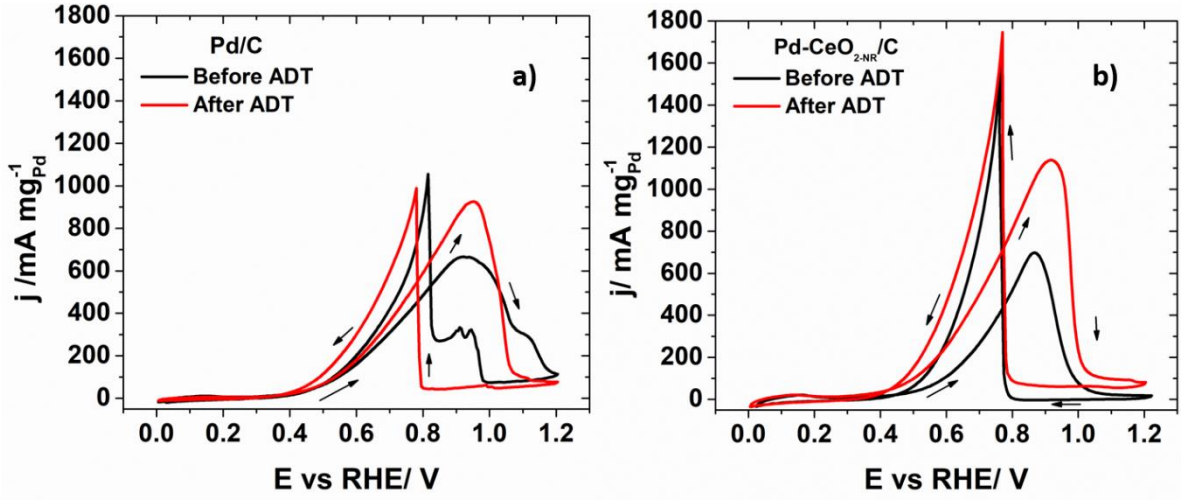


**Figure 4.13** Polarization curves for EOR before and after ADT at a) Pd/C and b) Pd-$CeO_{2\text{-NR}}$/C. Electrolyte: $N_2$-satured 0.5 mol $L^{-1}$ KOH. Scan rate: 20 mV $s^{-1}$.

Meanwhile, at Pd-$CeO_{2\text{-NR}}$/C, $E_{onset}$= 0.29 V/RHE before cycling, more negative than that at Pd/C (Table 4.6). After ADT, there is a shift towards more negative potentials, with the value remaining more favorable for the reaction at Pd-$CeO_{2\text{-NR}}$/C (Table 4.6). Interestingly, $j_m$ increases by 63% and 39% at Pd-$CeO_{2\text{-NR}}$/C and Pd/C after ADT related to their own values before cycling, respectively. If before ADT the performance of the cerium-containing nanocatalyst is better, remarkably, the $j_m$ produced by Pd-$CeO_{2\text{-NR}}$/C is 23% higher compared to that of Pd/C after cycling, with a peak maximum of 1138 mA $mg^{-1}_{Pd}$ (Table 4.6).

The enhancement in EOR after ADT in Pd-$CeO_{2\text{-NR}}$/C and Pd/C suggests that metal catalytic sites become activated. It is also likely that surface oxides such as PdO catalyze the reaction. This species promotes the catalytic activity of Pd nanocatalysts for the oxidation of organic molecules, as concluded from the findings by Sawangphruk et al. [54], Chen et al. [55] and Manzo-Robledo et al. [56] It has been suggested that Pd-oxides limit the poisoning effect of adsorbed carbonaceous species by forming $OH^-$ species. As concluded from XPS analysis, Pd-$CeO_{2\text{-NR}}$/C forms more PdO species than Pd/C, positively affecting its catalytic behavior.

The polarization curves in Figure 4.13 demonstrate that Pd-$CeO_{2\text{-}NR}$/C oxidizes ethanol at more negative potentials than Pd/C, with better performance over the whole potential scanned even with a lower Pd content. Such enhancement in electrocatalytic behavior is attributed to the synergetic effect between Pd and $CeO_{2\text{-}NR}$.

It is well known that $CeO_2$ acts as an oxygen buffer, forming $OH^-$ species at more negative potentials than some noble metals [57]. The $OH^-$ species transferred onto neighboring Pd sites participate in the removal of carbonaceous species, making them available to carry out the oxidation reaction, i.e., the bifunctional mechanism [58]. There is also the possibility of the redeposition of dissolved Pd from the solution to the nanocatalyst [59, 60].

**Table 4.6** Electrochemical parameters for EOR at Pd/C and Pd-$CeO_{2\text{-}NR}$/C.

| **Nanocatalyst** | **$E_{onset}$ (V/RHE)** | **$j_m$ ($mA\ mg^{-1}_{Pd}$)** |
|---|---|---|
| **Before ADT** | | |
| Pd/C | 0.30 | 665 |
| Pd-$CeO_{2\text{-}NR}$/C | 0.29 | 697 |
| **After ADT** | | |
| Pd/C | 0.28 | 925 |
| Pd-$CeO_{2\text{-}NR}$/C | 0.26 | 1138 |

Moreover, since the reaction takes place at more negative potentials at Pd-$CeO_{2\text{-}NR}$/C, i.e., the species are more easily removed from the catalytic surface, thus an electronic effect also occurs when using the nanorods as co-catalysts.

Table 4.7 shows the comparison of catalytic activity for the EOR of Pd-$CeO_{2\text{-}NR}$/C with some nanocatalysts from the literature. It can be observed that Pd-$CeO_{2\text{-}NR}$/C performs well in alkaline media for the oxidation of the alcohol, considering $E_{onset}$ and $j_m$. Unfortunately, no reports which include the values of $j_m$ after an accelerated degradation test have been found.

**Table 4.7** Electrochemical parameters of the EOR at Pd-based nanocatalysts.

| **Catalyst** | **$E_{onset}$** | **$j_m$** | **$j_m$ after ADT** | **Electrolyte** | **Ref.** |
|---|---|---|---|---|---|
| | **(V/RHE)** | **(mA $mg^{-1}_{Pd}$)** | | | |
| PdAu/Co-nanofilm/C | 0.38 | 800 | - | 1 mol $L^{-1}$ NaOH+ 1 mol $L^{-1}$ EtOH | [61] |
| $Pt_1Pd_1$ | 0.37 | 656 | - | 1 mol $L^{-1}$ KOH+ 0.3 mol $L^{-1}$ EtOH | [62] |
| $Cu_1Pd_2$/C | 0.47 | 520 | - | 0.5 mol $L^{-1}$ KOH+ 0.5 mol $L^{-1}$ EtOH | [63] |
| Pd/GO | 0.50 | 530 | - | 1 mol $L^{-1}$ KOH+ 1 mol $L^{-1}$ EtOH | [64] |
| **Pd-$CeO_{2\text{-}NR}$/C** | **0.29** | **697** | **1138** | 0.5 mol $L^{-1}$ KOH+ 0.5 mol $L^{-1}$ EtOH | **This work** |

-Undetermined

## 4.3 Conclusion

$CeO_{2\text{-}NR}$ enhanced the electrochemical stability and catalytic activity for the ORR and the EOR of the Pd-$CeO_{2\text{-}NR}$/C nanocatalyst, compared to Pd/C. Due to the chemical interactions between the nanorods and Pd nanoparticles, the former retained about 98% of ECSA after ADT. Before potential cycling, Pd-$CeO_{2\text{-}NR}$/C showed a higher mass and specific activity for the ORR than Pd/C, with a Tafel slope

that indicates faster kinetics for the reaction. Both nanocatalysts had a similar performance after the polarization cycling. Also, the production of $HO_2^-$ and the electron transfer number at Pd-$CeO_{2\text{-}NR}$/C approached those of Pd/C.

Moreover, the evaluation of catalytic activity for the EOR demonstrated a higher performance before and after ADT of Pd-$CeO_{2\text{-}NR}$/C, with more negative $E_{onset}$ and higher $j_m$ values, in comparison with Pd/C. The enhanced performance of Pd-$CeO_{2\text{-}NR}$/C was attributed to the formation of surface oxide species, in particular PdO, which promoted the reactions. Being an oxygen buffer, $CeO_{2\text{-}NR}$ formed $OH^-$ species which also facilitated the electrochemical reactions. Therefore, the performance of Pd-$CeO_{2\text{-}NR}$/C was notoriously enhanced by a synergetic effect between $CeO_{2\text{-}NR}$ and Pd leading to a beneficial electronic effect and the bifunctional mechanism.

## 4.4 References

[1] S. Song, K. Wang, L. Yan, A. Brouzgou, Y. Zhang, Y. Wang, P. Tsiakaras. Ceria promoted Pd/C catalysts for glucose electrooxidation in alkaline media. Appl. Catal. B: Environ. 176-177 (2015) 233-239.

[2] W.J. Pech-Rodríguez, C. Calles-Arriaga, D. González-Quijano, G. Vargas-Gutiérrez, C. Morais, T.W. Napporn, F.J. Rodríguez-Varela. Electrocatalysis of the Ethylene glycol oxidation reaction and in situ Fourier-transform infared study on PtMo/C electrocatalysts in alkaline and acid media. J. Power Sources. 375 (2018) 335-344.

[3] Q. Tan, C. Shu, J. Abbott, Q. Zhao, L. Liu, T. Qu, Y. Chen, H. Zhu, Y. Liu, G. Wu. Highly dispersed Pd-$CeO_2$ nanoparticles supported on n-doped core–shell structured mesoporous carbon for methanol oxidation in alkaline media. ACS Catal. 9 (2019) 6362-6371.

[4] M. Bellini, M.V. Pagliaro, A. Lenarda, P. Fornasiero, M. Marelli, C. Evangelisti, M. Innocenti, Q. Jia, S. Mukerjee, J. Jankovic, L. Wang, J.R. Varcoe, C.B. Krishnamurthy, I. Grinberg, E. Davydova, D.R. Dekel, H.A. Miller, F. Vizza. Palladium–Ceria catalysts with enhanced alkaline hydrogen oxidation activity for anion exchange membrane fuel cells. ACS Appl. Energy Mater. 2 (2019) 4999-5008.

[5] L.C. M. J. Lázaro, V. Celorrio, J.I. Pardo, S. Perathoner, R. Moliner, in: T.P. I. J. Sanders (Ed.) Carbon Black: Production, Properties and Uses, Nova Science, New York, 2011, pp. 41-70.
[6] R. Pérez-Hernández, G. Mondragón-Galicia, A. Allende Maravilla, J. Palacios. Nano-dimensional $CeO_2$ nanorods for high Ni loading catalysts: $H_2$ production by autothermal steam reforming of methanol reaction. PCCP. 15 (2013) 12702-12708.
[7] T.S. Almeida, Y. Yu, A.R. de Andrade, H.D. Abruña. Employing iron and nickel to enhance ethanol oxidation of Pd-based anodes in alkaline medium. Electrochim. Acta. 295 (2019) 751-758.
[8] T. Li, S. Vongehr, S. Tang, Y. Dai, X. Huang, X. Meng. Scalable synthesis of ag networks with optimized sub-monolayer Au-Pd nanoparticle covering for highly enhanced SERS detection and catalysis. Sci. Rep. 6 (2016) 37092.
[9] Y. Li, Y. Yu, J.-G. Wang, J. Song, Q. Li, M. Dong, C.-J. Liu. CO oxidation over graphene supported palladium catalyst. Appl. Catal. B: Environ. 125 (2012) 189-196.
[10] S. Drewniak, R. Muzyka, A. Stolarczyk, T. Pustelny, M. Kotyczka-Morańska, M. Setkiewicz. Studies of reduced graphene oxide and graphite oxide in the aspect of their possible application in gas sensors. Sensors. 16 (2016).
[11] A.N. Geraldes, D.F. da Silva, E.S. Pino, J.C.M. da Silva, R.F.B. de Souza, P. Hammer, E.V. Spinace, A.O. Neto, M. Linardi, M.C. dos Santos. Ethanol electro-oxidation in an alkaline medium using Pd/C, Au/C and PdAu/C electrocatalysts prepared by electron beam irradiation. Electrochim. Acta. 111 (2013) 455-465.
[12] M. Ren, Y. Kang, W. He, Z. Zou, X. Xue, D.L. Akins, H. Yang, S. Feng. Origin of performance degradation of palladium-based direct formic acid fuel cells. Appl. Catal. B: Environ. 104 (2011) 49-53.
[13] D. Zemlyanov, B. Klötzer, H. Gabasch, A. Smeltz, F.H. Ribeiro, S. Zafeiratos, D. Teschner, P. Schnörch, E. Vass, M. Hävecker, A. Knop-Gericke, R. Schlögl. Kinetics of palladium oxidation in the mbar pressure range: ambient pressure xps study. Top. Catal. 56 (2013) 885-895.
[14] S.M. Senthil Kumar, J. Soler Herrero, S. Irusta, K. Scott. The effect of pretreatment of Vulcan XC-72R carbon on morphology and electrochemical oxygen

reduction kinetics of supported Pd nano-particle in acidic electrolyte. J. Electroanal. Chem. 647 (2010) 211-221.

[15] H. Ali, S. Zaman, I. Majeed, F.K. Kanodarwala, M.A. Nadeem, J.A. Stride, M.A. Nadeem. Porous carbon/rGO composite: An ideal support material of highly efficient palladium electrocatalysts for the formic acid oxidation reaction. ChemElectroChem. 4 (2017) 3126-3133.

[16] H.A. Miller, A. Lavacchi, F. Vizza, M. Marelli, F. Di Benedetto, F. D'Acapito, Y. Paska, M. Page, D.R. Dekel. A Pd/C-$CeO_2$ Anode catalyst for high-performance platinum-free anion exchange membrane fuel cells. Angew. Chem. 55 (2016) 6004-6007.

[17] H. Yu, E.S. Davydova, U. Ash, H.A. Miller, L. Bonville, D.R. Dekel, R. Maric. Palladium-ceria nanocatalyst for hydrogen oxidation in alkaline media: Optimization of the Pd–$CeO_2$ interface. Nano Energy. 57 (2019) 820-826.

[18] J. Saleem, S.K. Safdar Hossain, A. Al-Ahmed, A. Rahman, G. McKay, M.M. Hossain. Evaluation of Pd nanoparticle-decorated $CeO_2$-MWCNT nanocomposite as an electrocatalyst for formic acid fuel cells. J. Electron. Mater. 47 (2018) 2277-2289.

[19] L. Feng, J. Yang, Y. Hu, J. Zhu, C. Liu, W. Xing. Electrocatalytic properties of $PdCeO_x$/C anodic catalyst for formic acid electrooxidation. Int. J. Hydrogen Energy. 37 (2012) 4812-4818.

[20] S. Rajendran, M.M. Khan, F. Gracia, J. Qin, V.K. Gupta, S. Arumainathan. $Ce^{3+}$-ion-induced visible-light photocatalytic degradation and electrochemical activity of ZnO/$CeO_2$ nanocomposite. Sci. Rep. 6 (2016) 31641.

[21] H. Gabasch, W. Unterberger, K. Hayek, B. Klötzer, E. Kleimenov, D. Teschner, S. Zafeiratos, M. Hävecker, A. Knop-Gericke, R. Schlögl, J. Han, F.H. Ribeiro, B. Aszalos-Kiss, T. Curtin, D. Zemlyanov. In situ XPS study of Pd(111) oxidation at elevated pressure, Part 2: Palladium oxidation in the 10−1mbar range. Surf. Sci. 600 (2006) 2980-2989.

[22] J.P. Holgado, R. Alvarez, G. Munuera. Study of $CeO_2$ XPS spectra by factor analysis: reduction of $CeO_2$. Appl. Surf. Sci. 161 (2000) 301-315.

[23] J.C. Carrillo-Rodriguez, S. Garcia-Mayagoitia, R. Perez-Hernandez, M.T. Ochoa-Lara, F. Espinosa-Magana, F. Fernandez-Luqueno, P. Bartolo-Perez, I.L. Alonso-

Lemus, F.J. Rodriguez-Varela. Evaluation of the novel Pd-$CeO_{2\text{-}NR}$ electrocatalyst supported on N-doped graphene for the Oxygen Reduction Reaction and its use in a Microbial Fuel Cell. J. Power Sources. 414 (2019) 103-114.

[24] J. Chen, Y. Li, N. Lu, C. Tian, Z. Han, L. Zhang, Y. Fang, B. Qian, X. Jiang, R. Cui. Nanoporous PdCe bimetallic nanocubes with high catalytic activity towards ethanol electro-oxidation and the oxygen reduction reaction in alkaline media. J. Mater. Chem. A. 6 (2018) 23560-23568.

[25] M.M. Wolf, H. Zhu, W.H. Green, G.S. Jackson. Kinetic model for polycrystalline Pd/$PdO_x$ in oxidation/reduction cycles. Appl. Catal. A. 244 (2003) 323-340.

[26] F.D. Speck, F.S.M. Ali, M.T.Y. Paul, R.K. Singh, T. Böhm, A. Hofer, O. Kasian, S. Thiele, J. Bachmann, D.R. Dekel, T. Kallio, S. Cherevko. Improved hydrogen oxidation reaction activity and stability of buried metal-oxide electrocatalyst interfaces. Chem. Mater. 32 (2020) 7716-7724.

[27] R.K. Singh, E.S. Davydova, J. Douglin, A.O. Godoy, H. Tan, M. Bellini, B.J. Allen, J. Jankovic, H.A. Miller, A.C. Alba-Rubio, D.R. Dekel. Synthesis of $CeO_x$-decorated Pd/C catalysts by controlled surface reactions for hydrogen oxidation in anion exchange membrane fuel cells. Adv. Funct. Mater. 30 (2020) 2002087.

[28] H.A. Miller, F. Vizza, M. Marelli, A. Zadick, L. Dubau, M. Chatenet, S. Geiger, S. Cherevko, H. Doan, R.K. Pavlicek, S. Mukerjee, D.R. Dekel. Highly active nanostructured palladium-ceria electrocatalysts for the hydrogen oxidation reaction in alkaline medium. Nano Energy. 33 (2017) 293-305.

[29] C. Lo Vecchio, C. Alegre, D. Sebastián, A. Stassi, A.S. Aricò, V. Baglio. Investigation of supported Pd-based electrocatalysts for the oxygen reduction reaction: performance, durability and methanol tolerance. Materials. 8 (2015) 7997-8008.

[30] Y. Garsany, O.A. Baturina, K.E. Swider-Lyons, S.S. Kocha. Experimental methods for quantifying the activity of platinum electrocatalysts for the oxygen reduction reaction. Anal. Chem. 82 (2010) 6321-6328.

[31] S. Agarwal, L. Lefferts, B.L. Mojet. Ceria Nanocatalysts: Shape dependent reactivity and formation of OH. ChemCatChem. 5 (2013) 479-489.

[32] S. Kabir, A. Serov, P. Atanassov. 3D-Graphene supports for palladium nanoparticles: Effect of micro/macropores on oxygen electroreduction in Anion Exchange Membrane Fuel Cells. J. Power Sources. 375 (2018) 255-264.
[33] W. Jiao, C. Chen, W. You, G. Chen, S. Xue, J. Zhang, J. Liu, Y. Feng, P. Wang, Y. Wang, H. Wen, R. Che. Tuning strain effect and surface composition in PdAu hollow nanospheres as highly efficient ORR electrocatalysts and SERS substrates. Appl. Catal. B: Environ. 262 (2020) 118298.
[34] Y. Zhu, W. Zhou, Y. Chen, J. Yu, X. Xu, C. Su, M.O. Tadé, Z. Shao. Boosting oxygen reduction reaction activity of palladium by stabilizing its unusual oxidation states in perovskite. Chem. Mater. 27 (2015) 3048-3054.
[35] H. Yang, K. Wang, Z. Tang, Z. Liu, S. Chen. Bimetallic PdZn nanoparticles for oxygen reduction reaction in alkaline medium: The effects of surface structure. J. Catal. 382 (2020) 181-191.
[36] J.C. Calderón, V. Celorrio, M.J. Nieto-Monge, D.J. Fermín, J.I. Pardo, R. Moliner, M.J. Lázaro. Palladium–nickel materials as cathode electrocatalysts for alkaline fuel cells. Int. J. Hydrogen Energy. 41 (2016) 22538-22546.
[37] X. Lu, M. Ahmadi, F.J. DiSalvo, H.D. Abruña. Enhancing the electrocatalytic activity of Pd/M (M = Ni, Mn) nanoparticles for the oxygen reduction reaction in alkaline media through electrochemical dealloying. ACS Catalysis. 10 (2020) 5891-5898.
[38] X. Peng, T.J. Omasta, J.M. Roller, W.E. Mustain. Highly active and durable Pd-Cu catalysts for oxygen reduction in alkaline exchange membrane fuel cells. Front. Energy. 11 (2017) 299-309.
[39] T.Z. Li, Z.H. Tang, K. Wang, W. Wu, S.W. Chen, C.H. Wang. Palladium nanoparticles grown on beta-$Mo_2C$ nanotubes as dual functional electrocatalysts for both oxygen reduction reaction and hydrogen evolution reaction. Int. J. Hydrogen Energy. 43 (2018) 4932-4941.
[40] L. An, Y. Chen, J. Shi, J. Cao, B. Liu, J. Yang. Oxygen reduction activity and stability of composite $Pd_{(x)}$/Co-Nanofilms/C electrocatalysts in acid and alkaline media. Front. Chem. 6 (2018) 596-596.

[41] J. Ju, X. Wang, C. zhang, W. Chen. Design and facile one-pot synthesis of uniform PdAg cubic nanocages as efficient electrocatalyst for the oxygen reduction reaction. Int. J. Hydrogen Energy. 45 (2020) 6437-6446.
[42] N. Ramaswamy, S. Mukerjee. Influence of inner- and outer-sphere electron transfer mechanisms during electrocatalysis of oxygen reduction in alkaline media. J. Phys. Chem. C. 115 (2011) 18015-18026.
[43] T. Shinagawa, A.T. Garcia-Esparza, K. Takanabe. Insight on Tafel slopes from a microkinetic analysis of aqueous electrocatalysis for energy conversion. Sci. Rep. 5 (2015) 13801.
[44] Y. Xue, S. Sun, Q. Wang, Z. Dong, Z. Liu. Transition metal oxide-based oxygen reduction reaction electrocatalysts for energy conversion systems with aqueous electrolytes. J. Mater. Chem. A. 6 (2018) 10595-10626.
[45] G. Wu, A. Santandreu, W. Kellogg, S. Gupta, O. Ogoke, H. Zhang, H.-L. Wang, L. Dai. Carbon nanocomposite catalysts for oxygen reduction and evolution reactions: From nitrogen doping to transition-metal addition. Nano Energy. 29 (2016) 83-110.
[46] D.C. Martínez-Casillas, O. Solorza-Feria. Synthesis and Characterization of bimetallic PdM nanoparticles (M =Ag, Cu) oxygen reduction electrocatalysts. ECS Transactions. 20 (2019) 275-280.
[47] A. Oliveira Neto, J. Perez, E.R. Gonzalez, E.A. Ticianelli. Platinum/cobalt electrocatalysts dispersed on high surface area carbon: study of the oxygen reduction reaction. J. New Mater. Electrochem. Syst. 2 (1999) 189-195.
[48] C. Goswami, K.K. Hazarika, P. Bharali. Transition metal oxide nanocatalysts for oxygen reduction reaction. Mater. Sci. Technol. 1 (2018) 117-128.
[49] M.V. Castegnaro, W.J. Paschoalino, M.R. Fernandes, B. Balke, M.A. MC, E.A. Ticianelli, J. Morais. Pd-M/C (M = Pd, Cu, Pt) electrocatalysts for oxygen reduction reaction in alkaline medium: correlating the electronic structure with activity. Langmuir. 33 (2017) 2734-2743.
[50] W. Sun, A. Hsu, R. Chen. Palladium-coated manganese dioxide catalysts for oxygen reduction reaction in alkaline media. J. Power Sources. 196 (2011) 4491-4498.

[51] A. Altamirano-Gutiérrez, A.M. Fernández, F.J. Rodríguez Varela. Preparation and characterization of Pt-$CeO_2$ and Pt-Pd electrocatalysts for the oxygen reduction reaction in the absence and presence of methanol in alkaline medium. Int. J. Hydrogen Energy. 38 (2013) 12657-12666.
[52] K. Mohanraju, L. Cindrella. Impact of alloying and lattice strain on ORR activity of Pt and Pd based ternary alloys with Fe and Co for proton exchange membrane fuel cell applications. RSC Advances. 4 (2014) 11939-11947.
[53] Y.-Y. Yang, J. Ren, Q.-X. Li, Z.-Y. Zhou, S.-G. Sun, W.-B. Cai. Electrocatalysis of Ethanol on a Pd Electrode in Alkaline Media: An in Situ Attenuated Total Reflection Surface-Enhanced Infrared Absorption Spectroscopy Study. ACS Catalysis. 4 (2014) 798-803.
[54] A. Krittayavathananon, S. Duangdangchote, P. Pannopard, N. Chanlek, S. Sathyamoorthi, J. Limtrakul, M. Sawangphruk. Elucidating the unexpected electrocatalytic activity of nanoscale PdO layers on Pd electrocatalysts towards ethanol oxidation in a basic solution. Sustain. Energy Fuels. 4 (2020) 1118-1125.
[55] T.-J. Wang, F.-M. Li, H. Huang, S.-W. Yin, P. Chen, P.-J. Jin, Y. Chen. Porous Pd-PdO Nanotubes for Methanol Electrooxidation. Adv. Funct. Mater. 30 (2020) 2000534.
[56] L.P.A. Guerrero-Ortega, E. Ramírez-Meneses, R. Cabrera-Sierra, L.M. Palacios-Romero, K. Philippot, C.R. Santiago-Ramírez, L. Lartundo-Rojas, A. Manzo-Robledo. Pd and Pd@PdO core–shell nanoparticles supported on carbon Vulcan XC-72R: comparison of electroactivity for methanol electro-oxidation reaction. J. Mater. Sci. 54 (2019) 13694-13714.
[57] A. Altamirano-Gutiérrez, A.M. Fernández, K.K. Aruna, R. Manoharan, P. Karthikeyan, A. Siller-Ceniceros, P. Meléndez-González, P. Bartolo-Pérez, F.J. Rodríguez-Varela. Evaluation of supported and unsupported Pd–$CeO_2$ nanostructured anode electrocatalysts for the formic acid and the glycerol oxidation reactions in acid media. J. Appl. Electrochem. 45 (2015) 1195-1204.
[58] D.X. González-Quijano, S. Dessources, W. J. Pech-Rodríguez, in: T.W. Napporn, F. J. Rodríguez-Varela (Ed.) Advanced Electrocatalysts for Low-Temperature Fuel Cells, Springer International Publishing AG, 2018, pp. 263-290.

[59] N. Hodnik, M. Zorko, B. Jozinović, M. Bele, G. Dražič, S. Hočevar, M. Gaberšček. Severe accelerated degradation of PEMFC platinum catalyst: A thin film IL-SEM study. Electrochem. Commun. 30 (2013) 75-78.
[60] J. Li, J. Chen, Q. Wang, W.-B. Cai, S. Chen. Controllable increase of boron content in B-Pd interstitial nanoalloy to boost the oxygen reduction activity of palladium. Chem. Mater. 29 (2017) 10060-10067.
[61] Y. Sun, J. Shi, Y. Chen, M. Chen, L. An, J. Cao, B. Liu, B. Liu. Pre-deposited Co nanofilms promoting high alloying degree of $Pd_xAu$ nanoparticles as electrocatalysts in alkaline media. Int. J. Hydrogen Energy. 45 (2020) 28024-28033.
[62] L.L. Carvalho, A.A. Tanaka, F. Colmati. Palladium-platinum electrocatalysts for the ethanol oxidation reaction: comparison of electrochemical activities in acid and alkaline media. J. Solid State Electrochem. 22 (2018) 1471-1481.
[63] H. Mao, T. Huang, A. Yu. Surface Palladium rich $Cu_xPd_y$/carbon catalysts for methanol and ethanol oxidation in alkaline media. Electrochim. Acta. 174 (2015) 1-7.
[64] H. Xiao, J. Zhang, M. Zhao, T. Hu, J. Jia, H. Wu. Hydrogenated graphene as support of Pd nanoparticles with improved electrocatalytic activity for ethanol oxidation reaction in alkaline media. Electrochim. Acta. 297 (2019) 856-863.

# Chapter V

# Evaluation of Pd nanocatalysts supported on Vulcan XC-72 functionalized with Cu organometallic compounds for the EOR.

## 5.1 Physicochemical characterization of Cu organometallic compounds

### 5.1.1 $^{1}$H-NMR

The $^{1}$H-NMR spectrum of the mesityl copper (Cu-mes) organometallic compound is shown in Figure 5.1. Its chemical structure is confirmed by analyzing the chemical shifts (δ) of the protons contained in the compound. The shift at 1.96 ppm corresponds to three methyl protons in *para* (**p**) position (H1), while the shift at 2.80 ppm is assigned to six methyl protons in *orto* (**o**) position (H2), and that at 6.54 ppm is assigned to two phenyl protons (H3) (Table 5.1)[1].

During the synthesis of Cu-mes, tetrahydrofuran (THF) has been used having two signals at 1.43 and 3.35 ppm, 1,4 dioxane ($C_4H_8O_2$) has also been employed showing one signal at 3.56 ppm [2-4]. Signals at 2.16 and 7.14 ppm can be ascribed to benzene ($C_6D_6$) and acetone $(CD_3)_2CO$ [5].

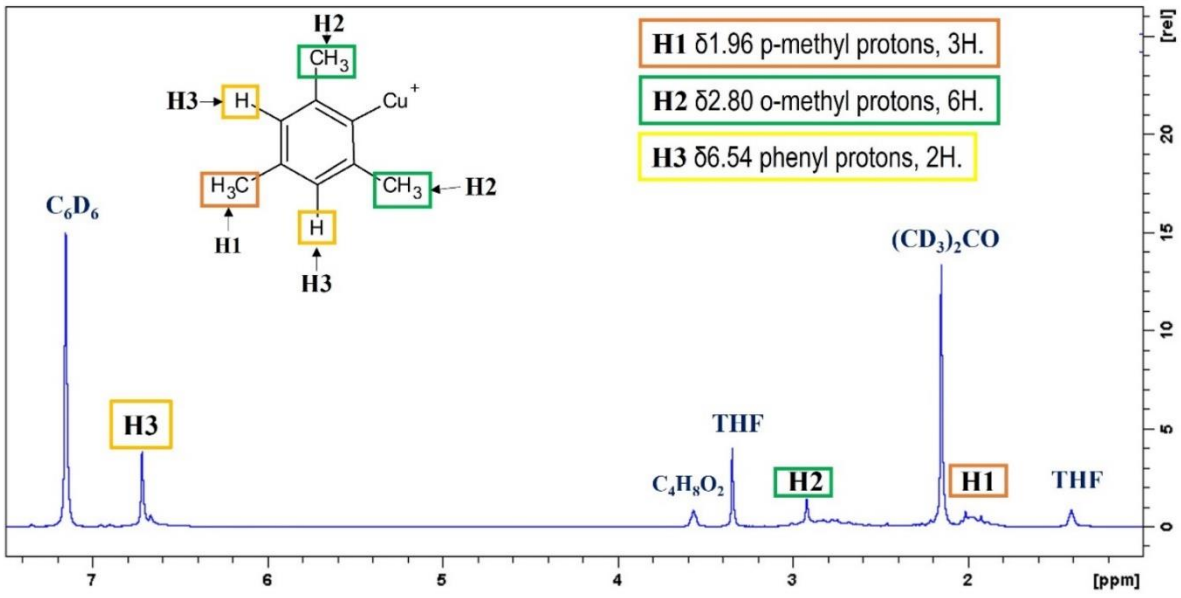


**Figure 5.1** $^{1}$H-NMR ($(CD_3)CO$, 500mHz) spectrum of Cu-mes.

**Table 5.**1 $^{1}$H-NMR chemical shift of Cu-mes.

| Position proton | Chemical shift (δ) |
|---|---|
| p-methyl | 1.96 (3H) |
| o-methyl | 2.80 (6H) |
| phenyl | 6.54 (2H) |

### 5.1.2 FE-SEM and EDS

The chemical composition of Cu-mes is shown in Table 5.2. It has 48.17, 18.87, and 32.95 (wt. %) of C, O, and Cu, respectively. The Cu content is similar to that reported in the literature (33-35 %) [4]. These results confirm the chemical stability during the synthesis of the organometallic compound. Figures 5.2 a) and b) show high magnification FE-SEM micrographs of Cu-mes, having irregularly agglomerated shape and relatively smooth surface. It is important to note that, to the best our knowledge, this is the first time that FE-SEM analysis of this organometallic compound is reported.

**Table 5.2** Chemical composition of Cu-mes.

| Organometallic compounds | Chemical composition (wt. %) | | |
|---|---|---|---|
| | **C** | **O** | **Cu** |
| Cu-mes | 48.17 ± 1.89 | 18.87 ± 4.42 | 32.95 ± 6.02 |

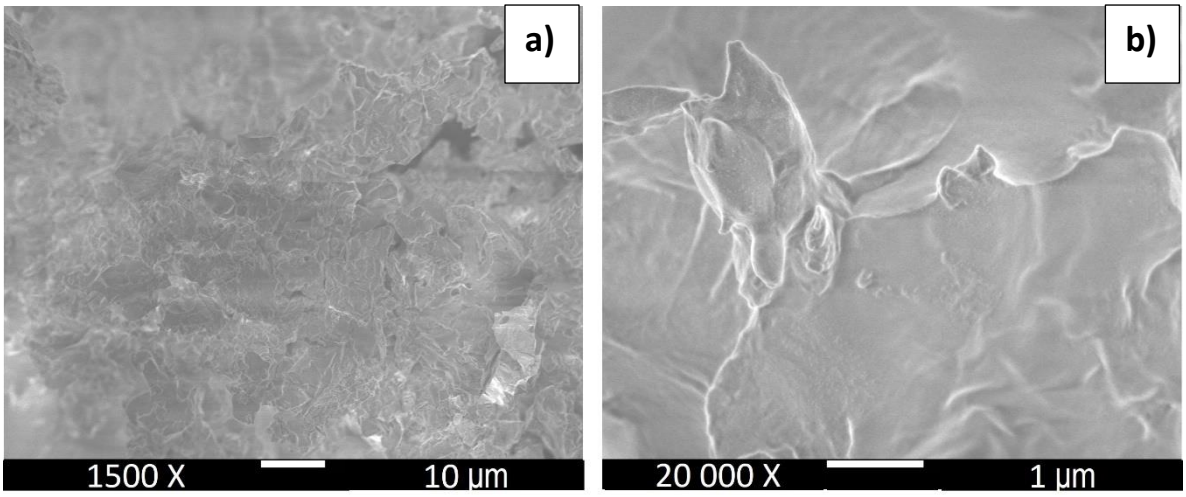


**Figure 5.2** a) and b) high magnification FE-SEM micrographs of Cu-mes.

### 5.1.3 FT-IR

Figure 5.3 displays the FT-IR spectrum of. Cu-mes. The signal of the OH-stretching vibration from hydroxyl groups at 3422 $cm^{-1}$ can be due to residual solvents in the sample. The bands at 2928 $cm^{-1}$ and in the 1421–1046 $cm^{-1}$ range correspond to alkanes in the organometallic compound and emerge due to vibrations of arene rings and methyl groups, respectively. Meanwhile, the band in the 1617–1424 $cm^{-1}$ range is attributed to vibrations of C=C bonds from the arene rings. Also, the signals that correspond to Cu-O vibrations is observed in the 640–500 $cm^{-1}$ interval [6, 7]. The presence of these bands confirms the formation of the Cu-mes compound.

The spectrum of Cu(dmpz)L2 in Figure 5.3 confirms the presence of the characteristic NH bands at 3358 $cm^{-1}$, due at the dmpz ligand which coordinated within the compound. Carboxylate bands in 1509–1298 $cm^{-1}$ range are also observed [8]. Moreover, in the 700–500 $cm^{-1}$ region the bands are assigned to the Cu(I)-O and Cu(II)-O vibrations, which confirm the coordination of the Cu organometallic compound.

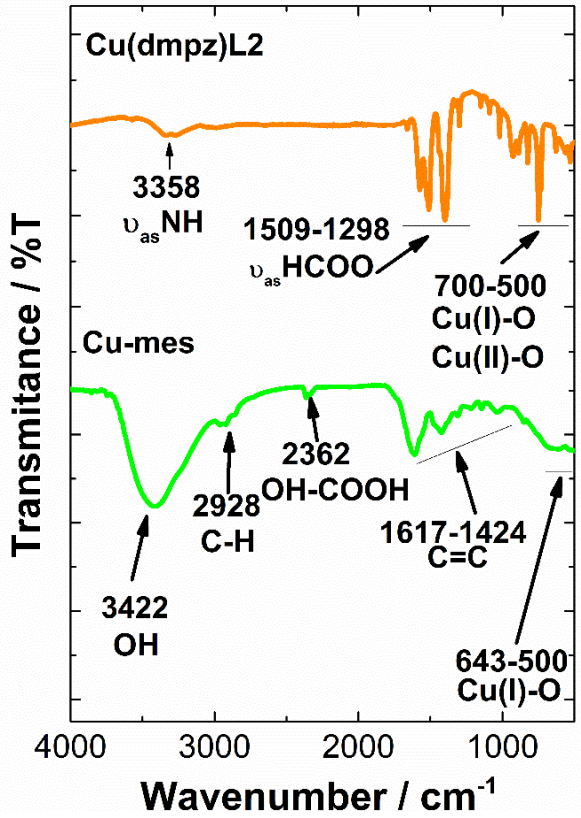


**Figure 5.3** FT-IR spectra of the Cu-mes and Cu(dmpz)L2 organometallic compounds.

## 5.2 Physicochemical characterization of the functionalized carbon.

### 5.2.1 FT-IR

The FT-IR spectra of the three carbon supports are shown in Figure 5.4. Non-functionalized C shows a band at around 3440 $cm^{-1}$ due to the OH stretching vibration from hydroxyl groups. It also displays the band at 2900 $cm^{-1}$ attributed to C-H vibrations of alkane and alkyl groups. The band at 2368 $cm^{-1}$ corresponds to the stretching of O-H bonds and vibrations of COOH groups. In the 1700–1200 $cm^{-1}$ range, bands attributed to stretching vibrations of C-O species in carbonyl $HCOO^-$ as well as carboxyl groups are detected [9-12]. These bands emerge due to the functional groups already developed at Vulcan.

Additionally, the FTIR spectrum of $C_{Cu\text{-}mes}$ shows a band assigned to Cu-O stretching vibrations in the 660-520 $cm^{-1}$ range [6, 13]. Moreover, the spectrum of $C_{Cu(dmpz)L2}$ shows the characteristic signals ascribed to carboxylate and NH bands due to the (dmpz) ligand, which suggest the coordination of the compound [14].

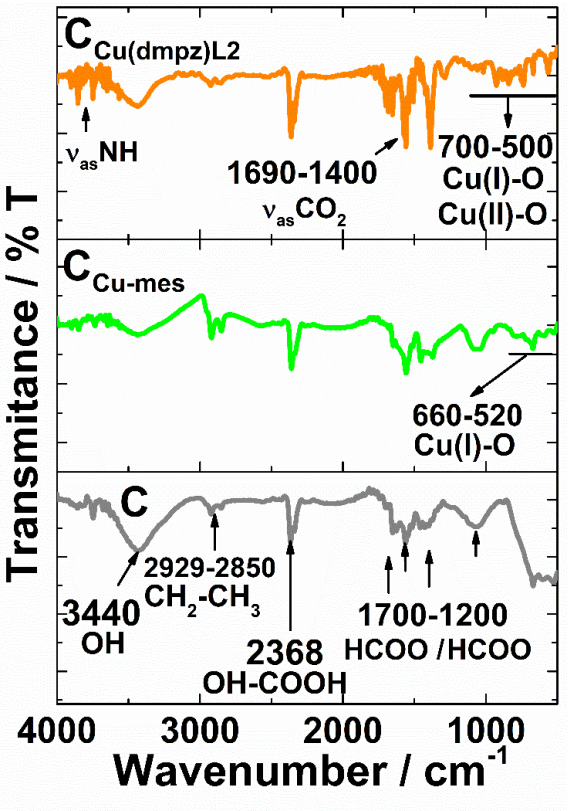


**Figure 5.4** FT-IR spectra of C, $C_{Cu\text{-}mes}$ and $C_{Cu(dmpz)L2}$.

### 5.2.2 Raman

The Raman spectra of C, $C_{Cu\text{-}mes}$, and $C_{Cu(dmpz)L2}$ are shown in Figure 5.5. The plots display the D and G bands characteristic of carbon materials at 1324 and 1584 $cm^{-1}$, respectively. In addition, the D' (~1615 $cm^{-1}$), D'' (~1500 $cm^{-1}$), and D* (~1170 $cm^{-1}$) interbands have been developed from the deconvolution of the spectra. The D band corresponds to $sp^3$ hybridization, directly related to impurities in the carbon structure. On the other hand, the G band is attributed to the $sp^2$ hybridization of

carbon, characteristic of graphitic materials. The ratio of the intensity of the D and G bands ($I_D/I_G$) is proportional to the degree of $sp^3/sp^2$ hybridization of the carbon atoms [15, 16].

In Figure 5.5 a) C has an $I_D/I_G$ ratio of 1.87, i.e., it is carbon with relatively high structural disorder. Meanwhile, the intensity of the G band increases at $C_{Cu\text{-}mes}$ and $C_{Cu(dmpz)L2}$ compared to C (spectra in Figures 5.5 b and c, respectively), so their $I_D/I_G$ ratio decreases to 1.75 and 1.18 (Table 5.3), respectively, due to an increase in $sp^2$ domains. Such changes at $C_{Cu\text{-}mes}$ and $C_{Cu(dmpz)L2}$ are attributed to an effect of $\pi$-$\pi$ bonds between the graphitic structure of C and the Cu organometallic compounds (Figures 5.6 a and b), leading to constructive rehybridization that increases the $sp^2$ nanodomains at C during functionalization [17, 18].

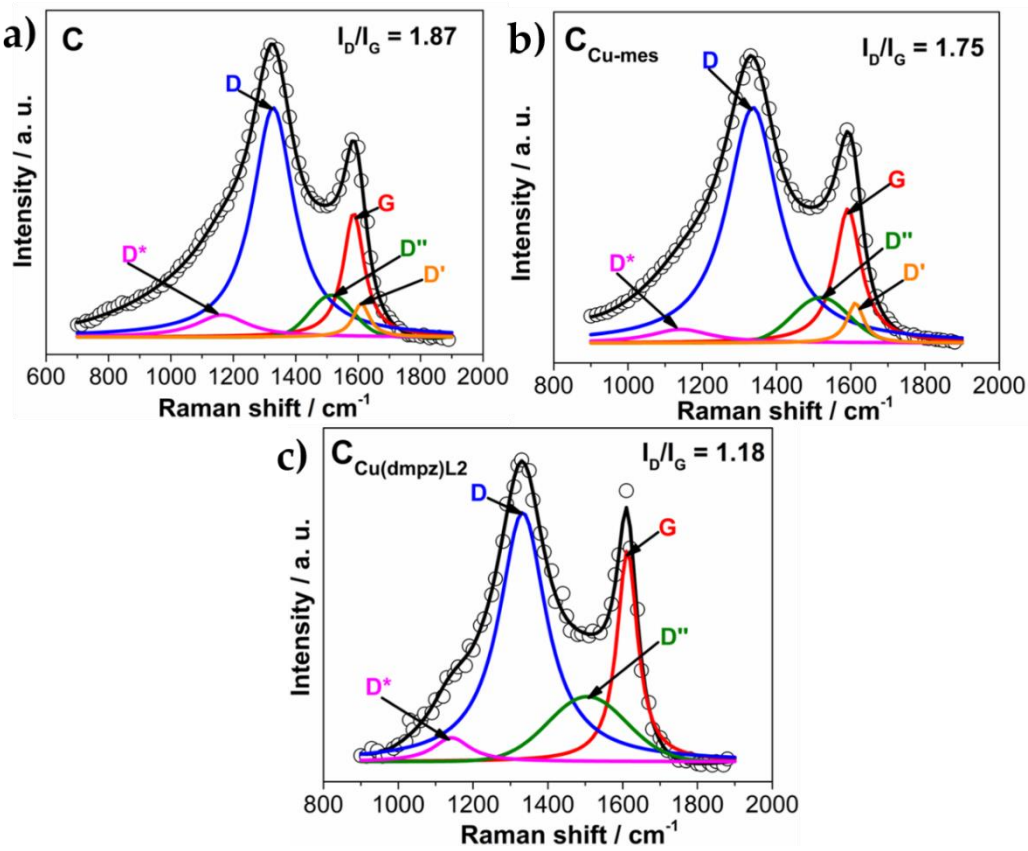


**Figure 5.5** Raman spectra of a) C, b) $C_{Cu\text{-}mes}$ and c) $C_{Cu(dmpz)L2}$.

The D' interband usually merges with the G band and is due to the phonon confinement caused by structural defects [19]. In the case of $C_{Cu(dmpz)L2}$, D' is not detected due to overlapping with its G band (~1609 $cm^{-1}$), which is confirmed by the shift of the latter compared to C (G= ~1588 $cm^{-1}$), and $C_{Cu\text{-}mes}$ (G= ~1589 $cm^{-1}$). This is a particular modification of the carbon structure resulting from its functionalization with Cu(dmpz)L2, which differs from that with Cu-mes. Meanwhile, the D'' interband has been assigned to interstitial defects of amorphous carbon fragments containing $sp^2$ bonds [20]. On this matter, the relative intensity of D'' is 19, 22, and 26 for C, $C_{Cu\text{-}mes}$, and $C_{Cu(dmpz)L2}$, respectively. Such increase in D'' at the functionalized carbons is assigned to the presence of organic fragments and functional groups in their structure [21].

Moreover, the D* interband can be attributed to the stretching vibration of the $sp^2$-$sp^3$ (C-C and C=C) bonds [22, 23], and the $I_{D^*}/I_G$ ratio has been determined as 0.17, 0.09, and 0.11 for C, $C_{Cu\text{-}mes}$, and $C_{CudmpzL2}$, respectively as seen in Table 5.3. Thus, it can be confirmed that the crystalline phases increase after functionalization of Vulcan with the organometallic compounds.

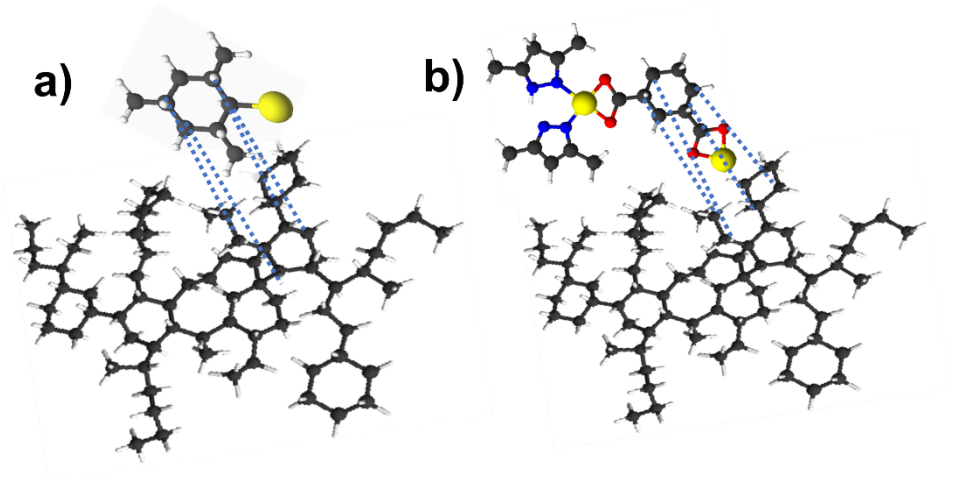


**Figure 5.6** Scheme of the π interactions between C and a) Cu-mes and b) Cu(dmpz)L2.

**Table 5.3** Raman data of C, $C_{Cu\text{-}mes}$, and $C_{CudmpzL2}$.

| **Nanocatalyst** | **Raman Shift / $cm^{-1}$** | | | | | **$I_D/I_G$** | **$I_{D''}$** | **$I_{D^*}/I_G$** |
|---|---|---|---|---|---|---|---|---|
| | D | G | D′ | D′′ | D* | | | |
| C | 1327 | 1588 | 1607 | 1519 | 1154 | 1.87 | 19 | 0.17 |
| $C_{Cu\text{-}mes}$ | 1332 | 1589 | 1614 | 1519 | 1140 | 1.75 | 22 | 0.09 |
| $C_{Cu(dmpz)L2}$ | 1325 | 1609 | - | 1497 | 1137 | 1.18 | 26 | 0.11 |

– Undetermined.

### 5.2.3 XRD

The XRD patterns of C, $C_{Cu\text{-}mes,}$ and $C_{Cu(dmpz)L2}$ are shown in Figure 5.7. The diffractogram of C displays peaks around 2θ = 25.40 and 43.54 °, which correspond to the (002) and (101) planes characteristic of graphite (JCPDS 74-2329), confirming the turbostratic structure of Vulcan, i.e., a structure having both amorphous and graphitic features [24].

Besides the (002) reflection, pattern of $C_{Cu\text{-}mes}$ shows reflections at 32.57, 35.76, 38.97, 47.05, 61.03, 67.41 and 74.13° (2θ), corresponding to the (110), (002), (111), (202), (113), (220), and (004) planes of the tenorite structure of CuO (JCPDS 41-0254) [25, 26]. On the other hand, the pattern of $C_{Cu(dmpz)L2}$ shows high-intensity reflections ascribed to $C_{14}H_{14}CuN_4O_7$, which hinders those of graphite. The features shown by $C_{Cu\text{-}mes}$ and $C_{Cu(dmpz)L2}$ evidently show the effect of functionalizing C with the organometallic compounds on their structural characteristics.

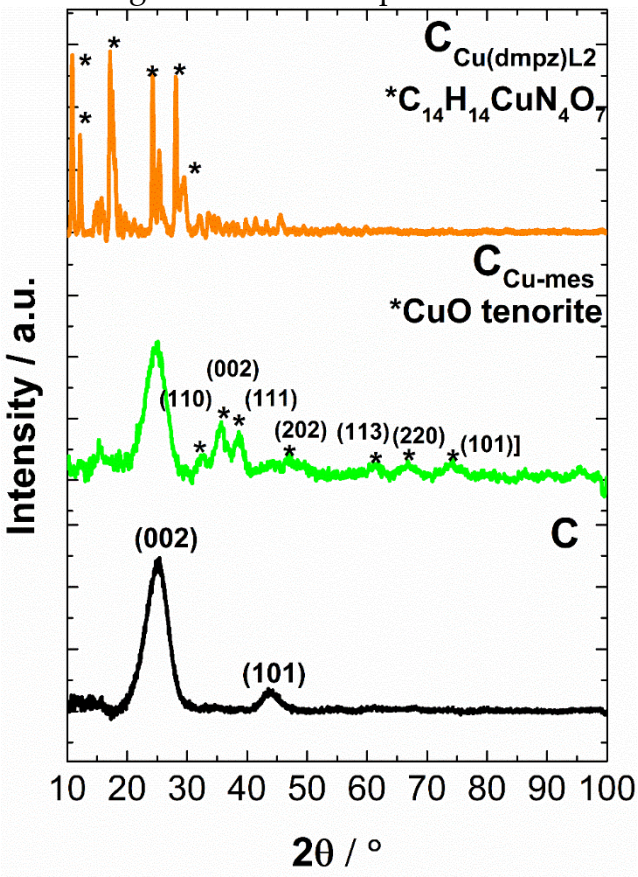


**Figure 5.7** XRD patterns of C, $C_{Cu\text{-}mes}$ and $C_{Cu(dmpz)L2}$.

### 5.2.4 SEM-EDS and FE-SEM

Table 5.4 shows the chemical composition of the supports. C has 89.86 and 10.14 (wt. %) C and O, respectively [27]. $C_{Cu\text{-}mes}$ has a content of 80.51, 12.89, and 6.59 (wt. %) C, Cu, and O, respectively. The Cu content is lower than the theoretically expected value (i.e., 20 wt. %), however, some can be attached to the surface of the carbon as copper oxides. This is supported by the fact that the concentration of C is basically the 80 wt. % nominally expected. Meanwhile, $C_{Cu(dmpz)L2}$ shows 71.31, 22.36, and 6.32 (wt. %) of C, Cu, and O, respectively. In this case, the concentration of Cu is only slightly lower than the theoretically expected (25 wt. %).

**Table 5.4** Chemical composition of C, $C_{Cu\text{-}mes}$ and $C_{Cu(dmpz)L2}$.

| Support functionalized | Chemical composition (wt. %) | | |
|---|---|---|---|
| | C | O | Cu |
| C | 89.86 | 10.14 | - |
| $C_{Cu\text{-}mes}$ | 80.51 ± 0.86 | 6.59 ± 0.60 | 12.89 ± 1.38 |
| $C_{Cu(dmpz)L2}$ | 71.31 ± 0.18 | 6.32 ± 0.29 | 22.36 ± 0.37 |

– Undetermined.

The high magnification FE-SEM micrographs in Figures 5.8 a) and b) show the morphology of $C_{Cu\text{-}mes}$, with semi-spherical carbon particles. The smoothness and agglomeration are attributed to the functionalization, which indicate that there is surface coverage by the organometallic compound. Figure 5.9 shows a) distribution of elements and the elemental mapping of b) C, c) O and d) Cu of $C_{Cu\text{-}mes}$, where both Cu and O show some agglomerated zones over carbon.

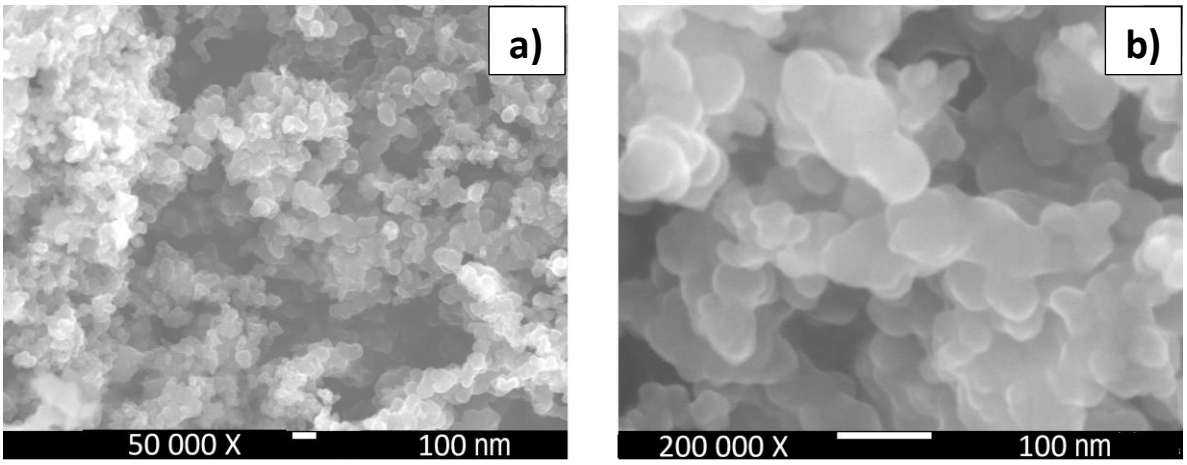


**Figure 5.8** a) and b) high magnification FE-SEM micrographs of $C_{Cu\text{-}mes}$.

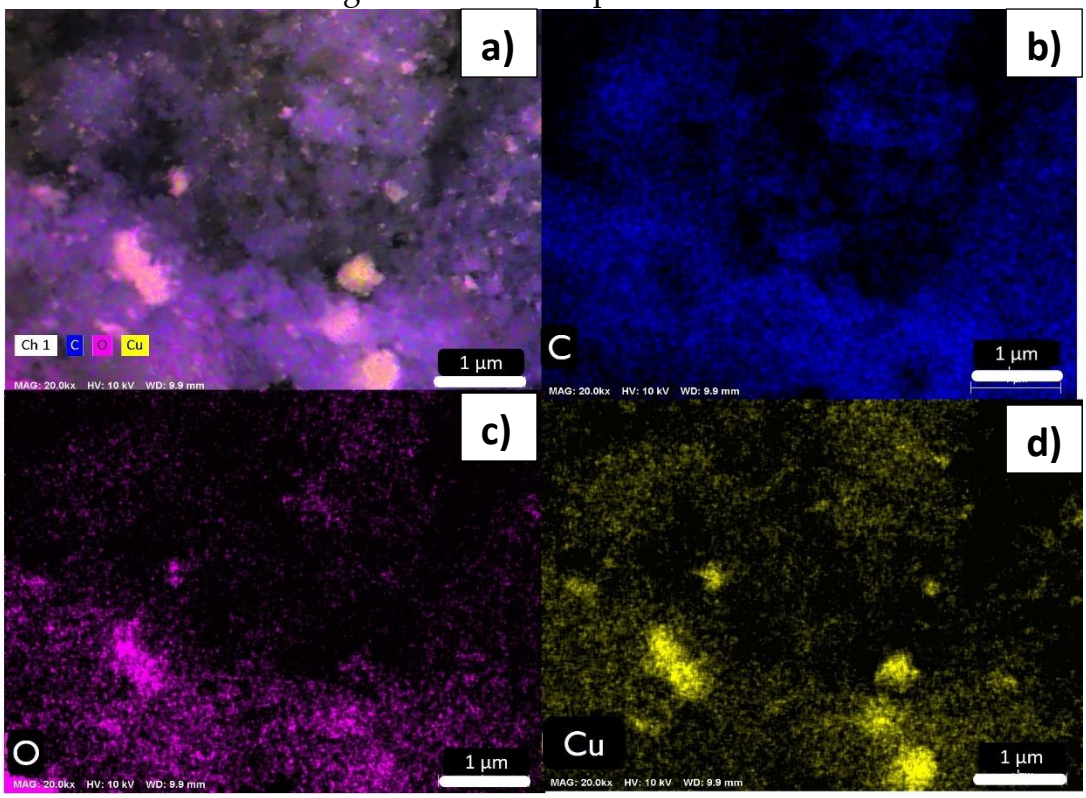


**Figure 5.9** a) Distribution of C, O, and Cu elements and b) C, c) O and d) Cu the elemental mapping of $C_{Cu\text{-}mes}$.

### 5.2.5 XPS

Figure 5.10 displays the XPS spectra of $C_{Cu\text{-}mes}$. Its C 1s region is deconvoluted into three peaks (Figure 5.9 a) with the most intense signal being that of the $sp^2$ hybridization (C=C bond, BE= 284.71 eV) as seen in Table 5.5, followed by the less intense $sp^3$ hybridization (C-C bond, BE= 285.63), and the C-O-C species (BE= 286.62). Their relative concentration is 75.2, 17.6, and 7.1 at %, respectively (Table 5.5). The presence of $sp^2$ C=C bonds is due to graphitic phases in the structure of $C_{Cu\text{-}mes}$, which is in good agreement with the Raman spectra in Figure 5.5.

Figure 5.10 b) shows the O 1s region of $C_{Cu\text{-}mes}$, having signals at 530.69 and 531.73 eV assigned to CuO (9 at. %) and $Cu_2O$ (27.7 at. %) bonds, respectively, confirming copper and oxygen interactions [28]. It is important to note that these

signals do not appear in the O 1s region of non-functionalized Vulcan [29]. It also shows signals ascribed to C=O (BE= 532.61) and C-O (BE= 533.79) bonds. The relative concentration of the former is higher compared to that of the latter (43.8 and 19.5 at. %, respectively, Table 5.5).

The deconvoluted Cu 2p region of $C_{Cu\text{-}mes}$ is shown in Figure 5.10 c). The signals centered at 935.02 and 954.81 eV are associated to the cuprous ion ($Cu^{+}$) in the Cu $2p_{3/2}$ and Cu $2p_{½}$ states, respectively. The peaks at 937.43 and 957.85 eV correspond to $Cu^{2+}$ species also in both states. The presence of satellite signals in the 940-950 eV and 960-970 eV regions indicates a significant contribution of Cu oxidized species in the spectra [30-32]. These results agree with the identification of copper oxides from XRD analysis (see Figure 5.7).

Figure 5.10 also shows the XPS spectra of $C_{Cu(dmpz)L2}$. The most intense signal in the C 1s region (Figure 5.10 d) is that due to the $sp^2$ hybridization (C=C bond, BE=284.63 eV). Less intense signals correspond to the C-C, C-O-C, and C=O species (285.26, 286.39, and 287.50 eV, respectively, Table 5.4). The C=O peak is related to functional groups wherein oxygen is attached to the carbon by a double bond, such as quinine, carbonyl, carboxylic, and lactone groups [33]. It is important to note that this peak does not appear in the deconvoluted C 1s region of $C_{Cu\text{-}mes}$, most probably due to the concentration of carboxylates (5.7 at. %) which are found within the chemical structure of $C_{Cu(dmpz)L2}$.

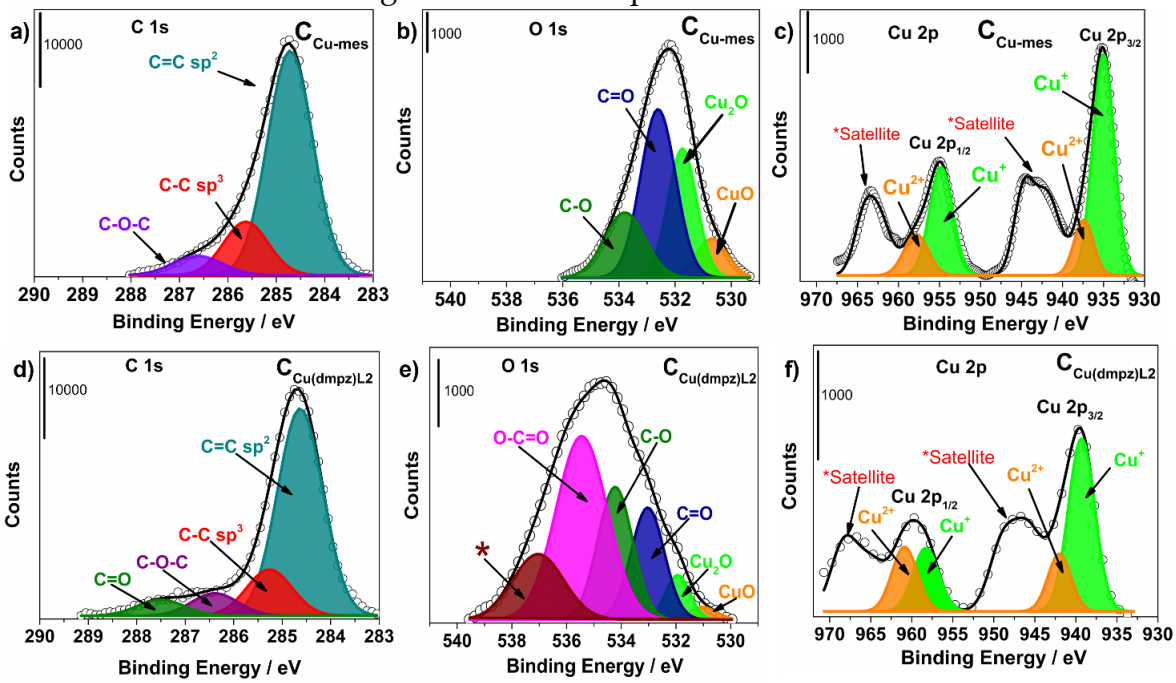


**Figure 5.10** XPS spectra of $C_{Cu\text{-}mes}$ in the a) C 1s, b) O 1s and c) Cu 2p regions, and $C_{Cu(dmpz)L2}$ in the d) C 1s, e) O 1s and f) Cu 2p regions.

The O 1s region (Figure 5.10 e) at $C_{Cu(dmpz)L2}$ shows two low-intensity peaks assigned to CuO (BE=532.04), and $Cu_2O$ (BE= 531.94), as in the case $C_{Cu\text{-}mes}$. The C=O, C-O, and O-C=O (not observed at $C_{Cu\text{-}mes}$) species are also detected at 533.04, 534.23, and 535.45 eV, respectively. The relative concentration of the species is shown in Table 5.5. The peak at 537.04 eV is attributed to traces (-O-C(O)-$C_6H_4$-C(O)-O- $CH_2$-$CH_2$-)$_n$ species from the organometallic compound, which has been reported in that BE elsewhere [34]. It is important to note the shift to higher BE of the C=O and C-O bonds of $C_{Cu(dmpz)L2}$ compared to $C_{Cumes}$ (Table 5.5), which are related to the specific interactions of the compounds with the carbon support. The identification of the O-C=O and (-O-C(O)-$C_6H_4$-C(O)-O- $CH_2$-$CH_2$-)$_n$ species can be correlated with the features of the XRD pattern of $C_{Cu(dmpz)L2}$ in Figure 5.7.

Figure 5.10 f) shows that the Cu 2p region of $C_{Cu(dmpz)L2}$ can be deconvoluted into the $Cu^+$ and $Cu^{2+}$ species. The $Cu^+$ peaks are located at 938.67 and 958.73 eV, respectively, corresponding to the Cu $2p_{3/2}$ and Cu $2p_{1/2}$ states [35]. The peaks

centered at 941.2 eV and 943 eV are those of $Cu^{2+}$ in both Cu states. Satellites are also displayed at $C_{Cu(dmpz)L2}$, as in the case of $C_{Cu\text{-}mes}$.

**Table 5.5** XPS parameters of $C_{Cu\text{-}mes}$ and $C_{Cu(dmpz)L2}$.

| **Support** | **State** | **Species** | **BE / eV** | **Composition at. %** |
|---|---|---|---|---|
| **$C_{Cu\text{-}mes}$** | C 1s | C=C $sp^2$ | 284.71 | 75.2 |
| | C 1s | C-C $sp^3$ | 285.63 | 17.6 |
| | C 1s | C-O-C | 286.62 | 7.1 |
| | O 1s | CuO | 530.69 | 9.0 |
| | O 1s | $Cu_2O$ | 531.73 | 27.7 |
| | O 1s | C=O | 532.61 | 43.8 |
| | O 1s | C-O | 533.79 | 19.5 |
| | Cu $2p_{3/2}$ | $Cu^+$ | 935.02 | 45.5 |
| | Cu $2p_{3/2}$ | $Cu^{2+}$ | 937.43 | 7.0 |
| | Cu $2p_{1/2}$ | $Cu^+$ | 954.81 | 38.1 |
| | Cu $2p_{1/2}$ | $Cu^{2+}$ | 957.85 | 9.6 |
| **$C_{Cu(dmpz)L2}$** | C 1s | C=C $sp^2$ | 284.63 | 70.7 |
| | C 1s | C-C $sp^3$ | 285.26 | 15.8 |
| | C 1s | C-O-C | 286.39 | 7.8 |
| | C 1s | C=O | 287.50 | 5.7 |
| | O 1s | CuO | 531.04 | 1.5 |
| | O 1s | $Cu_2O$ | 531.94 | 4.7 |
| | O 1s | C=O | 533.03 | 16.6 |
| | O 1s | C-O | 534.23 | 20.5 |
| | O 1s | O-C=O | 535.45 | 41.7 |
| | O 1s | (-O-C(O)-$C_6H_4$-C(O)-O-$CH_2$-$CH_2$-)$_n$ | 537.04 | 14.9 |
| | Cu $2p_{3/2}$ | $Cu^+$ | 938.67 | 34.7 |
| | Cu $2p_{3/2}$ | $Cu^{2+}$ | 940.47 | 17.3 |

| | | | |
|---|---|---|---|
| Cu $2p_{1/2}$ | $Cu^{+}$ | 958.73 | 26.5 |
| Cu $2p_{1/2}$ | $Cu^{2+}$ | 961.32 | 22.4 |

## 5.3 Physicochemical characterization of the nanocatalysts

### 5.3.1 XRD

Figure 5.11 shows the XRD patterns of the nanocatalysts. In the diffractogram of Pd/C, the (002) plane attributed to the carbon structure can be observed, followed by the (111), (200), (220), and (311) reflections corresponding to the fcc structure of Pd. In the case of $Pd/C_{Cu\text{-}mes}$ the Pd planes shift towards higher degrees (2θ) which suggests a modification of the Pd lattice due to the formation of PdCu alloyed phases [36, 37]. There are no additional diffraction peaks related to Cu or its oxides. Nevertheless, their presence should not be discarded, alongside the PdCu alloy [38]. Such displacement in the Pd planes is more evident in $Pd/C_{Cu(dmpz)L2}$. Moreover, this nanocatalyst show several peaks in the 15-25° (2θ) interval attributed to the organometallic compound, as observed in the diffractogram of $C_{Cu(dmpz)L2}$ in Figure 5.6.

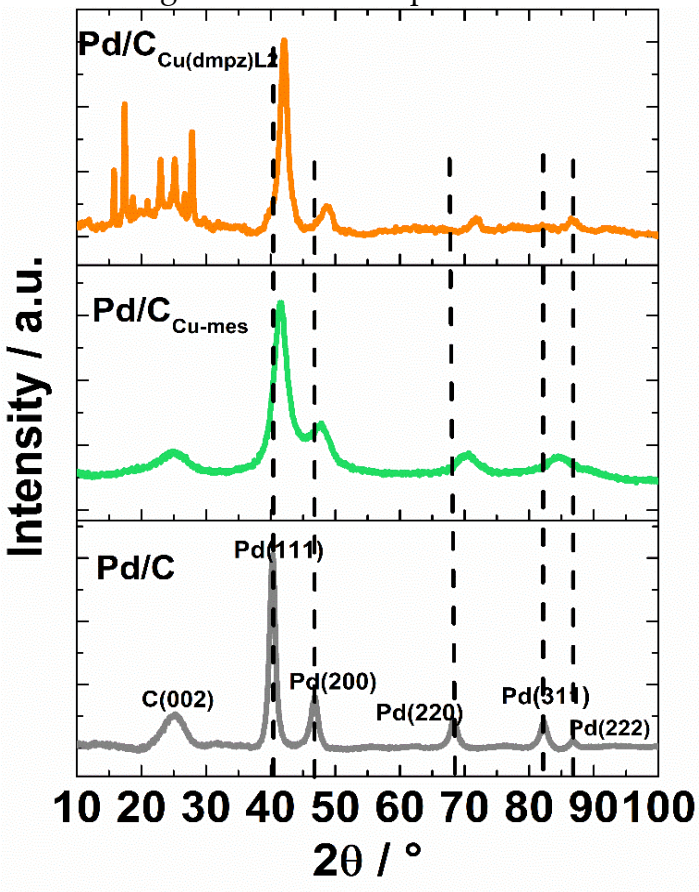


**Figure 5.11** XRD patterns of nanocatalysts.

Table 5.6 shows the d values of the nanocatalysts. $Pd/C_{Cu\text{-}mes}$ has the smallest d compared to $Pd/C_{Cu(dmpz)L2}$. The d values can be correlated to a presence of nucleation centers (surface functional groups and Cu sites) which limited the particle size growth from functionalization with $C_{Cu\text{-}mes}$. This differs from $C_{CudmpzL2}$ in which the crystallite size of the nanoparticles increases suggesting a low presence of nucleation centers [39, 40].

**Table 5.6** Crystallite size and structural parameters of nanocatalysts.

| Nanocatalyst | d / nm | Position / ° | $a_{fcc}$ / nm | D / % |
|---|---|---|---|---|
| Pd/C | 7.9* | 40.30 | 0.387 | - |
| $Pd/C_{Cu\text{-}mes}$ | 2.9 | 41.57 | 0.375 | 31 |
| $Pd/C_{Cu(dmpz)L2}$ | 6.3 | 42.35 | 0.369 | 33 |

Note: d and structural parameters obtained from the (220) and (111) Pd planes, respectively.
* Result reported in Section 4.1.2.
– Undetermined.

As already mentioned, the shift or the reflections towards higher 2θ degrees (as can be seen in Table 5.6) is attributed to the formation of PdCu alloyed phases. To confirm this, the lattice parameter ($a_{fcc}$) and fraction of Cu alloyed (D) have been determined (Equations 3.2 and 3.3, respectively) and are shown in Table 5.6. $Pd/C_{Cu\text{-}mes}$ and $Pd/C_{Cu(dmpz)L2}$ have a clear contraction resulting in $a_{fcc}$= 0.375 and 0.369 nm, respectively. This is evidence that Cu atoms from the organometallic compounds and Pd nanoparticles form PdCu alloyed phases at both nanocatalysts. Additionally, the D value of $Pd/C_{Cu\text{-}mes}$ and $Pd/C_{Cu(dmpz)L2}$ is 31 and 33%, respectively. These $a_{fcc}$ and D values are similar to those reported in the literature for conventional PdCu alloys synthesized by different methods [41-43]. Thus, there is strong evidence of the formation of alloyed PdCu phases at $Pd/C_{Cu\text{-}mes}$ and $Pd/C_{Cu(dmpz)L2}$.

### 5.3.2 FE-SEM and EDS

Table 5.7 shows the chemical composition of $Pd/C_{Cu\text{-}mes}$ obtained from EDS analysis. The C and O show a concentration of 69 ± 1.4 and 1.97 ± 0.2, the latter due to the formation of oxidized Pd or Cu phases or oxygen contained in the carbon. The Pd content is 19.18 ± 0.93, very close to the nominally expected value (20 wt. %). The concentration of Cu from the functionalization is 9.34 ± 0.7 wt. %. Even though this value is slightly lower when compared to $C_{Cu\text{-}mes}$ (Table 5.4), it confirms that Cu from the organometallic compound is stable even after being submitted to the reduction atmosphere of the polyol method during the synthesis of the nanocatalyst.

The FE-SEM micrographs in Figures 5.12 a) and b) show the morphology of $Pd/C_{Cu\text{-}mes}$ at high magnifications, with spherical shape particles corresponding to Vulcan and brighter small nanoparticles attributed to Pd. The elemental mapping of $Pd/C_{Cu\text{-}mes}$, confirming the homogeneous dispersion of C, O, Pd, and Cu is shown in Figure 5.13.

**Table 5.7** Chemical composition of $Pd/C_{Cu\text{-}mes}$.

| **Nanocatalyst** | **Chemical composition (wt. %)** | | | |
|---|---|---|---|---|
| | C | Pd | O | Cu |
| $Pd/C_{Cu\text{-}mes}$ | 69 ± 1.4 | 19.18 ± 0.93 | 1.97 ± 0.2 | 9.34 ± 0.7 |

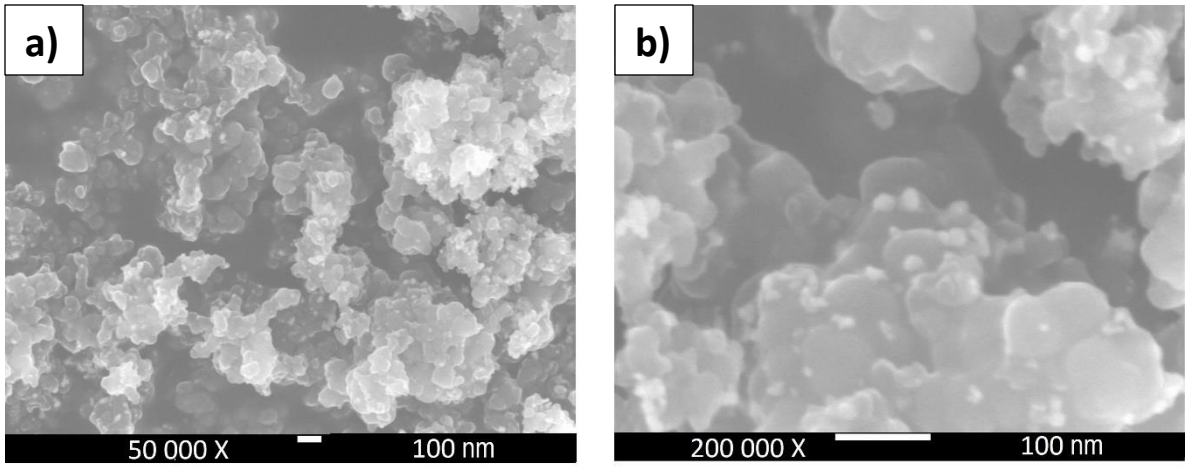


**Figure 5.12** a) and b) high magnification FE-SEM micrographs of $Pd/C_{Cu\text{-}mes}$.

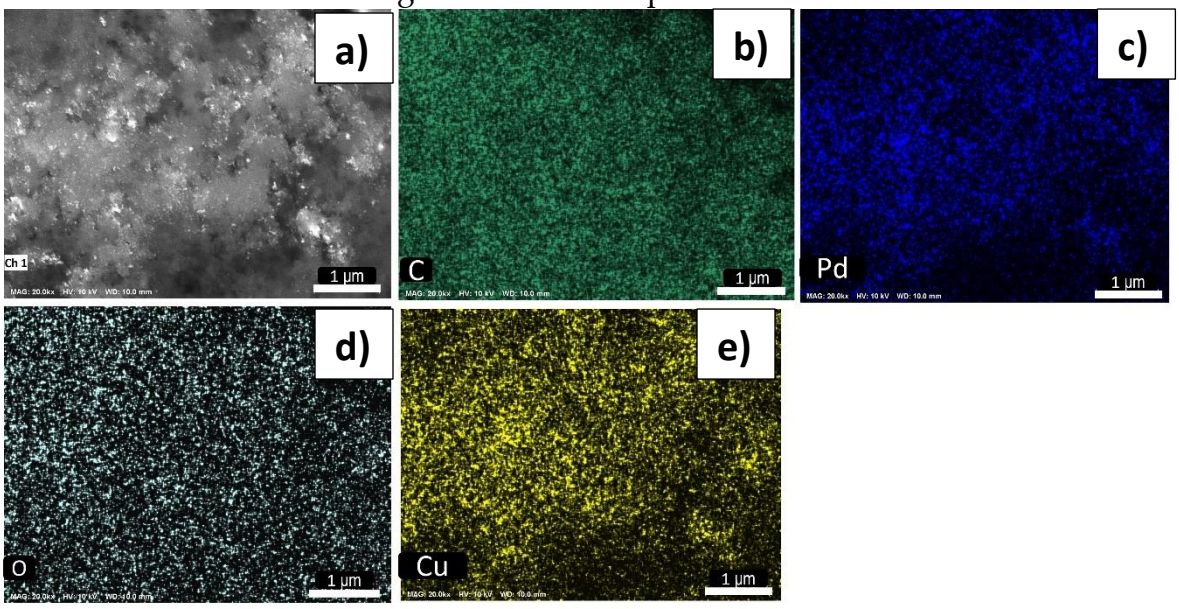


**Figure 5.13** a) FE-SEM imagen and b) C, c) Pd, d) O and e) Cu elemental mapping of Pd/$C_{Cu\text{-}mes}$.

### 5.3.3 Raman

The deconvoluted Raman spectra of Pd/C, Pd/$C_{Cumes}$, and Pd/$C_{Cu(dmpz)L2}$ are shown in Figures 5.14 a), b) and c), respectively. The characteristic D and G bands already described in Figure 5.5 can be observed, as well as the D', D'', and D* interbands. The $I_D/I_G$ ratio of Pd/C is 1.69 (Table 5.8), lower than C without Pd nanoparticles (1.87, Figure 5.5 a) suggesting an effect of the dispersion of Pd nanoparticles on the $sp^2$ domains of the support during the synthesis of the nanocatalyst. Such effect has been discussed previously [44].

The $I_D/I_G$ ratio of Pd/$C_{Cu\text{-}mes}$ increases to 1.92, from 1.75 at $C_{Cu\text{-}mes}$ (Table 5.8). This same effect is observed when comparing Pd/$C_{Cu(dmpz)L2}$ and $C_{Cu(dmpz)L2}$ (Figure 5.5 c), i.e., the ratio increases to 1.80 related to 1.18 for the latter. Some authors have attributed the increase in the $I_D/I_G$ ratio of the carbon support with the addition of Pd nanoparticles to two possible reasons: i) The removal of oxygenated groups generates a reestablishment of the graphitic lattice; producing a higher concentration of $sp^3$ nanodomains; and ii) the nanoparticles can be treated as defects

that induce structural disorder, which is undesirable but plays an important role in the development of catalytic activity [45-48].

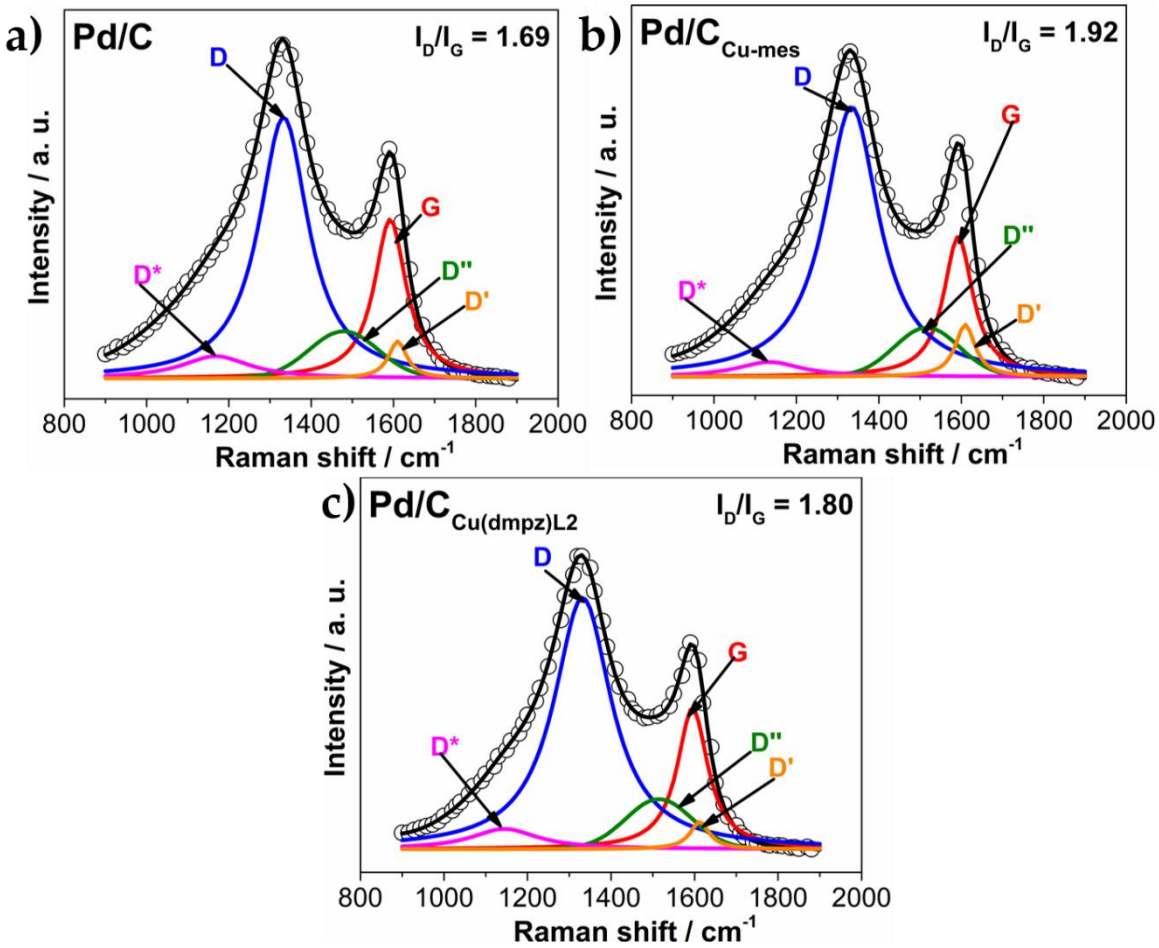


**Figure 5.14** Raman spectra of a) Pd/C, b) Pd/$C_{Cu\text{-}mes}$, and c) Pd/$C_{Cu(dmpz)L2}$.

The relative intensity of D'' is 22.1, 27.2, and 28.4 for Pd/C, Pd/$C_{Cu\text{-}mes}$, and Pd/$C_{Cu(dmpz)L2}$ respectively. As can be seen in Table 5.8, it is higher at Pd/$C_{Cu\text{-}mes}$ and Pd/$C_{Cu(dmpz)L2}$ which suggest a modification on $sp^3$ domains during the synthesis of the nanocatalysts due to the presence of Pd nanoparticles. The $I_{D^*}/I_G$ ratio has been determined as 0.15, 0.11, and 0.13 for Pd/C, Pd/$C_{Cu\text{-}mes}$ and Pd/$C_{Cu(dmpz)L2}$, respectively

(Table 5.8). In this case, the ratio decreases for nanocatalysts supported on functionalized carbon confirming the modification of the $sp^3$ domains.

**Table 5.8** Raman data of Pd/C, $Pd/C_{Cu\text{-}mes}$ and $Pd/C_{Cu(dmpz)L2}$.

| **Nanocatalyst** | **Raman Shift / $cm^{-1}$** | | | | | **$I_D/I_G$** | **$I_{D''}$** | **$I_{D^*}/I_G$** |
|---|---|---|---|---|---|---|---|---|
| | D | G | D′ | D′′ | D* | | | |
| Pd/C | 1330 | 1592 | 1613 | 1485 | 1163 | 1.69 | 22.1 | 0.15 |
| $Pd/C_{Cu\text{-}mes}$ | 1332 | 1597 | 1611 | 1516 | 1130 | 1.92 | 27.2 | 0.11 |
| $Pd/C_{Cu(dmpz)L2}$ | 1332 | 1597 | 1611 | 1508 | 1135 | 1.80 | 28.4 | 0.13 |

### 5.3.4 XPS

The XPS spectra of $Pd/C_{Cu\text{-}mes}$ in Figure 5.15 shows the a) C 1s, b) O 1s, c) Pd 3d and d) Cu 2p regions. The C 1s region has the most intense signal at 284.77 eV assigned to $sp^2$ hybridizations (C=C bonds) with a relative concentration of 77.5 at. % (Table 5.9), followed by the $sp^3$ hybridizations (C-C bonds, BE= 285.73 eV) and the C-O-C species (BE= 288.77 eV). Meanwhile, the O 1s region has been deconvoluted into seven peaks. The signals at 529.94 and 530.82 eV correspond to CuO and $Cu_2O$ bonds, respectively. These species have lower relative concentrations than the other species detected (Table 5.9). However, their detection confirms the presence of Cu species boding with O atoms.

Additionally, the signals assigned to PdO and $PdO_2$ are displayed at 531.72 and 532.52 eV, which confirms the bonding interaction between Pd and O (see their relative concentration in Table 5.9). The other peaks correspond to C=O, C-O, and O-C=O bonds ascribed to the functional groups from support. At the Pd 3d region, four doublets from the spin-orbit splitting into the Pd $3d_{5/2}$ and $Pd_{3/2}$ states confirm the formation of the PdCu phase (BE= 335.0 and 340.26 eV) [49], metallic Pd ($Pd^0$,

BE= 335.54 and 340.71 eV), PdO ($Pd^{2+}$, BE= 336.03 and 341.14 eV), and $PdO_2$ ($Pd^{4+}$, BE= 336.58 and 341.62 eV). The higher relative concentration is that of $Pd^0$ (35.3 at. %), followed by the $Pd^{4+}$, $Pd^{2+}$, and PdCu species (Table 5.9).

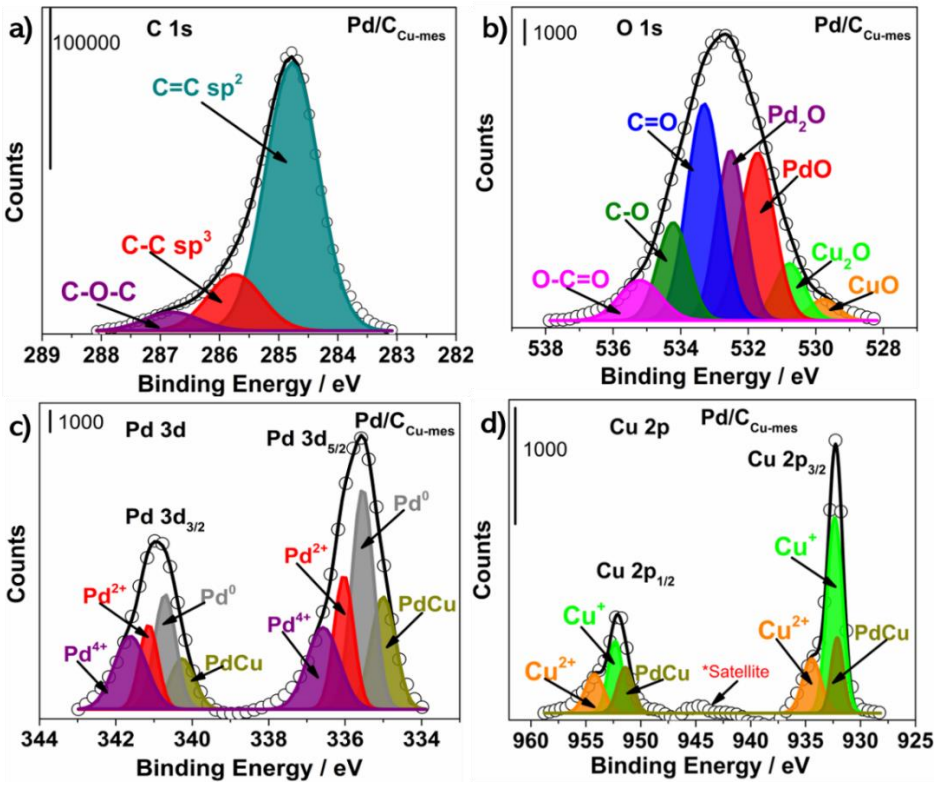


**Figure 5.15** XPS spectra of $Pd/C_{Cu\text{-}mes}$ in the a) C 1s, b) O 1s, c) Pd 3d and d) Cu 2p regions.

It is important to note a shift towards higher BE of the Pd doublets in $Pd/C_{Cu\text{-}mes}$ compared to the Pd/C nanocatalyst (Section 4.1.5, Table 4.2). Specifically, $Pd^0$ in the Pd $3d_{5/2}$ state is centered in 335.54 eV at $Pd/C_{Cu\text{-}mes}$, a shift of 0.4 eV compared to 335.14 eV of the same species at Pd/C. The displacement is attributed to a modification of the d band of Pd due to an electron transfer from Cu to Pd atoms, which indicates the formation of PdCu alloyed phases, as reported elsewhere [50, 51], in good agreement with the observations made from XRD analysis.

The Cu 2p spectra is deconvoluted also into three doublets at the spin-orbit splitting into Cu $2p_{3/2}$ and Cu $2p_{1/2}$. The peaks at around 932.13 and 951.41 eV emerge from PdCu phases, with a relative concentration of 21.8 at. % (Table 5.9). Meanwhile, the doublets at 932.35 and 952.33 eV are due to $Cu^{+}$ species (with the highest relative concentration: 54.9 at. %), and those at 934.45 and 954.22 eV are attributed to $Cu^{2+}$ species (23.3 at %, Table 5.9). In addition, the presence of a satellite peak at BE= 945 eV confirms the formation of Cu oxides as discussed in section 5.2.5.

Figure 5.16 shows the XPS spectra of $Pd/C_{Cu(dmpz)L2}$ in the a) C 1s, b) O 1s, c) Pd 3d and d) Cu 2p regions. In the C 1s region, besides the C=C ($sp^2$ hybridization), C-C ($sp^3$ hybridization), and C-O-C as in the case of $Pd/C_{Cu\text{-}mes}$ (in Figure 5.15 a), the C=O (BE= 287.76 eV), and O-C=O (BE= 289.50 eV) bonds also emerge. This is an evident effect of the different chemical structure of Cu(dmpz)L2 compared to Cu-mes. Meanwhile, the O 1s region displays the peaks corresponding to CuO, $Cu_2O$, PdO, and $Pd_2O$, the latter with the highest relative concentration (25.5 at %, Table 5.8). Additionally, signals ascribed to C=O, C-O, and O-C=O bonds are shown.

The deconvoluted spectra of the Pd 3d region in $Pd/C_{Cu(dmpz)L2}$ display four doublets corresponding to PdCu bonds (BE= 335.23 and 340.70), $Pd^0$ (BE= 335.74 and 341.08 eV), $Pd^{2+}$ (BE= 336.72 and 341.96 eV), and $Pd^{4+}$ (BE= 338.64 and 342.52 eV). $Pd^0$ in the Pd $3d_{5/2}$ state exhibits a shift of 0.6 eV towards higher BE compared to Pd/C (Tables 5.9 and 4.2, respectively). The shift is more important than that shown by $Pd/C_{Cu\text{-}mes}$, indicating stronger interactions tending to form PdCu alloyed phases at $Pd/C_{Cu(dmpz)L2}$, which agrees with the results in Table 5.6. Even more, three doublets are observed in the Cu $2p_{3/2}$ and Cu $2p_{1/2}$ states, due to the $Cu^{+}$, $Cu^{2+}$ and PdCu species. Similar to the previous nanocatalyst, the highest relative concentration is that of $Cu^{+}$ (72.6 at. %, Table 5.9).

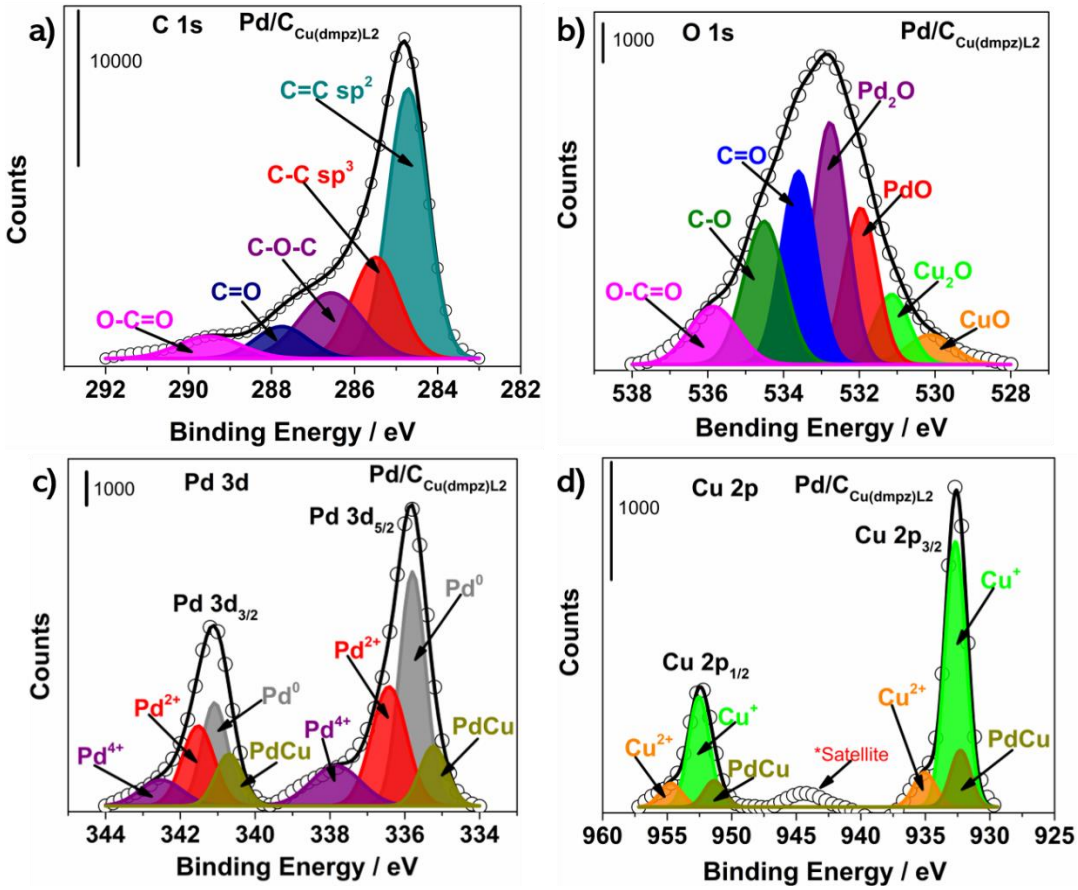


**Figure 5.16** XPS spectra of Pd/$C_{Cu(dmpz)L2}$ in the a) C 1s, b) O 1s, c) Pd 3d and d) Cu 2p regions.

**Table 5.9** XPS parameters of Pd/$C_{Cu\text{-}mes}$ and Pd/$C_{Cu(dmpz)L2}$.

| Nanocatalyst | State | Species | BE / eV | Composition at. % |
|---|---|---|---|---|
| **Pd/$C_{Cu\text{-}mes}$** | Pd $3d_{5/2}$ | PdCu | 335.00 | 13.6 |
| | Pd $3d_{5/2}$ | $Pd^0$ | 335.54 | 23.3 |
| | Pd $3d_{5/2}$ | $Pd^{2+}$ | 336.63 | 12.8 |
| | Pd $3d_{5/2}$ | $Pd^{4+}$ | 338.58 | 13.6 |
| | Pd $3d_{3/2}$ | PdCu | 340.26 | 6.1 |
| | Pd $3d_{3/2}$ | $Pd^0$ | 340.71 | 12.0 |

| | | | | |
|---|---|---|---|---|
| | Pd $3d_{3/2}$ | $Pd^{2+}$ | 341.94 | 7.7 |
| | Pd $3d_{3/2}$ | $Pd^{4+}$ | 341.62 | 11.6 |
| | C 1s | C=C $sp^2$ | 284.77 | 77.5 |
| | C 1s | C-C $sp^3$ | 285.73 | 16.6 |
| | C 1s | C-O-C | 286.77 | 5.9 |
| | O 1s | CuO | 529.94 | 2.4 |
| | O 1s | $Cu_2O$ | 530.82 | 6.8 |
| | O 1s | PdO | 531.73 | 22.7 |
| | O 1s | $Pd_2O$ | 532.52 | 19.6 |
| | O 1s | C=O | 533.30 | 29.5 |
| | O 1s | C-O | 534.23 | 12.0 |
| | O 1s | O-C=O | 535.10 | 6.7 |
| | Cu $2p_{3/2}$ | PdCu | 932.13 | 12.1 |
| | Cu $2p_{3/2}$ | $Cu^{+}$ | 932.35 | 40.9 |
| | Cu $2p_{3/2}$ | $Cu^{2+}$ | 934.45 | 13.5 |
| | Cu $2p_{1/2}$ | PdCu | 951.41 | 9.7 |
| | Cu $2p_{1/2}$ | $Cu^{+}$ | 952.33 | 14.0 |
| | Cu $2p_{1/2}$ | $Cu^{2+}$ | 954.22 | 9.8 |
| **Pd/$C_{Cu(dmpz)L2}$** | Pd $3d_{5/2}$ | PdCu | 335.23 | 7.6 |
| | Pd $3d_{5/2}$ | $Pd^{0}$ | 335.74 | 28.1 |
| | Pd $3d_{5/2}$ | $Pd^{2+}$ | 336.42 | 19.4 |
| | Pd $3d_{5/2}$ | $Pd^{4+}$ | 338.24 | 9.3 |
| | Pd $3d_{3/2}$ | PdCu | 340.70 | 6.5 |
| | Pd $3d_{3/2}$ | $Pd^{0}$ | 341.08 | 12.2 |
| | Pd $3d_{3/2}$ | $Pd^{2+}$ | 341.96 | 11.8 |
| | Pd $3d_{3/2}$ | $Pd^{4+}$ | 342.52 | 5.1 |
| | C 1s | C=C $sp^2$ | 284.71 | 47.0 |
| | C 1s | C-C $sp^3$ | 285.49 | 21.1 |
| | C 1s | C-O-C | 286.57 | 18.2 |
| | C 1s | C=O | 287.76 | 7.5 |
| | C 1s | O-C=O | 289.50 | 6.3 |
| | O 1s | CuO | 530.15 | 4.1 |

| | | | |
|---|---|---|---|
| O 1s | $Cu_2O$ | 531.12 | 7.4 |
| O 1s | PdO | 531.96 | 16.0 |
| O 1s | $Pd_2O$ | 532.77 | 25.5 |
| O 1s | C=O | 533.59 | 20.6 |
| O 1s | C-O | 534.45 | 17.8 |
| O 1s | O-C=O | 535.64 | 8.6 |
| Cu $2p_{3/2}$ | PdCu | 932.28 | 10.6 |
| Cu $2p_{3/2}$ | $Cu^+$ | 932.67 | 51.1 |
| Cu $2p_{3/2}$ | $Cu^{2+}$ | 935.06 | 7.1 |
| Cu $2p_{1/2}$ | PdCu | 951.37 | 4.9 |
| Cu $2p_{1/2}$ | $Cu^+$ | 952.53 | 21.5 |
| Cu $2p_{1/2}$ | $Cu^{2+}$ | 954.71 | 4.8 |

**5.4 Electrochemical characterization of the nanocatalysts**

Figure 5.17 shows the CVs of the nanocatalysts. The characteristic peaks related to Pd-based materials are shown, i.e., the hydrogen adsorption/desorption ($H_{ads/des}$) between 0.05 and 0.40 V/RHE, the double layer region between ~0.50 and 0.60 V/RHE, and the Pd oxides formation/reduction between 0.60 and 1.2 V/RHE. The nanocatalysts supported on functionalized C show a higher j over the potential scanned, particularly a remarkable increase in the peak due to the reduction of Pd oxides, compared to Pd/C. Pd/$C_{Cu\text{-}mes}$ and Pd/$C_{Cu(dmpz)L2}$ show j peaks at 0.65 and 0.90 V/RHE in the anodic scan. The latter also shows a broad shoulder at ca. 0.50 V/RHE. These features are attributed to redox properties of Cu-based sites [52]. Morais et al. [50], suggests that the reactions that occur in the formation of the pre-peak at 0.65 V/RHE are:

$Cu + OH^- = CuOH + e^-$ Reaction 5.1

$2CuOH = Cu_2O + H_2O$ Reaction 5.2

While the peak at ca. 0.9 V/RHE is mainly due to the reactions:

$Cu + 2OH^- = Cu(OH)_2^-$ Reaction 5.3

$Cu(OH)_2 = CuO + H_2O^-$ Reaction 5.4

$Cu_2O$ and CuO as subproducts are insoluble species, probably leading to the passivation of Cu atoms at the surface of the nanocatalyst. The j peaks between 0.8-0.7 V/RHE in the backward scan can be attributed to the reduction of the Pd oxides, as well as to the reprecipitation of Cu from soluble $Cu^+$ and $Cu^{2+}$ species [53, 54].

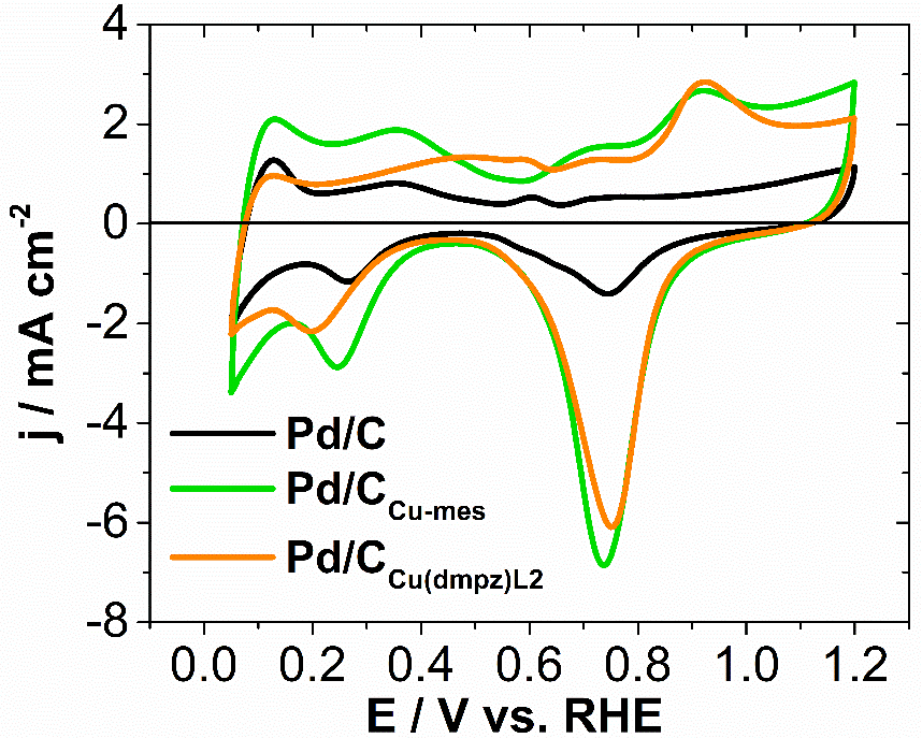


**Figure 5.17** CVs of Pd/C, Pd/$C_{Cu\text{-}mes}$ and Pd/$C_{Cu(dmpz)L2}$. Electrolyte: 0.5 mol $L^{-1}$ KOH. Scan rate: 20 mV $s^{-1}$.

Figure 5.18 shows the CO-stripping curves of the Pd/C, Pd/$C_{Cu\text{-}mes}$ and Pd/$C_{Cu(dmpz)L2}$ nanocatalysts. Pd/C shows a CO oxidation with $E_{onset}$ of 0.70 V/RHE and an oxidation potential ($E_{ox}$) of 0.82 V/RHE (Table 5.10). Meanwhile, the Pd/$C_{Cu\text{-}mes}$ nanocatalyst, has a remarkable shift of both potentials to more negative values ($E_{onset}$ = 0.19 and $E_{ox}$= 0.79 V/RHE) Pd/$C_{Cu(dmpz)L2}$ shows a positive effect, with values of $E_{onset}$ =0.13 and $E_{ox}$= 0.81 V/RHE. It is interesting to observe that Pd/C oxidized CO featuring a single peak, while Pd/$C_{Cu\text{-}mes}$ develops a pre-peak at 0.59, and the already

mentioned peak at 0.79 V/RHE. The j peak at 0.92 V/RHE most likely corresponds to the Cu-species observed in Figure 5.17 and described by Reactions 5.3-5.4. $Pd/C_{Cu(dmpz)L2}$, also shows pre-peak, CO-oxidation peak, and a third peak due to the Cu-species (0.58, 0.81 and 0.90 V/RHE, respectively).

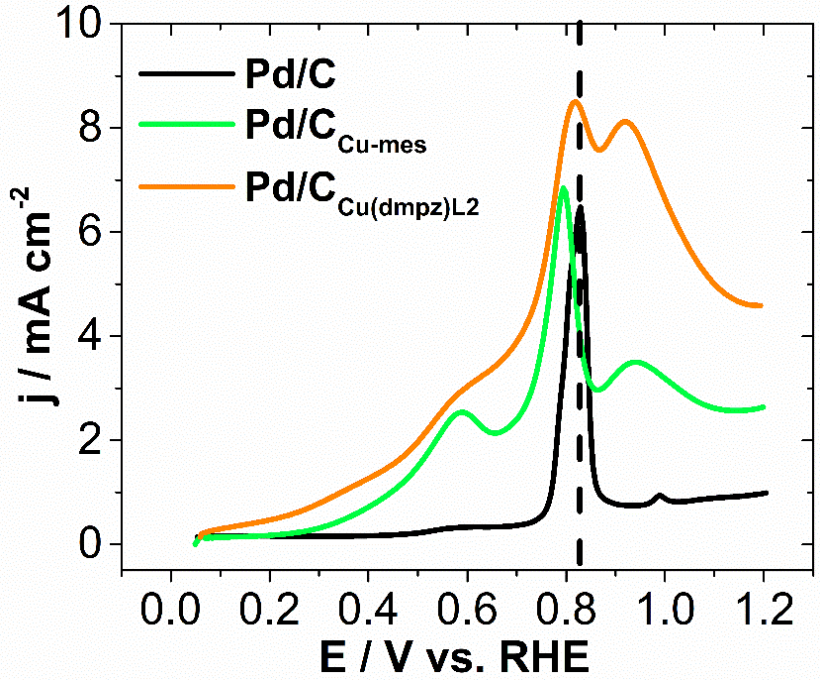


**Figure 5.18** CO-stripping curves at the nanocatalysts. Electrolyte: 0.5 mol $L^{-1}$ KOH. Scan rate: 20 mV $s^{-1}$.

The oxidation of adsorbed CO species ($CO_{ads}$) at negative potentials is promoted by the bifunctional mechanism and the electronic effect. By the former, Cu-atoms form surface $OH^-$ species at more negative potentials which are transported to Pd sites, promoting an easier oxidation of $CO_{ads}$. Moreover, the formation of PdCu alloyed phases leads to a modification of the electronic structure of Pd, weaking the adsorption energy of $CO_{ads}$ species, facilitating their oxidation [55].

The broadness and the presence of multiple CO-stripping peaks at $Pd/C_{Cu\text{-}mes}$ and $Pd/C_{Cu(dmpz)L2}$ is attributed to the oxidation of weakly and strongly $CO_{ads}$ at

different Pd planes. In contrast, Pd/C seems to oxidize only one strongly adsorbed $CO_{ads}$ species at more positive potentials. Another reason of such feature is that the nanocatalysts contain unalloyed Pd (as seen from XPS analysis, Figures 5.15 and 5.16) which provoke the desorption of $CO_{ads}$ at more negative potentials than in the case of Pd/C. In addition, the CO mobility is low in alkaline solution [56, 57].

The Electrochemically Active Surface Area from CO-stripping ($ECSA_{CO}$) has been determined obtained using Equation 3.8 as 69.15 and 48.86 $m^2\ g^{-1}$ for Pd/C and $Pd/C_{Cu\text{-}mes}$, respectively (Table 5.10). These values are similar to those reported in the literature [58]. However, that of $Pd/C_{Cu\text{-}mes}$ value is lower probably due to the presence of Cu which hinders some active sites with high activity for CO oxidation. On the other hand, the synergistic effect between Pd and Cu promote a high catalytic activity in tems of $E_{onset}$ and $E_{ox}$.

**Table 5.10** Electrochemical parameters of the CO-stripping at the nanocatalysts.

| **Nanocatalysts** | $\mathbf{E_{onset}}$ | $\mathbf{E_{ox}}$ | $\mathbf{ECSA_{CO}}$ |
|---|---|---|---|
| | V/RHE | | $m^2\ g^{-1}$ |
| Pd/C | 0.70 | 0.82 | 69.15 |
| $Pd/C_{Cu\text{-}mes}$ | 0.19 | 0.79 | 48.86 |
| $Pd/C_{Cu(dmpz)L2}$ | 0.13 | 0.81 | - |

– Undetermined.

The polarization curves of the EOR at the Pd/C, $Pd/C_{Cu\text{-}mes}$, and $Pd/C_{Cu(dmpz)L2}$ nanocatalysts are shown in Figure 5.19. The nanocatalysts display a typical behavior for the reaction, except for Pd/C which shows two peaks in the backward scan, same that are discussed in detail in section 4.2.2. At the more negative potentials, the ethanol adsorption proceeds on the surface active sites at the nanocatalyst, followed by its dissociation. Such surface reactions hinder the $H_{ads/des}$ region seen in Figure 5.17.

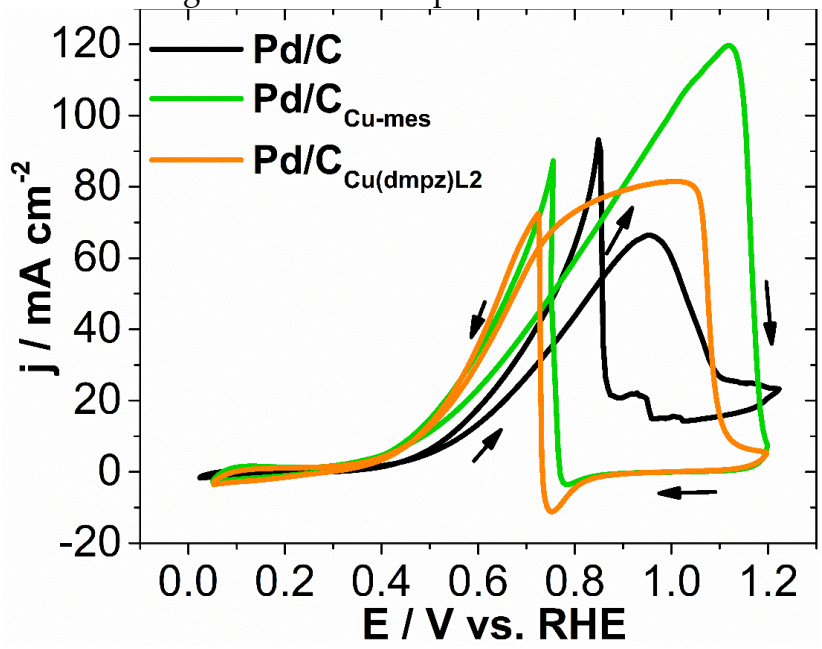


**Figure 5.19** Polarization curves of the EOR at Pd/C, Pd/$C_{Cu\text{-}mes}$ and Pd/$C_{Cu(dmpz)L2}$. Electrolyte: 0.5 KOH mol $L^{-1}$+ 0.5 mol $L^{-1}$ solution EtOH. Scan rate: 20 mV $s^{-1}$.

The Pd/$C_{Cu\text{-}mes}$ and Pd/$C_{Cu(dmpz)L2}$ nanocatalysts promote the reaction at a more negative $E_{onset}$ (0.38 V/RHE) compared to Pd/C (0.41 V/RHE) as seen in Table 5.11 due to a modification of the Pd lattice because of PdCu alloying. Moreover, the peak j is considerable higher at Pd/$C_{Cu\text{-}mes}$ (119.66 mA $cm^{-2}$), 1.47 and 1.80 more intense than those of Pd/$C_{Cu(dmpz)L2}$ and Pd/C, respectively (see also Table 5.11), showing that the electronic effect is very influential at this nanocatalysts by modifying the energy of adsorption of ethanol and intermediates.

Nevertheless, it should be highlighted that Pd/$C_{Cu(dmpz)L2}$ delivers higher j values in the potential ranging from ca. 0.45 to 0.9 V/RHE than Pd/$C_{Cu\text{-}mes}$. The curve at the former is broader, indicating the oxidation of ethanol and intermediate species over a wider, more negative, potential interval. This electrocatalytic behavior shows that the bifunctional mechanism is highly relevant at Pd/$C_{Cu(dmpz)L2}$.

Moreover, ratio between the current density in the forward and backward scan ($j_f/j_b$), is 0.7, 1.3, and 1.10 for Pd/C, Pd/$C_{Cu\text{-}mes}$, and Pd/$C_{Cu(dmpz)L2}$, respectively (Table

5.11). The higher the ratio, it indicates that the nanocatalyst completes to a larger extent the oxidation of ethanol, and that it is more tolerant to carbonaceous species formed during the scan. Evidently, the nanocatalysts supported on carbon functionalized with Cu organometallic compounds have an enhanced performance for the reaction.

Such high catalytic activity can be related to the high $ECSA_{PdO}$ value of $Pd/C_{Cu\text{-}mes}$ (118.72 $m^2\ g^{-1}$ before ADT, Table 5.11), attributed to a large number of active sites participating in the reaction, including those of Cu oxides, as seen in Figure 5.17. The $ECSA_{PdO}$ values have been determined according to the procedure described in Section 3.6.2, Equation 3.4. Unfortunately, due to the lack of chemical composition analysis, the $ECSA_{PdO}$ of $Pd/C_{Cu(dmpz)L2}$ is not show in this work.

**Table 5.11** Electrochemical parameters of the EOR and $ECSA_{PdO}$ values at the nanocatalysts.

| **Nanocatalysts** | $E_{onset}$ (V) | **j** ($mA\ cm^{-2}$) | $j_f/j_b$ | **$ECSA_{PdO}$** ($m^2\ mg^{-1}_{Pd}$) |
|---|---|---|---|---|
| **Before ADT** | | | | |
| Pd/C* | 0.41 | 66.21 | 0.70 | 29.43 |
| $Pd/C_{Cu\text{-}mes}$ | 0.38 | 119.66 | 1.3 | 118.72 |
| $Pd/C_{Cu(dmpz)L2}$ | 0.38 | 81.25 | 1.1 | - |
| **After ADT** | | | | |
| Pd/C* | 0.41 | 75.53 | 0.93 | 15.05 |
| $Pd/C_{Cu\text{-}mes}$ | 0.38 | 107.14 | 1.5 | 63.95 |
| $Pd/C_{Cu(dmpz)L2}$ | 0.38 | 88.31 | 1.1 | - |

– Undetermined.

*Values presented in the section 4.2.2.

The improvement in catalytic activity for the EOR of $Pd/C_{Cu\text{-}mes}$ and $Pd/C_{Cu(dmpz)L2}$ in terms of $E_{onset}$ and the shift toward more negative potentials of the polarization curves, compared to Pd/C, can be ascribed to an easier removal of $CO_{ads}$ (as seen in Figure 5.18) due to the bifunctional mechanism, according to the following reactions:

$$Pd + CH_3CH_2OH \rightarrow Pd(CO)_{ads} + CH_2^- + 4H^+ + 4e^- \quad \text{Reaction 5.5}$$

$$Cu + H_2O \rightarrow Cu(OH^-)_{ads} + H^+ + e^- \quad \text{Reaction 5.6}$$

$$PdCO_{ads} + Cu(OH^-)_{ads} \rightarrow CO_2 + Pd + Cu + H^+ + e^- \quad \text{Reaction 5.7}$$

The Cu atoms adsorb/desorb OH- species at more negative potentials that Pd (Reaction 5.6), catalyzing the oxidation of $CO_{ads}$ to $CO_2$ as can be seen in Reaction 5.7.

Moreover, their improved j and $j_f/j_b$ ratio is related to a modification of the electronic structure of Pd (electronic effect) because of the formation of PdCu alloyed phases. As a result, the adsorption energy of species such as ethanol and/or intermediates becomes weaker, facilitating bonds cleavages and thus promoting the generation of higher j values [59, 60].

According to Norskov, there is a strong correlation between the d-band center of a catalyst and the adsorption energy of reaction intermediates, which is critical for its catalytic activity and electrochemical stability [41, 61, 62]. Therefore, the downshift of the d-band center of Pd (as inferred from the BE of $Pd^0$ in XPS analysis, Table 5.8) enhances the catalytic activity of $Pd/C_{Cu\text{-}mes}$ and $Pd/C_{Cu(dmpz)L2}$, leading to the generation of higher j values.

Figure 5.20 shows a) CVs and b) polarization curves of the EOR before and after ADT of $Pd/C_{Cu\text{-}mes.}$ Although the shape of CV remains almost unchanged, it is remarkable to note the decrease of j over the potential scanned. Before ADT, $Pd/C_{Cu\text{-}mes}$ has an ECSA of 118.72 $m^2\ g^{-1}$ (Table 5.11) which is higher than those reported in the literature [61, 63, 64]. After submitting it to ADT, the intensity of the peak due to

the reduction of Pd oxides decreases, as it slightly shifts towards more positive potentials. The $ECSA_{PdO}$ after ADT is determined as 63.95 $m^2\ g^{-1}$, i.e., a 46.14 % of retention. During the test, $Pd/C_{Cu\text{-}mes}$ may undergo changes in morphology and surface chemistry because of different degradation mechanisms. For instance, the dissolution of nanoparticles can occur. Also, the migration of Pd atoms is not unusual, resulting in the aggregation of nanoparticles that generates agglomerates, thus provoking $ECSA_{PdO}$ losses [65, 66].

Comparing the polarization curves of the EOR at $Pd/C_{Cu\text{-}mes}$ before and after ADT, it can be seen that the nanocatalyst show a slight decrease in peak j of ca. 10 %, despite the relatively large $ECSA_{PdO}$ losses (Table 5.11). These results suggest that most of the Pd and PdCu sites remain active to promote the reaction. The concentration of Pd active sites correlates with the results obtained by XPS in which a higher concentration of $Pd^0$ (35.5 at. %) is obtained compared to Pd oxides. Therefore, it can be considered as an electrochemically stable anode. Moreover, the $j_f/j_b$ ratio of the nanocatalyst after ADT is 1.5, slightly higher than that before (Table 5.11), indicating that its capacity to oxidize ethanol molecules and its tolerance to carbonaceous species is maintained.

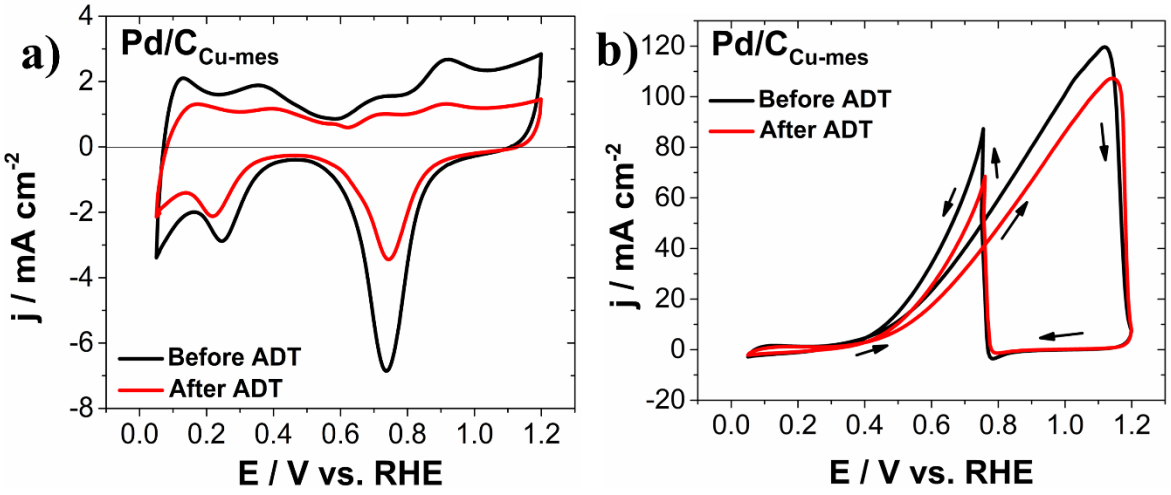


**Figure 5.20** a) CVs and b) polarization curves of EOR before and after of ADT of $Pd/C_{Cu\text{-}mes}$. Electrolyte: $N_2$-saturade 0.5 mol $L^{-1}$ KOH and 0.5 mol $L^{-1}$ KOH + 0.5 mol $L^{-1}$ EtOH solution. Scan rate: 20 mV $s^{-1}$.

Figure 5.21 a) presents the CVs before and after ADT of Pd/$C_{Cu(dmpz)L2}$. The same degradation mechanisms as described in the previous case may have caused the notable decrease in j, clearly observed in the Pd-oxides reduction peak at this nanocatalyst.

Figure 5.21 b) shows the polarization curves of EOR on Pd/$C_{Cu(dmpz)L2}$. In this case, there is a change in the shape of the curve after ADT, becoming a relatively narrow peak. In contrast to Pd/$C_{Cu\text{-}mes}$, Pd/$C_{Cu(dmpz)L2}$ shows a slight increase in j maximum by ~8 % (Table 5.11), suggesting that after ADT some sites, likely Pd-oxides that promote the oxidation of organic molecules, become activated[67] correlated with the results obtained by XPS in which a percentage of 31.2 and 14.4 at. % (PdO and $Pd_2O$, respectively) obtained. However, it is to be acknowledged that the potential window at which species are oxidized is more limited after the test, probably because some other site (especially those that catalyzed the reaction at more negative potentials) are deactivated or degraded. The j peak of Pd/$C_{Cu(dmpz)L2}$ is lower than that of Pd/$C_{Cu\text{-}mes}$ after ADT, but the maximum is at a more negative potential, which reinforces the observation that the bifunctional mechanism is more relevant at the former that the electronic effect. The $j_f/j_b$ ratio is 1.1, which is the same as before ADT (Table 5.11).

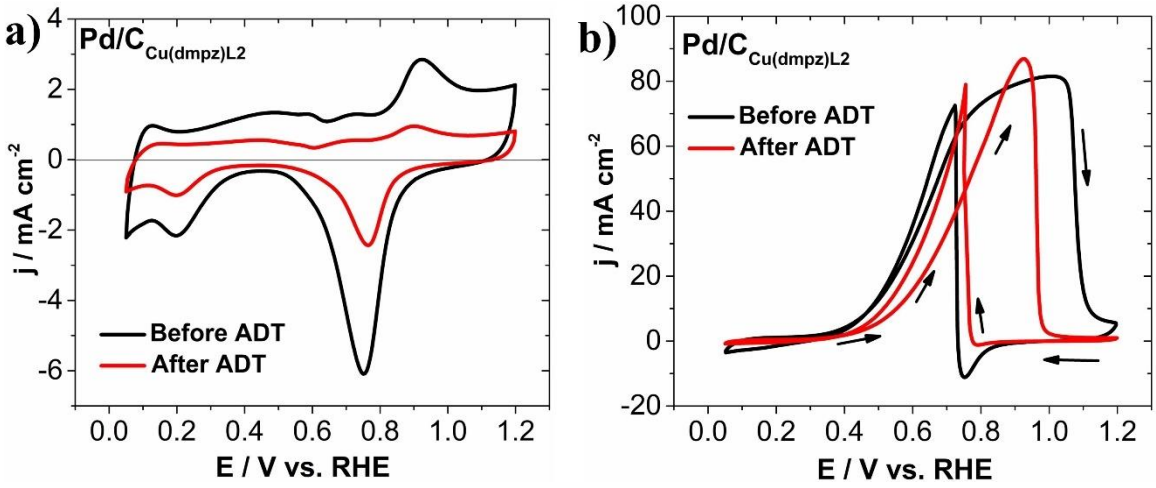


**Figure 5.21** a) CVs and b) polarization curves before and after of ADT of $Pd/C_{Cu(dmpz)L2}$. Electrolyte: $N_2$-saturade 0.5 mol $L^{-1}$ KOH. Scan rate: 20 mV $s^{-1}$.

Table 5.12 shows a comparison of electrochemical parameters of $Pd/C_{Cu\text{-}mes}$ and $Pd/C_{Cu(dmpz)L2}$ with some Pd and Cu-containing nanocatalyst from the literature. As can be seen, the $ECSA_{PdO}$ of $Pd/C_{Cu\text{-}mes}$ is significantly higher. Regarding the EOR, the $E_{onset}$ values of the nanocatalysts supported on Vulcan functionalized with Cu organometallic compounds are among those more negative. As for the j peak, $Pd/C_{Cu\text{-}mes}$ delivers the second highest compared to those reported by other Laboratories, only below that of references [66].

**Table 5.12** Electrochemical parameters of the EOR at Pd-based nanocatalysts.

| Nanocatalyst | $ECSA_{PdO}$ ($m^2\ g^{-1}$) | $E_{onset}$ V/RHE | j ($mA\ cm^{-2}$) | Electrolyte | Ref. |
|---|---|---|---|---|---|
| PdCu/C-DA15 | 97.5 | 0.36 | 108.6 | 1 mol $L^{-1}$ NaOH+ 1 mol $L^{-1}$ EtOH | [61] |
| Pd-Cu/C | 43.45 | 0.46 | 111.25 | 1 mol $L^{-1}$ KOH+ 1mol $L^{-1}$ EtOH | [63] |

| | | | | | |
|---|---|---|---|---|---|
| Pd-NiO/MWCNT/rGO | 42.05 | 0.44 | 90.89 | 1 mol $L^{-1}$ KOH+ 1mol $L^{-1}$ EtOH | [64] |
| Pd/Ni/MOFDC | 25.77 | 0.39 | 30.4 | 0.5 mol $L^{-1}$ KOH +0.5 mol $L^{-1}$EtOH | [68] |
| $PdAu_3/C$ | - | 0.56 | 54.56 | 1 mol $L^{-1}$ KOH+ 1 mol $L^{-1}$ EtOH | [69] |
| Pt/PdCu | - | 0.46 | 183 | 1 mol $L^{-1}$ KOH+ 1 mol $L^{-1}$ EtOH | [66] |
| $Pd/C_{Cu\text{-}mes}$ | **118.72** | **0.38** | **119.66** | 0.5 mol $L^{-1}$ KOH +0.5 mol $L^{-1}$EtOH | **This work** |
| $Pd/C_{Cu(dmpz)L2}$ | **-** | **0.38** | **81.25** | | |

In order to identify the products of the ethanol oxidation at the nanocatalysts, electrolysis test at 0.8 V/RHE have been performed. The percentage of ethanol consumed is 47, 61, and 59 % for Pd/C, $Pd/C_{Cu\text{-}mes}$, and $Pd/C_{Cu(dmpz)L2}$, respectively as shown in Figure 5.22. In addition, from these values and using the ex-situ HPLC technique, it has been determined that subproducts during the reaction.

Acetaldehyde ($CH_3CHO$) and acetic acid or acetate ion ($C_2H_3O_2^-$) are the main reaction compounds often obtained $CO_2$ (or carbonate $CO_3^{-2}$) is obtained under traces state. In this case, the main product of the reaction at the nanocatalysts is the acetate ion ($C_2H_3O_2^-$) Table 5.13. Considering only the reaction product detected by HPLC analysis, a general mechanism for the conversion of ethanol to $C_2H_3O_2^-$ on nanocatalysts can be proposed according to the following reaction 5.8:

$$CH_3\text{-}CH_2OH + 5HO^- \xrightarrow[Pd/C_{Cu(dmpz)L2}]{Pd/C_{Cu\text{-}mes}} C_2H_3O_2^- + 4H_2O + 4e^-$$

Reaction 5.8

$CH_3CHO$ and $CO_3^{-2}$ have not been detected. In the case of acetaldehyde, it has been reported that it reacts to produce the acetate ion through a nucleophilic attack by OH [70]. As future work, the use of an in-situ technique such as infrared spectroscopy is proposed to determine the production of intermediates such as acetaldehyde and carbonate.

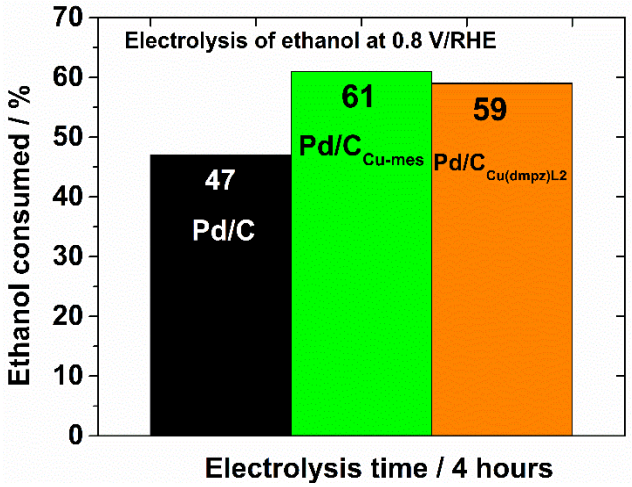


**Figure 5.22** Ethanol consumed during 4 h at the nanocatalysts. Polarization potential: 0.8 V/RHE.

**Table 5.13** Percentage of acetate formed during electrolysis of ethanol at 0.8 V/RHE on the nanocatalysts.

| Nanocatalyst | Acetate ion produced / % |
|---|---|
| Pd/C | 30 |
| $Pd/C_{Cu\text{-}mes}$ | 47 |
| $Pd/C_{Cu(dmpz)L2}$ | 32 |

As indicated in the Experimental section (Chapter 3, Figures 3.7 and 3.8), the configuration chosen for the tests in the AEM-DEFC is that if the same nanocatalysts at the anode and cathode of each membrane-electrodes assembly (MEA). Figure 5.23 shows the individual polarization curves of Pd/C, $Pd/C_{Cu\text{-}mes}$, and $Pd/C_{Cu(dmpz)L2}$ showing the behavior of a) the anode potential ($E_a$) and b) the cathode potential ($E_c$) in fuel cell configuration (i.e., the plots show the potential difference between anode and cathode, and the reference electrode, as each fuel cell is polarized over a given j window).

$Pd/C_{Cu\text{-}mes}$ shows an enhanced performance as anode, with an open circuit potential (OCP) of 0.42 V/RHE, a value 0.13 and 0.26 V lower than Pd/C and

$Pd/C_{Cu(dmpz)L2}$, respectively. Therefore, the overpotential of the EOR at $Pd/C_{Cu\text{-}mes}$ is significantly smaller than that of the other nanocatalysts, while its high performance is sustained over the whole polarization curve. Opposite to that, $Pd/C_{Cu(dmpz)L2}$ shows the poorest performance among the three nanocatalysts.

$Pd/C_{Cu\text{-}mes}$ also shows a better performance in the polarization curve as cathode, with an OCP of 1.00 V/RHE, followed by 0.99 and 0.98 V/RHE of $Pd/C_{Cu(dmpz)L2}$ and Pd/C, respectively. This means that the overpotential of the ORR at $Pd/C_{Cu\text{-}mes}$ over the scan is clearly lower compared to the other nanocatalysts. Moreover, $Pd/C_{Cu\text{-}mes}$ has a more stable behavior, having a less significant potential drop as j increases.

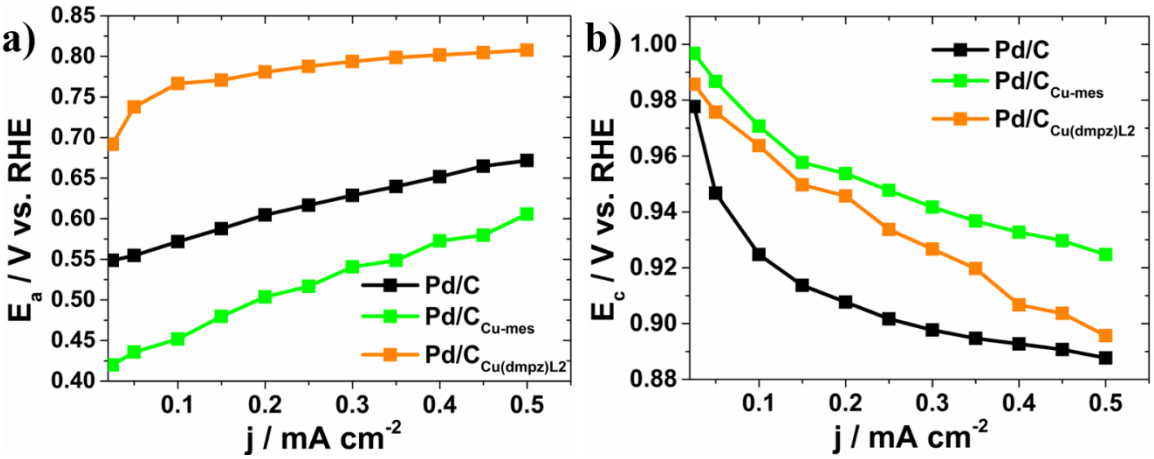


**Figure 5.23** Individual polarization curves of the nanocatalysts showing the behavior of a) the anode potential, $E_a$, and b) the cathode potential, $E_c$.

The cell voltage ($E_{cell}$) vs j polarization curves of the AEM-DAFC separately equipped with the nanocatalysts as anodes and cathodes are shown in Figure 5.24 a). $Pd/C_{Cu\text{-}mes}$ at both electrodes generates the highest open circuit voltage (OCV), with a value of 0.60 V, followed by Pd/C (OCV= 0.50 V) and $Pd/C_{Cu(dmpz)L2}$ (OCV = 0.38 V), as seen in Table 5.14. It is to be highlighted that the $E_{cell}$ values of the AEM-DEFC having $Pd/C_{Cu\text{-}mes}$ is significantly higher compared to the other nanocatalysts at each j. For example, $E_{cell}$ at 0.25 mA cm$^{-2}$ is 0.43 with this nanocatalysts compared

to 0.27 and 0.15 V/RHE with Pd/C and Pd/$C_{Cu(dmpz)L2}$, respectively as can see in Table 5.14. This outcome is a result of the high performance of Pd/$C_{Cu\text{-}mes}$ as anode and cathode (Figure 5.22). Even more, Pd/$C_{Cu(dmpz)L2}$ shows a lower performance than Pd/C in the AEM-DEFC, a behavior ascribed to its poor catalytic activity as anode, as discussed in Figure 5.21 a).

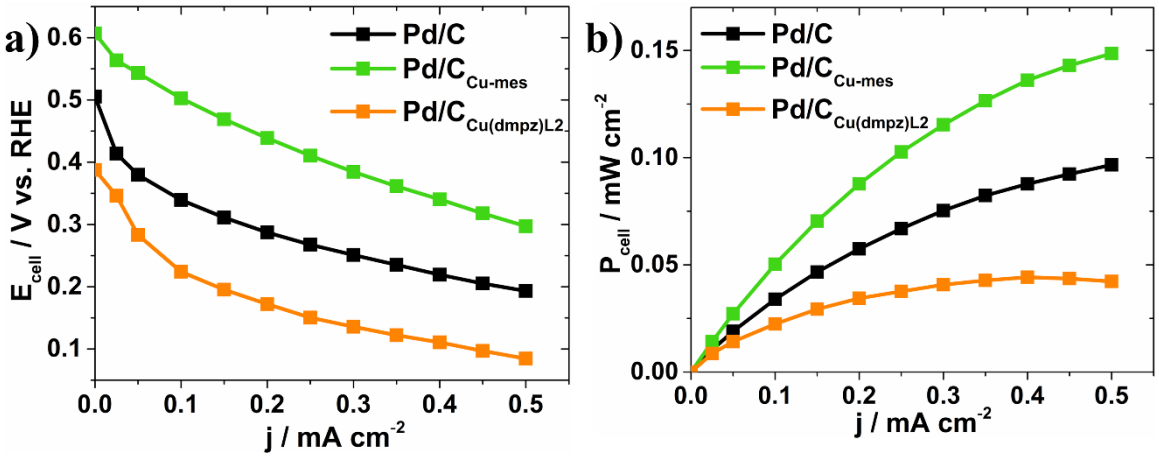


**Figure 5.24** a) Polarization curves and b) power density curves of the AEM-DEFC equipped with the nanocatalysts as anodes and cathodes. Fuel: 0.5 mol $L^{-1}$ EtOH + 0.5 mol $L^{-1}$ KOH. AEM: Fumatech® FAA. Feed at the cathode: $O_2$ + 0.5 mol $L^{-1}$ KOH.

The maximum cell power density ($P_{cell}$) from the AEM-DEFC is 14.85 mW $cm^{-2}$ (Table 5.14) generated when Pd/$C_{Cu\text{-}mes}$ is used as anode and cathode, as can be seen in Figure 5.24 b). In view of the performance of the AEM-DEFC, Pd/$C_{Cu\text{-}mes}$ is a high-performance nanocatalyst with application as anode and cathode in alkaline environment.

**Table 5.14** OCV and $P_{cell}$ values of Pd/C, Pd/$C_{Cu\text{-}mes}$ and Pd/$C_{Cu(dmpz)L2}$.

| Nanocatalyst | OCV (V) | $E_{cell}$ at 0.25 mA $cm^{-2}$ (V/RHE) | $P_{cell}$ (mW $cm^{-2}$) |
|---|---|---|---|
| **Pd/C** | 0.50 | 0.27 | 9.66 |
| **Pd/$C_{Cu\text{-}mes}$** | 0.60 | 0.43 | 14.85 |
| **Pd/$C_{Cu(dmpz)L2}$** | 0.38 | 0.15 | 4.22 |

Table 5.15 depicts a comparison of OCV and $P_{cell}$ of Pd/$C_{Cu\text{-}mes}$ with Pd-based nanocatalysts reported in the literature. The nanocatalysts developed in this work shows lower OCV but compares favorably in $P_{cell}$ with a lower ethanol concentration fed at the anode.

**Table 5.15** OCV and $P_{cell}$ at Pd-based nanocatalysts.

| Nanocatalyst | OCV (V) | $P_{cell}$ (mW $cm^{-2}$) | Electrolyte | Ref |
|---|---|---|---|---|
| Pd/C | 0.82 | 25 | 2 M EtOH in 2 M KOH | [71] |
| Pd/C | 0.79 | 5.2 | 1 M EtOH in 1 M KOH | [72] |
| PdNiSn/$C_f$ | 0.85 | 38.8 | 2 M EtOH in 6 M KOH | [73] |
| Pd/$C_{Cu\text{-}mes}$ | **0.60** | **14.85** | 0.5 M EtOH in 0.5 M KOH | **This work** |

## 5.5 Conclusions

The functionalization of Vulcan with Cu-mes and Cu(dmpz)L2 was successfully achieved, promoting the formation of oxygenated functional groups and Cu sites on its surface. The functionalization promotes a constructive

rehybridization that increases the $sp^2$ nanodomains at Vulcan, which allows for a better anchorage of nanoparticles.

The presence of Cu atoms from the functionalization promoted the formation of PdCu alloyed phases, increasing the catalytic activity of Pd/$C_{Cu\text{-}mes}$ and Pd/$C_{Cu(dmpz)L2}$ for the EOR in terms of $E_{onset}$, j, $j_f/j_b$ and electrochemical stability due to a combination of bifunctional mechanism and electronic effect.

Pd/$C_{Cu\text{-}mes}$ showed the best performance compared to Pd/C and Pd/$C_{Cu(dmpz)L2}$ in terms of ethanol consumption and production of acetate ion. It also outperforms the other nanocatalysts when evaluated in $E_a$ and $E_C$ polarization curves. In a complete AEM-DEFC, Pd/$C_{Cu\text{-}mes}$ generated the highest OCV and $P_{cell}$ values, demonstrating that the functionalization of Vulcan with Cu-mes generates surface active sites that catalyze the EOR (and the ORR) in the alkaline environment. The results presented in this work showed that Pd/$C_{Cu\text{-}mes}$ can be used as high-performance anode (and cathode) in AEM-DEFC devices.

## 5.6 References

[1] A. Baici, A. Camus, G. Pellizer. $^1$H NMR spectra of arylcopper(I) compounds. J. Organomet. Chem. 26 (1971) 431-437.
[2] M. Stollenz, F. Meyer. Mesitylcopper – A powerful tool in synthetic chemistry. Organometallics. 31 (2012) 7708-7727.
[3] H. Eriksson, M. Håkansson. Mesitylcopper: Tetrameric and pentameric. organometallics. Organometallics. 16 (1997) 4243-4244.
[4] T. Tsuda, T. Yazawa, K. Watanabe, T. Fujii, T. Saegusa. Preparation of thermally stable and soluble mesitylcopper(I) and its application in organic synthesis. J. Org. Chem. 46 (1981) 192-194.
[5] N.R. Babij, E.O. McCusker, G.T. Whiteker, B. Canturk, N. Choy, L.C. Creemer, C.V.D. Amicis, N.M. Hewlett, P.L. Johnson, J.A. Knobelsdorf, F. Li, B.A. Lorsbach, B.M. Nugent, S.J. Ryan, M.R. Smith, Q. Yang. NMR Chemical shifts of trace impurities: industrially preferred solvents used in process and green chemistry. Org. Process Res. Dev. 20 (2016) 661-667.

[6] A.S. Ethiraj, D.J. Kang. Synthesis and characterization of CuO nanowires by a simple wet chemical method. Nanoscale Res. Lett. 7 (2012) 70.
[7] Z.N. Kayani, M. Umer, S. Riaz, S. Naseem. Characterization of copper oxide nanoparticles fabricated by the sol–gel method. J. Electron. Mater. 44 (2015) 3704-3709.
[8] S.-W. Jin, X.-H. Ye, L. Jin, L. Zheng, J.-W. Li, B.-P. Jin, D.-Q. Wang. Syntheses and structural characterization of nine coordination compounds assembled from copper acetate, 3,5-dimethylpyrazole and carboxylates. Polyhedron. 81 (2014) 382-395.
[9] I. Abidat, C. Morais, S. Pronier, N. Guignard, J.D. Comparot, C. Canaff, T.W. Napporn, A. Habrioux, A.S. Mamede, J.F. Lamonier, K.B. Kokoh. Effect of gradual reduction of graphene oxide on the CO tolerance of supported platinum nanoparticles. Carbon. 111 (2017) 849-858.
[10] C.K. Poh, S.H. Lim, H. Pan, J. Lin, J.Y. Lee. Citric acid functionalized carbon materials for fuel cell applications. J. Power Sources. 176 (2008) 70-75.
[11] S. Yin, P.K. Shen, S. Song, S.P. Jiang. Functionalization of carbon nanotubes by an effective intermittent microwave heating-assisted $HF/H_2O_2$ treatment for electrocatalyst support of fuel cells. Electrochim. Acta. 54 (2009) 6954-6958.
[12] N. Lakshmi, N. Rajalakshmi, K.S. Dhathathreyan. Functionalization of various carbons for proton exchange membrane fuel cell electrodes: analysis and characterization. J. Phys. D: Appl. Phys. 39 (2006) 2785-2790.
[13] V.V. Thekkae Padil, M. Černík. Green synthesis of copper oxide nanoparticles using gum karaya as a biotemplate and their antibacterial application. Int J Nanomedicine. 8 (2013) 889-898.
[14] Y. Sun, P. Cheng, S. Yan, Z. Jiang, D. Liao, P. Shen. Synthesis, crystal structure and properties of novel zinc(ii) and cobalt(ii) chain complexes with 3,5-dimethylpyrazole and thiocyanate. J. Coord. Chem. 55 (2002) 363-372.
[15] I.L. Alonso-Lemus, M.Z. Figueroa-Torres, D. Lardizabal-Gutíerrez, P. Bartolo-Pérez, J.C. Carrillo-Rodríguez, F.J. Rodríguez-Varela. Converting chicken manure into highly active N–P co-doped metal-free biocarbon electrocatalysts: effect of chemical treatment on their catalytic activity for the ORR. Sustain. Energy Fuels. 3 (2019) 1307-1316.

[16] J.C. Martínez-Loyola, I.L. Alonso-Lemus, M.E. Sánchez-Castro, B. Escobar-Morales, J.R. Torres-Lubián, F.J. Rodríguez-Varela. Surface Functionalization of ordered mesoporous hollow carbon spheres with Ru organometallic compounds as supports of low-Pt content nanocatalysts for alkaline hydrogen and oxygen evolution reactions. MRS Advances. 5 (2020) 2973-2989.
[17] A.A. Siller-Ceniceros, M.E. Sánchez-Castro, D. Morales-Acosta, J.R. Torres-Lubian, E. Martínez G, F.J. Rodríguez-Varela. Innovative functionalization of Vulcan XC-72 with Ru organometallic complex: Significant enhancement in catalytic activity of Pt/C electrocatalyst for the methanol oxidation reaction (MOR). Appl. Catal. B: Environ. 209 (2017) 455-467.
[18] J.C. Martínez-Loyola, A.A. Siller-Ceniceros, M.E. Sánchez-Castro, M. Sánchez, J.R. Torres-Lubián, B. Escobar-Morales, C. Ornelas, I.L. Alonso-Lemus, F.J. Rodríguez-Varela. High performance Pt nanocatalysts for the oxidation of methanol and ethanol in acid media by effect of functionalizing carbon supports with Ru organometallic compounds. J. Electrochem. Soc. 167 (2020) 164502.
[19] J.C. Carrillo-Rodríguez, A.M. Garay-Tapia, B. Escobar-Morales, J. Escorcia-García, M.T. Ochoa-Lara, F.J. Rodríguez-Varela, I.L. Alonso-Lemus. Insight into the performance and stability of N-doped ordered mesoporous carbon hollow spheres for the ORR: Influence of the nitrogen species on their catalytic activity after ADT. Int. J. Hydrogen Energy. 46 (2021) 26087-26100.
[20] S. Claramunt, A. Varea, D. López-Díaz, M.M. Velázquez, A. Cornet, A. Cirera. The importance of interbands on the interpretation of the raman spectrum of graphene oxide. J. Phys. Chem. C. 119 (2015) 10123-10129.
[21] P.A. Goodman, H. Li, Y. Gao, Y.F. Lu, J.D. Stenger-Smith, J. Redepenning. Preparation and characterization of high surface area, high porosity carbon monoliths from pyrolyzed bovine bone and their performance as supercapacitor electrodes. Carbon. 55 (2013) 291-298.
[22] O. Beyssac, B. Goffé, J.-P. Petitet, E. Froigneux, M. Moreau, J.-N. Rouzaud. On the characterization of disordered and heterogeneous carbonaceous materials by Raman spectroscopy. Spectrochim. Acta A Mol Biomol. Spectrosc. 59 (2003) 2267-2276.

[23] S.L.H. Rebelo, A. Guedes, M.E. Szefczyk, A.M. Pereira, J.P. Araújo, C. Freire. Progress in the Raman spectra analysis of covalently functionalized multiwalled carbon nanotubes: unraveling disorder in graphitic materials. PCCP. 18 (2016) 12784-12796.
[24] Y.J. Ma, H. Wang, S. Ji, J. Goh, H.Q. Feng, R.F. Wang. Highly active Vulcan carbon composite for oxygen reduction reaction in alkaline medium. Electrochim. Acta. 133 (2014) 391-398.
[25] N. Nasihat Sheno, A. Morsali. Synthesis of different copper oxide nano-structures from direct thermal decomposition of porous copper(ιι) metal-organic framework precursors. J. Nanosci. Nanotechnol. 8 (2012) 99-104.
[26] Z.-Q. Zhang, J. Huang, L. Zhang, M. Sun, Y.-C. Wang, Y. Lin, J. Zeng. Facile synthesis of Cu-Pd bimetallic multipods for application in cyclohexane oxidation. Nanotechnology. 25 (2014) 435602.
[27] S. García-Mayagoitia, F. Fernández-Luqueño, D. Morales-Acosta, J.C. Carrillo-Rodríguez, M.A. García-Lobato, L. de la Torre-Saenz, I.L. Alonso-Lemus, F.J. Rodríguez-Varela. Energy generation from pharmaceutical residual water in microbial fuel cells using ordered mesoporous carbon and bacillus subtilis as bioanode. ACS Sustain. Chem. Eng. 7 (2019) 12179-12187.
[28] Y. Wang, Y. Lü, W. Zhan, Z. Xie, Q. Kuang, L. Zheng. Synthesis of porous $Cu_2O$/CuO cages using Cu-based metal–organic frameworks as templates and their gas-sensing properties. J. Mater. Chem. A. 3 (2015) 12796-12803.
[29] A. Moraes, M.H.M.T. Assumpção, F.C. Simões, V.S. Antonin, M.R.V. Lanza, P. Hammer, M.C. Santos. Surface and catalytical effects on treated carbon materials for hydrogen peroxide electrogeneration. Electrocatalysis. 7 (2016) 60-69.
[30] D. Gao, J. Zhang, J. Zhu, J. Qi, Z. Zhang, W. Sui, H. Shi, D. Xue, in: Nanoscale research letters, 2010, pp. 769-772.
[31] J. Maya-Cornejo, R. Carrera-Cerritos, D. Sebastián, J. Ledesma-García, L.G. Arriaga, A.S. Aricò, V. Baglio. PtCu catalyst for the electro-oxidation of ethanol in an alkaline direct alcohol fuel cell. Int. J. Hydrogen Energy. 42 (2017) 27919-27928.
[32] X. Du, S. Luo, H. Du, M. Tang, X. Huang, P.K. Shen. Monodisperse and self-assembled Pt-Cu nanoparticles as an efficient electrocatalyst for the methanol oxidation reaction. J. Mater. Chem. A. 4 (2016) 1579-1585.

[33] S.M. Senthil Kumar, J. Soler Herrero, S. Irusta, K. Scott. The effect of pretreatment of Vulcan XC-72R carbon on morphology and electrochemical oxygen reduction kinetics of supported Pd nano-particle in acidic electrolyte. J. Electroanal. Chem. 647 (2010) 211-221.
[34] J.R. Salem, F.O. Sequeda, J. Duran, W.Y. Lee, R.M. Yang. Solventless polyimide films by vapor deposition. J. Vac. Sci. Technol. A. 4 (1986) 369-374.
[35] P. Jiang, D. Prendergast, F. Borondics, S. Porsgaard, L. Giovanetti, E. Pach, J. Newberg, H. Bluhm, F. Besenbacher, M. Salmeron. Experimental and theoretical investigation of the electronic structure of $Cu_2O$ and CuO thin films on Cu(110) using X-ray photoelectron and absorption spectroscopy. J. Chem. Phys. 138 (2013) 024704.
[36] M. Shao, K. Shoemaker, A. Peles, K. Kaneko, L. Protsailo. Pt monolayer on porous Pd−Cu alloys as oxygen reduction Electrocatalysts. J. Am. Chem. Soc. 132 (2010) 9253-9255.
[37] D.J. You, S.-a. Jin, K.H. Lee, C. Pak, K.H. Choi, H. Chang. Improvement of activity for oxygen reduction reaction by decoration of Ir on PdCu/C catalyst. Catal. Today. 185 (2012) 138-142.
[38] H. Zhang, Q. Hao, H. Geng, C. Xu. Nanoporous PdCu alloys as highly active and methanol-tolerant oxygen reduction electrocatalysts. Int. J. Hydrogen Energy. 38 (2013) 10029-10038.
[39] S. Esconjauregui, C.M. Whelan, K. Maex. The reasons why metals catalyze the nucleation and growth of carbon nanotubes and other carbon nanomorphologies. Carbon. 47 (2009) 659-669.
[40] M. Luty-Błocho, M. Wojnicki, G. Włoch, K. Fitzner. Green method for efficient PdNPs deposition on carbon carrier in the microreactor system. J. Nanopart. Res. 20 (2018) 239.
[41] M.-W. Hsieh, T.-J. Whang. Electrodeposition of PdCu alloy and its application in methanol electro-oxidation. Appl. Surf. Sci. 270 (2013) 252-259.
[42] Z. Guo, X. Kang, X. Zheng, J. Huang, S. Chen. PdCu alloy nanoparticles supported on $CeO_2$ nanorods: Enhanced electrocatalytic activity by synergy of compressive strain, PdO and oxygen vacancy. J. Catal. 374 (2019) 101-109.

[43] J. Wu, S. Shan, J. Luo, P. Joseph, V. Petkov, C.-J. Zhong. PdCu Nanoalloy electrocatalysts in oxygen reduction reaction: Role of composition and phase state in catalytic synergy. ACS Appl. Mater. Interfaces. 7 (2015) 25906-25913.
[44] J.C. Carrillo-Rodriguez, S. Garcia-Mayagoitia, R. Perez-Hernandez, M.T. Ochoa-Lara, F. Espinosa-Magana, F. Fernandez-Luqueno, P. Bartolo-Perez, I.L. Alonso-Lemus, F.J. Rodriguez-Varela. Evaluation of the novel Pd-$CeO_{2\text{-}NR}$ electrocatalyst supported on N-doped graphene for the Oxygen Reduction Reaction and its use in a Microbial Fuel Cell. J. Power Sources. 414 (2019) 103-114.
[45] J. Yang, C. Tian, L. Wang, H. Fu. An effective strategy for small-sized and highly-dispersed palladium nanoparticles supported on graphene with excellent performance for formic acid oxidation. J. Mater. Chem. 21 (2011) 3384-3390.
[46] Y. Jiang, Y. Lu, F. Li, T. Wu, L. Niu, W. Chen. Facile electrochemical codeposition of "clean" graphene–Pd nanocomposite as an anode catalyst for formic acid electrooxidation. Electrochem. Commun. 19 (2012) 21-24.
[47] Y. Li, Y. Yu, J.-G. Wang, J. Song, Q. Li, M. Dong, C.-J. Liu. CO oxidation over graphene supported palladium catalyst. Appl. Catal. B: Environ. 125 (2012) 189-196.
[48] A.R. Siamaki. Microwave-assisted synthesis of palladium nanoparticles supported on graphene: A highly active and recyclable catalyst for carbon–carbon cross-coupling reactions. J. Catal. 279 (2011) pp. 1-11.
[49] A. Serov, T. Asset, M. Padilla, I. Matanovic, U. Martinez, A. Roy, K. Artyushkova, M. Chatenet, F. Maillard, D. Bayer, C. Cremers, P. Atanassov. Highly-active Pd–Cu electrocatalysts for oxidation of ubiquitous oxygenated fuels. Appl. Catal. B: Environ. 191 (2016) 76-85.
[50] M.V. Castegnaro, W.J. Paschoalino, M.R. Fernandes, B. Balke, M.C. M. Alves, E.A. Ticianelli, J. Morais. Pd–M/C (M = Pd, Cu, Pt) Electrocatalysts for oxygen reduction reaction in alkaline medium: correlating the electronic structure with activity. Langmuir. 33 (2017) 2734-2743.
[51] H.L. Tierney, A.E. Baber, E.C.H. Sykes. Atomic-scale imaging and electronic structure determination of catalytic sites on Pd/Cu near surface alloys. J. Phys. Chem. C. 113 (2009) 7246-7250.
[52] A. Habekost. Experimental investigations of alkaline silver-zinv and copper-zinc batteries. World J. Chem. Educ. 4 (2016) 4-12.

[53] J. Wu, X. Li, B. Yadian, H. Liu, S. Chun, B. Zhang, K. Zhou, C.L. Gan, Y. Huang. Nano-scale oxidation of copper in aqueous solution. Electrochem. Commun. 26 (2013) 21-24.
[54] M. Scherzer, F. Girgsdies, E. Stotz, M.-G. Willinger, E. Frei, R. Schlögl, U. Pietsch, T. Lunkenbein. Electrochemical surface oxidation of copper studied by in situ grazing incidence X-ray diffraction. J. Phys. Chem. C. 123 (2019) 13253-13262.
[55] E.N. Sawy, H.A. Sayed, V.I. Birss. Clarifying the role of Ru in methanol oxidation at Rucore@Ptshell nanoparticles. PCCP. 17 (2015) 27509-27519.
[56] J.-X. Tang, Q.-S. Chen, L.-X. You, H.-G. Liao, S.-G. Sun, S.-G. Zhou, Z.-N. Xu, Y.-M. Chen, G.-C. Guo. Screw-like PdPt nanowires as highly efficient electrocatalysts for methanol and ethylene glycol oxidation. J. Mater. Chem. A. 6 (2018) 2327-2336.
[57] Y. Wang, T.S. Nguyen, X. Liu, X. Wang. Novel palladium–lead (Pd–Pb/C) bimetallic catalysts for electrooxidation of ethanol in alkaline media. J. Power Sources. 195 (2010) 2619-2622.
[58] C. Hu, Z. Bai, L. Yang, J. Lv, K. Wang, Y. Guo, Y. Cao, J. zhou. Preparation of high performance Pd catalysts supported on untreated multi-walled carbon nanotubes for formic acid oxidation. Electrochim. Acta. 55 (2010) 6036-6041.
[59] Y. Wang, F.-F. Shi, Y.-Y. Yang, W.-B. Cai. Carbon supported Pd–Ni–P nanoalloy as an efficient catalyst for ethanol electro-oxidation in alkaline media. J. Power Sources. 243 (2013) 369-373.
[60] Y.-F. Wang, C. Zhu, Y.-Y. Yang, Z.-G. Zhao. Surface-clean low-doped PdB/C as superior electrocatalysts toward ethanol oxidation in alkaline media. J. Energy Chem. 27 (2018) 389-394.
[61] C. Zhu, Y.-Y. Yang, Z.-G. Zhao. Surface voltammetric dealloying investigation on PdCu/C electrocatalysts toward ethanol oxidation in alkaline media. J. Nanopart. Res. 20 (2018) 314.
[62] F. Fouda-Onana, O. Savadogo. Study of $O_2$ and OH adsorption energies on Pd–Cu alloys surface with a quantum chemistry approach. Electrochim. Acta. 54 (2009) 1769-1776.
[63] A. Shafaei Douk, H. Saravani, M. Noroozifar. Novel fabrication of PdCu nanostructures decorated on graphene as excellent electrocatalyst toward ethanol oxidation. Int. J. Hydrogen Energy. 42 (2017) 15149-15159.

[64] D. Rajesh, P. Indra Neel, A. Pandurangan, C. Mahendiran. Pd-NiO decorated multiwalled carbon nanotubes supported on reduced graphene oxide as an efficient electrocatalyst for ethanol oxidation in alkaline medium. Appl. Surf. Sci. 442 (2018) 787-796.

[65] E. Pizzutilo, S. Geiger, J.P. Grote, A. Mingers, K.J.J. Mayrhofer, M. Arenz, S. Cherevko. On the need of improved accelerated degradation protocols (ADPs): examination of platinum dissolution and carbon corrosion in half-cell tests. J. Electrochem. Soc. 163 (2016) F1510-F1514.

[66] C. Hu, H. Cheng, Y. Zhao, Y. Hu, Y. Liu, L. Dai, L. Qu. Newly-designed complex ternary Pt/PdCu nanoboxes anchored on three-dimensional graphene framework for highly efficient ethanol oxidation. Adv. Mater. 24 (2012) 5493-5498.

[67] G. Spezzati, Y. Su, J.P. Hofmann, A.D. Benavidez, A.T. DeLaRiva, J. McCabe, A.K. Datye, E.J.M. Hensen. Atomically dispersed Pd–O Species on $CeO_2$(111) as highly active sites for low-temperature CO oxidation. ACS Catalysis. 7 (2017) 6887-6891.

[68] A.K. Ipadeola, N.Z. Lisa Mathebula, M.V. Pagliaro, H.A. Miller, F. Vizza, V. Davies, Q. Jia, F. Marken, K.I. Ozoemena. Unmasking the latent passivating roles of $Ni(OH)_2$ on the performance of Pd–Ni electrocatalysts for alkaline ethanol fuel cells. ACS Appl. Energy Mater. 3 (2020) 8786-8802.

[69] S. Shen, Y. Guo, L. Luo, F. Li, L. Li, G. Wei, J. Yin, C. Ke, J. Zhang. Comprehensive analysis on the highly active and stable PdAu/C electrocatalyst for Ethanol Oxidation Reaction in alkaline media. J. Phys. Chem. C.122 (2018) 1604-1611.

[70] T.F. Messa Moreira, S.A. Neto, C. Lemoine, K.B. Kokoh, C. Morais, T.W. Napporn, P. Olivi. Rhodium effects on Pt anode materials in a direct alkaline ethanol fuel cell. RSC Advances. 10 (2020) 35310-35317.

[71] L. Wang, A. Lavacchi, M. Bevilacqua, M. Bellini, P. Fornasiero, J. Filippi, M. Innocenti, A. Marchionni, H.A. Miller, F. Vizza. Energy efficiency of alkaline direct ethanol fuel cells employing nanostructured palladium Electrocatalysts. ChemCatChem. 7 (2015) 2214-2221.

[72] R.M. Modibedi, T. Mehlo, K.I. Ozoemena, M.K. Mathe. Preparation, characterisation and application of Pd/C nanocatalyst in passive alkaline direct ethanol fuel cells (ADEFC). Int. J. Hydrogen Energy. 40 (2015) 15605-15612.

[73] L.P.R. Moraes, B.R. Matos, C. Radtke, E.I. Santiago, F.C. Fonseca, S.C. Amico, C.F. Malfatti. Synthesis and performance of palladium-based electrocatalysts in alkaline direct ethanol fuel cell. Int. J. Hydrogen Energy. 41 (2016) 6457-6468.

# Chapter VI

# Evaluation of Pd-$CeO_{2\text{-}NR}$ nanocatalysts supported on Vulcan XC-72 functionalized with Cu organometallic compounds for the EOR.

# Chapter VI
# Evaluation of Pd-$CeO_{2\text{-}NR}$ nanocatalysts supported on Vulcan XC-72 functionalized with Cu organometallic compounds for the EOR

## 6.1 Physicochemical characterization of nanocatalysts

### 6.1.1 XRD

The XRD patterns of Pd-$CeO_{2\text{-}NR}$/C, Pd-$CeO_{2\text{-}NR}$/$C_{Cu\text{-}mes}$, and Pd-$CeO_{2\text{-}NR}$/$C_{Cu(dmpz)L2}$ in Figure 6.1 show the carbon (002) plane at 26.59° along with the (111), (200), and (220) planes at 39.78, 46.22, and 67.62° (2θ) attributed to the Pd fcc crystal structure. Pd-$CeO_{2\text{-}NR}$/C (from Chapter 4) also shows the (111), (200), and (311) planes at 28.6, 32.5, and 56.1° (2θ) assigned to the fluorite structure of $CeO_2$ [1]. At Pd-$CeO_{2\text{-}NR}$/$C_{Cu\text{-}mes}$, and Pd-$CeO_{2\text{-}NR}$/$C_{Cu(dmpz)L2}$ only the (111) and (220) planes are observed. In the diffractogram of Pd-$CeO_{2\text{-}NR}$/$C_{Cu(dmpz)L2}$ it is possible to observe two reflections in the 10 at 30° region, attributed to the organometallic compound (as seen in Figure 5.6), overlapping with the carbon reflection and the (111) plane of $CeO_2$. This feature can be viewed as an effect of the chemical stability of the compound functionalizing the support.

Pd-$CeO_{2\text{-}NR}$/$C_{Cu\text{-}mes}$, and Pd-$CeO_{2\text{-}NR}$/$C_{Cu(dmpz)L2}$ show a shift of the Pd reflections towards higher 2θ degrees, compared to Pd-$CeO_{2\text{-}NR}$/C. Moreover, Pd-$CeO_{2\text{-}NR}$/$C_{Cu\text{-}mes}$ has a broadening of the Pd peaks. As seen in Figure 4.1, there are no such changes in features between Pd/C and Pd-$CeO_{2\text{-}NR}$/C, i.e., there is no significant effect of the presence of ceria on the structural characteristics of Pd. Therefore, the modifications observed on the nanocatalysts supported on functionalized Vulcan can be ascribed to a modification of the Pd lattice by Cu atoms from the functionalization, resulting in the formation of PdCu alloyed phases analogous to those observed in Chapter 5. No planes corresponding to Cu or Cu oxides are observed in the diffractograms of Pd-$CeO_{2\text{-}NR}$/$C_{Cu\text{-}mes}$, and Pd-$CeO_{2\text{-}NR}$/$C_{Cu(dmpz)L2}$. However, their presence should not be discarded [2].

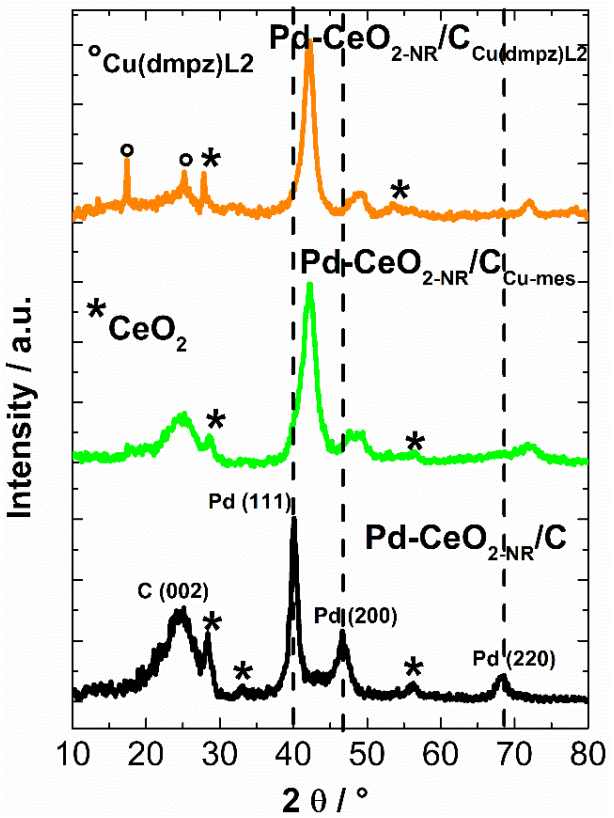


**Figure 6.1** XRD patterns of the Pd-$CeO_{2\text{-}NR}$/C, Pd-$CeO_{2\text{-}NR}$/$C_{Cu\text{-}mes}$ and Pd-$CeO_{2\text{-}NR}$/$C_{Cu(dmpz)L2}$ nanocatalysts.

**Table 6.1** Crystallite size of nanocatalysts.

| Nanocatalysts | d, XRD / nm |
|---|---|
| Pd-$CeO_{2\text{-}NR}$/C | 6.6* |
| Pd-$CeO_{2\text{-}NR}$/$C_{Cu\text{-}mes}$ | 4.7 |
| Pd-$CeO_{2\text{-}NR}$ /$C_{Cu(dmpz)L2}$ | 7.1 |

*Value reported in section 4.1.1.

From data of the Pd (220) plane, Pd-$CeO_{2\text{-}NR}$/$C_{Cu\text{-}mes}$ has a smaller d value than Pd-$CeO_{2\text{-}NR}$/$C_{Cu(dmpz)L2}$ and Pd-$CeO_{2\text{-}NR}$/C (Table 6.1), and similar to those reported in

the literature [3, 4]. The decrease in d at Pd-$CeO_{2\text{-}NR}$/$C_{Cu\text{-}mes}$ can be correlated to a presence of nucleation centers in this case probably delimited the particle size growth. In addition, an improved dispersion is expected, since some Pd nanoparticles tend to deposit on the cerium oxide nanorods [5]. Nevertheless, it should be mentioned that the d value of Pd/$CeO_{2\text{-}NR}$/$C_{Cu\text{-}mes}$ is larger than those functionalized nanocatalysts without $CeO_{2\text{-}NR}$ (Table 5.5).

The lattice parameter ($a_{fcc}$) and the fraction of Cu alloyed (D) have been determined from the Pd (111) plane, and the values are shown in Table 6.2. The nanocatalysts supported on functionalized carbon have a similar contraction in $a_{fcc}$ compared to Pd-$CeO_{2\text{-}NR}$/C because of the interactions with Cu atoms. Meanwhile, the D values of Pd-$CeO_{2\text{-}NR}$/$C_{Cu\text{-}mes}$ and Pd-$CeO_{2\text{-}NR}$/$C_{Cu(dmpz)L2}$ are 32 and 33 %, respectively, about the same value as those of the nanocatalysts without ceria (Table 5.6 in the previous Chapter), confirming that a relative high concentration of Cu becomes alloyed with Pd atoms as a result of the functionalization, regardless of the presence of CeO2-NR. The $a_{fcc}$ and D values are comparable with those reported in the literature for PdCu alloys [6, 7].

**Table 6.2** Structural parameters of nanocatalysts obtained from the (111) plane.

| Nanocatalyst | Position / ° | $a_{fcc}$ / nm | D / % |
|---|---|---|---|
| Pd-$CeO_{2\text{-}NR}$/C | 40.17 | 0.388 | - |
| Pd $CeO_{2\text{-}NR}$ /$C_{Cu\text{-}mes}$ | 42.18 | 0.371 | 32 |
| Pd $CeO_{2\text{-}NR}$ /$C_{Cu(dmpz)L2}$ | 42.21 | 0.370 | 33 |

### 6.1.2 FE-SEM and EDS

The chemical composition of Pd-$CeO_{2\text{-}NR}$/$C_{Cu\text{-}mes}$ is shown in Table 6.3. The C and Pd content are 72.52 and 8.56 wt. %, respectively. The Pd content is slightly lower than that nominally expected (10 wt. %). Meanwhile, the Cu content is 10.42 wt. %, roughly the same as that of the ceria-free Pd/$C_{Cu\text{-}mes}$ in Chapter 5. Additionally, Pd-$CeO_{2\text{-}NR}$/$C_{Cu\text{-}mes}$ has 8.44 wt. % of $CeO_{2\text{-}NR}$ resulting in a Pd: $CeO_2$ atomic ratio of 1.6:1, slightly higher than the 1:1 nominally expected.

The high magnification FE-SEM micrographs in Figure 6.2 a) and b) show the morphology of Pd-$CeO_{2\text{-}NR}$ /$C_{Cu\text{-}mes}$, with spherical shape particles corresponding to Vulcan and brighter small spherical particles attributed at Pd. The elemental mapping of Pd-$CeO_{2\text{-}NR}$ /$C_{Cu\text{-}mes}$ in Figure 6.3 confirms the homogeneous dispersion of C, Pd, and Cu, with O and Ce tending to group together because of the $CeO_2$ configuration. In addition, it is important to note the affinity between Cu and Pd, which are uniformly distributed over some of the same areas which suggests their alloying [8].

**Table 6.3**. Chemical composition of Pd-$CeO_{2\text{-}NR}$/$C_{Cu\text{-}mes}$.

| **Nanocatalyst** | **Chemical composition (wt. %)** | | | | **Ratio (at. %)** |
|---|---|---|---|---|---|
| | C | Pd | Cu | $CeO_2$ | Pd:$CeO_2$ |
| Pd-$CeO_{2\text{-}NR}$/$C_{Cu\text{-}mes}$ | 72.52 ± 1.59 | 8.56 ± 0.66 | 10.42 ± 1.40 | 8.49 ± 3.57 | 1.6:1 |

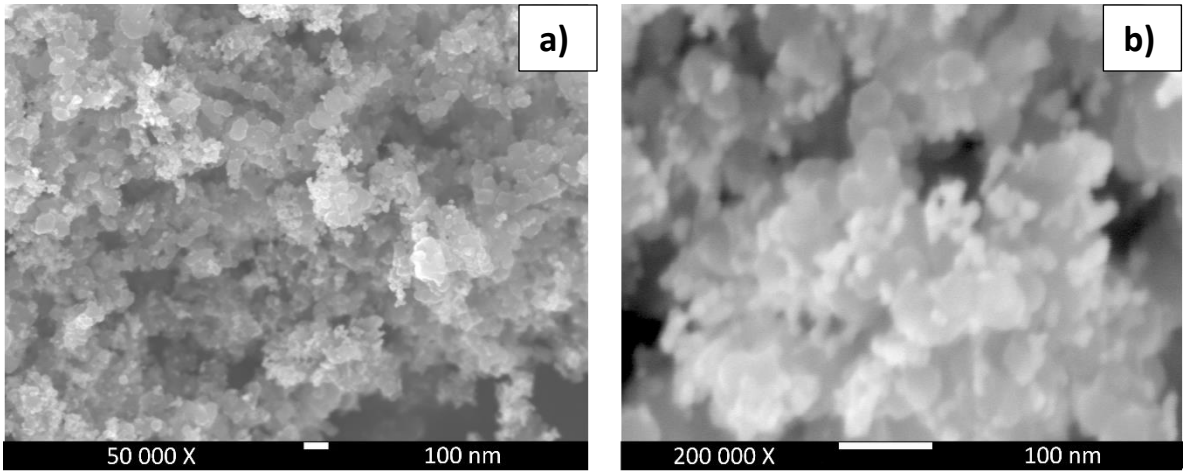


**Figure 6.2** a) and b) high magnification FE-SEM micrographs of Pd-$CeO_{2\text{-}NR}$/$C_{Cu\text{-}mes}$.

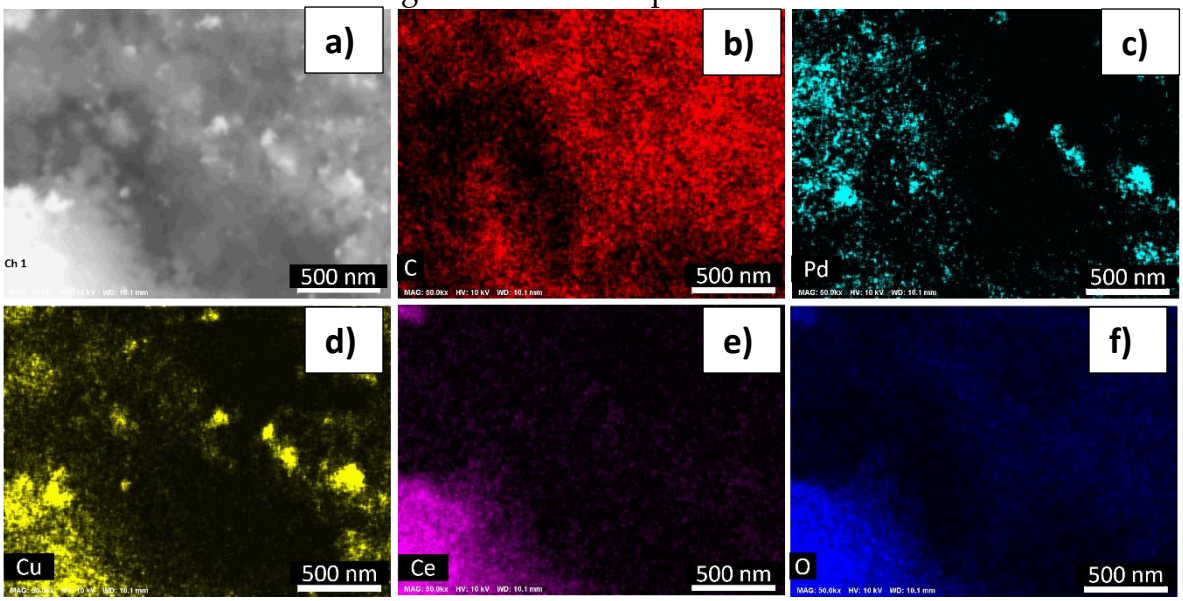


**Figure 6.3** a) FE-SEM imagen and b) C, c) Pd, d) Cu, e) Ce and f) O elemental mapping of Pd-$CeO_{2\text{-}NR}$/$C_{Cu\text{-}mes}$.

### 6.1.3 XPS

The XPS spectra of Pd-$CeO_{2\text{-}NR}$/$C_{Cu\text{-}mes}$ in the a) C 1s, b) O 1s, c) Pd 3d and d) Cu 2p regions is shown in Figure 6.4. The C 1s core-level spectrum of Pd-$CeO_{2\text{-}NR}$/$C_{Cu\text{-}mes}$ shows a strong graphite component (C=C $sp^2$) at 284.7 eV with a relative concentration of 75 at. % (Table 6.4), followed by C-C $sp^3$ and C-O-C at binding energies of 285.53 and 286.47 eV, respectively [9]. In the O 1s region it shows peaks attributed to lattice oxygen in $Cu_2O$ and CuO at 529.96 and 530.85 eV, respectively [10]. In addition, signals at 531.78 and 532.60 eV are assigned to PdO and $PdO_2$, respectively. These signals confirm the interactions between Pd and O atoms. The C=O, C-O, O-C=O species corresponding to the functional groups formed on the carbon support are also shown [11].

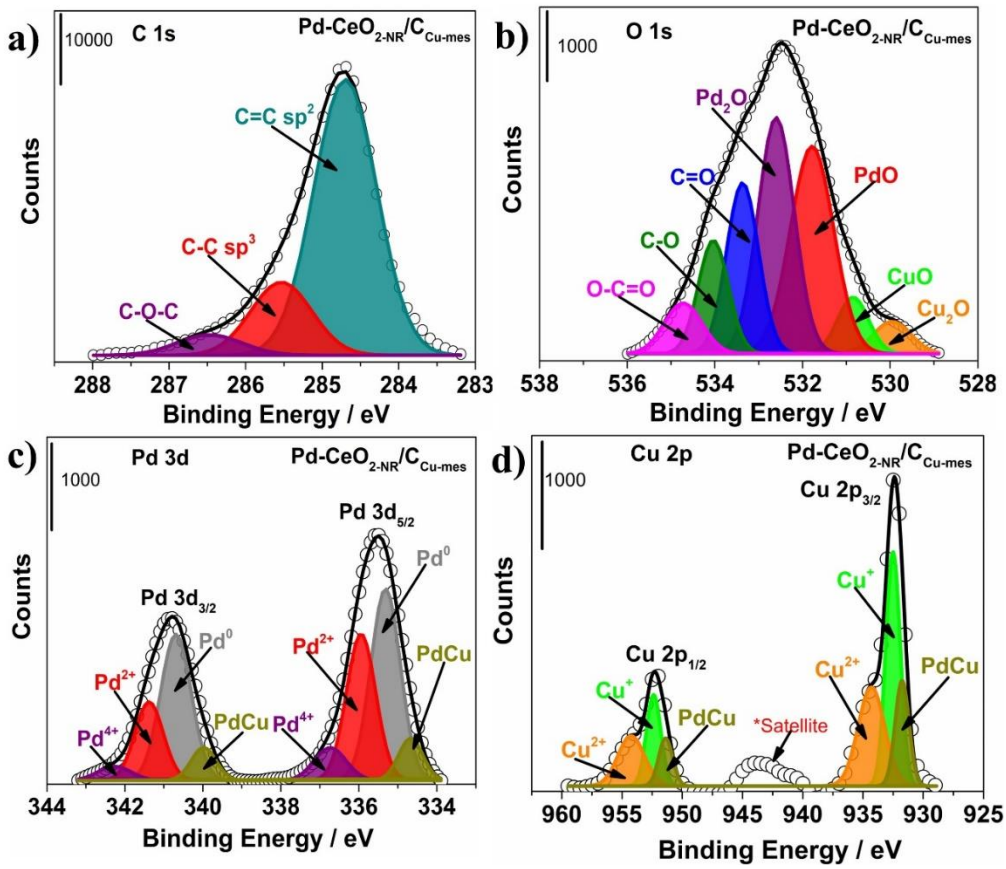


**Figure 6.4** XPS spectra of Pd-$CeO_{2\text{-}NR}$/$C_{Cu\text{-}mes}$ in the a) C 1s, b) O 1s, c) Pd 3d, and d) Cu 2p regions.

The high-resolution Pd 3d photoelectron spectra has two peaks due to spin-orbit splitting into $3d_{5/2}$ and $3d_{3/2}$ states. Four doublets of peaks are observed after deconvolution of the spectra, representing four species. It is possible to confirm the presence of an alloyed PdCu phase with signals at 334.07 and 339.98 eV [12]. On the other hand, the $Pd^0$ species which has the highest relative concentration (50.6 at. %, Table 6.4) has signals at 335.94 and 340.69 eV. $Pd^{2+}$ (335.94 and 341.38 eV), and $Pd^{4+}$ (336.73 and 342.27 eV) have also been detected.

Meanwhile, the Cu 2p region of Pd-$CeO_{2\text{-}NR}$/$C_{Cu\text{-}mes}$ splits into the $2p_{3/2}$ and $2p_{1/2}$ states, each one deconvoluted into three doublets due to the PdCu bonds (931.75 and 951.39 eV), and the $Cu^+$(932.51 and 951.39 eV) and $Cu^{2+}$ (932.51 and 952.38 eV)

species. The emergence of PdCu species also confirms the development of alloyed phases. In this case, the species with the highest relative concentration is $Cu^{+}$ (43.6 at. %, Table 6.4).

Figure 6.5 shows the XPS spectra of Pd-$CeO_{2\text{-}NR}$/$C_{Cu(dmpz)L2}$ in the a) C 1s, b) O 1s, c) Pd 3d, d) Cu 2p regions. From the deconvolution of the C 1s region, the $sp^2$ nanodomain (C=C bonds at BE= 284.77 eV) is the most intense and with the highest relative concentration (83.8 at. %, Table 6.4). The C-C $sp^3$ (285.75 eV) and C-O-C (286.64 eV) are observed as well (see Table 6.4). As for the O 1s region, it displays seven signals. The presence of CuO (529.51 eV) and $Cu_2O$ (530.55 eV) can be ascribed to the interaction of surface Cu and O atoms. In the same fashion, PdO (531.28 eV) and $Pd_2O$ (532.11 eV) can be correlated with Pd and O atoms interactions. Moreover, C=O, C-O, and O-C=O bonds have also been detected.

In the meantime, the deconvolution of the Pd 3d region results in the development of four doublets from the spin-orbit splitting into the $3d_{5/2}$ and $3d_{3/2}$ states. Once again, PdCu (335.38 and 340.60 eV) emerge, a strong indication of the formation of PdCu alloyed phases. Moreover, the $Pd^{0}$ (335.82 and 341.69 eV, 51.5 at. %, Table 6.4), $Pd^{2+}$ (336.69 and 341.96 eV), and $Pd^{4+}$ (338.62 and 343.28 eV) have also been detected.

In the Cu 2p region, the deconvolution of the spectrum leads to three doublets. PdCu bonds are observed at 932.22 and 951.81 eV. The species with the highest relative concentration is $Cu^{+}$ (932.77 and 952.61 eV), having 43.1 at. % (Table 6.4), while $Cu^{2+}$has peaks with BE= 934.94 and 954.80 eV.

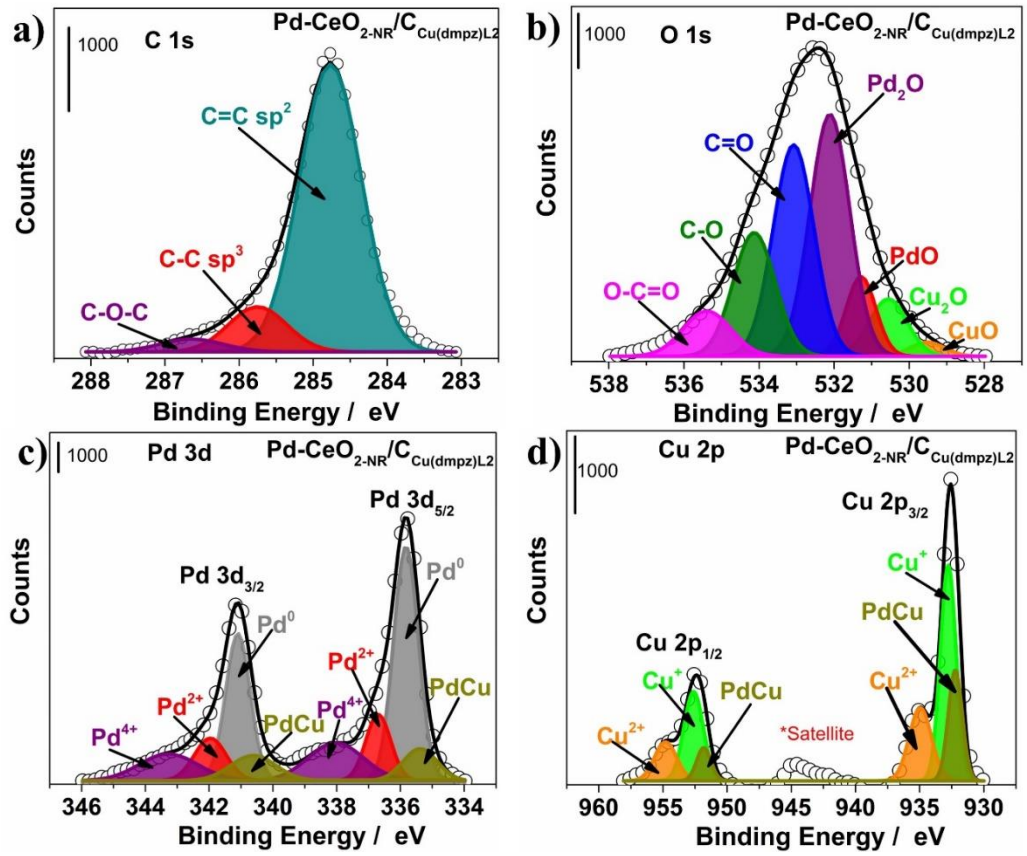


**Figure 6. 5** XPS spectra of Pd-$CeO_{2\text{-}NR}$/$C_{Cu(dmpz)L2}$ in the a) C 1s, b) O 1s, c) Pd 3d, and d) Cu 2p regions.

The $Pd^0$ species in the Pd 3d5/2 state shifts towards higher BE at Pd-$CeO_{2\text{-}NR}$/$C_{Cu\text{-}mes}$ and Pd-$CeO_{2\text{-}NR}$/$C_{Cu(dmpz)L2}$ (335.31 and 335.82 eV, respectively, Table 6.4), compared to Pd/C (335.14 eV, Table 4.2), which confirms an effect due to the addition of ceria [13], and because of the formation of PdCu alloyed phases.

It should be mentioned that the 3d Ce region could not be analyzed because it has not been detected from the XPS analysis.

**Table 6.4** XPS parameters of Pd-$CeO_{2\text{-}NR}$/$C_{Cu\text{-}mes}$ and Pd Pd-$CeO_{2\text{-}NR}$ /$C_{Cu(dmpz)L2}$.

| Nanocatalyst | State | Species | BE / eV | Composition at % |
|---|---|---|---|---|
| **Pd-$CeO_{2\text{-}NR}$/$C_{Cu\text{-}mes}$** | C 1s | C=C $sp^2$ | 284.70 | 75.0 |
| | C 1s | C-C $sp^3$ | 285.53 | 19.3 |
| | C 1s | C-O-C | 286.47 | 5.7 |
| | O 1s | $Cu_2O$ | 529.96 | 3.9 |
| | O 1s | CuO | 530.85 | 5.6 |
| | O 1s | PdO | 531.78 | 28.6 |
| | O 1s | $Pd_2O$ | 532.60 | 27.4 |
| | O 1s | C=O | 533.37 | 17.4 |
| | O 1s | C-O | 534.03 | 10.9 |
| | O 1s | O-C=O | 534.72 | 6.1 |
| | Pd $3d_{5/2}$ | PdCu | 334.67 | 5.1 |
| | Pd $3d_{5/2}$ | $Pd^0$ | 335.31 | 28.3 |
| | Pd $3d_{5/2}$ | $Pd^{2+}$ | 335.94 | 21.4 |
| | Pd $3d_{5/2}$ | $Pd^{4+}$ | 336.73 | 5.2 |
| | Pd $3d_{1/2}$ | PdCu | 339.98 | 4.1 |
| | Pd $3d_{1/2}$ | $Pd^0$ | 340.69 | 22.3 |
| | Pd $3d_{1/2}$ | $Pd^{2+}$ | 341.38 | 11.1 |
| | Pd $3d_{1/2}$ | $Pd^{4+}$ | 342.27 | 2.4 |
| | Cu $2p_{3/2}$ | PdCu | 931.75 | 13.6 |
| | Cu $2p_{3/2}$ | $Cu^+$ | 932.51 | 31.4 |
| | Cu $2p_{3/2}$ | $Cu^{2+}$ | 934.30 | 24.3 |
| | Cu $2p_{1/2}$ | PdCu | 951.39 | 6.2 |
| | Cu $2p_{1/2}$ | $Cu^+$ | 952.38 | 12.2 |
| | Cu $2p_{1/2}$ | $Cu^{2+}$ | 954.25 | 12.3 |
| **Pd-$CeO_{2\text{-}NR}$/$C_{Cu(dmpz)L2}$** | C 1s | C=C $sp^2$ | 284.77 | 83.8 |
| | C 1s | C-C $sp^3$ | 285.75 | 12.4 |
| | C 1s | C-O-C | 286.64 | 3.8 |
| | O 1s | $Cu_2O$ | 529.51 | 1.6 |

| | | | |
|---|---|---|---|
| O 1s | CuO | 530.55 | 7.0 |
| O 1s | PdO | 531.28 | 7.7 |
| O 1s | $Pd_2O$ | 532.11 | 31.4 |
| O 1s | C=O | 533.08 | 27.9 |
| O 1s | C-O | 534.12 | 16.1 |
| O 1s | O-C=O | 535.34 | 8.3 |
| Pd $3d_{5/2}$ | PdCu | 335.38 | 6.0 |
| Pd $3d_{5/2}$ | $Pd^0$ | 335.82 | 31.6 |
| Pd $3d_{5/2}$ | $Pd^{2+}$ | 336.69 | 9.0 |
| Pd $3d_{5/2}$ | $Pd^{4+}$ | 338.62 | 11.4 |
| Pd $3d_{1/2}$ | PdCu | 340.60 | 6.2 |
| Pd $3d_{1/2}$ | $Pd^0$ | 341.09 | 19.9 |
| Pd $3d_{1/2}$ | $Pd^{2+}$ | 341.96 | 7.4 |
| Pd $3d_{1/2}$ | $Pd^{4+}$ | 343.28 | 8.5 |
| Cu $2p_{3/2}$ | PdCu | 932.22 | 16.2 |
| Cu $2p_{3/2}$ | $Cu^+$ | 932.77 | 35.2 |
| Cu $2p_{3/2}$ | $Cu^{2+}$ | 934.94 | 16.8 |
| Cu $2p_{1/2}$ | PdCu | 951.81 | 5.0 |
| Cu $2p_{1/2}$ | $Cu^+$ | 952.61 | 17.9 |
| Cu $2p_{1/2}$ | $Cu^{2+}$ | 954.80 | 8.9 |

**6.2 Electrochemical characterization of nanocatalysts**

Figure 6.6 shows the CVs of the Pd-$CeO_{2\text{-}NR}$/C, Pd-$CeO_{2\text{-}NR}$/$C_{Cu\text{-}mes}$, and Pd-$CeO_{2\text{-}NR}$/$C_{Cu(dmpz)L2}$ nanocatalysts. The $H_{ads/des}$ region is inhibited (compare with the CVs in Figure 5.16), particularly at Pd-$CeO_{2\text{-}NR}$/$C_{Cu\text{-}mes}$, by the presence of the nanorods, a behavior related to the modulation of the electronic structure of Pd [14]. The other typical regions of Pd-based materials already discussed are observed.

Pd-$CeO_{2\text{-}NR}$/C shows lower j values compared to Pd-$CeO_{2\text{-}NR}$/$C_{Cu\text{-}mes}$ and Pd-$CeO_{2\text{-}NR}$/$C_{Cu(dmpz)L2}$, which display remarkable increase in intensity j over the potential scanned. It is, also possible to observe a j peak at ca.0.9 V/RHE attributed to Cu oxidation-reduction reactions [15] already detailed in section 5.4. Moreover, the

intensity of the peak at 0.7 V/RHE in the backward scan, a feature normally ascribed to the reduction of Pd-oxides, may have also been positively affected by the reduction of Cu-oxides [16]. Such j peak is more intense for Pd-$CeO_{2\text{-}NR}$/$C_{Cu(dmpz)L2}$.

Even more, the j observed in the CVs of Pd-$CeO_{2\text{-}NR}$/$C_{Cu\text{-}mes}$ and Pd-$CeO_{2\text{-}NR}$/$C_{Cu(dmpz)L2}$ in the potential window from 0.8 V/RHE (Forward scan) and 0.5 V/RHE (backward scan in Figure 6.6 is significantly higher than those of the nanocatalysts without $CeO_{2\text{-}NR}$ in Figure 5.16. This feature suggests a synergic effect between Cu species and the PdCu phases, with the nanorods, probably resulting in a higher concentration of metal-oxides at the surface of these nanocatalysts [17, 18].

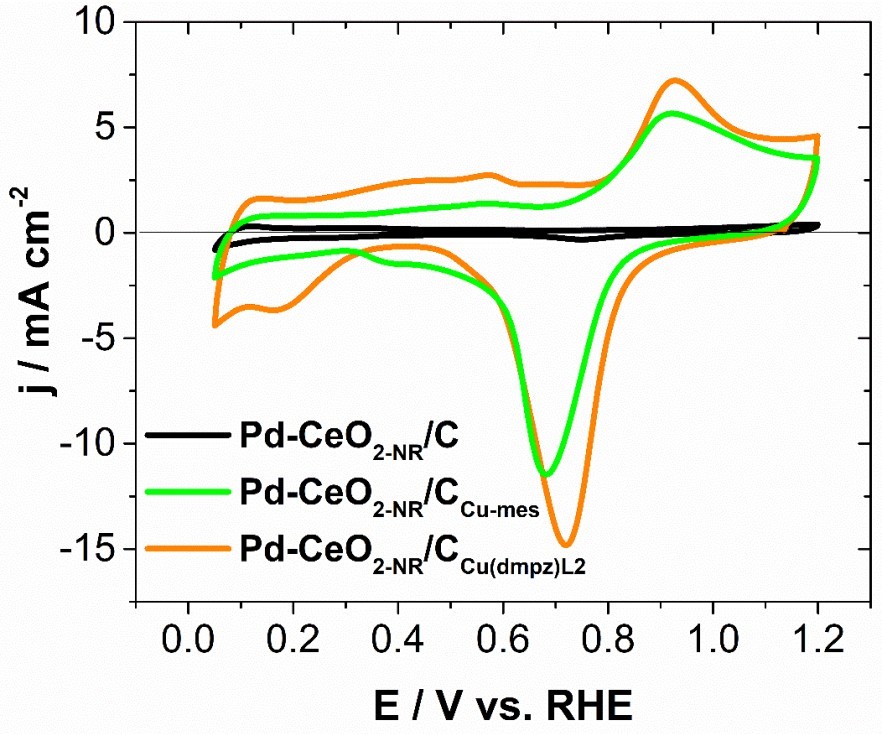


**Figure 6.6** CVs of Pd-$CeO_{2\text{-}NR}$/C, Pd-$CeO_{2\text{-}NR}$/$C_{Cu\text{-}mes}$ and Pd-$CeO_{2\text{-}NR}$/$C_{Cu(dmpz)L2}$. Electrolyte: 0.5 mol $L^{-1}$ KOH. Scan rate: 20 mV $s^{-1}$.

Figure 6.7 shows the polarization curves of the EOR at the nanocatalysts. Before ADT, Pd-$CeO_{2\text{-}NR}$/$C_{Cu\text{-}mes}$ and Pd-$CeO_{2\text{-}NR}$/$C_{Cu(dmpz)L2}$ promote the reaction at a more negative $E_{onset}$ (0.27 and 0.25 V/RHE, respectively) compared to Pd-$CeO_{2\text{-}NR}$/C

(0.29 V/RHE), as shown in Table 6.5. Clearly, the j generated from the reaction is considerable higher at Pd-$CeO_{2\text{-}NR}$/$C_{Cu(dmpz)L2}$ (109.60 mA $cm^{-2}$), than that by Pd-$CeO_{2\text{-}NR}$/$C_{Cu\text{-}mes}$ and Pd-$CeO_{2\text{-}NR}$/C (Table 6.5). It is important to note that the polarization curve at Pd-$CeO_{2\text{-}NR}$/$C_{Cu(dmpz)L2}$ is broader, oxidizing the molecule and reaction intermediates over a wide potential range, a feature analogous to that seen in Figure 5.18 with the same organometallic. This behavior allows to see that this nanocatalyst catalyzes the reaction at more negative potentials than the two other anode materials (i.e., the bifunctional mechanism). It can be seen as well that the performance of Pd-$CeO_{2\text{-}NR}$/$C_{Cu\text{-}mes}$ is better than that of Pd-$CeO_{2\text{-}NR}$/C, but evidently not as high the one demonstrated by Pd-$CeO_{2\text{-}NR}$/$C_{Cu(dmpz)L2}$.

The improved catalytic activity of Pd-$CeO_{2\text{-}NR}$/$C_{Cu(dmpz)L2}$ and to some extent Pd-$CeO_{2\text{-}NR}$/$C_{Cu\text{-}mes}$ can be attributed to the formation of alloyed PdCu phases which shows that Cu alloyed 32 and 33 % (Pd-$CeO_{2\text{-}NR}$/$C_{Cu\text{-}mes}$ and Pd-$CeO_{2\text{-}NR}$/$C_{Cu(dmpz)L2}$, respectively) obtained by XRD are suitable to obtain characteristics that promote bifunctional mechanism, and to the affinity of oxygen molecules towards Cu and $CeO_2$, which may have promoted a larger concentration of Pd and/or PdO active sites, know to catalyze the reaction [19]. This is confirmed according to the results obtained by XPS where a higher concentration of $Pd^0$, $Pd_2O$ and PdO species is obtained (Figure 6.5).

Moreover, it is worth noticing that Pd-$CeO_{2\text{-}NR}$/$C_{Cu(dmpz)L2}$ shows an enhanced catalytic activity than ceria free Pd/$C_{Cu(dmpz)L2}$ in Chapter 5. The behavior is quite the opposite in the case of Pd-$CeO_{2\text{-}NR}$/$C_{Cu\text{-}mes}$ when compared to Pd/$C_{Cu\text{-}mes}$ also from the previous Chapter (compare parameters in Tables 6.5 and 5.11). Therefore, besides the promoting effect of the PdCu alloyed phases when functionalizing Vulcan with the organometallic compounds, there is a synergic interaction between $C_{Cu(dmpz)L2}$ and $CeO_{2\text{-}NR}$, which improves the performance of Pd-$CeO_{2\text{-}NR}$/$C_{Cu(dmpz)L2}$ for the EOR in terms of bifunctional mechanism and electronic effect.

The $j_f/j_b$ ratios are 0.4,1.3. and 1.2 for Pd-$CeO_{2\text{-}NR}$/C, Pd-$CeO_{2\text{-}NR}$/$C_{Cu\text{-}mes}$ and Pd-$CeO_{2\text{-}NR}$/$C_{Cu(dmpz)L2,}$ respectively Table 6.5. These results indicate a higher extent of ethanol oxidation and tolerance to carbonaceous species formed during the scan at the nanocatalysts supported on functionalized Vulcan.

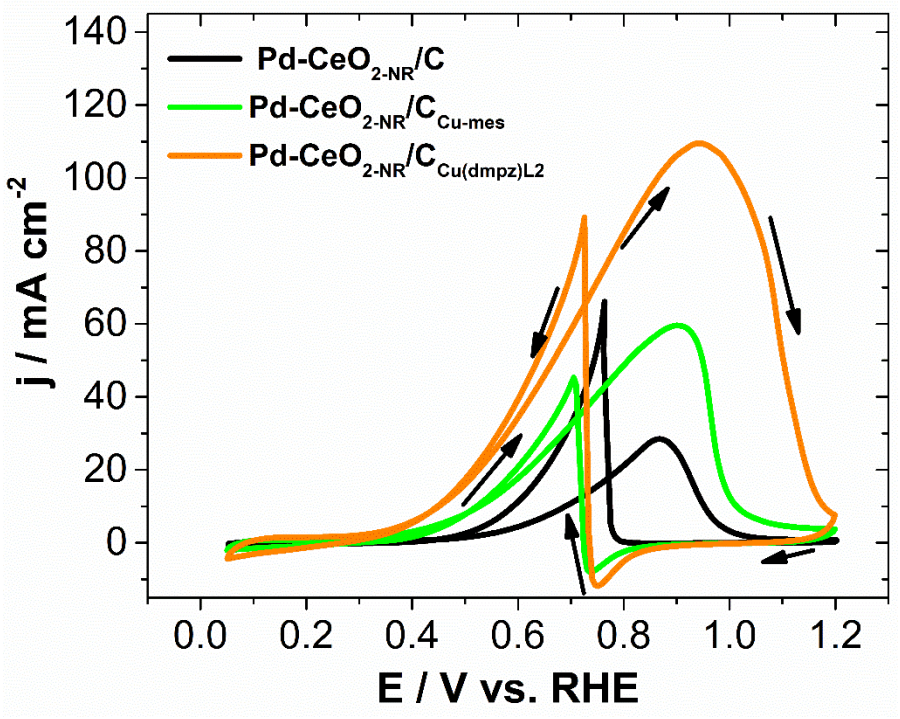


**Figure 6.7** Polarization curves of the EOR at Pd-$CeO_{2\text{-}NR}$/C, Pd-$CeO_{2\text{-}NR}$/$C_{Cu\text{-}mes}$ and Pd-$CeO_{2\text{-}NR}$/$C_{Cu(dmpz)L2}$. Electrolyte: 0.5 mol $L^{-1}$KOH + 0.5 mol $L^{-1}$ EtOH. Scan rate: 20 mV $s^{-1}$.

**Table 6.5** Electrochemical parameters of the EOR at the nanocatalysts.

| Nanocatalysts | $E_{onset}$ | j | $j_f/j_b$ |
|---|---|---|---|
| | (V) | (mA $cm^{-2}$) | |
| **Before ADT** | | | |
| Pd-$CeO_{2\text{-}NR}$ /C* | 0.29 | 28.39 | 0.42 |
| Pd $CeO_{2\text{-}NR}$ /$C_{Cu\text{-}mes}$ | 0.27 | 59.58 | 1.33 |
| Pd $CeO_{2\text{-}NR}$ /$C_{Cu(dmpz)L2}$ | 0.25 | 109.60 | 1.22 |
| **After ADT** | | | |
| Pd-$CeO_{2\text{-}NR}$ /C* | 0.29 | 46.46 | 0.65 |
| Pd $CeO_{2\text{-}NR}$ /$C_{Cu\text{-}mes}$ | 0.23 | 68.52 | 1.23 |
| Pd $CeO_{2\text{-}NR}$ /$C_{Cu(dmpz)L2}$ | 0.33 | 97.38 | 1.56 |

*Values reported in the section 4.2.2.

Figure 6.8 shows a) CVs and b) polarization curves of EOR before and after ADT of Pd-$CeO_{2\text{-}NR}$ /$C_{Cu\text{-}mes}$. It is remarkable that after the test there is a decrease in j over the potential scanned more clearly seen in the metal oxides formation/reduction region. It is hypothesized that, Cu oxides may have dissolved or become metallic (i.e., $Cu^0$) due to cycling.

Nevertheless, the change in chemical composition after ADT has no significant detrimental effect on the catalytic activity of Pd-$CeO_{2\text{-}NR}$/$C_{Cu\text{-}mes}$ for the EOR. Even though the polarization curve shifts to more positive potentials (effect of a less influential bifunctional mechanism) and the $j_f/j_b$ ratio slightly decreases from 1.33 to 1.23, the peal j shows a 15 % increase (a positive electronic effect) as shown in Table 6.5. Therefore, the elements that promote the EOR at Pd-$CeO_{2\text{-}NR}$/$C_{Cu\text{-}mes}$ remain after the test, i.e., PdCu alloyed phases, Pd and/or Pd-oxides active sites [20], and synergistic interactions between $C_{Cu(dmpz)L2}$ and $CeO_{2\text{-}NR}$.

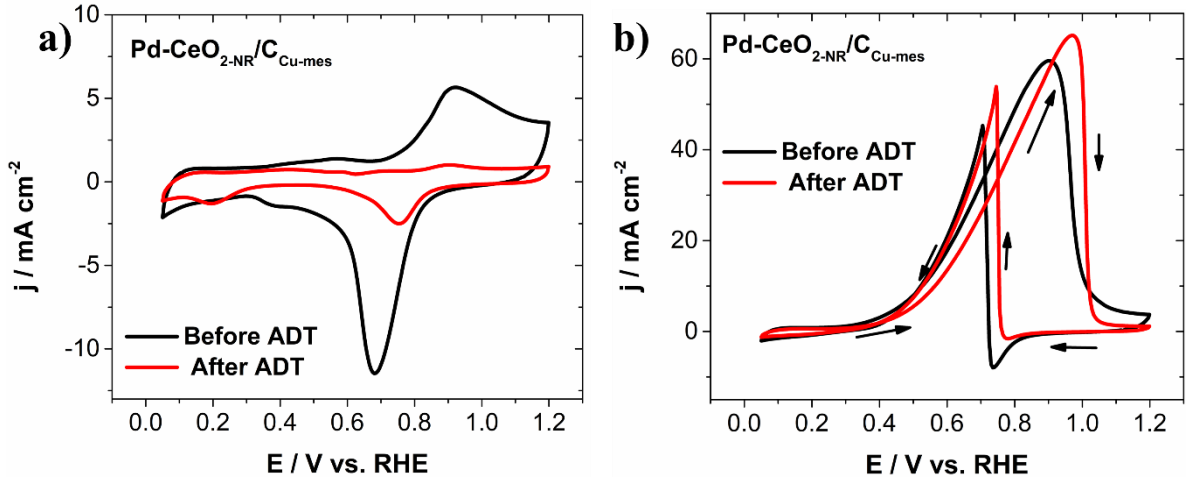


**Figure 6.8** a) CVs and b) polarization curves of EOR before and after of ADT of Pd-$CeO_{2\text{-}NR}$/$C_{Cu\text{-}mes}$. Electrolyte: $N_2$-saturaded 0.5 mol $L^{-1}$ KOH, and 0.5 mol $L^{-1}$ KOH + mol $L^{-1}$ EtOH, respectively. Scan rate: 20 mV $s^{-1}$.

Figure 6.9 shows a) CVs and b) polarization curves of the EOR before and after ADT of Pd-$CeO_{2\text{-}NR}$/$C_{Cu(dmpz)L2}$. As in the previous case, a significant decrease in j after cycling is noticeable. Moreover, the polarization curve after ADT shows a shift to higher potentials ($E_{onset}$=0.33, compared to 0.25 V/RHE before the test) and a decrease of 11.19 % in peak j (Table 6.5). Despite a slight increase in the $j_f/j_b$ ratio, it is evident that the ADT had a detrimental effect on the chemical composition of Pd-$CeO_{2\text{-}NR}$/$C_{Cu(dmpz)L2}$ and thus on its catalytic activity.

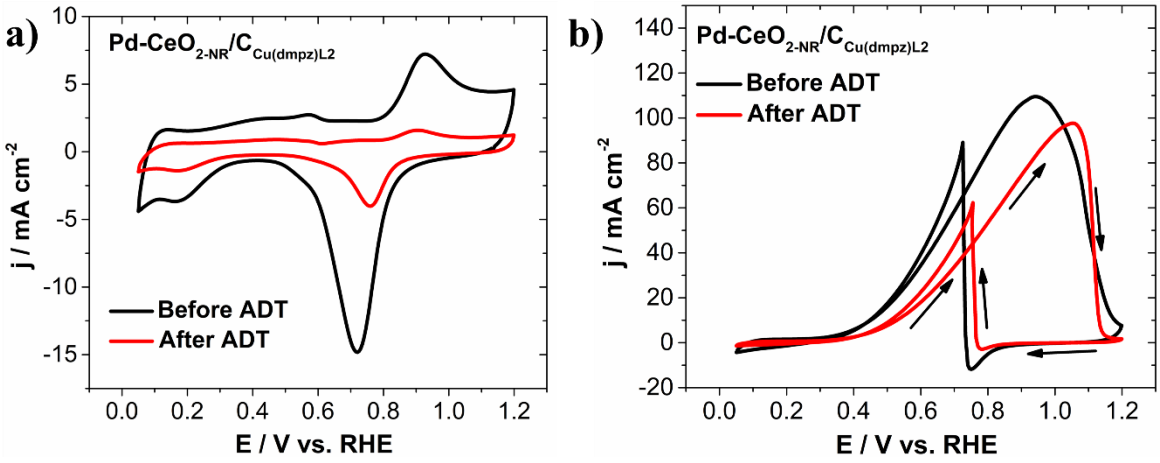


**Figure 6.9** a) CVs and b) polarization curves of EOR before and after of ADT of Pd-$CeO_{2\text{-}NR}$/$C_{Cu(dmpz)L2}$. Electrolyte: $N_2$-saturaded 0.5 mol $L^{-1}$ KOH, and 0.5 mol $L^{-1}$ KOH + mol $L^{-1}$ EtOH, respectively. Scan rate: 20 mV $s^{-1}$.

Table 6.6 depicts a comparison of electrochemical parameters of the EOR obtained from Pd-$CeO_{2\text{-}NR}$/$C_{Cu(dmpz)L2}$, before ADT with those of Pd-based nanocatalysts reported in the literature. As it can be observed, the nanocatalyst studied in this work shows enhanced values than those presented in the literature, more specifically in the peak j value.

**Table 6.6** Electrochemical parameters of the EOR at Pd-based nanocatalysts.

| Nanocatalyst | $E_{onset}$ (V) | j (mA $cm^{-2}$) | Electrolyte | Ref |
|---|---|---|---|---|
| Pd-$CeO_2$/C | 0.26 | 65.5 | 0.5 mol $L^{-1}$ KOH +2 mol $L^{-1}$EtOH | [4] |
| $Pd_{86}Sn_{14}$/C | 0.42 | 62.7 | 1 mol $L^{-1}$ NaOH + 1 mol $L^{-1}$EtOH | [21] |
| Pd/NWA | 0.30 | 73.8 | 1 mol $L^{-1}$ KOH + 1 mol $L^{-1}$EtOH | [22] |
| PdNiP/C | 0.31 | 75.00 | 0.5 mol $L^{-1}$NaOH+ 1 mol $L^{-1}$EtOH | [23] |
| Pd-$CeO_{2\text{-}NR}$/$C_{Cu(dmpz)L2}$ | **0.25** | **109.60** | 0.5 mol $L^{-1}$ KOH + 0.5 mol $L^{-1}$EtOH | **This Work** |

Figure 6.8 shows that the percentage of ethanol consumed during a 4 h test is: 42, 43, and 37 % for Pd-$CeO_{2\text{-}NR}$/C, Pd-$CeO_{2\text{-}NR}$/$C_{Cu\text{-}mes}$ and Pd-$CeO_{2\text{-}NR}$/$C_{Cu(dmpz)L2}$. The main reaction product has determined to be the $C_2H_3O_2^-$, of which the percentage produced is shown in Table 6.7. Overall, the values reported in Figure 6.10 and Table 6.7 demonstrate a poorer performance of the nanocatalysts in this Chapter compared to those in Chapter 5 (Figure 5.21 and 5.12), which can be correlated to the lower catalytic activity of the former for the EOR. Acetaldehyde ($CH_3CHO$) and carbonate ion $CO_3^{-2}$ have not been detected. Therefore, as mentioned before, it is proposed as future work to complement the characterization with other techniques.

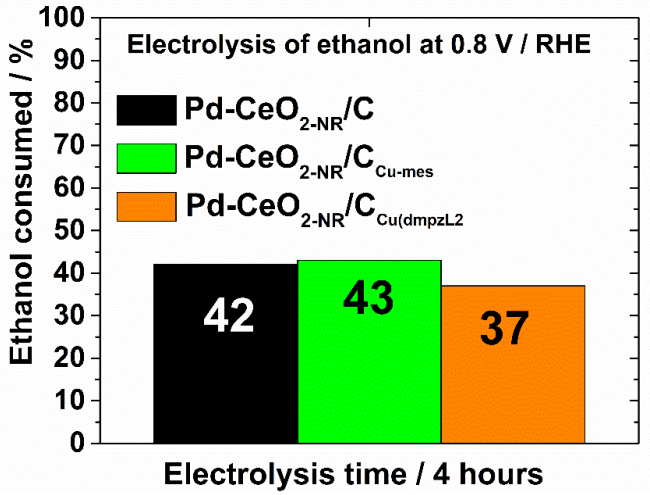


**Figure 6.8** Ethanol consumed during 4 h at the nanocatalysts. Polarization potential: 0.8 V/RHE.

**Table 6.7** Percentage of acetate ion produced during electrolysis for 4 h at 0.8 V/RHE on the nanocatalysts.

| Nanocatalyst | Acetate ion produced /% |
|---|---|
| Pd-$CeO_{2\text{-}NR}$/C | 30 |
| Pd-$CeO_{2\text{-}NR}$ /$C_{Cu\text{-}mes}$ | 31 |
| Pd-$CeO_{2\text{-}NR}$ /$C_{Cu(dmpz)L2}$ | 28 |

Figure 6.9 depicts the individual polarization curves of Pd-$CeO_{2\text{-}NR}$/C, Pd-$CeO_{2\text{-}NR}$/$C_{Cu\text{-}mes}$, and Pd-$CeO_{2\text{-}NR}$/$C_{Cu(dmpz)L2}$ showing the behavior of a) the anode potential ($E_a$), and b) the cathode potential ($E_c$) in fuel cell configurations (i.e., the plots show the potential difference between anode or cathode and the reference electrode as each fuel cell is polarized over a given j window). Clearly, Pd-$CeO_{2\text{-}NR}$/$C_{Cu(dmpz)L2}$ has an improved catalytic activity, with an OCP of 0.47 V/RHE and a smaller overpotential over the whole polarization curve compared to Pd-$CeO_{2\text{-}NR}$/C and Pd-$CeO_{2\text{-}NR}$/$C_{Cu\text{-}mes}$.

Meanwhile, up to ca. 0.15 $mAcm^{-2}$, Pd-$CeO_{2\text{-}NR}$/$C_{Cu(dmpz)L2}$ and Pd-$CeO_{2\text{-}NR}$/C show a similar high performance as cathodes (OCP of 0.98 and 1.00 V/RHE, respectively). However, the former has a significant potential drop at higher j values, increasing the cathode overpotential. On the other hand, Pd-$CeO_{2\text{-}NR}$/$C_{Cu\text{-}mes}$ shows a poorer performance than Pd-$CeO_{2\text{-}NR}$/C. Therefore, the cathode overpotential over the scan is lower at the latter.

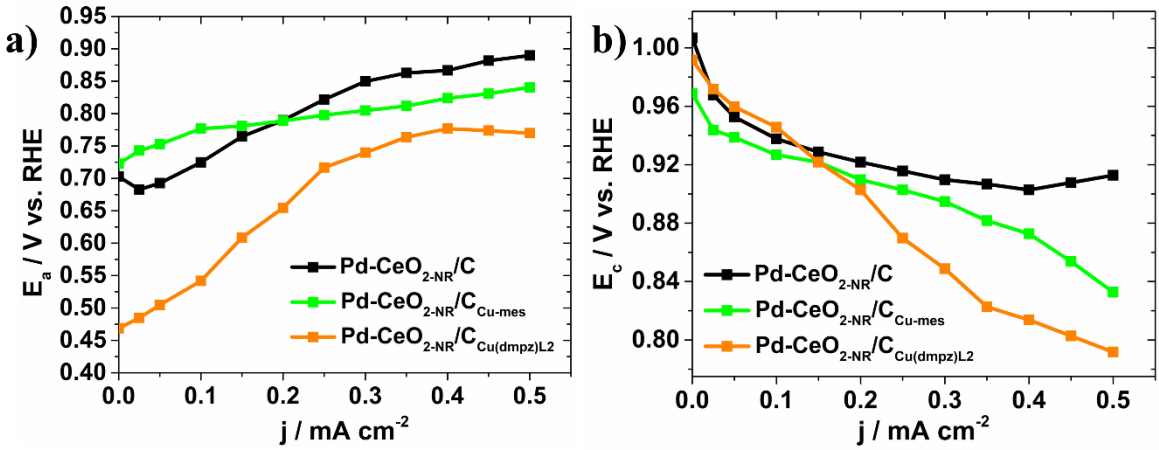


**Figure 6.9** In dividual polarization curves of the nanocatalysts showing the behavior of a) the anode potential, $E_a$, and b) the cathode potential, $E_c$.

The $E_{cell}$ vs. j polarization curves of AEM-DEFCs equipped with the nanocatalysts as anodes and cathodes are shown in Figure 6.10 a). Pd-$CeO_{2\text{-}NR}$/$C_{Cu(dmpz)L2}$ generates the highest open circuit voltage (OCV) 0.54 V, compared to Pd-$CeO_{2\text{-}NR}$/C and Pd-$CeO_{2\text{-}NR}$/$C_{Cu\text{-}mes}$ (Table 6.8). Up to 0.35 mA $cm^{-2}$ in the polarization curves, Pd-$CeO_{2\text{-}NR}$/$C_{Cu(dmpz)L2}$ outperforms the two other nanocatalysts. The $E_{cell}$ values of the AEM-DEFC having Pd-$CeO_{2\text{-}NR}$/$C_{Cu(dmpz)L2}$ are higher compared to the other nanocatalysts at each j. $E_{cell}$ at 0.25 mA $cm^{-2}$ is 0.20, 0.15 and 0.10 V/RHE for Pd-$CeO_{2\text{-}NR}$/$C_{Cu(dmpz)L2}$, Pd-$CeO_{2\text{-}NR}$/$C_{Cu\text{-}mes}$ and Pd-$CeO_{2\text{-}NR}$/C, respectively (see Table 6.8).

**Table 6.8** OCV, $E_{cell}$ and $P_{cell}$ values of Pd-$CeO_{2\text{-}NR}$/C, Pd-$CeO_{2\text{-}NR}$ /$C_{Cu\text{-}mes}$ and Pd-$CeO_{2\text{-}NR}$/$C_{Cu(dmpz)L2}$.

| Nanocatalyst | OCV (V) | $E_{cell}$ at 0.25 mA $cm^{-2}$ (V/RHE) | $P_{cell}$ (mW $cm^{-2}$) |
|---|---|---|---|
| **Pd-$CeO_{2\text{-}NR}$/C** | 0.35 | 0.10 | 0.05 |
| **Pd-$CeO_{2\text{-}NR}$/$C_{Cu\text{-}mes}$** | 0.25 | 0.15 | 0.025 |
| **Pd-$CeO_{2\text{-}NR}$/$C_{Cu(dmpz)L2}$** | 0.54 | 0.20 | 0.020 |

The maximum $P_{cell}$ has been obtained with Pd-$CeO_{2\text{-}NR}$/$C_{Cu(dmpz)L2}$ as anode and cathode (0.020 mW $cm^{-2}$, Figure 6.10 b and Table 6.8). Pd-$CeO_{2\text{-}NR}$/$C_{Cu\text{-}mes}$ and Pd-$CeO_{2\text{-}NR}$/C show a similar poor performance.

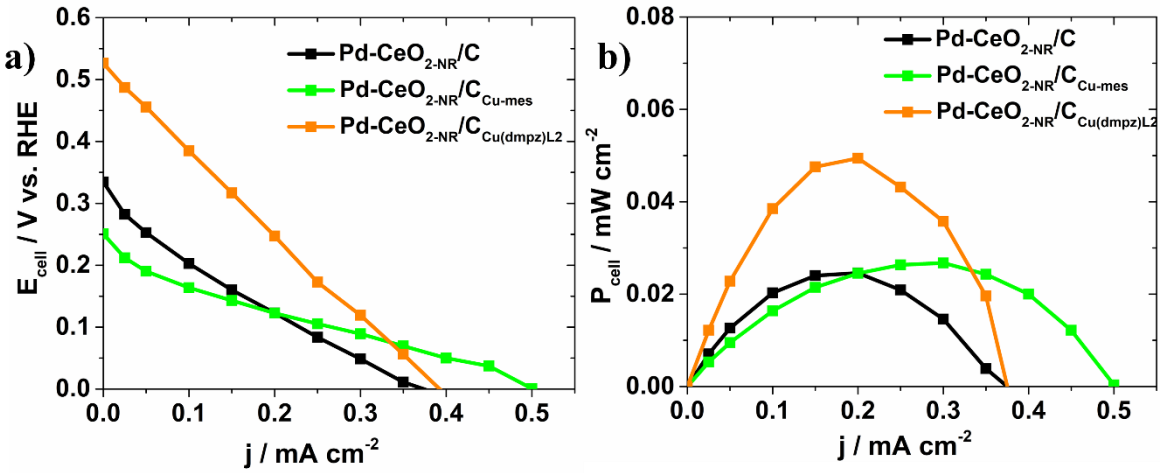


**Figure 6.10** a) Polarization curves and b) power density curves of the AEM-DEFC equipped with the nanocatalysts as anodes and cathodes. Fuel: 0.5 mol $L^{-1}$ EtOH + 0.5 mol $L^{-1}$ KOH. AEM: Fumatech® FAA. Feed at the cathode: $O_2$ + 0.5 mol $L^{-1}$ KOH.

## 6.3 Conclusions

The synthesis of Pd-$CeO_{2\text{-}NR}$ nanocatalysts supported on $C_{Cu\text{-}mes}$ and $C_{Cu(dmpz)L2}$ was successfully achieved, promoting the formation of Cu sites on its surface. The Cu atoms from functionalization promoted the formation of PdCu alloyed phases.

Pd-$CeO_{2\text{-}NR}$ nanocatalysts supported on carbon functionalized with Cu organometallic compounds show improved catalytic activity for EOR in terms of $E_{onset}$, j, electrochemical stability compared to Pd-$CeO_{2\text{-}NR}$/C in half cell. The improvement is attributed to the synergy between $CeO_2$ and Pd leading to the formation of active PdO catalyzing the reaction due to the oxygen vacancies generated by $CeO_2$, as well as promoted by the bifunctional mechanism. On the other hand, the alloying phases between Pd and Cu promote for the combination between bifunctional mechanism and the electronic effect improving the EOR kinetics.

Pd-$CeO_{2\text{-}NR}$/$C_{Cu\text{-}mes}$ showed a higher performance in terms of ethanol consumption and production of acetate ion. It also outperformed the other nanocatalysts when evaluating the $E_a$ polarization curve. In a complete AEM-DEFC, Pd-$CeO_{2\text{-}NR}$/$C_{Cu(dmpz)L2}$ generated the highest OCV and $P_{cell}$ values. The results demonstrated that the functionalization using such Cu organometallic compound generated surface sites that formed PdCu alloyed phases that promoted the electrochemical reactions in alkaline media.

## 6.4 References

[1] J.C. Carrillo-Rodríguez, S. García-Mayagoitia, R. Pérez-Hernández, M.T. Ochoa-Lara, F. Espinosa-Magaña, F. Fernández-Luqueño, I.L. Alonso-Lemus, F.J. Rodriguez-Varela. High performance Pd-$CeO_{2\text{-}NR}$ supported on graphene and N-Doped graphene for the ORR and its application in a Microbial Fuel Cell. ECS Transactions. 77 (2017) 1359-1365.

[2] X. Zhao, L. Dai, Q. Qin, F. Pei, C. Hu, N. Zheng. Self-Supported 3D PdCu alloy nanosheets as a bifunctional catalyst for electrochemical reforming of ethanol. Small. 13 (2017).
[3] Y. Wang, S. Wang, X. Wang. CeO[sub 2] Promoted electro-oxidation of formic acid on Pd⁄C nano-electrocatalysts. Electrochem. Solid-State Lett. 12 (2009) B73.
[4] V. Bambagioni, C. Bianchini, Y. Chen, J. Filippi, P. Fornasiero, M. Innocenti, A. Lavacchi, A. Marchionni, W. Oberhauser, F. Vizza. Energy Efficiency enhancement of ethanol electrooxidation on Pd–$CeO_2$/C in passive and active polymer electrolyte-membrane fuel cells. ChemSusChem. 5 (2012) 1266-1273.
[5] P.C. Meléndez-González, E. Sánchez-Castro, I.L. Alonso-Lemus, R. Pérez-Hernández, B. Escobar-Morales, A.M. Garay-Tapia, W.J. Pech-Rodríguez, J. Rodríguez-Varela. Bifunctional Pd-$CeO_2$ Nanorods/C nanocatalyst with high electrochemical stability and catalytic activity for the ORR and EOR in alkaline media. ChemistrySelect. 5 (2020) 14032-14040.
[6] M.-W. Hsieh, T.-J. Whang. Electrodeposition of PdCu alloy and its application in methanol electro-oxidation. Appl. Surf. Sci. 270 (2013) 252-259.
[7] K.-W. Wang, W.-D. Kang, Y.-C. Wei, C.-W. Liu, P.-C. Su, H.-S. Chen, S.-R. Chung. Promotion of PdCu/C catalysts for Ethanol Oxidation in alkaline solution by $SnO_2$ modifier. ChemCatChem. 4 (2012) 1154-1161.
[8] J. Wu, S. Shan, J. Luo, P. Joseph, V. Petkov, C.-J. Zhong. PdCu nanoalloy electrocatalysts in oxygen reduction reaction: role of composition and phase state in catalytic synergy. ACS Appl. Mater. Interfaces. 7 (2015) 25906-25913.
[9] M. Toupin, D. Bélanger. Spontaneous functionalization of carbon black by reaction with 4-nitrophenyldiazonium cations. Langmuir. 24 (2008) 1910-1917.
[10] R.X. Chen, S.L. Zhu, J. Mao, Z.D. Cui, X.J. Yang, Y.Q. Liang, Z.Y. Li. Synthesis of CuO/$Co_3O_4$ coaxial heterostructures for efficient and recycling photodegradation. Int. J. Photoenergy. 2015 (2015) 183468.
[11] S.M. Senthil Kumar, J. Soler Herrero, S. Irusta, K. Scott. The effect of pretreatment of Vulcan XC-72R carbon on morphology and electrochemical oxygen reduction kinetics of supported Pd nano-particle in acidic electrolyte. J. Electroanal. Chem. 647 (2010) 211-221.

[12] A. Serov, T. Asset, M. Padilla, I. Matanovic, U. Martinez, A. Roy, K. Artyushkova, M. Chatenet, F. Maillard, D. Bayer, C. Cremers, P. Atanassov. Highly-active Pd–Cu electrocatalysts for oxidation of ubiquitous oxygenated fuels. Appl. Catal. B: Environ. 191 (2016) 76-85.
[13] Z. Guo, X. Kang, X. Zheng, J. Huang, S. Chen. PdCu alloy nanoparticles supported on CeO2 nanorods: Enhanced electrocatalytic activity by synergy of compressive strain, PdO and oxygen vacancy. J. Catal. 374 (2019) 101-109.
[14] J. Chen, Y. Li, N. Lu, C. Tian, Z. Han, L. Zhang, Y. Fang, B. Qian, X. Jiang, R. Cui. Nanoporous PdCe bimetallic nanocubes with high catalytic activity towards ethanol electro-oxidation and the oxygen reduction reaction in alkaline media. J. Mater. Chem. A. 6 (2018) 23560-23568.
[15] M.V. Castegnaro, W.J. Paschoalino, M.R. Fernandes, B. Balke, M.C. M. Alves, E.A. Ticianelli, J. Morais. Pd–M/C (M = Pd, Cu, Pt) Electrocatalysts for oxygen reduction reaction in alkaline medium: correlating the electronic structure with activity. Langmuir. 33 (2017) 2734-2743.
[16] Z.X. Liang, T.S. Zhao, J.B. Xu, L.D. Zhu. Mechanism study of the ethanol oxidation reaction on palladium in alkaline media. Electrochim. Acta. 54 (2009) 2203-2208.
[17] T. Masuda, H. Fukumitsu, K. Fugane, H. Togasaki, D. Matsumura, K. Tamura, Y. Nishihata, H. Yoshikawa, K. Kobayashi, T. Mori, K. Uosaki. Role of Cerium Oxide in the Enhancement of Activity for the Oxygen Reduction Reaction at Pt–$CeO_x$ Nanocomposite Electrocatalyst - An in Situ Electrochemical X-ray Absorption Fine Structure Study. J. Phys. Chem. C. 116 (2012) 10098-10102.
[18] A. Altamirano-Gutiérrez, A.M. Fernández, F.J. Rodríguez Varela. Preparation and characterization of Pt-$CeO_2$ and Pt-Pd electrocatalysts for the oxygen reduction reaction in the absence and presence of methanol in alkaline medium. Int. J. Hydrog. Energy. 38 (2013) 12657-12666.
[19] L.P.A. Guerrero-Ortega, E. Ramírez-Meneses, R. Cabrera-Sierra, L.M. Palacios-Romero, K. Philippot, C.R. Santiago-Ramírez, L. Lartundo-Rojas, A. Manzo-Robledo. Pd and Pd@PdO core–shell nanoparticles supported on Vulcan carbon XC-72R: comparison of electroactivity for methanol electro-oxidation reaction. J. Mater. Sci. 54 (2019) 13694-13714.

[20] C. Xu, P.k. Shen, Y. Liu. Ethanol electrooxidation on Pt/C and Pd/C catalysts promoted with oxide. J. Power Sources. 164 (2007) 527-531.
[21] E.L.S. A.M. Sheikh, L. Moares, L. M. Antonini, Mohammed Y. Abellah, C.F. Malfatti. Pd-based catalyst for ethanol oxidation in alkaline electrolyte. J Min Metall. 2 (2014) 64-69.
[22] H. Wang, C. Xu, F. Cheng, S. Jiang. Pd nanowire arrays as electrocatalysts for ethanol electrooxidation. Electrochem. Commun. 9 (2007) 1212-1216.
[23] Y. Wang, F.-F. Shi, Y.-Y. Yang, W.-B. Cai. Carbon supported Pd–Ni–P nanoalloy as an efficient catalyst for ethanol electro-oxidation in alkaline media. J. Power Sources. 243 (2013) 369-373.

# Appendix

# Academic production

Journal publications:

- **P.C. Meléndez-González**, M.E. Sánchez-Castro, I.L. Alonso-Lemus, R. Pérez-Hernández, B. Escobar-Morales, A.M. Garay-Tapia, F.J. Rodríguez-Varela. Highly active Pd-$CeO_{2\text{-}NR}$/C (Cerium Oxide Nanorods) bifunctional nanocatalysts with remarkable stability for the ethanol oxidation and oxygen reduction reactions in alkaline media. ECS Trans. 2019 ;92: 671-678.

- **P.C. Meléndez-González**, M.E. Sánchez-Castro, I.L. Alonso-Lemus, R. Pérez-Hernández, B. Escobar-Morales, A.M. Garay-Tapia, W.J. Pech-Rodríguez, F.J. Rodríguez-Varela. Bifunctional Pd-$CeO_2$ nanorods/C nanocatalysts with high electrochemical stability and catalytic activity for the ORR and EOR in alkaline media. ChemistrySelect 2020; 5: 14032-14040.

- **P.C. Meléndez-González**, E. Garza-Duran, J.C. Martínez-Loyola, P. Quintana-Owen, I.L. Alonso-Lemus, F.J. Rodríguez-Varela. Enhanced catalytic activity of low-Pt content nanocatalysts supported on hollow carbon spheres for the ORR in alkaline media. MRS Advances 2020; 5: 2961-2972.

- **P.C. Meléndez-González**, O.J. Duarte-Urbina, F. Fernández-Luqueño, B. Escobar-Morales, P. Quintana, F.J. Rodríguez-Varela, I.L. Alonso-Lemus. Red onions waste-derived biocarbons with remarkably high catalytic activity for the oxygen reduction reaction and high capacitance. *In process*.

- X. Atanacio-Sánchez, W.J. Pech-Rodríguez, E.N. Armendáriz-Mireles, J.A. Castillo-Robles, **P.C. Meléndez-González**, E. Rocha-Rangel. Improving

performance of ZnO flexible dye sensitized solar cell by incorporation of graphene oxide. Microsyst. Technol. 2020; 26: 3591-3599.

- W.J. Pech-Rodríguez, F.J. Rodríguez-Varela, G.G. Suarez-Velázquez, **P.C. Meléndez-González**, E. N. Armendariz-Mireles. Insight into the effect of green methanol functionalization of Vulcan on the catalytic activity $Pt_1Sn_1$ alloy for the Ethanol Oxidation Reaction in acid and alkaline media. J. Mater. Res. 2021; 1-10.

- A. Hernández-Ramírez, F.J. Rodríguez-Varela, **P.C. Meléndez-González**, M.E. Sánchez Castro. Catalytic activity of Pt-$CoTiO_3$ nanocatalysts supported on reduced graphene oxide functionalized with Cr organometallic compounds for the oxygen reduction reaction J. Mater. Res. 2021; 1-15.

Congress:

- **P.C. Meléndez González**, M.E. Sánchez Castro, I.L. Alonso Lemus, R. Pérez Hernández and F.J. Rodríguez Varela. Pd-$CeO_{2\text{-}NR}$/C Nanocatalysts with high catalytic activity and stability for the electro-oxidation of ethanol in alkaline media. XVIII International Congress of the Mexican Hydrogen Society. September 18$^{th}$ to 21$^{st}$, 2018 in Mexico City, Mexico. Oral presentation.

- **P.C. Meléndez-González**, M.E. Sánchez-Castro, I.L. Alonso-Lemus, B. Escobar-Morales, W.J. Pech-Rodríguez, T.F. Messa-Moreira, T.W. Napporn, F.J. Rodríguez-Varela. Copper organometallic compounds as functionalizing agents of Vulcan XC-72: advanced support of Pd-based electrocatalysts with high catalytic activity for the electro-oxidation of ethanol. Second International Energy Storage Congress. March 12$^{th}$ to 13$^{th}$, 2020. Monterrey, Mexico. Poster presentation.

- **P.C. Meléndez-González**, M.E. Sánchez-Castro, I.L. Alonso-Lemus, B. Escobar-Morales, W.J. Pech-Rodríguez, T.W. Napporn, F.J. Rodríguez-Varela. Enhancing the catalytic activity of Pd nanoparticles for the ethanol oxidation reaction in alkaline media by developing a Vulcan support functionalized with the Mesityl Cu organometallic compound. 71$^{st}$ Annual

Meeting of the International Society of Electrochemistry. 31 August to 4 September 2020. Belgrade Serbia-Online. Poster presentation.

- **P.C. Meléndez-González**, M.E. Sánchez-Castro, I.L. Alonso-Lemus, B. Escobar-Morales, W.J. Pech-Rodríguez, T.W. Napporn, F.J. Rodríguez-Varela. High-performance Pd nanocatalyst supported on Vulcan XC-72 functionalized with Cu organometallic compounds for the ethanol oxidation reaction in alkaline media. XX International Congress of the Mexican Hydrogen Society. September 23-25, 2020. Oaxaca, Oaxaca-Online. Oral presentation.

- **P.C. Meléndez-González**, M.E. Sánchez-Castro, I.L. Alonso-Lemus, B. Escobar-Morales, W.J. Pech-Rodríguez, T.W. Napporn, F.J. Rodríguez-Varela. Mesityl Copper (Cu-mes): organometallic copper compound as agent functionalizing of carbon Vulcan XC-72 Pd based nanocatalysts support for the ethanol electro-oxidation in alkaline media. XXXV Congreso Nacional de la Sociedad Mexicana de Electroquímica (SMEQ) 2020 and 13th Meeting of the Mexican Section of the Electrochemical Society (ECS). 14-16 Octuber 2020, Cd. Juarez Chihuahua-Online. Poster presentation.

Research stay:

- Université de Poitiers, IC2MP UMR (septembre 2019-February 2020).

The doctoral stay was carried out in the SAMCat research group of the "Institut de Chimie des Milieux et des Matériaux de Poitiers"- IC2MP under the supervision of Dr. Têko W. Napporn, in the framework of the project "Mechanisms, efficiency and selectivity of electrocatalytic oxidation products of organic molecules". Electrochemical characterization of Pd-based nanocatalysts supported on Vulcan functionalized with Cu organometallic compounds for the ethanol oxidation reaction was performed to determine the by-products formed during the reaction, using in situ and ex situ techniques available at SAMCat.